

JANNE RUUSKANEN

Modelling Nonlinear Effects in High Temperature Superconducting Magnets

JANNE RUUSKANEN

Modelling Nonlinear
Effects in High
Temperature
Superconducting
Magnets

ACADEMIC DISSERTATION

To be presented, with the permission of
the Faculty of Information Technology and Communication Sciences
of Tampere University,
for public discussion in the auditorium TB109
of Tietotalo, Korkeakoulunkatu 1, Tampere,
on 10 January 2020, at 12 o'clock.

ACADEMIC DISSERTATION

Tampere University, Faculty of Information Technology and Communication Sciences
Finland

<i>Responsible supervisor and Custos</i>	Adj. Prof. Antti Stenvall Tampere University Finland	
<i>Supervisor</i>	Dr. Valtteri Lahtinen Tampere University Finland	
<i>Pre-examiners</i>	Assoc. Prof. Antonio Morandi University of Bologna Italy	Prof. Benoît Vanderheyden University of Liège Belgium
<i>Opponents</i>	Assoc. Prof. Antonio Morandi University of Bologna Italy	Dr. Francesco Grilli Karlsruhe Institute of Technology Germany

The originality of this thesis has been checked using the Turnitin OriginalityCheck service.

Copyright ©2020 author

Cover design: Roihu Inc.

ISBN 978-952-03-1418-7 (print)
ISBN 978-952-03-1419-4 (pdf)
ISSN 2489-9860 (print)
ISSN 2490-0028 (pdf)
<http://urn.fi/URN:ISBN:978-952-03-1419-4>

PunaMusta Oy – Yliopistopaino
Tampere 2020

PREFACE

I started working in the research group Electromagnetics in 2012 as a summer trainee. The next summer I got a project offer on programming a simulation tool for modelling high-temperature superconductors. It felt like I was at the base of a monumental mountain, and the goal was to reach the summit with style. The problem was, I did not know how to climb that mountain. Despite of that, I accepted the challenge.

Quite a few years and adventures later I am writing these words, being forever grateful for the education and knowledge I got from the research group of Electromagnetics. The atmosphere in that community was unique – it was an ideal research group to work in. I would like to thank all my colleagues for your kindness and support, and for the amazing atmosphere at work. My special gratitude goes to my supervisors Antti Stenvall and Valteri Lahtinen for the excellent guidance and support during these years. Thank you for the expedition into the world of science.

The research topics scrutinized in this thesis are mainly related to the EUCARD2 project partially targeted for designing and developing high-temperature superconducting particle accelerator magnets. During the academic year 2016-2017 I had a great privilege to work at CERN, in the focal point of the project, for a six month period. For that opportunity, and the research ideas that flourished during the research exchange, I am greatly thankful for Jeroen Van Nugteren and Glyn Kirby. In addition, I would like to thank all my colleagues at CERN. Your kindness and hospitality was one of the kind.

Finally, I would like to thank my family and all my friends for your support and all the great moments we have shared together.

In Tampere, December 19, 2019

Janne Ruuskanen

ABSTRACT

In the future particle colliders, the accelerator magnets keeping the particles on their tracks are required to produce magnetic fields above 20 T. This can be achieved only by using high temperature superconductors. The technology for producing the high temperature superconducting (HTS) conductors is relatively new and only recently the number of HTS conductor manufacturers has started to increase. It was only in 2016, when a 10 kA class Roebel cable made of REBCO tapes was tested in a small study coil, Feather-M0. Followed by that, in 2017 the first Roebel cable based 5 T accelerator magnet prototype Feather-M2 was constructed and tested to examine the prospects of HTS REBCO technology in accelerator magnets. The measurement results suggested that there is still a lot to learn in modelling those magnets.

This thesis begins by introducing the readers to the mathematical and physical background for understanding the research presented in the attached publications. The background is followed by the chapters reviewing and synthesizing the publications. The focus in this thesis is on the AC loss modelling and thermal stability modelling. First, AC losses and magnetic field quality are modelled in Feather-M0 using a self-implemented minimum magnetic energy variation principle based simulation tool. Then, the focus is moved on the thermal stability modelling of HTS magnets by formulating the thermal model utilized in this thesis work. Next, the thermal model is utilized for scrutinizing the behavior of Feather-M2 with an inverse problem based modelling approach. Using the Feather-M2 measurement data, the inverse problem solutions are obtained for the thermal model parameters characterizing the magnet in terms of the thermal model. Furthermore, the thermal model is utilized and an optimization problem is formulated in order to determine the maximum stable operation current of Feather-M2. Finally, an energy-extraction system (EES) design for 20 T range magnet is presented and optimized by formulating and solving an optimization problem.

CONTENTS

1	Introduction	1
1.1	Motivation	2
1.2	Structure of the Thesis	3
2	Background	5
2.1	From fundamentals of superconductivity to HTS Roebel cables	6
2.1.1	Basics	6
2.1.2	REBCO tapes	8
2.1.3	Roebel cables	10
2.2	HTS in high energy physics	11
2.2.1	From LHC toward HTS based high field accelerators	11
2.2.2	The Feather-magnet prototype series	13
2.2.2.1	Feather-M0	13
2.2.2.2	Feather-M2	14
2.3	An introduction to HTS modelling	17
2.3.1	$E(J)$ relation in superconductors	18
2.3.2	Losses	21
2.3.3	Quench	22
2.4	The Galerkin-FEM for solving 1-D heat diffusion equation in HTS magnet	23
2.4.1	Weak formulation of the problem	24
2.4.2	Discretization: The Ritz-Galerkin approximation	25
2.4.3	Constructing the basis functions	26
2.4.4	Heat transfer between cable turns using FDM	27

2.5	The minimum magnetic energy variation principle	29
2.5.1	The Maxwell's equations in magnetoquasistatics	30
2.5.2	The variational formulation of the CSM	31
2.6	On the practical optimization	32
2.6.1	Formulating an optimization problem	33
2.6.2	The primal-dual interior point methods	33
2.6.3	Inverse problems	34
2.7	Summary and remarks	34
3	Modelling AC losses in Feather-M0 with MMEV	37
3.1	Problem formulation	38
3.1.1	Modelling domain	38
3.1.2	Solving current distribution using MMEV principle	39
3.1.3	The critical state model and $J_c(\mathbf{B})$ dependency	41
3.1.4	AC loss computation	43
3.1.5	Magnetic distortion	44
3.2	Simulation results	44
3.2.1	Current distribution	45
3.2.2	AC losses	47
3.2.3	Magnetic distortion	48
3.3	Concluding remarks	51
4	Modelling thermodynamics in HTS magnets	55
4.1	The heat diffusion equation	56
4.2	Modelling domain and its discretization	56
4.3	Material properties	58
4.4	$E(J)$ relation in the superconductor	58
4.5	Heat generation	60
4.6	Cooling	61
4.7	Heat diffusion between the cable turns	61
4.8	Remarks	62

5	Modelling thermodynamics in Feather-M2	63
5.1	Modelling thermodynamics in Feather-M2 using an inverse problem based approach	64
5.1.1	Measurement data	64
5.1.2	Methodology	66
5.1.3	Simulation results	67
5.2	Computational determination of the maximum stable operation cur- rent	70
5.2.1	Methodology	72
5.2.2	Simulation results	73
5.2.3	Concluding remarks	76
5.3	Summary	76
6	E ³ SPreSSO: An energy-extraction system design for high-field HTS magnets	79
6.1	Methodology	80
6.1.1	Circuit model	80
6.1.2	Thermal model	83
6.1.3	Optimization problem formulation	84
6.2	Simulation results	86
6.2.1	Comparing different superconductors for the switch	86
6.2.2	Electro-thermal behaviour of design based on case 9	88
6.2.3	Varying allowed maximum temperature	89
6.3	Concluding remarks	90
7	Conclusions	93
	References	97
	Publication I	113
	Publication II	121
	Publication III	141
	Publication IV	149

Publication V	157
Publication VI	165

ABBREVIATIONS

A	Cross-sectional area
A^i	Area of element i
A^z	The z -component of A
A_c^z	The z -component of A_c
A_m	Cross-section area of magnet cable
A_{nc}	Cross-sectional area of normal conducting material
A_p	Cross-section area of the parallel resistor in E ³ SPreSSO system
A_{sc}	Cross-sectional area of superconducting material
A_s	Cross-section area of the switch cable in E ³ SPreSSO system
B	The norm of \mathbf{B}
B_0	A Kim model parameter
$B_{ }$	Magnetic field component parallel with the wide face of superconducting tape
B_{\perp}	Magnetic field component perpendicular with the wide face of superconducting tape
B_{c1}	Lower critical magnetic flux density
B_{c2}	Upper critical magnetic flux density
B_c	Critical magnetic flux density
B_m	Magnetic flux density in the HTS magnet winding
C	A vector representing the contribution of $\Delta\mathbf{A}_a$ on modelling domain Ω
C_V	Volumetric heat capacity

C_m	Heat capacity in the HTS magnet winding
C_p	Heat capacity of the parallel resistor of E ³ SPreSSO system
C_s	Heat capacity of the switch in E ³ SPreSSO system
C_i	The i th element in vector C
E	The norm of \mathbf{E}
E_c	Critical electric field
E_m	Magnet energy
E_{nc}	E in normal conducting fraction of cable
E_{sc}	E in superconducting fraction of cable
E_i	Measurement data set on average electric field
F	The functional \mathcal{F} in its discretized form.
H	The norm of \mathbf{H}
I	Electric current
I_T	Thyristor current
I_c	Critical electric current
I_{mas}	Maximum stable operation current
I_{nc}	I in normal conducting fraction of cable
I_{op}	Operation current
I_p	Current in parallel resistor
I_{sc}	I in superconducting fraction of cable
I_{st}	Current in the stabilizer of a superconductor
J	The norm of \mathbf{J} .
J_{c0}	A Kim model parameter
J_c	Critical electric current density
J_h	Homogeneous current density distribution
J_m	Magnetization current density distribution
J_{nc}	Current density in normal conducting fraction of cable

J_{sc}	Current density in superconducting fraction of cable
L	Inductance
M	Mutual inductance matrix
N	A dimension index
N_E	Number of E ³ SPreSSO units
Q	Source term
Q^+	Heat generation
Q^-	Cooling flux
$Q_{ }$	Heat flux between the cable turns in a magnet
Q_i	i th load vector element
R_p	Resistance of parallel resistor
R_{sc}	Resistance of superconducting material in superconducting wire
R_{st}	Resistance of stabilizer in superconducting wire
S	A function space
T	Temperature
T_0	Initial temperature
T_{adj}	Temperature in an adjacent cable turn
T_c	Critical temperature
T_{max}	Maximum temperature
T_m	Temperature in the HTS magnet winding
T_{op}	Operation temperature
T_p	Temperature of the parallel resistor in E ³ SPreSSO system
T_s	Temperature of the switch in E ³ SPreSSO system
T_j	The temperature related to the j th basis function ϕ_j
U	A function space
V_C	Capacitor voltage
V_E	Voltage over an E ³ SPreSSO unit

V_T	Thyristor voltage
V_{\max}	Maximum voltage
V_{th}	Thyristor threshold voltage
V_{c0}	Initial capacitor voltage
W	A magnetic energy integral
ΔI_s	Change of I in the sub-domain s
ΔJ	A variation in the current density distribution
ΔJ_i	Variation of J in element i
$\Delta \mathbf{A}_j$	A variation of \mathbf{A}_j in time.
$\Delta \mathbf{A}_a$	The variation of \mathbf{A}_a in time.
Δ_m	Maximum difference
Δ_r	Relative difference
Δt	Time-step
Ω	Modelling domain
Ω_s	A sub-domain
Π	Mass matrix
Π_{ij}	The mass matrix element at the i th row and j th column
α	J_c scaling law coefficient
$\bar{\lambda}_i$	Local thermal conductivity of insulation material evaluated at the average temperature of two adjacent cable turns in magnet winding
β	A Kim model parameter
δ_{ij}	The Dirichlet function for indices i and j
\dot{T}	The time-derivative of temperature
ϵ	Permittivity
\hat{A}_s	Cross-section area of a single superconductor strand
$\hat{\mathbf{B}}$	Magnetic flux density per unit current ($[T/A]$) in vector form.
λ	Thermal conductivity

λ_i	Insulation material thermal conductivity
\mathbb{R}	The set of real numbers
\mathbb{R}^N	The N -dimensional real coordinate space
\mathcal{F}	The MMEV functional
\mathcal{L}'	A functional density
\mathcal{L}	A functional density
\mathcal{P}	The AC loss power
\mathcal{Q}	AC loss per cycle
\mathcal{U}	A potential function
\mathfrak{C}	Capacitance
f	A function
g	A function
g_i	A function indexed with i
h	A function
h_j	A function indexed with j
C	Total cooling power in magnet winding
P	Total heating power in magnet winding
μ	Permeability
μ_0	The vacuum permeability
ω_{A_p}	E ³ SPreSSO optimization parameter weighted with A_p
ω_{A_s}	E ³ SPreSSO optimization parameter weighted with A_s
ω_{N_E}	E ³ SPreSSO optimization parameter weighted with N_E
$\omega_{V_{e0}}$	E ³ SPreSSO optimization parameter weighted with V_{e0}
$\omega_{\mathfrak{C}}$	E ³ SPreSSO optimization parameter weighted with \mathfrak{C}
ω_{l_p}	E ³ SPreSSO optimization parameter weighted with l_p
ω_{l_s}	E ³ SPreSSO optimization parameter weighted with l_s
∂_t	A short notation for the time-derivative operator $\partial/\partial t$

ϕ_i	The i th basis function
ϕ_j	The j th basis function
K	Stiffness matrix
K_{ij}	The stiffness matrix element at the i th row and j th column
M	A model, an operator, a mapping
nc	normal conducting
sc	superconducting
ρ	Electrical resistivity
ρ_m	Resistivity in the HTS magnet winding
ρ_{nc}	Resistivity of the normal conducting material
ρ_p	Resistivity of the parallel resistor in E ³ SPreSSO system
ρ_s	Resistivity of the switch in E ³ SPreSSO system
σ	Electrical conductivity
θ	Direction of \mathbf{B} with respect to the tape orientation
φ	A scalar function
A_c	Magnetic vector potential of the sub-critical region.
A	Magnetic vector potential
A_J	Magnetic vector potential produced by electric currents inside the modelling domain.
A_a	Applied magnetic vector potential due to electric currents outside the modelling domain.
B	Magnetic flux density, a vector field
D	Electric flux density
E	Electric field intensity, a vector field
H	Magnetic field intensity, a vector field
J_0	Current density at instant of time t_0 .
J	The electric current density, a vector field
Q	Load vector

T	A temperature vector with multiple elements
b_l	A vector of parameter-wise lower bounds
b_u	A vector of parameter-wise upper bounds
r'	Location with respect to the coordinate system origin
r	Location with respect to the coordinate system origin
x	Parameter vector containing multiple elements
c	Wetting coefficient
d	Measurement data
d_i	Insulation thickness
d_t	Total cable thickness
d_w	Total cable width
f	material fraction
f_A	An adjacency mapping
f_m	Fraction of superconducting material in magnet cable
f_{nc}	Fraction of normal conducting material in cable
f_{sc}	Fraction of superconducting material in cable
f_s	Fraction of superconducting material in the switch cable in E ³ SPreSSO system
b	Cooling coefficient
i	an index
i	an index
k	A Kim model parameter
l	Length
l_p	Length of the parallel resistor in E ³ SPreSSO system
l_s	Length of the switch cable in E ³ SPreSSO system
m	An index
m'	An index
n	Superconductor n -value

p	The wetting perimeter
t_0	Initial instant of time
t_c	Stability criterion time
t_m	Measurement duration time
v	A scalar function
x	A parameter
x_i	The i th x -coordinate
y	a parameter
$J_{c,j}$	J_c in element j
AC	Alternating current
BVP	Boundary value problem
CC	Current constraint
CERN	The European Organization for Nuclear Research
CLIQ	Coupling loss induced quench system
CSM	The critical state model
CuNi	Copper-Nickel
DC	Direct current
E ³ SPreSSO	External Energy Extraction Symbiotic Protection System for Series Operation
ECM	Eddy current model
EES	Energy-extraction system
EUCARD2	Enhanced European coordination of accelerator research and development
FEM	Finite difference method
FEM	Finite element method
GdBCO	Gadolinium barium copper oxide. A REBCO compound.
HTS	High-temperature superconductor
IBAD	The Ion Beam Assisted Deposition

IPOPT	The interior-point optimization algorithm
K	Stiffness matrix
KIT	Karlsruhe Institute of Technology
LHC	Large Hadron Collider
LTS	Low temperature superconductor
MEMEP	Minimum electro-magnetic entropy production principle
MgB ₂	Magnesium diboride. An HTS material.
MMEV	Minimum magnetic energy variation principle
Nb ₃ Sn	Niobium-tin, low temperature superconducting material.
NBC	Neumann boundary condition
NbTi	Niobium-titanium, low temperature superconducting material.
REBCO	Rare-earth barium copper oxide. A family of high temperature superconducting compounds.
SS	Stainless steel
YBCO	Yttrium barium copper oxide. A REBCO compound.

ORIGINAL PUBLICATIONS

- Publication I J. Ruuskanen, A. Stenvall and V. Lahtinen. Utilizing Triangular Mesh With MMEV to Study Hysteresis Losses of Round Superconductors Obeying Critical State Model. *IEEE Transactions on Applied Superconductivity* 25.3 (2015), 8200405. DOI: 10.1109/TASC.2014.2365408.
- Publication II J. Ruuskanen, A. Stenvall, V. Lahtinen and E. Pardo. Electromagnetic nonlinearities in a Roebel-cable-based accelerator magnet prototype: variational approach. *Superconductor Science and Technology* 30.2 (2016), 024008. DOI: 10.1088/1361-6668/30/2/024008.
- Publication III J. Ruuskanen, A. Stenvall and V. Lahtinen. Predicting heat propagation in Roebel-cable-based accelerator magnet prototype: One-dimensional approach with coupled turns. *IEEE Trans. Appl. Supercond.* 27.4 (2017), 0600205. DOI: 10.1109/TASC.2016.2630844.
- Publication IV J. Ruuskanen, A. Stenvall, J. van Nugteren and V. Lahtinen. Optimization of an E³SPreSSO Energy-Extraction System for High-Field Superconducting Magnets. *IEEE Transactions on Applied Superconductivity* 29.5 (2018), 4700805. DOI: 10.1109/TASC.2018.2794457.
- Publication V J. Ruuskanen, A. Stenvall, V. Lahtinen, J. van Nugteren, G. Kirby and J. Murtomäki. How to Computationally Determine the Maximum Stable Operation Current of an HTS Magnet. *IEEE Transactions on Applied Superconductivity* 29.5 (2019), 4701204. DOI: 10.1109/TASC.2019.2898315.

Publication VI J. Ruuskanen, A. Stenvall, V. Lahtinen, J. van Nugteren, G. Kirby and J. Murtomäki. Modelling thermodynamics in a high-temperature superconducting dipole magnet: an inverse problem based approach. *Superconductor Science and Technology* 32.9 (2019), 094007. DOI: 10.1088/1361-6668/ab2bc9.

Author's contribution

This thesis consists of 6 publications. The processes related to each of them went through a problem solving process where in order to solve an engineering problem, a modelling methodology was developed and implemented into computer program. Using the program, simulations were performed in order to obtain information for understanding and solving the original problem. In the publications, this process is detailed.

The collaboration with CERN's Superconducting Magnet Design and Technology Section was crucial for this thesis. J. van Nugteren, G. Kirby and J. Murtomäki provided essential information regarding the problems investigated in publications III-VI. Moreover, the measurement data utilized in solving the inverse problems in publication VI was provided by them.

The programming work in implementing the computer programs utilized in this thesis work was done by the author, who moreover performed all the simulations in the publications.

In all of publications, all the text was written by the author, with the exception of publication II where the co-author E. Pardo helped in the writing related to the utilized numerical method. Furthermore, collaboration with him was essential in the work done during the research and writing process of the publication. Furthermore, in the writing processes of all the publications, the discussions and guidance of A. Stenvall and V. Lahtinen were indispensable.

Detailed author's contribution for each publication

Publication I

The author adopted and implemented the algorithm based on the MMEV principle into a computer program in C++ programming language. E. Pardo helped in understanding the details related to the algorithm. The author utilized the program for simulating losses in round superconductors using different mesh types. A. Stenvall and V. Lahtinen helped in the proofreading process. The author wrote the publication.

Publication II

A modelling methodology was implemented in C++ where an optimization algorithm library IPOPT was utilized for solving the problem. The author implemented the simulation tool and performed the simulations for the publication. E. Pardo helped in understanding the physical background behind the utilized MMEV principle. He also helped in writing about the physical background. Otherwise, the author wrote the publication and was responsible for preparing the final manuscript for publication. E. Pardo, A. Stenvall and V. Lahtinen helped in the proofreading process.

Publication III

The author implemented a modelling methodology in Matlab for thermal simulation of superconducting magnets. In the implementation process, A. Stenvall and V. Lahtinen helped in designing the simulation tool architecture and functionalities. The author utilized the implementation for modelling heat propagation in Feather-MO prototype magnet. Crucial information regarding the magnet geometry and the operation parameters was provided by J. van Nugteren. The author was responsible for writing the publication. In the proofreading process, the help of A. Stenvall and V. Lahtinen was essential.

Publication IV

A methodology for optimizing a protection system design was developed by the author with the help of A. Stenvall and V. Lahtinen. J. van Nugteren provided invaluable insight in understanding the operational principle of the protection system. The author programmed a simulation tool based on the developed methodology, and utilized it optimizing the design. Moreover, the author wrote the publication with the proofreading help of A. Stenvall, V. Lahtinen and J. van Nugteren.

Publication V

The publication is based on an observation made when measuring the behavior of Feather-M2 in operation. In the measurements, it was not clear how to determine the maximum current of the magnet. Therefore, by the author, a modelling methodology was developed and implemented for solving the maximum current in magnets exhibiting gradual dependency between the measured voltage and the operation current. The developed simulation tool was based on the thermal modelling simulation tool implemented for publication III. A. Stenvall, V. Lahtinen and J. Murtomäki helped in ideation of the methodology. J. van Nugteren provided the measurement data for analyzing the magnet behavior. The author wrote the publication with the proofreading help of A. Stenvall, V. Lahtinen J. van Nugteren and G. Kirby.

Publication VI

Based on the Feather-M2 measurement data, provided by J. van Nugteren, an inverse problem based modelling methodology and simulation tool implementation was done by the author. Using the simulation tool, several inverse problems were solved using the measurement data in order to understand the magnet behavior. This work was done by the author. Moreover, the publication was written by the author, A. Stenvall and V. Lahtinen helped in the proofreading.

1 INTRODUCTION

Since the discovery of the superconductivity in 1911, various superconducting compounds and practical conductors made of them have been developed for different applications such as magnetic resonance imaging devices and particle accelerator magnets. The world's largest particle accelerator complex at CERN [110], the Large Hadron Collider [111] (LHC) utilizes accelerator magnets based on NbTi low temperature superconductors (LTS) being able to produce ~ 8 T magnetic field. To be able to accelerate the particles into higher energies, the accelerator magnets need to produce higher magnetic fields for keeping the particles in their tracks. Currently, several options for the successor of LHC are considered. One of them is to have 20 T bending magnets in a 80 km ring. With this kind of accelerator one could produce 100 TeV center of mass collisions with protons. According to current understanding, high temperature superconductor technology is the only option for realizing the required bending magnets. [11].

In terms of current carrying capacity in high magnetic field, the most promising technical high temperature superconductors (HTS) are the Rare-earth Barium Copper Oxide (REBCO) coated conductors [120]. The start did not look promising for them to become a part of accelerator magnets due to their high price and difficulties in manufacturing long length wires with uniform quality. Currently, however, there are many commercial manufacturers of REBCO tapes [97] and the first multi-tape REBCO cables, Roebel cables, anticipated for high current accelerator magnets have been already manufactured and tested [40].

The first REBCO Roebel accelerator magnet prototypes, Feather-M0 and Feather-M2, were designed and tested within the Enhanced European coordination of accelerator research and development [91] (EUCARD2) project at CERN. The latest prototype was designed to produce 5 T magnetic field. That being an intermediate step, designs for Roebel cable based accelerator magnets producing magnetic fields of ~ 20 T and above have been already made [74]. However, before being able to

design and construct successfully the 20 T range magnets, the HTS modelling needs to be further developed.

1.1 Motivation

REBCO Roebel cables and especially magnets made of them are very expensive devices. Therefore they need to be designed with the utmost care and with complete understanding related to modelling them.

Designing a magnet is an extensive process. The behavior of the magnet in operation needs to be simulated from the point of view of electromagnetic behavior, thermal stability and mechanical behavior. Simulating all of those behaviors at once using a coupled model is not practical. Thus, in the design process the magnet is simulated using separate models for ensuring the desired magnet behavior from the different point of views.

Closely related to the magnet design process is the design of the magnet protection system, which discharges the magnet safely in case of loss of stable operation. In the design process, by means of modelling, safe magnet discharge has to be ensured from all the point of views: electromagnetic, thermal and mechanical.

Modelling REBCO Roebel cables is not trivial, nor is modelling magnets based on them. The difficulties arise from the material properties that are not straightforward to characterize using macroscopic models. The voltage-current relation in a REBCO tape depends for example on the current, temperature, magnetic field and its direction with respect to the tape orientation. In addition, it depends on the mechanical forces and their directions with respect to the tape orientation.

There is still a lot of work in completing our understanding related behavior of REBCO materials and modelling them. Important part of this is the characterization of REBCO material in terms of the voltage-current relation. Moreover, modelling of HTS tapes and devices made of them is a relatively young branch in the field of modelling superconductors. Hence, different modelling methodologies need to be scrutinized in order to gain knowledge on, what kind of modelling approach or method works the best for a given problem [42]. A crucial driving force behind the HTS modelling is the HTS modelling workgroup [47].

In this thesis work, various modelling methodologies were developed for increasing the community's understanding on the behavior of the Roebel cable based mag-

nets. This will help the wide ranging science aiming on 20 T particle accelerator magnet technology. Using the developed methodologies, the Feather prototype magnets were scrutinized from the electromagnetic and thermal stability point of view. In addition in this thesis work, a methodology was developed for optimizing a magnet protection system suitable for 20 T range HTS magnets. An important part of the developed modelling approaches was the use of mathematical methods such as concepts of optimization, the finite element method and the inverse problem theory.

1.2 Structure of the Thesis

This thesis is structured as follows. Chapter 2 discusses on the physical and mathematical background related to the main focus of this thesis, modelling of high temperature superconducting magnets. First, after introducing the superconductivity as a phenomenon, REBCO Roebel cable based Feather-magnets, scrutinized in this thesis work, are presented. Then, modelling of superconductors is discussed. Based on that, two approaches for modelling losses in the Feather-magnets are presented in detail. Finally, the topic of practical optimization is discussed, being an essential concept in solving problems in this thesis work.

In chapter 3, using the minimum magnetic energy variation principle, the Feather-M0 is studied. The electric current distribution, AC losses, and magnetic field quality in the magnet are computed and the simulation results are presented.

Chapter 4 presents the formulation of the thermal model for predicting resistive losses and thermal stability in Feather-M2. Based on the thermal model, in chapter 5, modelling methodology for determining the maximum stable operation current of Feather-M2 is presented. In addition, the modelling methodology and simulation results are presented on the study where the thermal model was parametrized and the parameter values were solved by obtaining solutions to inverse problems based on Feather-M2 measurement data.

In chapter 6 a study on optimizing a magnet protection system design, where a coupled thermal and circuit model characterizing the physical system was parametrized. Optimal values for the parameters were obtained by solving an optimization problem, where the optimality was defined by the constraints and the objective function to be minimized.

Finally, the thesis work is summarized and conclusions are drawn in chapter 7.

2 BACKGROUND

In this chapter, the background knowledge for understanding the work done in this thesis is given. Target audience is beginning doctoral students of electrical engineering in the field of high temperature superconductor modelling. Section 2.1 briefly discusses those engineering concepts that are important for modelling applications utilizing superconductivity. Also, so called REBCO tapes and Roebel cables are introduced. In section 2.2, the topic of high temperature superconducting accelerator magnets, being the main context for research in this thesis, is presented. First, state-of-the-art accelerator magnets and some future directions are covered. Then, the high temperature superconductor based prototype magnets, analyzed in this thesis, are presented.

In section 2.3, an introduction to the modelling of high temperature superconductors and magnets made of them is given. Essentially, the modelling of superconductors comes down to modelling the generated losses and hence the thermal stability. This is of the utmost importance in the design process of devices such as superconducting magnets. In addition, closely related with the magnet design process is the design of the de-energization system. Such systems are crucial for protecting the magnet from damage in cases of an irreversible thermal runaway, i.e. a quench.

In this thesis, the losses that are generated in superconductors are categorized into two different types: resistive losses (or DC losses) and AC losses¹, as will be discussed later in section 2.3.2. In modelling the losses, the fundamental issues are related to describing the constitutive relation, resistivity, between electric field and electric current density. This topic is discussed in section 2.3.1.

A significant part of the contribution of this thesis is in developing modelling methodologies for solving heat transfer problems in superconducting magnets. This requires knowledge on modelling resistive losses in superconductors. In this thesis work, the heat transfer problems are formulated and solved as boundary value

¹The notations DC and AC denote the direct and the alternating electric current, respectively.

problems (BVP). In the utilized approach, the heat transfer problems are solved on 1-dimensional modelling domain, where the heat transfer between between the magnet's cable turns is taken into account. A widely used general solution method for BVPs, the Galerkin finite element method (FEM), is detailed in section section 2.4 where a method for taking into account the heat transfer between the cable turns by means of finite difference method is also detailed. The formulation of the partial differential equation of the BVP and its solution with FEM are presented in chapter 4.

In this thesis, the AC losses are investigated and modelled based on the minimum magnetic energy variation principle, for which, a theoretical background starting from the Maxwell's equations is given in section 2.5.

Formulating and solving optimization problems arising from engineering problems play a big role in this thesis. Hence, section 2.6 discusses optimization as follows. First, a way to formulate optimization problems is presented and then a class of algorithms, utilized in this thesis work, for solving these problems is briefly introduced.

2.1 From fundamentals of superconductivity to HTS Roebel cables

Superconductivity is a state of matter where the electrical resistivity has vanished. This phenomenon was discovered in 1911 by Kamerlingh Onnes for mercury[76]. This section reviews those concepts of superconductivity that are important for designing applications.

2.1.1 Basics

The superconducting materials were observed to exhibit the superconductivity in conditions where the temperature T , the norm of the magnetic flux density (B) and the norm of the electric current density (J) were below their certain material and manufacturing dependent critical values T_c , B_c and J_c , respectively². Moreover, among with the property of zero resistivity, superconductors are characterized by

²In this thesis, the vector formalism is utilized, i.e., the field quantities such as magnetic flux density and current density are represented as vector fields and denoted as \mathbf{B} and \mathbf{J} . Their norms are denoted as B and J , respectively.

the complete expulsion of the applied magnetic field, namely the Meissner effect. This phenomenon was discovered in 1933 by Walther Meissner and Robert Ochsenfeld [66].

Further investigations revealed the existence of two different types of superconducting materials, namely, type I and type II. The distinction manifested itself in the presence of external magnetic field. The type I materials in superconducting state exhibit the Meissner effect where the material is able to expel applied magnetic field up to B_c by screening currents that are generated in the thin surface layer. If $B > B_c$, the screening currents are not strong enough and consequently the magnetic field penetrates fully into the material and the superconducting state is lost.

Type II materials exhibit the Meissner effect purely only at low magnetic fields, up to the so-called lower critical magnetic field³ B_{c1} . When further increasing the applied field, the material first enters into the so-called mixed state until finally losing the superconductivity completely at certain value of applied field, called the upper critical field B_{c2} . In the mixed state between the lower- and upper critical fields, the material is in a partially normal conducting and partially superconducting state where the magnetic field has penetrated into the material in quantized flux tubes surrounded by the screening currents trying to shield the applied magnetic field [67]. While in the flux tube cores the material is in resistive state, outside these vortices superconducting current can flow. When B is higher than the upper critical field B_{c2} , the flux tube cores overlap in the material and consequently the superconducting state is lost completely [57]. Type II materials can be used in current and magnetic field applications because their B_{c2} is much higher than B_c in type I materials where the typical values are below 100 mT. In type II materials, B_{c2} can be more than 200 T.

In the presence of both the electric current density \mathbf{J} and magnetic flux density \mathbf{B} , the Lorentz force can move the flux tubes around in type II materials. Consequently heat is generated. The flux tube movement can be reduced by adding impurities into the superconducting material. They function as pinning centers where the flux tubes attach. Consequently, moving a flux tube away from it requires force. When the pinning is strong, the Lorentz force $(\mathbf{J} \times \mathbf{B})^4$ is not able to move the flux tubes around that easily and thus heat is not generated. Moreover, the type II superconductors that

³Magnetic field is a pair (\mathbf{B}, \mathbf{H}) , where \mathbf{B} is the magnetic flux density and \mathbf{H} is the magnetic field intensity. Magnetic flux density captures the essence of magnetic dipoles and \mathbf{H} the sources of the field. In this thesis magnetic field and magnetic flux density are used interchangeably.

⁴The Lorentz force can be computed using vector formalism as $\mathbf{J} \times \mathbf{B}$, where \times denotes the cross-product.

have strong pinning are called the hard superconductors. To conclude, all industrial high current carrying superconductors are type II hard superconductors [96].

The type II superconductors can be divided into two types: high temperature superconducting (HTS) materials and low-temperature superconducting (LTS) materials. The HTS materials are defined to have a critical temperature above 30 K and the LTS materials are defined to have T_c below 30 K.

There exists many different LTS and HTS material compounds used in practical conductors. In this thesis, the focus is fully on The Rare Earth Barium Copper-Oxide [21] (REBCO) based conductors. Their current carrying capability is superior to other conductors in high magnetic fields, i.e. above 20 T [115].

2.1.2 REBCO tapes

The Rare Earth Barium Copper Oxide is a family of high temperature superconducting compounds. The two most commonly used rare earth materials are Yttrium (Y) and Gadolinium (Gd), resulting in YBCO and GdBCO compounds, respectively [75, 120]. These conductors have a capability of carrying high current densities in high external magnetic fields. For example, in [13] the overall critical current density of a REBCO tape was measured to be 1200 A/mm² at 4.2 K and 20 T.

In REBCO tapes, the critical current density depends on the temperature and on the magnitude of magnetic flux density (B). Additionally, it strongly depends on the direction of B (θ) with respect to the wide face of the tape. The perpendicular magnetic field B_{\perp} ($\theta = 90^\circ$) is defined to be perpendicular with the wide face of the tape and the parallel magnetic field B_{\parallel} ($\theta = 0^\circ$) is defined to be parallel with the wide face of the tape as illustrated in figure 2.1. Moreover, J_c depend on mechanical aspects such as strain [8].

The critical temperature T_c in REBCO materials is around 93 K. The $J_c - B - T$ dependency of REBCO material in a particular case is illustrated in figure 2.2 (a) for fixed value of θ . The dependency of J_c on θ and B for an example sample at constant temperature is shown in figure 2.2 (b), where J_c is normalized with J_{c0} corresponding to its maximum value.

Due to the high performance of REBCO based conductors, they are considered as the most promising technology for the high current high field applications in the fu-

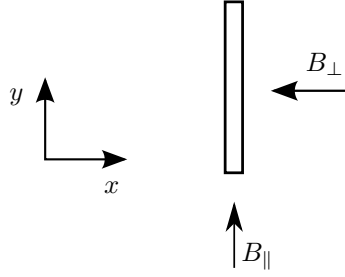


Figure 2.1 Parallel and perpendicular magnetic flux density components with respect to the wide face of a superconducting tape, when the wide face of the surface is parallel to y -axis.

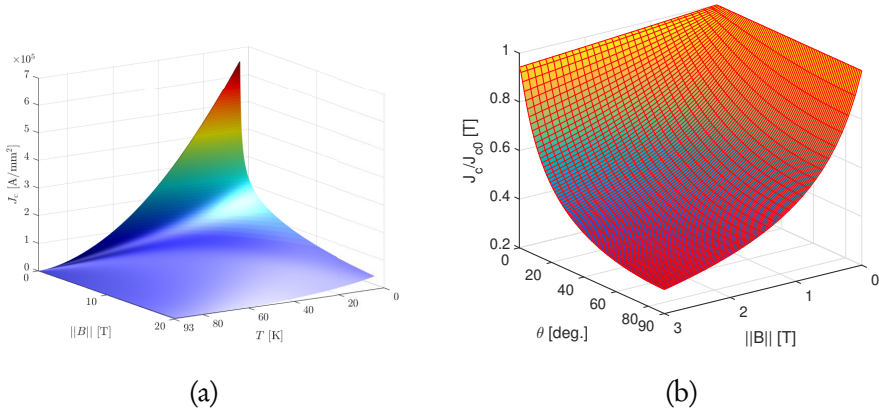


Figure 2.2 In (a), a typical critical surface of REBCO material from fixed direction of \mathbf{B} . In (b), J_{c0} normalized J_c as a function of B ($:= \|\mathbf{B}\|$) and its direction (θ) at constant temperature.

ture [39, 99]. Currently, REBCO superconductors are commercially available from many manufacturers [3, 15, 34, 106, 107, 108], to name some.

As an example of REBCO tape, figure 2.3 illustrates the structure of a REBCO tape manufactured by Fujikura [34]. All the REBCO tapes are manufactured in the form of layers. In this particular case, the tape has a $50 \mu\text{m}$ thick Hastelloy [62] substrate which provides mechanical rigidity for the tape because the REBCO layer is only $1 \mu\text{m}$ thick. The superconducting layer is coated with a copper stabilizer layer. It provides for the electric current an alternative, low resistive path in case of unexpected rise in the resistivity of the superconducting material. Furthermore, due to the high current the REBCO tapes can carry in operation, a loss of superconductivity can lead to aggressive heat generation and thermal runaway in the tape. Such event is called a quench. Therefore superconducting magnets require protection sys-

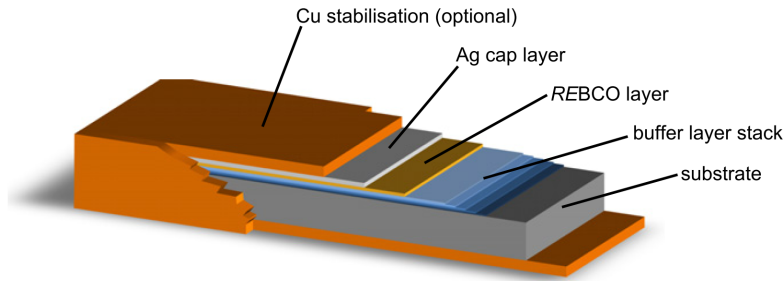


Figure 2.3 Depiction of a typical REBCO tape structure. Figure reprinted with permission from [8].

tems that de-energize the magnet rapidly if quench is detected.

Typical commercially available tapes are 4 or 12 mm wide. The REBCO tapes are manufactured using film deposition techniques [95]. For example, Fujikura utilizes the Ion Beam Assisted Deposition (IBAD) [99].

2.1.3 Roebel cables

Commercially available REBCO tapes can carry even 1000 A. However, some magnet applications, like particle accelerator magnets, require currents in the order of 10 kA. In order to harness the high current density carrying capability of REBCO tapes in high current applications, a multi-tape cable geometry is needed. Unlike in case of round wires [4], it is not straightforward to design such a cable from tapes. Fortunately, one solution for the problem was already made. This thesis focuses on that approach.

The Roebel cable geometry was invented and developed by Ludwig Roebel in the beginning of the 20th century for the needs of electric power industry, where the size of generators, for example, was limited by the generated AC losses of the cables [40]. In the cable geometry, AC losses are lower due to separate strands which are assembled together with full transposition.

Nearly a century later, the Roebel geometry was applied using the REBCO tapes for the first time by means of precision punching technique [38, 39, 40]. The first Roebel cable was assembled from 16 REBCO strands. The individual 5 mm wide strands were cut from a single 12 mm wide tape into a meandering sequential form allowing them to be wound around each other [38, 39]. In figure 2.4, an illustration of such cable is shown. The first REBCO Roebel cable was able to carry 500 A at

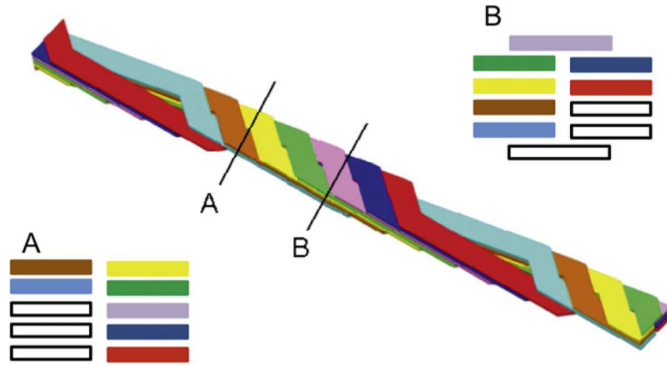


Figure 2.4 An illustration of Roebel cable geometry. Figure reprinted with permission from [40].

77 K.

Since the early steps, the REBCO tape performances and Roebel cable manufacturing processes have seen tremendous developed. The Roebel cables made of the most recent high-end REBCO tapes have a potential to carry 20 kA at fields around 13 T in 4.2-50 K temperatures, which makes their use for example in 10 kA class particle accelerator magnets feasible [40].

2.2 HTS in high energy physics

This thesis is mainly motivated by the needs of high energy physics, where particles are accelerated into high energies and then collided in order to experiment the smallest constituents of matter. In Europe, at the border of Switzerland and France locates the European Organization for Nuclear Research [110] (CERN) where the particle accelerator complex Large Hadron Collider [30, 111] (LHC) is built.

This section briefly describes the main components in the LHC accelerator complex, its ongoing High-Luminosity upgrade and recent development on accelerator magnet technology. Especially, the Feather-magnet prototype series developed with recently finished EuCARD2 project is discussed.

2.2.1 From LHC toward HTS based high field accelerators

The LHC is built underground into a tunnel in the depth of 175 m. The accelerator is a 27 km ring in circumference where the particle beams are accelerated in two

separate beam pipes in opposite directions. This kind of a circular accelerator which allows re-using the accelerating components synchronously with the other technical components is called synchrotron. The beams are accelerated into high energies (up to 6.5 TeV) using several pre-acceleration phases and finally with 400 MHz RF-cavities [12] of the main ring to give them their final energy before the collisions in the four experiments CSM [24], ATLAS [23], ALICE [22] and LHC-b [25].

In synchrotrons one utilizes magnets for example in keeping the charged particles in the circular track and in regularly focusing the necessarily diverging beam. The magnets for these purposes are called dipoles and quadrupoles, respectively, and in LHC they are implemented with superconducting cables [90].

The accelerator magnets in the LHC are made of NbTi [96] superconductors. These magnets can produce a magnetic field of around 8 T when cooled to 1.9 K temperature with superfluid helium in operation [30]. In order to reach out for higher collision energies, the accelerator magnets should be able to produce higher magnetic fields. This can be achieved by using other superconducting materials. The High-Luminosity LHC (HL-LHC) is an upgrade program for LHC, where the aim is to produce more than 4.5 times more collisions, compared to present, from each particle bunch at the ATLAS and CMS detectors. This will be achieved by installing 12 T Nb₃Sn quadrupole magnets close to the two detectors in order to focus the particle beams before the collisions. Moreover, two 15 m long bending magnets will be replaced with two pairs of 5.5 m long more compact and powerful 11 T Nb₃Sn magnets in order to install the additional collimators [2, 10] Currently, there is ongoing worldwide effort for investigating what could be the next circular accelerator after LHC. Activities under this umbrella are called Future Circular Collider study [35]. If the next generation accelerator requires magnet technology at or over 20 T, the use of high temperature superconductor technology is the only option [74].

Within the recently finished EUCARD2 project [91], the capability of HTS conductors in an accelerator kind magnet was demonstrated for the first time. In the project, REBCO Roebel cable based prototype dipole magnets, Feather-M0 and Feather-M2 were designed, built and tested. This thesis contributes to the understanding of modelling these magnets.

2.2.2 The Feather-magnet prototype series

EUCARD2 was a project supported by FP7-European commission targeted for development of high-field (above 20 T) HTS magnets [91, 92]. In order to study the suitability of HTS conductors in accelerator use, first as an intermediate step, a smaller racetrack coil Feather-M0 was built for testing the cable properties in winding and in operation [54, 55]. Then, a 5 T accelerator magnet prototype called Feather-M2 was designed and constructed with the aim on testing it in $\sim 13\text{-}15$ T background field inside the Fresca2 magnet test station in CERN [32, 54].

For the magnets the so-called aligned block layout was developed. In the layout, the coils are wound such that the cable tapes are aligned in parallel with the generated magnetic field. Consequently, the magnetic field has minimal impact in decreasing the critical current of the coil (See figure 2.2 (b)). The results of the electromagnetic designs of Feather-M0 and Feather-M2 are reported in [115].

Next, the Feather-M0 and Feather-M2 are presented. Their design and manufacturing processes are detailed in [115].

2.2.2.1 Feather-M0

The study coil Feather-M0 (FM0) was tested at CERN in August 2016 [53] being the first tested magnet made of REBCO Roebel cable. A depiction of the Feather-M0 racetrack coil is shown in figure 2.5. The nominal length of the coil is 400 mm. The coil was wound from 3 turns of Roebel cable. The manufacturing process for the cable was developed in Karlsruhe Institute of Technology [50] (KIT). The tape for the cable was manufactured by Bruker [15]. The 12 mm wide and ~ 1.7 mm thick cable consisted of 15 5.5 mm wide tapes coated with $20\ \mu\text{m}$ of copper. The assembled cable was insulated with fiber-glass. After the winding, the magnet was impregnated with epoxy resin and instrumented for the testing [53, 115].

The coil was tested in a cryostat cooled with helium gas. During the experiments issues were encountered related to quenches in cable joints. With additional cooling of the joints, the magnet could be powered with ~ 12 kA current at 25 K. Moreover, the magnet protection system utilizing a $80\ \text{m}\Omega$ dump resistor with 10 mV trigger voltage was successful and the coil was not damaged. Hence, the use the Roebel cable in a superconducting magnet was successfully demonstrated. With the lessons

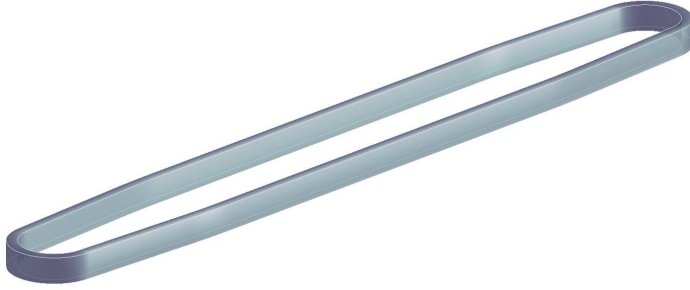


Figure 2.5 Depiction of the dipole magnet Feather-M0.

Table 2.1 Feather-M0 Roebel-cable specifications, as used in the modelling.

dimension	value	unit
number of tapes	15	
cable width	12.0	mm
cable thickness	0.8	mm
cable insulation thickness (G10)	0.1	mm

learned in mind, the design and building process of its successor, Feather-M2, could begin.

In this thesis however, the modelling was done for a Feather-M0 design were 0.8 mm thick cable, designed to be made of 0.1 mm thick SuperPower tapes, was utilized. This resulted in a coil with 5 turns of cable. The cable, tape and coil specifications are listed in table 2.1, table 2.2 and table 2.3, respectively.

2.2.2.2 Feather-M2

In 2017 at CERN the construction of the Feather-M2 design was finished and the testing could take place [73]. The magnet was wound of REBCO Roebel cable assembled by SuperOx from tapes manufactured by SuNam. the cable and the tape specifications are listed in table 2.4 and table 2.5, respectively. An illustration of this dipole magnet is shown in figure 2.6 and its specifications are listed in table 2.6.

The magnet consists of two poles wound into the aligned block layout [112] with the aperture diameter of 40 mm. The nominal length of the magnet is 720 mm. Each

Table 2.2 Feather-M0 tape specifications, as used in the modelling.

dimension	value	unit
tape width	5.5	mm
tape thickness	100	μm
Cu	40	μm
REBCO	1	μm
Hastelloy	50	μm
other	9	μm

Table 2.3 Feather-M0 specifications, as used in the modelling.

dimension	value	unit
number of turns	5	
total cable length in winding	6	m
total tape length	90	m
magnet length	440	mm
B in the aperture (computed) (6 kA, 4.2 K)	1.5	T

Table 2.4 Feather-M2 Roebel-cable specifications, as used in the modelling.

dimension	value	unit
number of tapes	15	
cable width	12.0	mm
cable thickness	1.2	mm
cable insulation thickness (G10)	0.1	mm

Table 2.5 Feather-M2 tape specifications, as used in the modelling.

dimension	value	unit
tape width	5.5	mm
tape thickness	150	μm
Ag	1	μm
Cu	40	μm
REBCO	1.4	μm
Hastelloy	100	μm
buffer	7.6	μm



Figure 2.6 Depiction of the dipole magnet Feather-M2.

Table 2.6 Feather-M2 specifications, as used in the modelling.

dimension	value	unit
number of turns (wing deck)	4	
number of turns (central deck)	8	
total cable length with current leads	37	m
total tape length	555	m
magnet length	720	mm
B in the aperture (6.5 kA, 5.7 K)	3.1	T

of the two poles consists of two racetrack coils: a 4-turn smaller and an 8-turn larger one. The cable had 15 $150 \mu\text{m} \times 5.5 \text{ mm}$ tapes resulting in cable width of 12 mm and thickness of 1.2 mm [31, 73]. The total length of the cable needed for winding the magnet was 37 m, hence, the total tape length needed was around 555 m. Moreover, as done in the winding process with Feather-M0, the cable was insulated with 0.1 mm thick fiber-glass and the coil was impregnated using epoxy resin.

The measurements were performed at CERN in SM18 facility [20]. The magnet was tested in a cryostat with forced helium gas with adjustable temperature and flow rate. The test results were presented in [73]. In summary, Feather-M2 was able to produce a magnetic field of 3.1 T in the aperture with 6.5 kA operation current at 5.7 K. A new joint system called the Fin-Block [68] was developed to connect the two poles together and to connect the magnet to the current leads. This time no heating issues with the cable joints were encountered. Moreover, the magnet exhibited a gradual voltage development as a function of the operation current. This behavior was investigated in publication VI.

2.3 An introduction to HTS modelling

In modelling superconductors, especially the HTS ones, the key thing is to be able to model the constitutive relations. In this thesis, in terms of the constitutive relations of Maxwell's equations, the interest is mainly in the relation between electric field⁵ \mathbf{E} and current density \mathbf{J} . The relation can be modelled using the Ohm's law as $\mathbf{E} = \rho\mathbf{J}$, if the resistivity ρ of the material is known.

The $E(J)$ relation in practical HTS conductors is difficult to characterize due to its high non-linearity and dependencies on many variables. On the other hand, the modelling of LTS conductors is well established and many useful results simplify the modelling. Based on the gained understanding on LTS modelling, effort is put on developing the modelling of HTS conductor based applications.

In this section, two conventional ways used to approximate the $E(J)$ relation in HTS materials are presented: the critical state model and the power law. In addition to those, a novel approach for characterizing directly the resistivity of HTS material

⁵Electric field is a pair (\mathbf{E}, \mathbf{D}) , where \mathbf{E} is the electric field intensity and \mathbf{D} is the electric flux density. Their norms are denoted as E and D , respectively. In this thesis, the terms electric field and electric field intensity are used interchangeably.

is presented. Based on the discussion of the $E(J)$ models, different approaches for predicting the losses that are generated in superconductors are briefly presented.

2.3.1 $E(J)$ relation in superconductors

In superconducting material, the relation between the electric field and current density can be complex. In modelling, often it is not necessary to take all the aspects of it into account. In thermal modelling of superconducting magnets for example, it is common to neglect the effect of mechanical strain in the $E(J)$ relation.

In the scope of this thesis, the interest is on practical HTS conductors designed to carry great amount of electric current. Hence, when modelling conductor based applications, like magnets, the typical approach is to set the level of abstraction to the conductor level and model the conductor as the smallest constituent in the system. Therefore, in applied superconductivity modelling, being able to model the $E(J)$ relation of a conductor, consisting of the stabilizer and the superconducting material itself, is of the utmost importance. Hence, the $E - J$ characterization of HTS conductors is an intensively studied topic within the community at the moment. Such research is presented e.g. in [33, 97, 123], where the $E(J)$ model in [33] is also detailed in [115, p. 246-248].

The critical state model

The critical state model (CSM) [9] is a model describing the current penetration in the superconductor. In the CSM, current density is modelled as

$$J = J_c \text{ or } 0, \quad (2.1)$$

where any electric field E produces the codirectional current density J_c , called the critical current density. In the absence of E , no current flows in the superconductor. This $E - J$ relation is illustrated in figure 2.7 with the dashed graph.

The critical current density J_c in (2.1) can be described using the Bean model [9] or the Kim model [51, 52]. In the Bean model, J_c is assumed constant and in the Kim model the magnetic field dependency of J_c is taken into account.

While the critical state model describes very accurately the behavior of most of the LTS conductors, HTS conductors exhibit more gradual behavior where $E \propto J^n$

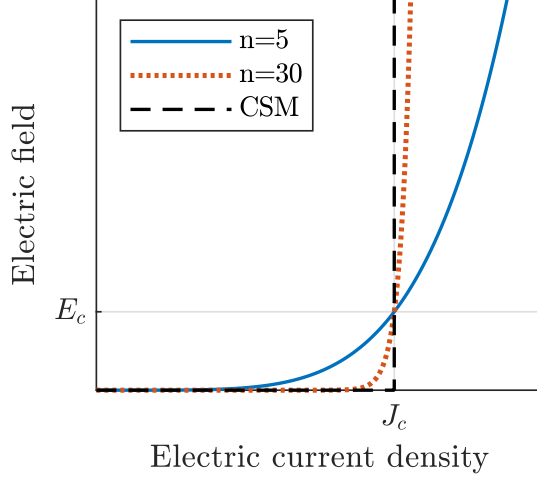


Figure 2.7 The $E(J)$ relations described by the CSM (dashed graph) and the power law for $n = 5$ (solid graph) and $n = 30$ (dotted graph).

with the power n of 5 to 30 (see figure 2.7) [37]. In that case, the CSM is not necessarily the most accurate choice for a model at least when J is close to J_c .

The power law

The power law [16, 88] can be used for modelling gradual $E(J)$ relation. For co-directional \mathbf{E} and \mathbf{J} in the superconductor, the power law can be expressed as

$$E = E_c \left(\frac{J}{J_c} \right)^n, \quad (2.2)$$

where E_c is the critical electric field and n is the power determining the steepness of the relation. A macroscopic form of the power law, used in conductor characterization, is

$$E = E_c \left(\frac{I}{I_c} \right)^n, \quad (2.3)$$

where I_{sc} is the electric current in the superconductor and $I_c = J_c A_{sc}$ is the critical current. Here it is assumed that E, J and J_c are homogeneous in the cross-sectional area of the superconducting material (A_{sc}).

Using the power law, the $E - I$ dependency is characterized by E_c, n and I_c . In

the short-sample measurements, where practical superconductors are characterized, it is typical to utilize the concept of critical current I_c . The I_c of a conductor is determined by using a selected value for the average critical electric field E_c : typically E_c for LTS conductors is $10 \mu\text{V/m}$ and for HTS, it is $100 \mu\text{V/m}$.

The determination of I_c of a superconductor can be illustrated with figure 2.7, where now the correspondence between I_c and the average J_c is $I_c = J_c A_{sc}$. Let the solid graph in the figure, corresponding to power n of 5 in the power law, represent the $E - J$ relation of an HTS conductor. For conductors exhibiting gradual $E - I$ relation, the definition of the critical current is not as unambiguous as for conductors with high n -value.

The experimental I_c (or J_c) characterization of HTS conductors, especially RE-BCO tapes, can be quite demanding. Often the I_c needs to be characterized based on certain E_c as a function of temperature T , and magnetic flux density \mathbf{B} , where I_c not only depends on the magnitude of \mathbf{B} (B) but also on its direction with respect to the tape's wide face. In the I_c measurement the sample is cooled down to selected operation temperature T_{op} at selected background field. Then, the operation current is increased until the average electric field over the sample reaches the value of E_c , the corresponding electric current is the critical current. This is how a single I_c data point ($I_c, E_c, T_{op}, \mathbf{B}$) is obtained. Inaccuracy can be introduced to the measurement by the fact the sample heats up during the measurement.

Characterizing the resistivity of HTS material

The earlier described issues related to arbitrariness of characterizing $E(J)$ dependency in HTS conductors using the power law and the experimental data based I_c fits determined using a certain voltage criterion. The problem arises especially in operation conditions where the superconductor current exceeds the E_c -determined value of critical current, i.e., when operating with overcritical currents. Moreover, regarding to the power law, the n value depends significantly on the temperature and the applied magnetic field. Consequently, the HTS $E(J)$ relation cannot be modelled adequately with this approach at overcritical currents. This is the bottle neck in HTS modelling at the moment. After all, resistivity is the most fundamental material property in HTS modelling. Fortunately, this issue is recognized within the HTS community.

Characterizing the overcritical current resistivity of HTS material can be chal-

lenging. The overcritical current can destroy the sample quickly due to the rapid heat generation. To overcome this issue, an ultra-fast current pulse method was developed in [100]. In this method, the amount of energy injected into the sample is very low, therefore the material can be characterized with overcritical currents.

In [89], this measurement technique is also utilized for characterizing the resistivity of HTS material. In the research, finite element analysis was utilized to correct the heating effects occurring during the measurement and to extract the overcritical current resistivity.

2.3.2 Losses

Modelling losses in superconductors is a widely studied branch in the field of applied superconductivity. In this thesis, the losses are separated into two types: resistive losses (DC losses) and AC losses. Resistive losses are due to non-zero resistivity of the superconducting material, even with constant electric current and magnetic field. The AC losses occur due to time-varying magnetic field, applied or caused by produced transport current [45]. These losses can be separated into three different types: hysteresis losses, coupling losses and eddy current losses. However, in continuum physics, they all can be computed as $\mathbf{E} \cdot \mathbf{J}$, where \cdot denotes the dot product.

In alternating magnetic field, the coupling losses are generated due to mutual coupling of the conductors of a cable, or filaments of a strand. The losses are produced by the screening currents, where according to the Faraday's law, a time-varying magnetic field through a conductor loop produces an electric current in conductive material. When the current distributes between the tapes, passing through the stabilizers of the tapes, losses are generated. The generation of this loss type can be reduced by transposing the conductors in the cable along the length. Consequently, the conductor loops are smaller and hence the coupling losses are smaller.

Eddy current losses are generated in the normal conducting stabilizer materials of superconducting wire with a similar principle as the coupling losses. As the resistive stabilizer material of the conductor is exposed to time-varying magnetic field, screening currents are produced in the material and hence losses are generated. These losses can be reduced using highly resistive stabilizer materials but on the other hand, the thermal stability of the conductor gets weaker with increasing resistivity of the stabilizer [26].

Hysteresis loss in REBCO conductors is the dominant loss mechanism [43, 49, 59]. In microscopic level this loss is related to the magnetization of the superconducting material, where the magnetic flux tubes in the material get stuck on the pinning centers and a reversal magnetic field has to be applied to clear off all the trapped flux. When the material is exposed to time-varying magnetic field, the flux tubes move and losses are generated. [96] This phenomenon can be modelled in terms of continuum physics as the ohmic losses: these losses generate in case of simultaneous presence of co-directional \mathbf{E} and \mathbf{J} , such that $\mathbf{E} \cdot \mathbf{J} > 0$, where \mathbf{E} is induced in the material by the time-varying magnetic field.

The two most common models for predicting hysteresis losses in superconductors are the critical state model and eddy current model (ECM) [16, 58], where in the CSM the $E - J$ relation is sharp and in the ECM the relation is modelled smoothly using the power law. The predictive capability of these two models in AC loss modelling of HTS conductors has been investigated in [101]. Numerous methods have been developed to solve the AC losses based on the CSM [41, 44, 72, 78, 79] and ECM [44, 69, 70, 104, 114].

2.3.3 Quench

Quench is an irreversible transition from superconducting state to normal conducting resistive state where aggressive heat generation in the quench area is typical [96, 122]. In case of LTS conductors, the transition is very rapid due to $E(J)$ relation they exhibit. The current at which the transition, i.e. the quench, occurs corresponds accurately to the critical current. Thus, in the etymological sense, this sudden phenomenon deserved to be named. In HTS conductors, quench can be gradual. Hence, a better term for quench in HTS conductors could be for example thermal runaway [60].

In magnet applications quench can destroy a whole magnet. Therefore quench detection and protection systems are needed in order to protect the magnet in case of a quench [27, 93]

2.4 The Galerkin-FEM for solving 1-D heat diffusion equation in HTS magnet

The heat diffusion equation can be used to describe the thermal state of a system. The unknown quantity to be solved is the temperature that develops according to the heat sources, heat sinks, thermal conductivity and the heat capacity defined on the modelling domain.

The boundary value problem describing thermodynamics on the 1-dimensional domain $\Omega = \{x|x \in [0, l] \subset \mathbb{R}\}$ can be formulated as

$$C_V(T(t, x)) \frac{d}{dt} T(t, x) - \frac{d}{dx} \left(\lambda(T(t, x)) \frac{d}{dx} T(t, x) \right) - Q(T(t, x)) = 0 \quad (2.4)$$

$$\frac{d}{dx} T(t, x) \Big|_{x=0} = \frac{d}{dx} T(t, x) \Big|_{x=l} = 0 \quad (2.5)$$

$$T(t_0, x) = T_{op} \quad \forall x, \quad (2.6)$$

where (2.5) are the Neumann boundary conditions and T_{op} the initial temperature. The solution to (2.4) has to satisfy the both, (2.5) and (2.6).

In choosing the boundary conditions for the problem, there are two options: the Dirichlet boundary conditions (DBC) and the natural boundary conditions (NBC). In DBC the temperature is fixed, i.e. constant, at the cable ends $x = 0$ and $x = l$. If NBC were utilized, one assumes zero heat flux flowing out (or in) at the cable ends in the cable's longitudinal direction.

In formulating the BVP for Feather-M2, the NBC were utilized for the following reasons. As explained in section 2.2.2.2, Feather-M2 is connected to the current terminals with Fin-block joint system. The cable parts that connect each magnet pole to the Fin-blocks at the current terminals are called *current leads*. In case of Feather-M2, the length of each current lead is over 1 meter (~ 1.35 m).

Compared to the cable in the winding, the current leads are assumed to be in low magnetic field and exposed to efficient cooling. In other words, the current leads are assumed to be in very stable state compared to the winding. Therefore, the Fin-blocks are assumed to have very little influence to the possible loss generation in the current leads. Hence, Fin-blocks are not taken into account in modelling. Consequently modelling the complex structure of the joint system could be avoided with presumably no significant loss of accuracy. Moreover, if the Fin-blocks are

not modelled, there is no sense to use DBC in the problem without knowing the temperature at the cable ends.

In summary, based on the assumptions and modelling decisions made, using the natural boundary conditions in the problem formulation is a reasonable choice. It can be justified with the relatively long current leads and their good stability in operation compared to the winding.

One approach for solving numerically the problem the Galerkin finite element method (FEM) where the modelling domain is discretized into a mesh consisting of finite number of mesh elements. In the method, the unknown quantity is approximated with a linear combination of known basis functions whose coefficients are solved. The basis functions are defined using the mesh. In case of scalar fields, one way is to define the basis functions as piece-wise linear polynomials ϕ_i corresponding to node index i located at x_i . Further, it is required that $\phi_i(x_j) = 1$ when $j = i$ and otherwise $\phi_i(x_j) = 0$. Using this method, linearly independent basis functions are obtained.

In this section, the weak formulation of the problem is first presented. Then, the problem is finite-dimensionalized using the Ritz-Galerkin approximation and finally, the basis functions are defined using the mesh set on the modelling domain.

2.4.1 Weak formulation of the problem

Let us denote (2.4) as the function

$$f = C_V \frac{d}{dt} T - \frac{d}{dx} \left(\lambda \frac{d}{dx} T \right) - Q = 0 \quad (2.7)$$

that fulfills (2.5) and (2.6), such that $f \in U$, where U is a function space from where the solution for f is sought for.

The space U can be viewed as a Hilbert space [119], complete with respect to the inner-product (\cdot, \cdot) . In addition, special derivatives, weak derivatives, for piece-wise linear functions and their inner-products are defined in U [14].

Since U is a Hilbert space, it holds that [124]

$$f \in U, f = 0 \Leftrightarrow (f, v) = 0 \quad \forall v \in U, \quad (2.8)$$

which is the variational formulation of the problem [14, p. 2], where the inner-

product (f, v) is computed as⁶

$$\begin{aligned}
(f, v) &= \int_0^l f v \, dx \\
&= \int_0^l C_V \dot{T} v - (\lambda T')' v - Q v \, dx \\
&= \int_0^l C_V \dot{T} v \, dx - \int_0^l (\lambda T')' v \, dx - \int_0^l Q v \, dx. \tag{2.9}
\end{aligned}$$

To further simplify the result, let us focus on the second term of (2.9) for a moment. Using the product rule and integration by parts the term becomes

$$\begin{aligned}
-\int_0^l (\lambda T')' v \, dx &= -\int_0^l \lambda' T' v + \lambda T'' v \, dx \\
&= -\int_0^l \lambda' T' v \, dx - \int_0^l \lambda T' v + \int_0^l \lambda' T' v \, dx + \int_0^l \lambda T' v' \, dx \\
&= \int_0^l \lambda T' v' \, dx, \tag{2.10}
\end{aligned}$$

since the first and third term cancel out and the second term vanishes as required by the boundary conditions (2.5). Hence, the inner-product (f, v) takes the form

$$(f, v) = \int_0^l C_V \dot{T} v \, dx + \int_0^l \lambda T' v' \, dx - \int_0^l Q v \, dx = 0 \tag{2.11}$$

2.4.2 Discretization: The Ritz-Galerkin approximation

Let $S \subset U$ be any finite dimensional subspace of U having a basis $\{\phi_i : 1 \leq i \leq N\}$. Then the weak formulation of (2.8) is

$$f \in S, f = 0 \iff (f, v) = 0 \quad \forall v \in S. \tag{2.12}$$

Expressed with the basis of S , $T \in S$ is $T = \sum_{j=1}^N T_j \phi_j$. Since $(f, v) = 0$ has

⁶In the following derivation, the derivatives dT/dx , d^2T/dx^2 and dT/dt are denoted as T' , T'' and \dot{T} , respectively.

to apply for any $v \in S$, we test the inner-product with all the basis functions ϕ_i ($i = 1 \dots N$) individually. The inner-product (f, ϕ_i) thus becomes

$$(f, \phi_i) = \sum_{j=1}^N \int_0^l C_V \dot{T}_j \phi_j \phi_i \, dx + \sum_{j=1}^N \int_0^l \lambda T_j \phi_j' \phi_i' \, dx - \sum_{j=1}^N \int_0^l Q \phi_j \phi_i \, dx = 0. \quad (2.13)$$

Then, (2.12) is equivalent to solving the matrix equation

$$\Pi \frac{d}{dt} \mathbf{T} = \mathbf{K} \mathbf{T} + \mathbf{Q}, \quad (2.14)$$

where the stiffness matrix

$$K_{ij} = - \int_0^l \lambda \phi_j' \phi_i' \, dx, \quad (2.15)$$

the load vector

$$\mathbf{Q}_i = \int_0^l Q \phi_i \, dx, \quad (2.16)$$

and the mass matrix

$$\Pi_{ij} = \int_0^l C_V \phi_j \phi_i \, dx. \quad (2.17)$$

The matrix equation of this form can be solved numerically using time-stepping methods [46, p. 36] [61, 98]. Note that the material parameters are element-wise homogeneous. Moreover, a practical method for assembling similar matrices as in (2.14) is presented in [105].

2.4.3 Constructing the basis functions

In this section the finite element method is used to construct a basis $\{\phi_i\}$ for S , defined in the previous section. The basis functions are constructed based on the geometry of the modelling domain Ω depicted in figure 2.8.

As illustrated in the figure, Ω is discretized into its partition such that $0 = x_1 < x_2 < x_3 \dots < x_N = l$, where the points x_i are called the nodes. Based on this partition, we define the basis functions to be piecewise linear and behave such that $\phi_i(x_j) = \delta_{ij}$. Conclusively, using the described procedure starting from the partial differential equation through its weak formulation and discretization of space

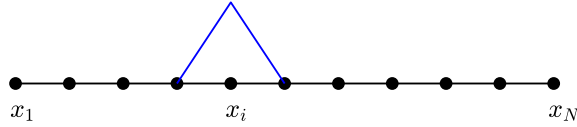


Figure 2.8 Depiction of the modelling domain Ω . The node coordinates x_i are marked with dots. The blue line represents the basis function ϕ_i .

and constructing the basis using the finite element method, is often referred as the Galerkin Finite element method.

2.4.4 Heat transfer between cable turns using FDM

In this thesis, heat transfer problem is solved in a magnet structures using 1-dimensional modelling domain Ω . As in the formulation of the heat diffusion equation (2.4) in chapter 4, the source term Q consists also of the heat flux term $Q_{||}$ which is a model for the heat flux between adjacent cable turns due to the temperature difference between them. Hence, the flux contributes to the source term of the problem. However, its contribution cannot be taken into account using the basis of Ω since the space between the cable turns is not part of the modelling domain and derivatives of T in the radial, turn-to-turn, direction are not defined.

In order to model the heat transfer between the cable turns the finite different method (FDM) was utilized. The FDM is an often used numerical discretization method for solving partial differential equation where the derivatives are approximated with finite differences [61]. In FDM a regular grid is set on the modelling domain. The unknown quantities are solved at the grid points. Moreover, based on the finite spatial differences of the grid points, with respect to each other, the spatial derivatives are approximated.

In order to model the heat flux between the cable turns ($Q_{||}$), a regular grid is defined based on the nodes of Ω defined in the discretizing the problem with Galerkin-FEM. Figure 2.9 illustrates the discretization of the modelling domain. In the upper sub-figure, the coil representation of the 1-dimensional domain, shown in the lower sub-figure, is illustrated. The figure shows how the different locations on Ω are related to each other in terms of the adjacency of cable turns. For example, in the upper

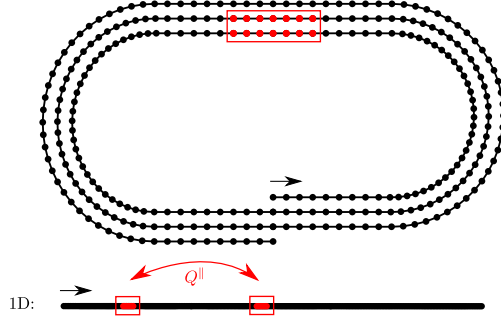


Figure 2.9 A visualization of the progression and adjacency of the homogenized cable. In the upper sub-figure, the boxed region covers a piece of the inner-most cable turn and of the turn adjacent to it.

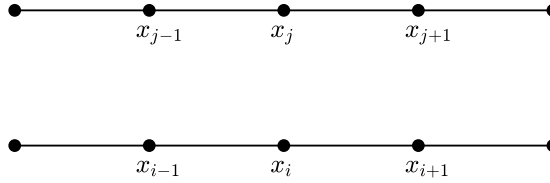


Figure 2.10 A depiction of the FDM grid.

sub-figure, the node locations in the first and second cable turn inside the boxed region are related to each other as illustrated in the lower sub-figure with the boxed regions where the left-most region corresponds to the nodes of the inner-most turn.

The information on the adjacency of the nodes in Ω needs to be investigated using the 3-dimensional magnet geometry, based on which an adjacency mapping f_A is determined. Hence the coordinate adjacent to coordinate $x \in \Omega$ is $f_A(x)$. To further illustrate this, figure 2.10 shows more in detail a part of the grid in two adjacent cable turns with the same node locations as in Ω . Now, for example, the coordinate x_i and x_j in figure 2.10 are related as $f_A(x_i) = x_j$.

To take the physics into the play, the local heat flux between the cable turns Q^{\parallel} can be modelled using the Fourier's law as

$$-\lambda_i \frac{dT}{cd\tau}, \quad (2.18)$$

where λ_i is the thermal conductivity of the insulation material between the cable turns. The wetting coefficient c is related to the dimensions of the area through which heat is exchanged (See (4.11)). Here the heat is exchanged through the wide face of the cable. Using the Taylor series expansion, (2.18) at $x \in \Omega$ can be approximated as

$$Q^{\parallel}(x) = \bar{\lambda}_i \frac{T(f_A(x)) - T(x)}{cd_i}, \quad (2.19)$$

where d_i is the thickness of the insulation material between the cable turns and $\bar{\lambda}_i$ is the thermal conductivity of the insulation material evaluated at the average temperature of $T(f_A(x))$ and $T(x)$. Note that in (2.19) the direction of the heat flux is now defined to be from the temperature $T(f_A(x))$ to $T(x)$.

Now, using the basis functions ϕ_i , the inner-products (2.16) of Q^{\parallel} can be computed and hence the heat transfer between the cable turns can be taken into account on the 1-dimensional Ω .

2.5 The minimum magnetic energy variation principle

The minimum magnetic energy variation (MMEV) principle is a numerical method for solving eddy current problems formulated with the CSM. The principle was first developed by Prigozhin for the critical state model to predict the hysteresis losses in superconductors [85, 86].

Enric Pardo and his group took the early steps in developing the MMEV-principle based modelling tools, where computations were performed using a single rectangular domain, the use of the principle has been extended to simulate losses in coils wound of multitape cables [77, 81, 87, 102].

In this section, the theoretical background of the MMEV-principle is outlined based on publication II, where the MMEV-formulation using the CSM was based on the more general minimum electro-magnetic entropy production (MEMEP) - principle being applicable for any $E(J)$ relation [6, 83].

2.5.1 The Maxwell's equations in magnetoquasistatics

In differential form the Maxwell's equations [65] are

$$\text{curl}(\mathbf{E}) = -\partial_t \mathbf{B}, \quad (2.20)$$

$$\text{curl}(\mathbf{H}) = \mathbf{J} + \partial_t \mathbf{D}, \quad (2.21)$$

$$\text{div}(\mathbf{B}) = 0, \quad (2.22)$$

$$\text{div}(\mathbf{D}) = \sigma, \quad (2.23)$$

where the vector fields \mathbf{E} , \mathbf{D} , \mathbf{J} , \mathbf{B} , \mathbf{H} , are the electric field intensity, electric flux density, electric current density, magnetic flux density and magnetic field intensity.⁷ The time-derivative operator ∂/∂_t is denoted with ∂_t . Respectively, the equations are Faraday's law, Ampère-Maxwell's equation, and Gauss's laws for \mathbf{B} and \mathbf{D} . The field quantities are paired via the constitutive relations such that

$$\mathbf{E} = \epsilon \mathbf{D} \quad (2.24)$$

$$\mathbf{B} = \mu \mathbf{H} \quad (2.25)$$

$$\mathbf{J} = \sigma \mathbf{E}, \quad (2.26)$$

where ϵ , μ and σ are the permittivity, permeability and conductance, respectively.

In magnetoquasistatic approximation of Maxwell's equations, frequencies are assumed to be low enough so that no charge packing takes place [56]. Thus, the displacement current term $\partial_t \mathbf{D}$ is neglected in (2.21). Hence, it becomes

$$\text{curl}(\mathbf{H}) = \mathbf{J}, \quad (2.27)$$

which is called the Ampère's law. Consequently, (2.23) and (2.24) become needless. Thus, (2.20), (2.22) and (2.27) together with the constitutive relations (2.25) and (2.26) form the magnetoquasistatic Maxwell's theory.

⁷Their norms are denoted respectively as E , D , J , B and H .

2.5.2 The variational formulation of the CSM

Based on the Maxwell's equations, different formulations can be made. In this thesis, the variation formulation of the CSM is based on the $\mathbf{A} - \varphi - \mathbf{J}$ formulation in magnetoquasistatics [56]. The corresponding partial differential equation is

$$\text{curl}(\mu^{-1}\text{curl}(\mathbf{A})) = \sigma(-\partial_t \mathbf{A} - \text{grad}(\varphi)), \quad (2.28)$$

where \mathbf{A} is the magnetic vector potential such that $\mathbf{B} = \text{curl}(\mathbf{A})$ and φ is the electric potential such that $\mathbf{E} = -\partial_t \mathbf{A} - \text{grad}(\varphi)$. The conductivity σ is defined by the non-linear constitutive relation $\mathbf{J} = \sigma \mathbf{E}$. Equation (2.28) is the Euler-Lagrange equation of the functional

$$\mathcal{F} = \int_{\Omega} \mathcal{L} \, d\Omega, \quad (2.29)$$

and hence, the solution of (2.28) for \mathbf{A} or \mathbf{J} , minimizes the functional [83].

In (2.29), the functional density \mathcal{L} , in time discretized situation, is

$$\mathcal{L} = \frac{1}{2} \frac{\Delta \mathbf{A}_J}{\Delta t} \cdot \Delta \mathbf{J} + \frac{\Delta \mathbf{A}_a}{\Delta t} \cdot \Delta \mathbf{J} + \mathcal{U}(\mathbf{J}_0 + \Delta \mathbf{J}) + \text{grad}(\varphi) \cdot (\mathbf{J}_0 + \Delta \mathbf{J}), \quad (2.30)$$

where the current densities \mathbf{J}_0 and $\mathbf{J}_0 + \Delta \mathbf{J}$ correspond to ones at the instants of times t at t_0 and $t_0 + \Delta t$, respectively. Moreover, the function $\mathcal{U}(\mathbf{J})$ is defined as $\mathcal{U}(\mathbf{J}) = \int_0^{\mathbf{J}} E(\mathbf{J}') \cdot d\mathbf{J}'$. The terms $\frac{\Delta \mathbf{A}_J}{\Delta t}$ and $\frac{\Delta \mathbf{A}_a}{\Delta t}$ are the changes in the magnetic vector potential generated by the currents inside and outside of the modelling domain Ω , respectively. [83]

In (2.30), the $E(\mathbf{J})$ relation is assumed to be differentiable. However, the CSM can be approximated by taking a limit of the smooth power law model $E(\mathbf{J}) = E_c(\mathbf{J}/J_c)^n$, when $n \rightarrow \infty$. Then, $\mathcal{U}(\mathbf{J}) = 0$ for $\mathbf{J} \leq J_c$ and $\mathcal{U}(\mathbf{J}) \rightarrow \infty$ when $\mathbf{J} > J_c$. Consequently, $\mathcal{U}(\mathbf{J})$ (2.30) can be omitted but the constraints for the current density need to be imposed separately.

The term with $\text{grad}(\varphi)$ can be dropped out from the functional density too, if the transport current constraint is imposed separately [83]. In 2-dimensional translation symmetric problems the term becomes $\int_{\Omega} \text{grad}(\varphi) \cdot \mathbf{J} d\Omega = \varphi I$. Hence, any current distribution transporting the electric current I , results in the same value of the functional density and therefore the term can be omitted. Finally, by multiplying \mathcal{L} by

Δt , the functional density that also minimizes \mathcal{F} takes the form

$$\mathcal{L}' = \frac{1}{2} \Delta \mathbf{A}_J \cdot \Delta \mathbf{J} + \Delta \mathbf{A}_a \cdot \Delta \mathbf{J}. \quad (2.31)$$

The physical interpretation of \mathcal{F} with \mathcal{L}' is that it represents the magnetic energy of the current variation due to change in the transport current or applied magnetic field in Ω .

2.6 On the practical optimization

Using the concept of optimization, very complex decision problems can be solved. In [63, p. 1], optimization is described as follows. "Using this optimization philosophy, one approaches a complex decision problem, involving the selection of values for a number of interrelated variables, by focusing attention on a single objective designed to quantify performance and measure the quality of the decision."

An optimization problem consists of the objective function and the constraints. The objective function is to be maximized or minimized depending on the formulation⁸. The constraints are inequality or equality constraints. They can be functions of the optimization variables. Typically the variables are given their own individual constraints too in order to define the feasible region from where the optimal solution is sought for.

In this section, optimization problems and their formulation are discussed at a general level by first presenting a standard form of an optimization problem. Then, a class of optimization algorithms, the primal-dual interior point methods, is introduced. Last, a background to inverse problems is given, which is essential for understanding the methodology to be presented in chapter 5.1

⁸Finding the maximum of an objective function $f(\mathbf{x})$ is equivalent to finding the minimum of $-f(\mathbf{x})$.

2.6.1 Formulating an optimization problem

A standard optimization problem is formulated as

$$\begin{aligned} \min_{\mathbf{x}} \quad & f(\mathbf{x}) \\ \text{s.t.} \quad & \mathbf{g}_i(\mathbf{x}) \leq 0 \\ & \mathbf{h}_j(\mathbf{x}) = 0 \\ & \mathbf{x} \in X, \end{aligned} \tag{2.32}$$

where f , \mathbf{g}_i and \mathbf{h}_j are real-valued functions from \mathbb{R}^N to \mathbb{R} , where the dimension N is the number of the optimization variables in the vector \mathbf{x} , and where the indices $i \in \{1..m\}$ and $j \in \{1..m'\}$. The indices m and m' are the number of the inequality (\mathbf{g}_i) and the equality (\mathbf{h}_j) constraints, respectively. The search space $X \subset \mathbb{R}^N$ is defined by setting an upper and lower bound for each variable. Moreover, this is the form in which the problem is structured for most of the interfaces of optimization libraries.

2.6.2 The primal-dual interior point methods

The background of this wide ranging thesis could cover only briefly the interrelated topics: superconductivity, accelerator magnets, modelling and various mathematical concepts present in modern engineering.

Optimization algorithms divided into different classes. For example linear and non-linear as well as constrained and unconstrained problem require different methods for solving the optimization problems. The class of primal-dual interior point methods are suitable for solving large scale non-linear constrained optimization problems. In this thesis, the optimization problem in chapter 3 was solved using a C++ implementation *IPOPT* of a primal-dual interior point filter line search algorithm [48, 71, 116, 117]. The inverse problems presented in chapter 5.1 were solved using Matlab's optimization toolbox and its implementation [17, 18, 118] of an interior point optimization algorithm [64].

In the primal-dual interior point methods, a barrier term is augmented into the objective function. Violation of the constraints causes the barrier term to increase to infinity and consequently the objective function increases to infinity. Hence, the

optimal solution is forced to be searched inside the feasible region.

2.6.3 Inverse problems

Inverse problems present the inverse to the more typical forward problem where results of experiments are predicted using a model characterizing the physical system under study from a given point of view [109]. In the inverse problem, a measurement results of the physical system is used to find out the values of the parameters of the model. Hence, consequently the solved parameter values together with the model characterize the physical system based on the measurements.

Formulating an inverse problem can be summarized as follows. First, a model needs to be constructed from physical laws so that it describes the physical system under study from a given point of view. Then, the model is parametrized with the minimal amount of model parameters so that their values, together with the model, completely characterize the physical system. [109] Finally, using measurement data of the system, values of the model parameters are solved with the model.

An inverse problem can be expressed as

$$d = M(\mathbf{x}), \quad (2.33)$$

where d is the measured data, M is the model as a function of the model parameters \mathbf{x} . In summary, a solution for \mathbf{x} is sought for that (2.33) holds at least approximately. The way, how M relates \mathbf{x} with the data, is rarely linear. Hence, inverse problems are often solved as non-linear optimization problems as will be shown in this thesis in chapter 5.1.

2.7 Summary and remarks

In this thesis, the main focus is on developing modelling methodologies in order to gain understanding of HTS based magnets and their modelling. This was done by scrutinizing the REBCO Roebel cable based magnet prototypes Feather-M0 and Feather-M2 in terms of AC loss modelling and thermal stability modelling. The developed modelling approaches utilized mathematical concepts such as the finite element method and the optimization theory. In modelling of superconductors,

one of the most important aspects in Maxwell's theory based continuum physical modelling is the $E(J)$ relation. Up to my best knowledge, difficulties related to characterizing this property at the fundamental level for modelling purposes are yet to be solved. In this thesis two $E(J)$ models, the critical state model and the power law model, are utilized in modelling AC losses and thermal stability.

The AC losses are generated in superconductors due to time-varying transport current or magnetic field. The chapter 3 of this thesis focuses on modelling AC losses and magnetic field quality in Feather-M0. The utilized approach for modelling the losses is based on the MMEV-principle where the CSM, a model for sharp $E(J)$ relation, is utilized with two models characterizing the superconductors $J_c(\mathbf{B})$ dependency: the Bean and the Kim model.

In addition to the AC loss modelling part of thesis, the rest of this thesis work is dedicated to modelling thermal stability in HTS magnets where AC losses are not considered. The heat generation is assumed to be due to resistive losses that are generated even in operation conditions of constant transport current and magnetic field. The resistive losses can have significant influence on magnet's stability in operation. In this thesis, these losses are simulated in Feather-M2 using a thermal model formulated in chapter 4, for which mathematical background was provided in this chapter. In the formulation, the utilized $E(J)$ relation is the power law which enables describing a smooth relation between co-directional \mathbf{E} and \mathbf{J} . The simulation results are presented in chapter 5.

In this thesis, numerical solving methods are essential in obtaining solutions to the formulated problems. The Galerkin-FEM and the finite difference method (FDM) are utilized for discretizing and solving the heat transfer problems in Feather-M2. Discretizing the magnet along the cable with FEM and the space between the turns with FDM allowed a significant reduction in degrees of freedom and thus rapid simulations compared to a case where a 3-dimensional mesh would have been utilized.

In addition to FEM and FDM, mathematical optimization is an important concept in this thesis as follows. In chapter 3, an optimization algorithm was utilized for minimizing the MMEV-functional and thus solving the current distribution in Feather-M0 cross-section. Optimization was also utilized in chapter 5 where the maximum stable operation current of Feather-M2 was determined, and inverse problems related Feather-M2 and its cooling environment were solved. Furthermore, in chapter 6 a protection system parameters were obtained using optimization meth-

ods.

3 MODELLING AC LOSSES IN FEATHER-M0 WITH MMEV

An important branch of HTS accelerator magnet research and development is AC loss modelling. AC losses occur in superconductors when applied electric current or magnetic field changes in time, as discussed in chapter 2.5. It is important to estimate these losses since they can have significant influence on the stability of the magnet in operation. AC losses can be modelled utilizing approaches based on various different formulations. In the studies presented in this chapter, the minimum magnetic energy variation (MMEV) principle was utilized and further developed.

This chapter is based on publication I and publication II, where MMEV principle based modelling methodology was developed and presented. In publication I, an algorithm for solving MMEV principle problems was implemented based on [82] and further extended for triangular elements. The implemented simulation tool was utilized to simulate AC losses in round superconductors using the critical state model. Furthermore, it was demonstrated that when modelling round conductors, the required number of degrees of freedom was significantly lower when triangular elements were utilized.

In publication II, the MMEV principle was formulated as a minimization problem and solved using an open source optimization algorithm library *IPOPT* [117]. Using this simulation tool, AC loss and magnetic field quality simulations were performed for a Roebel cable based dipole magnet, Feather-M0. This chapter is mainly based on this publication, hence, the utilized methodology and the main simulation results are presented.

3.1 Problem formulation

In this section the MMEV functional is discretized and a minimization problem is formulated in order to solve the current distribution as a function of time in the cross-section of Feather-M0. Though, Feather-M0 is a racetrack like magnet, this study focuses on 2-dimensional translation symmetric case which neglects the transposition present in the Roebel cable. However, as will be seen there are methods to consider the effect of transposition in 2-dimensions. In these 2-dimensional problems \mathbf{J} and \mathbf{A} have only one component: that towards the plane. In this chapter, in order to simplify the equations, we denote \mathbf{A} with A^z and \mathbf{J} with J . This translation symmetric approach would cover most of the coil volume in accelerator dipoles which can be even 15 m long. Based on the current distribution, the methods for computing the AC losses and the non-linearity of the magnetic field in the magnet's bore are detailed.

3.1.1 Modelling domain

The modelling domain $\Omega \subset \mathbb{R}^2$ shown in figure 3.1, represents one half of the Feather-M0 cross-section, taken in the middle of the straight section. The coordinate axes are specified in the figure. The y -axis is the axis of symmetry for this problem. Moreover, it is assumed that the coil is infinitely long. This means that the coil ends and their effect on the current distribution is neglected. Hence, we can focus on modelling on the 2-dimensional cross-section. A 3-dimensional depiction of the magnet was shown in figure 2.5. As figure 3.1 shows, the modelled magnet has 5 turns of Roebel cable and the cable is made of 15 tapes, as discussed in chapter 2.2.2.1. The 2-dimensional modelling domain consists of the superconducting material layers of the tapes only. In the model, the thickness of the superconducting layer is $1 \mu\text{m}$. The dimensions of the cable are $1 \text{ mm} \times 12 \text{ mm}$ and a single tape is 5.5 mm wide. The distance, from the innermost cable to the center of the magnet's bore, the axis of symmetry in figure 3.1, is 23 mm . Moreover, the modelling domain was discretized using a mesh with rectangular elements.

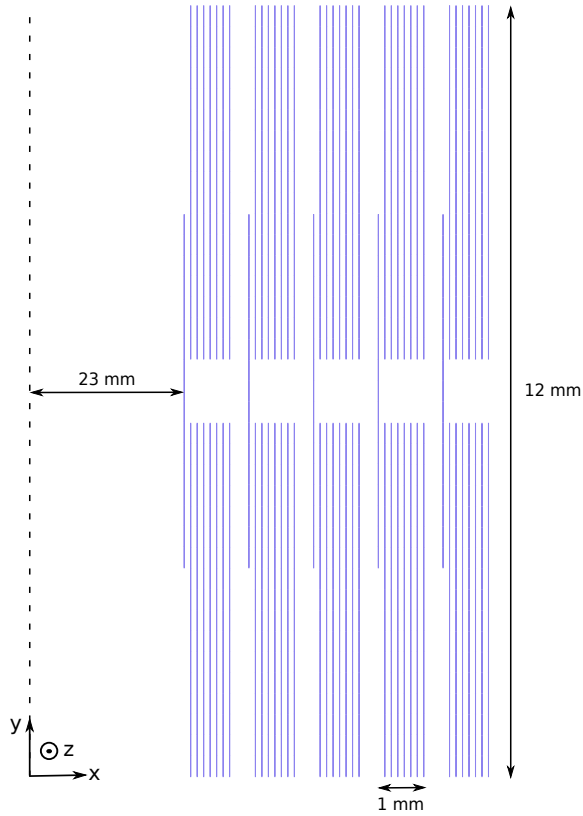


Figure 3.1 Half of the magnet's cross-section, where the lines represent the superconducting tapes. The dashed line represents the symmetry axis. Orientation of the modelling domain is fixed. The figure is not in scale.

3.1.2 Solving current distribution using MMEV principle

In chapter 2.5, it was deduced that due to a change in applied operation current or applied magnetic field, the electric current distribution in Ω varies by $\Delta \mathbf{J}$ such that the functional

$$\mathcal{F} = \int_{\Omega} \mathcal{L}' d\Omega, \quad (3.1)$$

with

$$\mathcal{L}' = \frac{1}{2} \Delta A_J \cdot \Delta \mathbf{J} + \Delta A_a \cdot \Delta \mathbf{J}. \quad (3.2)$$

is minimized. In order to solve the change in the electric current density, (3.1) is discretized and formulated into an optimization problem

$$F(\Delta J) = \frac{1}{2} \Delta J^T M \Delta J + C^T \Delta J \quad (3.3a)$$

subject to

$$(A^i \Delta J_i)_s = \Delta I_s \quad (3.3b)$$

$$(J_0 + \Delta J)_j \leq J_{c_j} \quad (3.3c)$$

$$(J_0 + \Delta J)_j \geq -J_{c_j}, \quad (3.3d)$$

where the objective function F is the functional (3.1) in discretized form. Here, ΔJ represents element-wisely the time-change in the current density, i.e., ΔJ in the j th element is denoted as ΔJ_j . Similarly, J_0 denotes the element-wise electric current density at instant of time t_0 , where J_0 in the j th element is denoted as J_{0_j} . The element-wise critical current density is denoted with an index as J_{c_j} . The equality constraint (3.3b), is the electric current constraint requiring that the current ΔI_s flows in the sub-domain Ω_s of Ω . That is the sum of $A^i \Delta J_i$ over the index i , where the Einstein summation convention¹ is utilized and A^i is the area of the i th element in Ω_s . Inequality constraints (3.3c) and (3.3d) require that the electric current density in element j is not greater than the absolute value of J_c in element j , i.e., J_{c_j} .

In solving (3.1) as a minimization problem, posing the constraints for J is not straightforward. In the formulation of the problem the critical state model was chosen to model the $E(J)$ relation in the superconductor (Recall section 2.5.2). In this context this means that $J \in [-J_c, 0, J_c]$. Optimization problems where the variables are restricted to have discrete values are called discrete optimization problems. Obtaining solutions for those kind of problems tend to be harder than solving continuous optimization problems. Therefore, in this work the discrete optimization problem obeying the CSM is approximated as a continuous optimization problem where $J \in [-J_c, J_c]$. When problems are solved in discrete meshes, this approach results in considerably better convergence. Nonetheless, from now on we will refer to this model as the critical state model in this thesis.

The functional (3.1) was discretized based on the discretization of Ω using a mesh with rectangular elements. The calculation of the matrix M and the vector C is

¹The Einstein summation convention is utilized throughout this chapter.

formulated as follows. The change in the magnetic vector potential ΔA_j^z at \mathbf{r} , due to ΔJ at \mathbf{r}' , can be computed using

$$\Delta A_j^z(\mathbf{r}) = -\frac{\mu_0}{2\pi} \int_{\Omega} \Delta J(\mathbf{r}') \ln(\|\mathbf{r} - \mathbf{r}'\|) d\Omega'. \quad (3.4)$$

Consequently, the integral over Ω of $\Delta A_j^z \Delta J$ in (3.1) is

$$W = \int_{\Omega} \Delta A_j^z(\mathbf{r}) \Delta J(\mathbf{r}) d\Omega, \quad (3.5)$$

and the matrix M , representing the mutual inductance between elements i and j , is computed as

$$M_{ij} = -\frac{\mu_0}{2\pi} \int_{e_i} \int_{e_j} \ln(\|\mathbf{r} - \mathbf{r}'\|) d\mathbf{r}' d\mathbf{r}. \quad (3.6)$$

The contribution of the change of the external magnetic vector potential ΔA_a to element i can be computed as

$$\mathbf{C}_i = \int_{e_i} \Delta A_a^z(\mathbf{r}) d\mathbf{r}. \quad (3.7)$$

The detailed formula for calculating the matrix M and the vector C can be found in appendix A of [5].

3.1.3 The critical state model and $J_c(\mathbf{B})$ dependency

As discussed in chapter 2.3.1, one way of modelling the $E(J)$ relation in the superconductor is with the critical state model (CSM) [9], where any electric field differing from zero, causes codirectional electric current density having the magnitude of J_c . In this modelling approach, the CSM is utilized with two different kind of J_c scaling laws: the Bean model [9] and the Kim model [51, 52]. In the Kim model, the J_c depends on the magnetic field, while in the Bean model, J_c is constant.

In the simulations, the $J_c(\mathbf{B})$ in the superconductor was modelled using the ellip-

Table 3.1 The coefficient values utilized in (3.8)

parameter	value	unit
J_{c0}	$2.787 \cdot 10^{11}$	A/m ²
k	0.019	
B_0	0.65	T
β	0.7	

tical anisotropic magnetic field dependency

$$J_c(B_{\parallel}, B_{\perp}) = \frac{J_{c0}}{\left(1 + \frac{\sqrt{k^2 B_{\parallel}^2 + B_{\perp}^2}}{B_0}\right)^{\beta}}, \quad (3.8)$$

where the coefficients J_{c0} , k , B_0 and β characterize the dependency together with the local parallel (B_{\parallel}) and perpendicular (B_{\perp}) components of the magnetic field with respect to the tape orientation shown in figure 3.1. The coefficients were chosen such that the dependency corresponded with a J_c scaling law fitted to match with short-sample measurements on a REBCO tape manufactured by Fujikura [33]. The values of the coefficients are shown in table 3.1.

In the modelling domain Ω , the magnetic field and its parallel and perpendicular components are computed using the 2-dimensional Biot-Savart law for infinitely long bodies

$$\mathbf{B}(\mathbf{r}) = \frac{\mu_0}{2\pi} \begin{bmatrix} 0 & -1 \\ 1 & 0 \end{bmatrix} \int_{\Omega} \frac{J(\mathbf{r}')(\mathbf{r} - \mathbf{r}')}{\|\mathbf{r} - \mathbf{r}'\|^2} d\mathbf{r}'. \quad (3.9)$$

Using (3.9), matrices B_x and B_y , where the element at i th row and j th column is the magnetic flux density in mesh element i due to unit current in mesh element j , can be assembled using

$$\begin{bmatrix} B_x^{ij} \\ B_y^{ij} \end{bmatrix} = \frac{\mu_0}{2\pi} \begin{bmatrix} 0 & -1 \\ 1 & 0 \end{bmatrix} \int_{e_j} \frac{\mathbf{r}_i - \mathbf{r}_j}{\|\mathbf{r}_i - \mathbf{r}_j\|^2} d\mathbf{r}_j. \quad (3.10)$$

Using the x and y axis directions shown in figure 3.1, the parallel component of the magnetic field, at the center of mass of element i , e_i , can be obtained as

$$B_{\parallel}^i = B_y^{ij} J_j. \quad (3.11)$$

Similarly, the perpendicular magnetic field component in element i is computed as

$$B_{\perp}^i = B_x^{ij} J_j. \quad (3.12)$$

3.1.4 AC loss computation

AC losses can be computed from the current density distribution as a function of time as

$$\mathcal{P}(t) = \int_{\Omega} J(\mathbf{r}, t) E(\mathbf{r}, t) d\mathbf{r}, \quad (3.13)$$

where $\mathbf{E} = -\frac{d}{dt}\mathbf{A} - \text{grad}(\varphi)$ and $\text{grad}(\varphi) = -\frac{d}{dt}\mathbf{A}_c$ [80]. The quantity \mathbf{A}_c is the magnetic vector potential of the sub-critical region of Ω , that is the region where \mathbf{J} and \mathbf{E} are zero.²

To proceed the simulation in time, an equidistant (step Δt) time span with time instants t_i was created. For loss computations, we integrated the losses at $t_i + \Delta t/2$ for all i except the last. Then, differentiating (3.13) numerically results in

$$\mathcal{P}\left(t_i + \frac{\Delta t}{2}\right) = \int_{\Omega} \frac{J(\mathbf{r}, t_i + \Delta t) + J(\mathbf{r}, t_i)}{2} \left(\frac{A_c^z(\mathbf{r}, t_i + \Delta t) - A_c^z(\mathbf{r}, t_i)}{\Delta t} - \frac{A^z(\mathbf{r}, t_i + \Delta t) - A^z(\mathbf{r}, t_i)}{\Delta t} \right) d\mathbf{r}. \quad (3.14)$$

The detailed deduction of the formula can be found in [5, 80]. The AC loss \mathcal{Q} , over one cycle per unit length, from t_1 to t_2 , is obtained by integrating (3.14) as

$$\mathcal{Q} = \int_{t_1}^{t_2} \mathcal{P}(t) dt. \quad (3.15)$$

The integral can be computed numerically using for example the trapezoid rule, as done in this work.

²Note that A_c^z is uniform in the sub-critical region of Ω .

3.1.5 Magnetic distortion

The magnetic distortion quantifies the non-linearity in the magnetic field in the magnet's bore in the direction of y -axis specified in figure 3.1. The magnetic distortion is the difference between the actual produced magnetic field and the linear magnetic field. The linear magnetic field depends linearly on the homogeneously distributed operation current such that $\mathbf{B}(I_{\text{op}}) = I_{\text{op}}\mathbf{B}(1 \text{ A})$. In summary, we are interested in the maximum absolute values of that difference which we call the magnetic distortion.

The magnetic distortion in the magnet's bore is due to the magnetization current $J_{\text{m}}(I(t))$ [83]. The magnetization current is defined as

$$J_{\text{m}}(I(t)) = J(I(t)) - J_{\text{h}}(I(t)), \quad (3.16)$$

where $J(I(t))$ is the current density distribution obtained as a solution of the minimization problem (3.3) and $J_{\text{h}}(I(t))$ is the homogeneous current density distribution in Ω corresponding to the amount of applied net current $I(t)$ at time t , i.e. $\int_{\Omega} J(t) \, d\Omega = \int_{\Omega} J_{\text{h}}(t) \, d\Omega = I(t)$. Consequently, $\int_{\Omega} J_{\text{m}}(t) \, d\Omega = 0$. In other words, J_{m} represents the non-linear portion of J corresponding to the difference between the actual current density distribution and the homogeneous one. In order to calculate the magnetic distortion in the center of the magnet's bore, the magnetic flux density produced by J_{m} is computed using the 2-dimensional Biot-Savart law, (3.9).

3.2 Simulation results

In the simulations, the electric current density distribution $J(I(t))$ was solved in four different cases in the modelling domain representing one half of Feather-M0 cross-section. In the four cases, $J(I(t))$ was computed using the Bean and the Kim model with two different ways to set the applied net current constraints (CC) in Ω . In the first way, an equal net current is forced through each tape. Hence, there is no electric current division between the tapes. In the second way, an equal current was forced through each cable. In this case, the net current can be distributed between the tapes of a cable. The tape-wise current constraint corresponds to transposed tapes each going in same x and y location equally long distance. The real situation is somewhere in between these two approaches depending on the contact resistances

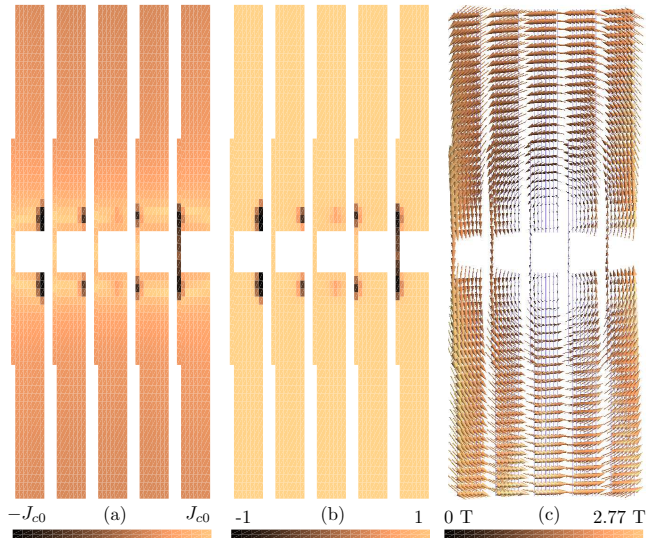


Figure 3.2 Coil I_c determination with Kim model. Figures (a)-(c) present the state of the system just before saturation. (a): Current distribution. (b): Elementwise J/J_c distribution. (c): Magnetic flux density \mathbf{B} .

between the tapes.

The utilized operation temperature was 4.2 K, at which the nominal operation current of Feather-M0 is 6 kA. In order to determine computationally the critical current I_c of the magnet, (3.3) was solved with the Kim model and cable-wise current constraints increasing the operation current up to the point where one of the cable turns was fully saturated. Figure 3.2 (a) shows the current distribution in the magnet cross-section just before the third turn was saturated. In figures (b) and (c), the J/J_c distribution and the magnetic field \mathbf{B} is shown, respectively. For the critical current a value of 11.5 kA was obtained. From the I_c , the critical current density of the superconductor, J_c , was calculated for the Bean model to be $1.3939 \cdot 10^{11}$ A/m².

3.2.1 Current distribution

The current distribution was computed by solving (3.3) with the Bean and the Kim models with two current constraints, where in the first one, CC was set cable-wise and in the second, CC was set tape-wise. In the simulation, the coil was submitted to 6 cycles of subsequent ramps of charges and discharges. The operation current as a function of time is shown in figure 3.3 for 1.25 cycles. Note that the time is arbitrary

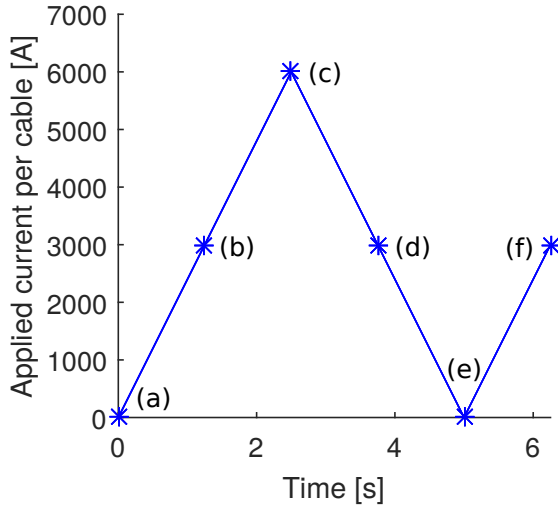


Figure 3.3 The coil is submitted to subsequent ramp charges and discharges.

for losses per cycle in CSM based computations.

Using the Bean model, for both CCs the current distribution in the Feather-M0 half cross-section is shown in figure 3.4 at the time instants labeled with (a)-(f) in figure 3.3. The upper row of figures shows the current distributions for tape-wise CC and the lower row shows the distributions with cable-wise CC. The current distributions are significantly different as can be seen from the current distributions at time instant (c), i.e. at the amplitude of the operation current. Unlike in the upper figure, in the lower figure screening currents appear in the first, second and fifth cable turns to cancel out the parallel magnetic field produced by currents in the other turns.

Figure 3.5 shows the solved current distributions at the same time instants (a)-(f), when the Kim model was utilized for both current constraints. The first row of figures represents the current distributions for tape-wise CC, and the second row shows the current distributions for cable-wise CC. Taking a look at the current distributions at time instant (c), similarly as with the Bean model, the screening currents appear in case of cable-wise CC. Moreover, the use of the Kim model can be seen clearly as the local reduction of J_c at the top and the bottom of the modelling domain, i.e. in the regions of high perpendicular magnetic field (see the magnetic field in figure 3.2 (c)).

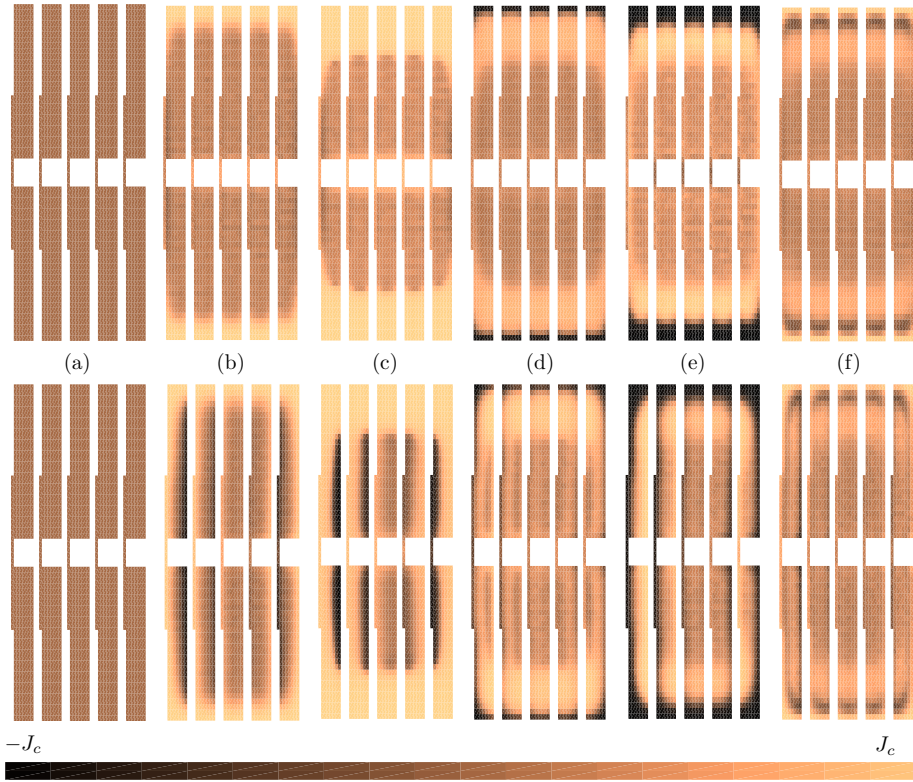


Figure 3.4 Current distributions, computed using Bean model, of points marked in figure 3.3 of the first cycle. The first row of figures presents the current distributions in case where current conditions were set per tape, while the second row of figures presents the current distributions where current conditions were set per cable. $J_c = 1.3939 \cdot 10^{11} \text{ A/m}^2$.

3.2.2 AC losses

The AC losses in the modelling domain as a function of time were computed from the solved current distributions in all the 4 cases using (3.14). The losses predicted using the Bean model are shown for 6 cycles of operation current in figure 3.6 with both CCs. Similarly, the losses predicted using the Kim model are shown figure 3.7. Figure 3.8 shows the losses in all of the simulation cases for comparison over the 5th and 6th cycles. The losses over the 6th cycle are computed using (3.15), the results are shown in table 3.2.

The loss per cycle was smaller when tape-wise current constraint was utilized and yet, the Kim model predicted smaller losses than the Bean model. In summary, the smallest loss per cycle was predicted to be 2.47 J/m with the Kim model and setting

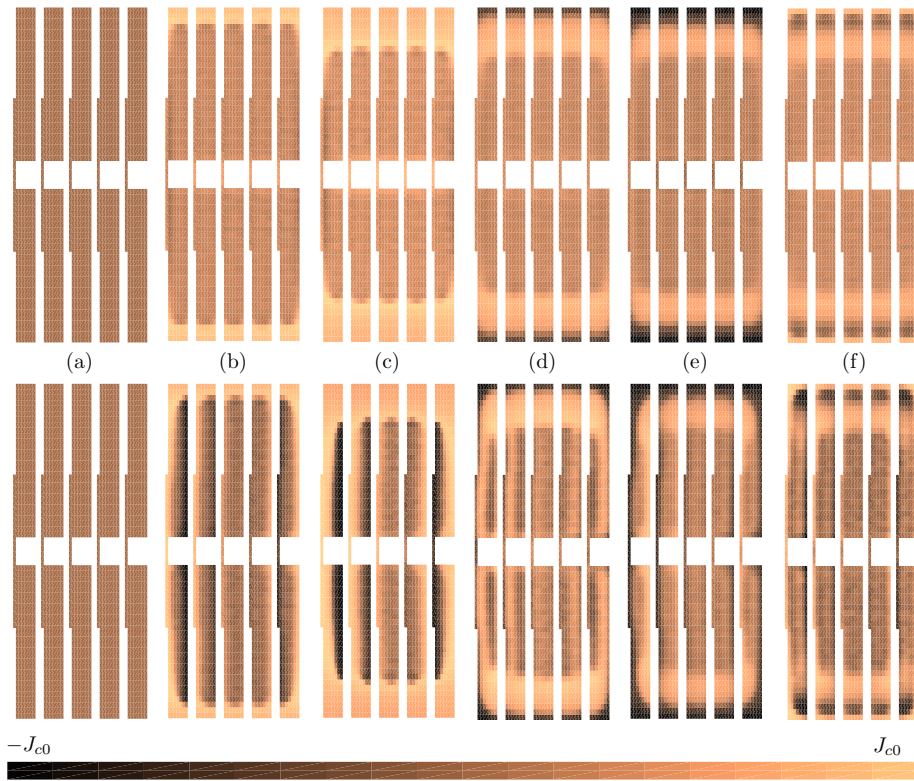


Figure 3.5 Current distributions, computed using Kim model, of points marked in figure 3.3 of the first cycle. The first row of figures presents the current distributions in case where current conditions were set per tape, while the second row of figures presents the current distributions where current conditions were set per cable. $J_{c0} = 2.787 \cdot 10^{11} \text{ A/m}^2$.

tape-wise CC. The largest loss per cycle was predicted to be 5.38 J/m with the Bean model setting cable-wise current constraint. The higher losses when using cable-wise CCs are due to the magnetization currents produced by the parallel in-time changing magnetic field. The reason for the Kim model predicting lower losses is that in some regions J_c was higher than in the Bean model utilized $J_c (1.3939 \text{ A/m}^2)$, determined with the Kim model.

3.2.3 Magnetic distortion

In order to investigate magnetic field quality of Feather-M0, the non-linearity of the magnetic flux density in the y -direction was computed in the center of the magnet's bore (The y -axis direction is specified in figure 3.1). The non-linearity in the

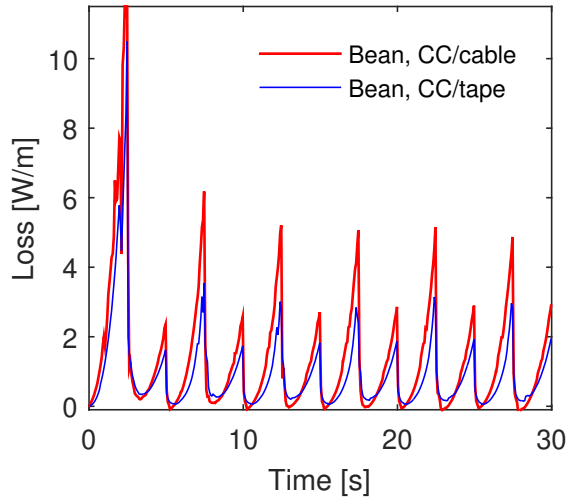


Figure 3.6 Loss curves of the magnet during six ramps. Thicker line presents the case where current condition is per cable, and the thin line presents the loss in case of current condition per tape. The both curves were computed utilizing Bean model.

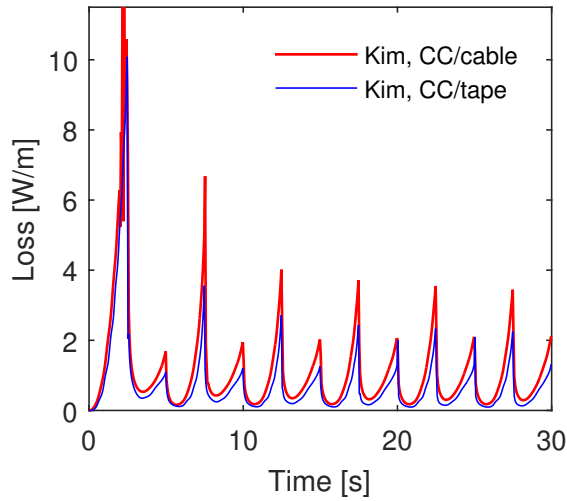


Figure 3.7 Loss curve of the magnet during six ramps. Thicker line presents the case in which the current condition is given for each cable, and the thin line presents the loss in case of current condition per tape. The both curves were computed utilizing Kim model, i.e. non-constant $J_c(\mathbf{B})$ -relation.

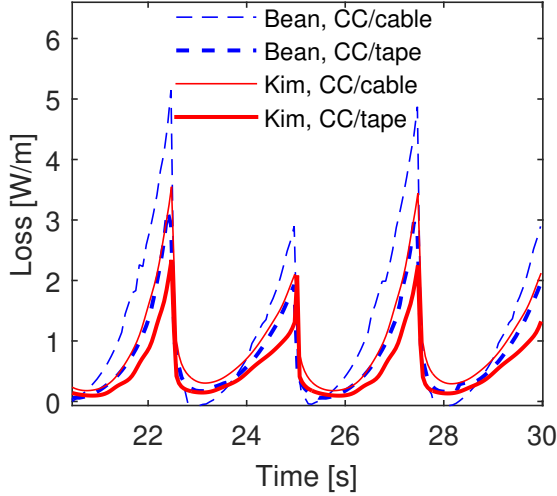


Figure 3.8 A close up of the two last cycles of all the computed loss curves.

Table 3.2 Hysteresis losses in the modelling domain over the 6th cycle of the transport current ramp in different simulation cases

Model	CC	Loss/cycle [J/m]
Bean	cable	5.38
Bean	tape	3.52
Kim	cable	4.33
Kim	tape	2.47

y -direction due to the magnetization currents defined in (3.16) was computed using (3.9).

For the Bean and Kim model, with both current constraints, figure 3.9 shows the magnetic field non-linearity, the magnetic distortion, in the bore as a function of operation current during the sixth cycle of operating the magnet. The maximum distortions in each of the cases are listed in table 3.3. Overall, the Bean model predicted larger distortion than the Kim model and, moreover, forcing tape-wise current constraints, larger distortion was predicted. Hence, the largest distortion was obtained using the Kim model with tape-wise CC: 3.23 mT at 6 kA.

The lower magnetic distortion in case of cable-wise CC can be explained as fol-

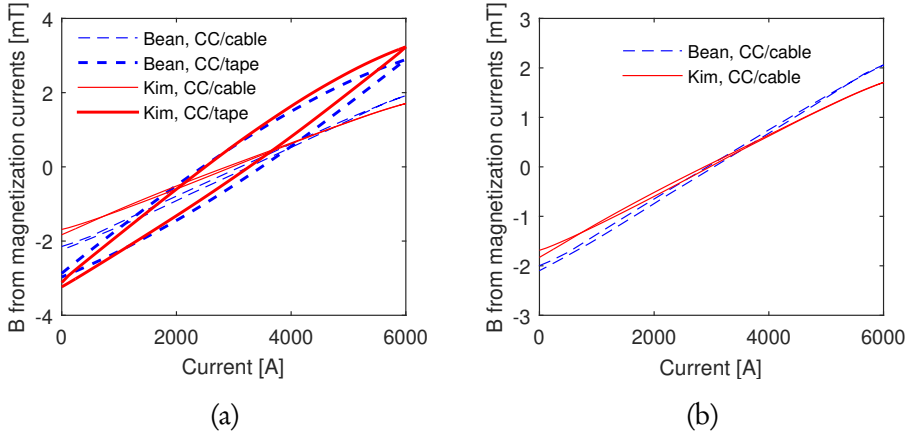


Figure 3.9 In (a), the magnetic distortion in all the 4 cases is shown. Figure (b) is a close up of the distortion in the cases where current condition is per cable.

Table 3.3 The largest magnetization was obtained in CC/tape cases and smallest in CC/cable cases. The 'Max distortion'-data presents the maximum difference from the linear $B(I)$ -field at certain current.

Model	CC/	Max distortion [mT]
Bean	cable	1.92 (6 kA)
Bean	tape	2.89 (6 kA)
Kim	cable	1.71 (6 kA)
Kim	tape	3.23 (6 kA)

lows. During operation, two different directional magnetization currents are produced in the cable turns due to time-varying parallel and perpendicular magnetic field, as illustrated in figure 3.10. Yet, the directions of these two magnetic fields, produced by the magnetization currents, are such that they partially cancel each other out, which reduces the magnetic distortion significantly.

3.3 Concluding remarks

Using the implemented MMEV principle based simulation tool with IPOPT optimization library, simulations on a Roebel-cable based accelerator magnet prototype

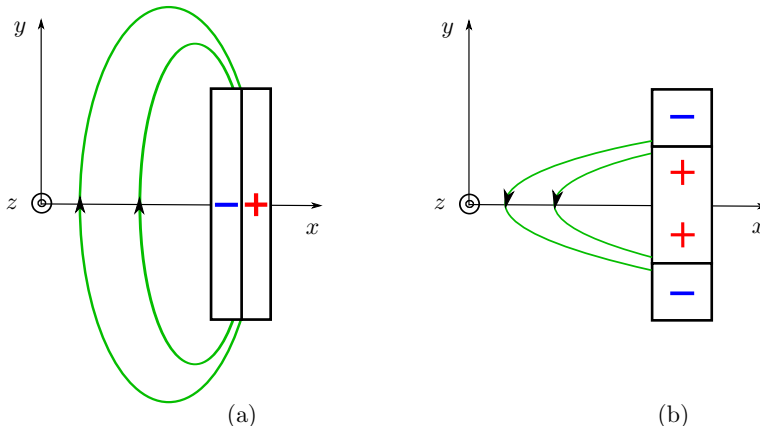


Figure 3.10 Magnetization field and -currents due to parallel (figure (a)) and perpendicular (figure (b)) magnetic field in a cable partially cancel to each other.

magnet Feather-M0 were performed. In the simulations, four different simulation cases were investigated, where the electric current distributions were obtained by solving the MMEV problem, where the critical current J_c in the CSM was modelled using the Bean and Kim model. Furthermore, using the Kim and Bean models, the current constraints were posed tape-wise and the cable-wise. In each case, the current distribution in the magnet was solved for 6 cycles of triangular operation current where the peak current was 6 kA and frequency 0.2 Hz. From the current distributions, AC losses and the field quality were computed.

Based on the results, the lowest AC losses were predicted by the Kim model with tape-wise current constraint, and in case of tape-wise CC the losses were lower with both of the models. On the other hand, the lowest magnetic distortion was obtained using the cable-wise current constraint. In summary, in terms of AC losses, it would be beneficial if the contact resistance between the tapes was as high as possible. Contrarily, for better field quality it would be beneficial if the contact resistance was as small as possible. That is, the results suggest that there is a trade-off between field quality and AC losses. However, experiments are required to study how the magnet behaves, and for evaluating the predictive capability of the simulation approach.

In the simulations, the utilized $E(J)$ relation was the critical state model where the relation is discrete. In order to obtain better convergence for the problem, solutions were obtained by solving a continuous optimization problem where $J \in [-J_c, J_c]$. Consequently, the obtained results for the current density distribution were smooth.

Therefore, they can estimate the $E(J)$ relation of high-temperature superconducting material better than the true CSM would (See figure 2.2). In addition, in the simulations we were interested in the long term effects in the modelled magnet. In such simulations, the CSM can be a better option compared to power law. The power law tends to over estimate the homogenization of the current density profiles, as observed in [58]. However, further investigations on the predictive capability of the utilized approach should be done.

4 MODELLING THERMODYNAMICS IN HTS MAGNETS

Thermal modelling of high-temperature superconducting magnets can be challenging due to highly non-linear $E(J)$ relation in the superconductor. Another difficulty-increasing aspect is their nature of being finely detailed in structure, as in case of Roebel cable based accelerator magnets: what kind modelling decisions should be made in order to be able simulate the magnets in reasonable period of time? Moreover, in simulating the magnet behavior in operation it is essential to take cooling into account in the modelling too.

In this chapter, a thermal model is constructed and outlined based on publication III and publication VI. The heat diffusion equation is used to model the thermodynamics in the system consisting of a superconducting magnet and its cooling environment. The equation to be solved consists of different sub-models which model the different aspects of the system. These sub-models are the models for different material properties, cooling model, model for heat generation and the model for the $E(J)$ relation in the superconductor. In the utilized modelling approach, the modelling domain representing the magnet winding is reduced to 1-dimensional. In this chapter, details on how to take into account the 3-dimensional aspects such as heat transfer between the cable turns are presented. The thermal model was implemented in Matlab on an open source platform *dp* [84]. For generating the modelling domain and the mesh, an open source platform GMSH was utilized [36].

This chapter is strictly limited to the presentation of the physics in the modelling tool. Results are presented in the subsequent chapter.

4.1 The heat diffusion equation

The thermal model is based on the heat diffusion equation

$$C_V \frac{d}{dt} T = \nabla \cdot (\lambda \nabla T) + Q, \quad (4.1)$$

where the temperature T is the unknown quantity to be solved. Moreover, C_V and λ are the volumetric heat capacity and the thermal conductivity, respectively. The last term, Q , is the volumetric heat source of the problem. The term on the left-hand side in (4.1), describes the change in the internal energy. The first term on the right-hand side is the the Fourier's law that describes the heat transfer within the modelling domain. The last term, as mentioned already, describes the heat source, i.e, the net effect of the heat generation and the cooling.

In this approach, the modelling domain was reduced to one-dimensional in order to be able to perform thermal simulations for large magnets efficiently. Consequently, the general form (4.1) in Cartesian coordinate system takes the form

$$C_V \frac{d}{dt} T = \frac{d}{dx} \left(\lambda \frac{d}{dx} T \right) + Q^+ + Q^- + Q^{\parallel}, \quad (4.2)$$

where the temperature has spatial derivatives only in the x -direction. In (4.2), the heat source term Q is now broken down into its constituents, where Q^+ and Q^- are the heat generation and the cooling, i.e. the heat transfer between the magnet and the coolant, respectively. Specific for this approach is the term Q^{\parallel} , which is a volumetric heat source term describing the heat diffused from neighboring cable turns. In this heat flux, the information about the 3-dimensional geometry of the magnet, i.e. the location of the cable turns with respect to each other, needs to be embedded.

4.2 Modelling domain and its discretization

A 3-dimensional illustration of the geometry of Feather-M2 was shown in figure 2.6. A close up of a piece of that geometry is illustrated in figure 4.1, where a piece of two adjacent cable turns are shown. The dimensions d_w and d_t correspond to the width and the thickness of the cable, including the thickness of the cable insulation,

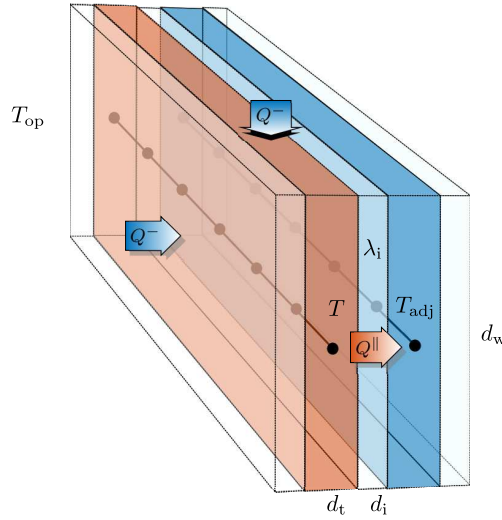


Figure 4.1 An illustration of a piece of two adjacent insulated cable turns. The heat flux term between the cable turns (Q^{\parallel}) and the cooling flux (Q^-) on the exposed surfaces of the winding are also illustrated. Cable insulation is visible only in between the cable turns.

respectively. The total thickness of insulation between the two cable turns is denoted with d_t .

The cable cross-section is assumed to be isothermal. Therefore, in the cable cross-section, the temperature can be expressed with only one degree of freedom.¹ Hence, it is sufficient to solve the magnet's temperature along a single dimension that is discretized into elements and nodes. The nodes, at which the temperature is to be solved, are marked with black dots in figure 4.1. In case of a whole coil, the domain, with nodes marked with black dots, where the domain is further reduced into 1-dimensional form. This means that, even if the temperature can be solved in a 1-dimensional domain, the 3-dimensionality of the problem still has to be embedded into the problem by other means. In this approach, the 3-dimensionality is embedded via the magnetic field and the heat fluxes Q^{\parallel} and Q^- . Moreover, the discretization of the 1-dimensional modelling domain is done using the Galerkin finite element method with piece-wise linear basis functions. The heat flux between the cable turns was discretized using the finite difference method. The process was explained in chapter 2.4.3.

¹Further theoretical and experimental work is required to study the validity of this assumption.

4.3 Material properties

The material properties utilized in describing the problem are the volumetric heat capacity C_V , the thermal conductivity λ and the electrical resistivity of the normal conducting fraction of the cable's cross-section ρ_{nc} . The magnet is modelled on a 1-dimensional modelling domain. Therefore, the material properties of the different materials in the cable are homogenized. The concept of effective material properties is utilized to describe the different material properties of the homogenized cable [103].

The formulas for computing the different effective material properties are the following:

$$C_V = \sum_{i=1}^m f_i C_V^i, \quad (4.3)$$

$$\lambda = \sum_{i=1}^m f_i \lambda^i, \quad (4.4)$$

$$\rho_{nc} = \left(\sum_{i=1}^{m'} \frac{f_i}{\rho_{nc}^i} \right)^{-1}. \quad (4.5)$$

The index m refers to the total number of different materials in the cable, including the cable insulation material. In computing ρ_{nc} , the index m' refers to the number of the normal conducting materials, hence $m = m' + 1$. Moreover, f_i denotes the cross-sectional material fraction of the material i . Similarly, the superscript i is used to denote the material properties of material i in the compound.

4.4 $E(J)$ relation in the superconductor

Different models for describing the $E(J)$ relation in superconducting material have been developed of which the two commonly used relations are the critical state model and the power law. Out of those two, the power law is a more general model being able to describe $E(J)$ relations of arbitrary steepness determined by its parameters such as the power n . In order to formulate the thermal model to be as general as possible, the power law was chosen to describe the $E(J)$ relation in the superconducting material.

In the power law, the electric field in superconductor (E_{sc}) as a function of the

electric current I_{sc} flowing in the superconductor can be modelled as

$$E_{\text{sc}} = E_{\text{c}} \left(\frac{I_{\text{sc}}}{I_{\text{c}}} \right)^n, \quad (4.6)$$

where E_{c} , the electric field criterion, and the power n determine the $E(J)$ relation with the critical current I_{c} .

To remark, we are interested in the local quantities on the one dimensional modelling domain representing the cable of the magnet winding. In order to calculate E_{sc} , the local cross-sectional critical current of the cable need to be computed. The local critical current is computed by integrating the critical current density over the superconducting layers of the cable cross-section as

$$I_{\text{c}}(T, I_{\text{op}}, \alpha) = \int_{A_{\text{sc}}} \alpha J_{\text{c}}(T, \hat{\mathbf{B}} I_{\text{op}}) \, dA, \quad (4.7)$$

where J_{c} is a scaling law and α its scaling coefficient. The J_{c} scaling law is a fitting function that is based on short-sample $V-I$ measurements of superconducting tape, where certain voltage criterion is utilized for determining J_{c} of the superconductor. The fit depends on the temperature and the magnetic field².

Characterizing the $J_{\text{c}}(T, \mathbf{B})$ of an HTS tape requires a great amount of measurements. Therefore, it is common that a J_{c} scaling law may not exist for the specific superconductor under investigation. The purpose of the coefficient α is to generalize, to some extent, the J_{c} scaling law, which is based on J_{c} measurements of certain superconductor. Consequently, the same scaling law can be scaled with α to describe the J_{c} characteristics of another similar superconductor.

In this modelling approach, linear $\mathbf{B}-I$ dependency is assumed such that $\mathbf{B} = \hat{\mathbf{B}}I$. Therefore, the magnetic field per unit current $\hat{\mathbf{B}}$ on the 3-dimensional geometry can be precomputed. Consequently, significant savings in simulation time can be achieved but on the flip side, the non-linearity in the magnetic field is neglected.

²In case of REBCO tapes, the $E(J)$ relation depends, not only on the magnitude of \mathbf{B} , but also on its direction with respect to the wide face of the tape.

4.5 Heat generation

The heat in a superconducting cable is generated in the superconducting fraction f_{sc} and in the normal conducting fraction f_{nc} . Hence, by Kirchoff's current law, it holds that the applied operation current I_{op} is divided between the two fractions such that $I_{op} = I_{sc} + I_{nc}$, where I_{sc} and I_{nc} denote the electric current flowing in the superconducting fraction and in the normal conducting fraction of the cable, respectively.

To solve the current division, it is assumed that the electric field in the normal conducting fraction equals the electric field in f_{sc} . It is further assumed that the electric field and the electric current density in both fractions are constant, such that $I_{nc} = J_{nc}A_{nc}$ and $I_{sc} = J_{sc}A_{sc}$, where A is the cross-sectional area of the fraction specified by the subscript. Furthermore, it is assumed that for the normal conducting fraction, it holds that $E_{nc} = \rho_{nc}J_{nc}$ and for the superconducting fraction, (4.6) holds. Hence, the non-linear equation for solving I_{nc} can be formulated as follows³.

$$\begin{aligned}
 E_{nc} &= E_{sc} \\
 \Leftrightarrow \rho_{nc} \frac{I_{nc}}{A_{nc}} &= E_c \left(\frac{I_{sc}}{I_c} \right)^n \\
 \Leftrightarrow I_{nc} &= E_c \left(\frac{I_{sc}}{I_c} \right)^n \frac{A_{nc}}{\rho_{nc}} \\
 \Leftrightarrow I_{nc} &= E_c \left(\frac{I_{op} - I_{nc}}{I_c} \right)^n \frac{A_{nc}}{\rho_{nc}} \\
 \Leftrightarrow I_{nc} - E_c \left(\frac{I_{op} - I_{nc}}{I_c} \right)^n \frac{A_{nc}}{\rho_{nc}} &= 0
 \end{aligned} \tag{4.8}$$

Now, since the electric currents I_{op} , I_{sc} and I_{nc} are known, the heat generation in the cable can be computed as

$$\begin{aligned}
 Q^+ &= f_{sc} E_{sc} J_{sc} + f_{nc} E_{nc} J_{nc} \\
 &= f_{sc} E_c \left(\frac{I_{sc}}{I_c} \right)^n \frac{I_{sc}}{A_{sc}} + f_{nc} \rho_{nc} \left(\frac{I_{nc}}{A_{nc}} \right)^2.
 \end{aligned} \tag{4.9}$$

³In the implementation of the thermal model, the Newton-Raphson method is utilized for solving (4.8) for I_{nc} .

The heat generation is the sum of the heat generated in both, the superconducting and the normal conducting materials, both weighted with the corresponding fraction such that $f_{nc} + f_{sc} = 1$.

4.6 Cooling

The cooling, i.e., the heat transfer from coolant to the magnet is modelled using

$$Q^- = b \frac{T_{op} - T}{c}, \quad (4.10)$$

where T_{op} is the temperature of the coolant and b is the heat transfer coefficient. The wetting coefficient c is defined as

$$c = \frac{A}{p}, \quad (4.11)$$

where the wetting perimeter p determines the length of the cable perimeter that is exposed to the heat exchanging medium⁴.

4.7 Heat diffusion between the cable turns

In this modelling approach, the modelling domain was determined to be one dimensional. Hence, the heat transfer between the different cable turns has to be taken into account using the finite difference method as discussed in chapter 2.4.4. In this thermal model, the heat flux to a cable turn from a neighboring turn is modelled as

$$Q^{\parallel} = \bar{\lambda}_i \frac{T_{adj} - T}{d_i c}, \quad (4.12)$$

where $\bar{\lambda}_i$ is the thermal conductivity of the insulation material of the cable, d_i is the total thickness of the insulation material between the two cable turns, and c is the wetting coefficient defined as earlier in (4.11). In this case, p is the width of the cable since the heat transfers through the wide faces of adjacent cable turns. Moreover, T

⁴The wetting perimeter is normally chosen such that the surface of the winding is exposed to the cooling. On the other hand, in some designs, the winding can be surrounded by some support structures for example and hence realistic estimations on p should be done.

and T_{adj} are the temperatures at adjacent locations in the two adjacent cable turns. On the 1-dimensional modelling domain Ω , at $x \in \Omega$, T_{adj} , corresponding to $T(x)$, is $T(f_A(x))$ where f_A is the adjacency mapping as explained in chapter 2.4.4.

4.8 Remarks

The heat diffusion equation (4.2) was discretized as detailed in chapter 2.4. In order to take the heat diffusion between the cable turns into account, the finite difference method was utilized as detailed in chapter 2.4.3. Hence, it was possible to use the nodal values of the modelling domain for computing Q^{\parallel} in each element of the modelling domain as the solution dependent source term. In addition, using this method for taking into account the thermal coupling between the cable turns, there is no need for meshing the region in-between the turns — consequently the number of unknowns in the problem can be reduced significantly.

5 MODELLING THERMODYNAMICS IN FEATHER-M2

There are many useful results that simplify the modelling of LTS magnets significantly. For example, the critical current I_c corresponds very accurately to the maximum operation current of an LTS magnet due to the very steep $V - I$ relation. When modelling Roebel cable based HTS magnets, the magnet's $V - I$ relation can be very gradual and hence the concept of I_c does not correspond anymore to the maximum current the magnet can be operated with. Depending on the available cooling, the magnet can be operated stably even if the average electric field in the winding was higher than E_c . In this chapter, the implementation of the thermal model, presented in chapter 4 is utilized for studying the Roebel cable based HTS dipole magnet, Feather-M2. The following two studies focus on the magnet's behavior in operation where cooling and stability are important aspects. Moreover, the Feather-M2 specifications utilized in the modelling are as detailed in chapter 2.2.2.2.

In the first section of this chapter, $V(I)$ measurement data on the Roebel cable based HTS magnet Feather-M2 is first presented. Based on the measurement data, the observed behavior was investigated using the thermal model presented in chapter 4. In the utilized methodology, an inverse problem based approach was developed for understanding the magnet behavior. Using the methodology it was possible to investigate the predictive capability of the thermal model and also, to explain the behavior in terms of the utilized thermal model. This discussion is based on publication VI

The second section presents the methodology and the simulation results on how to computationally determine the maximum stable operation current of Feather-M2. Due to the rather arbitrary definition of I_c for magnets exhibiting gradual $V - I$ dependency, a methodology was developed for computationally determining the maximum operation current the magnet could be continuously operated with. This is based on publication V.

5.1 Modelling thermodynamics in Feather-M2 using an inverse problem based approach

Feather-M2 magnet was designed, constructed and tested in 2017 at CERN within the EUCARD2 project [91]. In the measurements, unexpected magnet behavior was observed where the voltage developed very slowly with the operation current and consequently the magnet could be operated above its critical current. Despite the significant heat generation, by lowering the operation current, stable magnet operation could be attained without thermal runaway. This kind of very robust and gradual behavior needed to be explained.

The aim of this work was to explain the observed magnet behavior in terms of the thermal model presented in chapter 4. In the approach, the thermal model was parametrized and the parameters were obtained by solving an inverse problem, formulated using Feather-M2 measurement data. Hence, the magnet behavior could be characterized based on the thermal model and the solved parameter values. In addition, this kind of inverse problem based approach proved to be a valuable method to test the predictive capability of the thermal model and its sub-models.

5.1.1 Measurement data

Feather-M2 was tested at CERN in SM18 facility [20]. The magnet was cooled in a cryostat with forced flow helium gas. Moreover, the operation temperature T_{op} in the cryostat was adjustable. The magnet was tested in various different operation temperatures within the range from 5 K to 85 K with numerous different operation current (I_{op}) time-series [73]. In figures 5.1(a)-(j), 10 measurement cases, indexed with i , are shown where the average resistive electric field¹ (E_i) over the magnet and the corresponding operation current (I_i) are shown as a function of time. The T_{op} -range in these cases was from 6 K to 70 K.

¹In this work, the average resistive electric field is defined as the measured resistive voltage divided by the length of the cable. Moreover, in this chapter, the average resistive electric field is denoted simply with the symbol E .

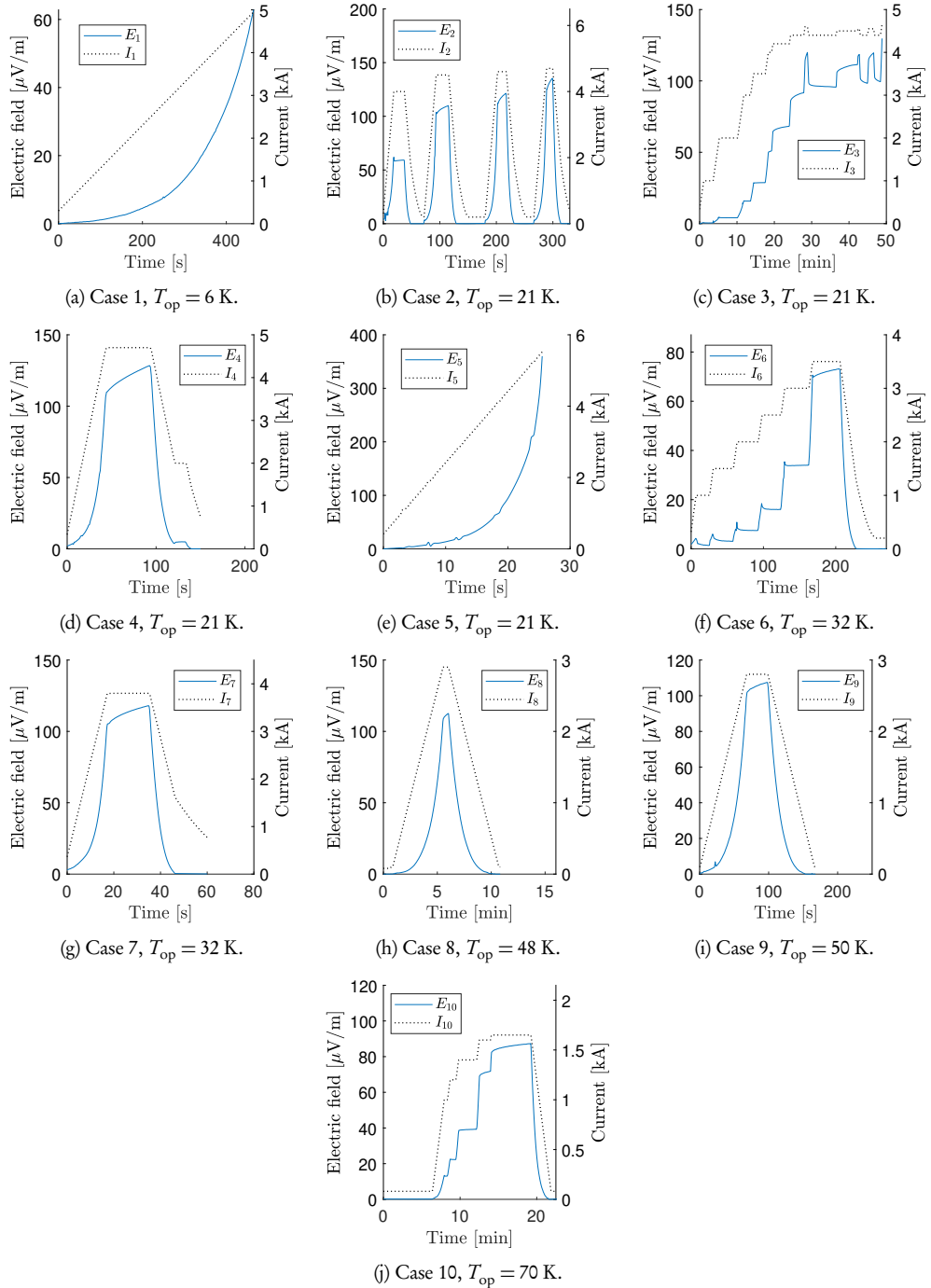


Figure 5.1 Figures (a)-(j) represent, in each case $i = 1 \dots 10$, the measured average electric field E_i as a function of the operation current I_i and time in Feather-M2.

5.1.2 Methodology

A methodology was developed for learning about the Feather-M2 behavior in operation in terms of the thermal model. The methodology relies on the mathematical concept of inverse problems, where one solves the causalities from the observations based on a model describing this relationship. This process should not be confused with the so-called fine tuning where a model, say an arbitrary polynomial not based on physics describing the phenomena, is fitted to match with the observations. The process of inverse problem is an inverse to the usual forward problem in which one tries to predict the observations from the causal factors. Sometimes, however, not all the required inputs for making such predictions are available, but observations are. Then solving an inverse problem is the only way to proceed in order to avoid making too wild assumptions on the inputs of the problem [109].

The following inverse problem formulation is based on the thermal model constructed in chapter 4. Let us denote the thermal model as a mapping $M(\mathbf{x}, I_{\text{op}})$ where the parameters of the model as elements of vector are $\mathbf{x} = [\alpha, n, E_c, b]$.

The parameters could have been chosen differently too, and it would be a valid research case to scrutinize the different possible parametrizations. In this work, we focus only on one parametrization reasoned as follows. In this work the focus is on the thermal stability modelling of Feather-M2. Therefore, the greatest interest is in the heat generation and cooling, and the corresponding models. Hence, based on the measurements on the magnet, the aim is to scrutinize, what kind of power law based $E(J)$ characteristics the utilized superconductor in the application manifests. In order to fully characterize the power law, all the parameters of the utilized $E(J)$ relation (See (4.6)) need to be taken into account, i.e. α , n and E_c . In order to obtain estimations about the heat exchange between the cooling environment and the winding, the heat transfer coefficient b in (4.10) is chosen to be one of the model parameters. In regards to the chosen parameters, one could criticize especially the choice of taking E_c as one. In the measurements, when determining J_c characteristics of a superconductor, E_c is typically fixed to $10 \mu\text{V}/\text{m}$. However, in these simulations, we distinguish E_c from that context and define it as a parameter of the model whose value is obtained as a solution of inverse problems, to be formulated next.

The inverse problems for solving \mathbf{x} in different measurement cases can be formulated as follows. Given a measurement case i , where the measurement data on

average electric field as a function of time is denoted with E_i , and the corresponding operation current as a function of time is denoted with I_i , the aim is to find the values of parameters in \mathbf{x} , such that

$$E_i = M(\mathbf{x}, I_i). \quad (5.1)$$

The problem is highly, non-linear. Therefore, in order to obtain a solution of (5.1), the non-linear minimization problem

$$\begin{aligned} \min_{\mathbf{x}} \quad & \int_0^{t_m} |(E_i - M(\mathbf{x}, I_i))(t)| dt \\ \text{s.t.} \quad & \mathbf{b}_l \leq \mathbf{x} \leq \mathbf{b}_u \end{aligned} \quad (5.2)$$

is solved where \mathbf{b}_l and \mathbf{b}_u are the lower and upper bounds for each parameter, respectively. There are many possible alternatives for the objective function to be minimized. However, the aim is to find the best model parameters \mathbf{x} so that (5.1) is satisfied with an acceptable tolerance. The chosen objective function is defined to be the time integral of the the absolute value of the difference $(E_i - M(\mathbf{x}, I_i))(t)$ over the time interval $[0 \ t_m]$ corresponding to the duration of the measurement which started at $t = 0$ and ended at $t = t_m$. The obtained solution in case i is denoted as \mathbf{x}_i .

The difference between the model predictions and the experimental data is calculated as the relative and maximum difference. In case i , the relative difference Δ_r is calculated as

$$\Delta_r = 1 - \frac{\int_0^{t_m} (M(\mathbf{x}_i, I_i))(t) dt}{\int_0^{t_m} E_i(t) dt} \quad (5.3)$$

and the maximum difference Δ_m as

$$\Delta_m = \max \{|(E_i - M(\mathbf{x}_i, I_i))(t)|\}, \quad t \in [0, t_m]. \quad (5.4)$$

5.1.3 Simulation results

Figure 5.2 shows the solution for each inverse problem case $E_i = M(\mathbf{x}_i, I_i)$, where the measured average electric field of the i th case is compared with the thermal model predictions with inputs \mathbf{x}_i and and operation current I_i as a function of time. The parameter values of the solutions \mathbf{x}_i are listed in table 5.1.

Table 5.1 The solutions of the inverse problems.

	α	n	E_c	h	T_{op}
\mathbf{x}_1	0.17	2.3	102	69	6
\mathbf{x}_2	0.17	2.8	109	85	21
\mathbf{x}_3	0.16	3.1	91	55	21
\mathbf{x}_4	0.18	3.0	108	45	21
\mathbf{x}_5	0.15	2.9	84	75	21
\mathbf{x}_6	0.17	2.9	90	77	32
\mathbf{x}_7	0.17	3.3	87	86	32
\mathbf{x}_8	0.19	2.8	74	60	48
\mathbf{x}_9	0.20	2.5	72	42	50
\mathbf{x}_{10}	0.19	3.1	10	44	70
unit			$\mu\text{V/m}$	$\text{W/m}^2\text{K}$	K

Table 5.2 shows the computed relative and the maximum difference in each case. Worth noticing is that over all the cases, the average of the relative differences was only 2.4 % and the average of the absolute differences was 15 $\mu\text{V/m}$. This means that with the presented methodology decent case-wise solutions can be found.

The parameter values listed in table 5.1, vary the most in case of E_c and h , the variance in α and n is smaller. The values obtained for n are quite low compared to typical values of around 20-30 for HTS tapes [37]. However, similar values were obtained for the magnet it-self in the measurements [73]. This can be related to the current distribution between the cable tapes where current passing from tape to another contributes to the measured resistive voltage [121]. The obtained values for h are difficult to compare with literature values. This is due to the various structures and materials around the magnet affecting to the heat exchange between the winding and the coolant.

In order to test the predictiveness of the model, we parametrized it with the parameter values of the solution \mathbf{x}_6 corresponding to the case for which the smallest Δ_r and Δ_m were obtained. Hence, using the model $M(\mathbf{x}_6, I_i)$, the average electric field was computed for each of the 10 cases using the operation condition scheme of each case. The results are shown in figure 5.3 and table 5.3. The model's pre-

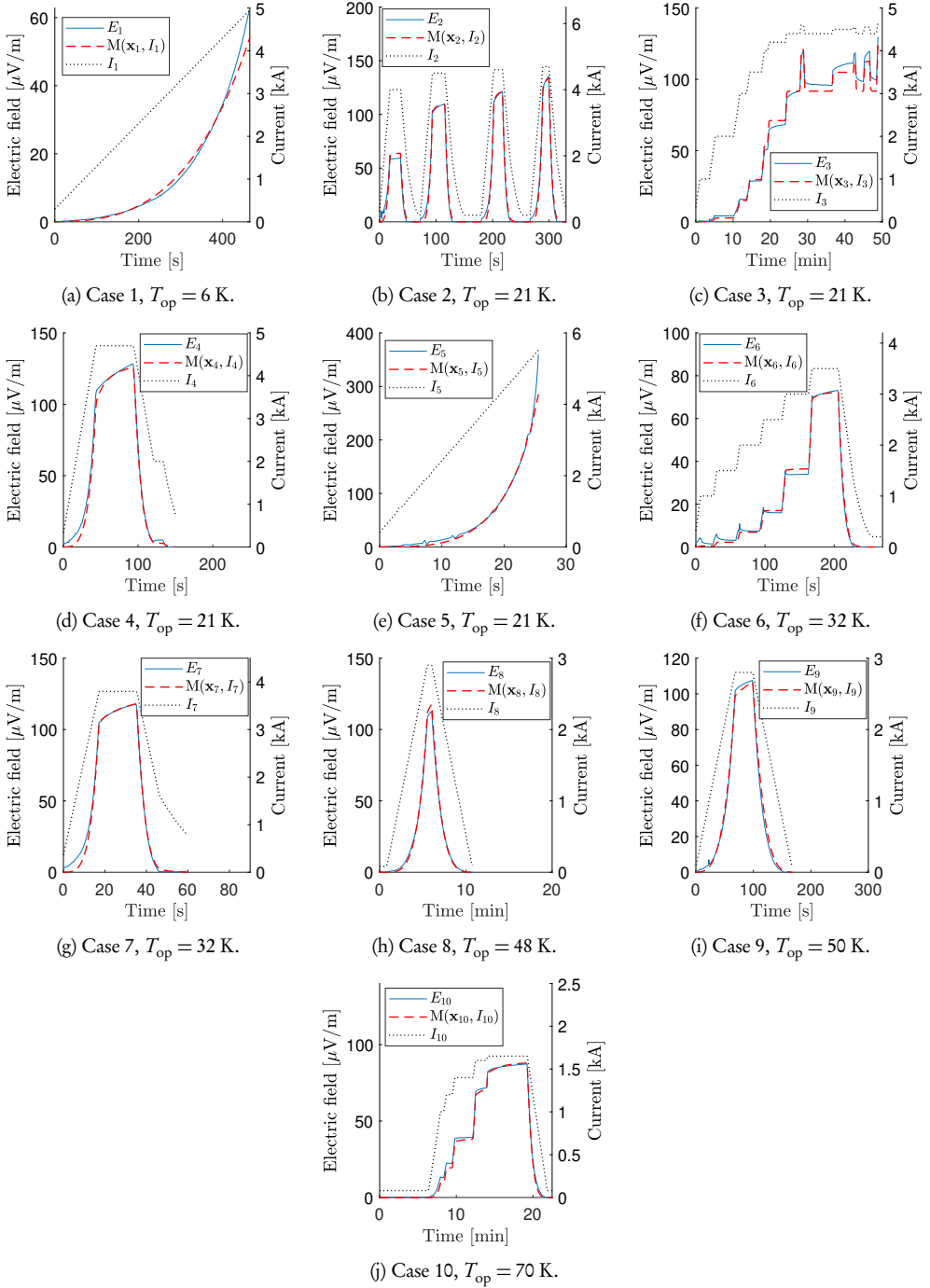


Figure 5.2 Figures (a)-(j) represent, in each case $i = 1...10$, the measured and simulated average electric field E_i as a function of the operation current I_i and time in Feather-M2.

Table 5.2 Relative and maximum differences of the inverse problem solutions.

case	Δ_r [%]	Δ_m [$\mu\text{V}/\text{m}$]	T_{op} [K]
1	1.5	9	6
2	0.9	10	21
3	2.8	9	21
4	5	11	21
5	5.6	75	21
6	0.4	4	32
7	2.6	9	32
8	-0.7	5	48
9	-1.9	6	50
10	2.4	4	70

dictive capability is not satisfying over the whole temperature range. The solution \mathbf{x}_6 was obtained for $T_{\text{op}} = 32$ K. Close to that temperature, the predictions corresponded better with the measurements. This can indicate that something in the thermal model does not model the system desirably. Possible reasons can lie for example in the temperature dependence of the $E(J)$ relation [7] or the cooling model. Or it can be that the cooling conditions are different from measurement case to another in terms of the flow rate of the helium. However, this gives important insight regarding the predictive capability of the model: the results suggest that the temperature dependent models, such as the power law or the cooling model should be replaced with other ones and then tested again. These issues should be investigated in the close future in order to gain more understanding in modelling HTS magnets in different cooling environments.

5.2 Computational determination of the maximum stable operation current

The stability of the Feather-M2 magnet was inspected by means of power balance, i.e., the sum of heating power and cooling power in the magnet's windings. Using

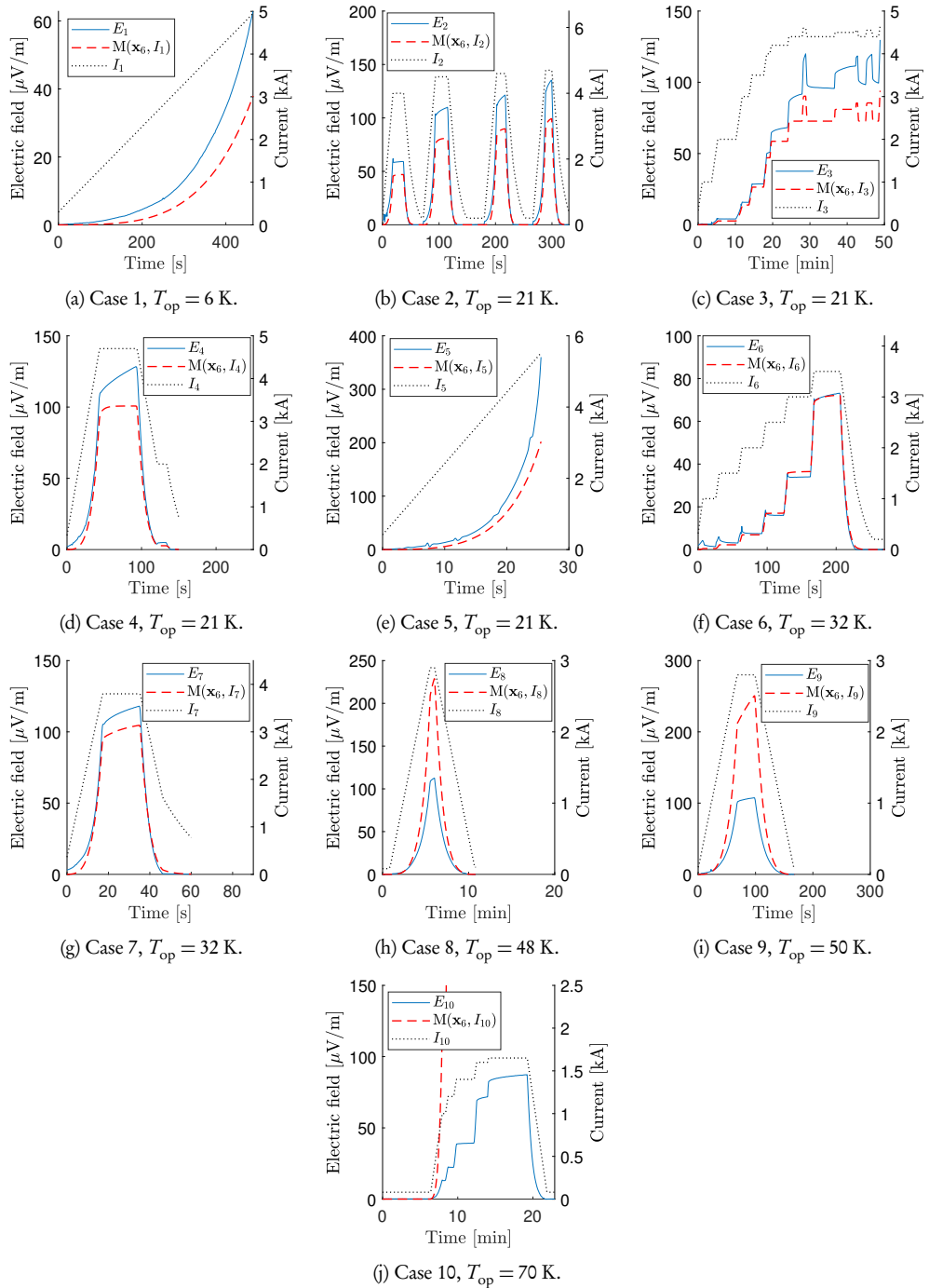


Figure 5.3 Figures (a)-(j) represent, in each case $i = 1 \dots 10$, the measured and simulated average electric field E_i as a function of the operation current I_i and time in Feather-M2. Simulations were performed using parameter values of the solution \mathbf{x}_6 .

Table 5.3 Relative and maximum differences of $M(\mathbf{x}_k)$ in all of the simulation cases. In case 10, the differences could not be computed due to the early thermal runaway.

case	Δ_r [%]	Δ_m [$\mu\text{V}/\text{m}$]	T_{op} [K]
1	44.0	25	6
2	26.8	36	21
3	22.5	36	21
4	18.7	28	21
5	31.6	158	21
6	0.4	4	32
7	10.5	13	32
8	-81.9	116	48
9	-113.4	144	50
10	—	—	70

this concept, a definition for stable magnet operation was given and simulations were done in order to computationally determine the maximum stable operation current I_{mas} of Feather-M2. In this section, the methodology and the simulation results are presented.

5.2.1 Methodology

Let us first define the quantities the total heating power P and the total cooling power C that are essential for developing the methodology. The total heating power is the power at which heat is generated in the winding. It is defined as the volume integral of the heat generation Q^+ (See (4.9)) over the winding volume as

$$P(t) = A \int_0^l Q^+ dx.$$

The total cooling power is computed as the surface integral of the heat flux between the magnet and the coolant over the surface of the magnet's windings as

$$C(t) = A \int_0^l Q^- dx = \int_0^l ph (T_{\text{op}} - T) dx.$$

Based on the quantities P and C , we define a magnet to be thermally stable according to the following definition.

Definition 1. A magnet, operated in constant conditions $(T_{\text{op}}, I_{\text{op}})$, is thermally stable if and only if $\exists t_c > 0$ such that

$$(P + C)(t) \leq 0, \forall t \geq t_c. \quad (5.5)$$

From the definition it follows that

Corollary 1. At constant operation conditions,

$$\exists t_c > 0 \text{ s.t. } (P + C)(t_c) \leq 0 \Rightarrow (P + C)(t) \leq 0, \forall t \geq t_c.$$

This corollary allows the modeller to determine whether the operation is stable, or not, by simulating the magnet only until $t = t_c$, instead of investigating the stability when $t \rightarrow \infty$. Based on the stability definition and the corollary, the problem for determining I_{mas} can be now formulated. In this approach, I_{mas} was determined by solving an optimization problem, where the time-invariant operation current of the magnet was maximized with the constraint that required the magnet to be stable. Hence, the optimization problem can be formulated as

$$\begin{aligned} \max \quad & I \\ \text{s.t.} \quad & (P + C)(t_c) \leq 0 . \end{aligned} \quad (5.6)$$

5.2.2 Simulation results

The thermal model was parametrized based on the research done in [31], presented earlier in this chapter. The model parameters and the other simulation parameters

Table 5.4 Simulation parameters.

parameter	value	unit	description
α	0.17		scaling factor for J_c scaling law
n	2.8		n -value
E_c	109	$\mu\text{V}/\text{m}$	electric field criterion
h	85	$\text{W}/\text{m}^2\text{K}$	heat transfer coefficient
t_c	200	s	stability criterion time
T_{op}	21	K	coolant temperature

are listed in table 5.4. The model parameters values were obtained as a solution to the inverse problem corresponding to the case 2 (Recall chapter 5.1). These values are utilized in the following simulations, unless otherwise stated. Moreover, in order to determine an adequate value for t_c , a pre-simulation can be done where one investigates the P + C dynamics in the system. For the system under study, we observed that 200 s was long enough time-period to be able to say if the magnet was in stable state or not. However, appropriate t_c should be investigated case by case.

The maximum stable operation current for Feather-M2 was simulated to be 5162 A. The corresponding maximum temperature in the windings (T_{max}) and the power balance P + C are shown as a function of time in figure 5.4 where for comparison P + C and T_{max} are also shown for operation currents 1 % lower and 1 % higher than I_{mas} . With $I_{\text{op}} = 1.01I_{\text{mas}}$, stable magnet operation was not possible anymore as can be deduced from the thermal runaway. With the two I_{op} values lower than $1.01I_{\text{mas}}$, the operation is stable: T_{max} levels to a constant.

The time-behavior of P + C can be explained as follows. In the beginning, C is low because the temperature difference between the winding and the coolant is small but P is high due to high operation current causing losses in the winding. Once the temperature difference between the coolant and the winding starts to increase, the cooling power C increases. With operation currents of $0.99I_{\text{mas}}$ and I_{mas} , P + C goes to zero: the available cooling is enough to stabilize the magnet.

In order to investigate the dependency between the maximum stable operation current and the model parameters, I_{mas} was computed and the parameters n -value,

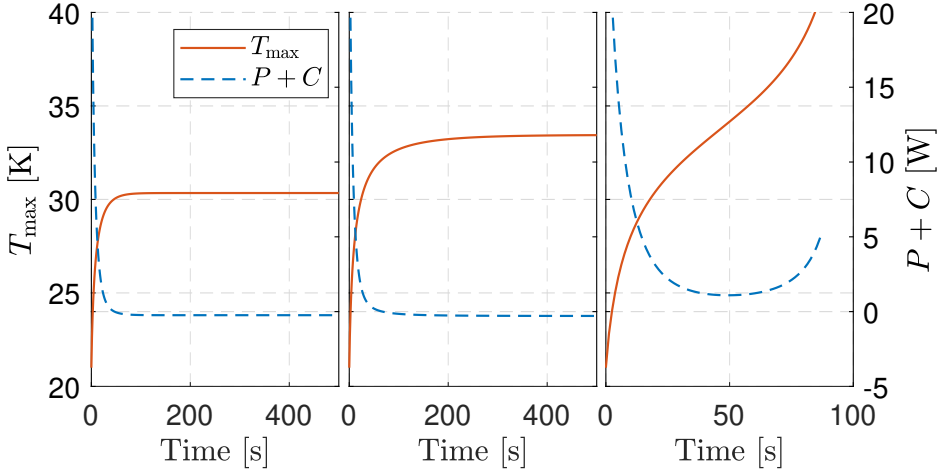


Figure 5.4 The maximum temperature and the power balance as a function of time in the magnet at three different operation currents. The figures from left to right correspond to I_{op} of $0.99I_{\text{mas}}$, I_{mas} and $1.01I_{\text{mas}}$, respectively. The operation currents are constant in time.

α and h were varied. Before presenting the simulation results, few words are spent on explaining the choice of the parameters to be varied. The n -value determines how steep the $V - I$ dependency of the superconducting material is. Therefore, by varying this parameter, superconducting materials with different n -value can be investigated. The J_c scaling law coefficient α determines the magnitude of the $J_c(T, \mathbf{B})$ dependency. Therefore, by varying α we can simulate superconducting materials exhibiting J_c of different magnitudes. The heat transfer coefficient h is the last parameter that was varied. It defines, how well the heat is transferred between the winding and the coolant. In summary, n and α have effect on the heating power, and h effects only to the cooling power.

The simulations results are shown in figure 5.5. Expected dependency was obtained in the cases of $I_{\text{mas}} - \alpha$ and $I_{\text{mas}} - h$: I_{mas} increased with increasing α and h . The effect of n -value on I_{mas} was non-trivial: with decreasing n , I_{mas} increased exponentially and on the other hand, I_{mas} leveled off to a value around 3550 A, when n was higher than 10 and increased up to 30.

The effects of n on I_{mas} may be explained in terms of the power balance. As higher n -value results in more aggressive heat generation, the cooling is able to compensate it only up to certain level. Hence, at lower n the magnet can be operated at higher I_{op} because less heat is generated compared to case with higher n . That I_{mas}

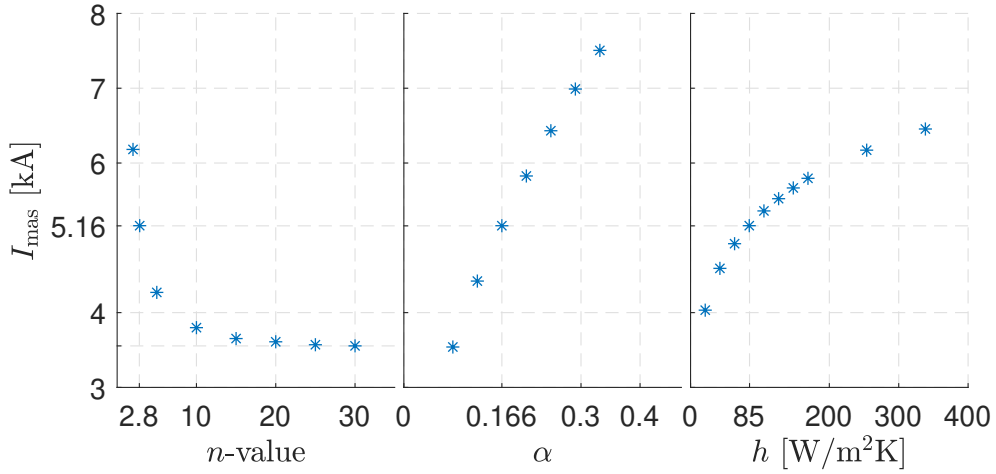


Figure 5.5 From left to right, respectively, the maximum stable operation current as a function of n -value, α and the heat transfer coefficient.

leveled off when $n \rightarrow 30$, can be explained similarly: the cooling is able to balance the heating only upto certain level, that does change significantly anymore when n is high enough.

5.2.3 Concluding remarks

The developed methodology is a promising approach in generalizing the I_c concept for magnets exhibiting gradual $V-I$ dependency. As discussed earlier, the LTS magnets have high- n behavior where the critical current corresponded to the maximum operation current. This kind of behavior was observed in the simulation case where I_{mas} was computed as a function of n : with high enough n , I_{mas} was constant.

5.3 Summary

The two publications, synthesized in this chapter, focused on interpreting the behavior of the Roebel cable based Feather-M2 magnet that was designed, built and tested within the EUCARD2 project at CERN during 2017. The two studies were motivated by the observed gradual $E-I_{\text{op}}$ relation which was not fully understood earlier.

In the first study, an inverse problem based approach was developed in order to be able to understand the behavior of Feather-M2 based on a parametrized thermal model. It turned out that using the methodology, deductions could be made on both, the magnet behavior and the predictive capability of the thermal model itself. According to the results, the thermal model, with fixed parameters obtained based on one measurement case, failed to predict the observed magnet behavior over the whole temperature range. Hence, this points out that there are incapacibilities in the temperature dependency of the utilized $E(J)$ model or the cooling model. What was learned from the magnet behavior, based on inverse problem solutions, was that the magnet behavior corresponded to low n -value of around 3. This can be related to the low current carrying capacity of the utilized superconductor [73]. In all the simulated cases, the variation of α and n in obtained solutions was small. More variance was obtained in case of E_c and h which indicates once again, that the cooling model was not sufficiently good as a function of temperature.

In the second study, motivated by the first one, the maximum current was computationally determined based on a methodology that relied on the generalized definition of the maximum stable operation current. Three parametric studies were performed based on the methodology: I_{mas} was computed as a function of n -value, α and h . The study on $I_{\text{mas}} - n$ dependency revealed an interesting result: for n -values lower than 10, I_{mas} exponentially increased with decreasing n . For $n > 10$, I_{mas} decreased and leveled off when n was increased to 30. Thus, for high n and for given E_c , the definition of I_c , in the sense of it meaning the maximum current, is no longer as arbitrary as it is in case of gradual $V - I$ dependency due to low n -value.

6 E³SPRESSO: AN ENERGY-EXTRACTION SYSTEM DESIGN FOR HIGH-FIELD HTS MAGNETS

The design, manufacturing and testing of Feather-series prototype magnets demonstrated the potential of high temperature superconductors in use of accelerator magnet applications. The dipole magnet Feather-M2 was designed to produce 5 T magnetic field. Thus, the natural next step was to design an HTS magnet producing magnetic field in 20 T range and above [74]. An issue related to the quench protection of the magnet was realized. The problem is the high energy density in a magnet that exhibits low thermal conductivity and low heat capacity.

The protection methods, the quench heaters and CLIQ, used for LTS magnets are inapplicable for a typical large HTS magnet [94]. The idea of those is to cause a wide quench artificially, so that the magnets energy would be dissipated internally, at least for the most part. However, for HTS magnets these methods are inapplicable for example due to the high thermal margin and low thermal conductivity of the magnet structure. Therefore, the energy must be dissipated externally, for the most part. In energy-extraction protection methods, the main requirements for the system are the following two. The first requirement is that the magnet de-energization has to be fast enough so that the magnet's T_{\max} will not get too high. In the second one, the voltage-to-ground should not get too high in order to avoid short circuits in case of insulation breakdown. These two requirements do contradict with each other: fast decay would result in low T_{\max} but too high voltage to ground, and slow decay vice versa.

In this chapter, one possible protection system design for high-field HTS magnets is optimized, namely External Energy Extraction Symbiotic Protection System for Series Operation (E³SPreSSO). The methodology for the design optimization

and the simulation results are presented based on publication IV. The protection system design itself was first presented in [113]. The idea of the system is to divide the magnet into a number of sections and protect each with an in-series-connected protection unit. A unit is basically a superconducting switch with a parallel resistor. By using this method, voltage-to-ground can be kept low and still the magnet can be de-energized fast keeping T_{\max} as low as possible.

This chapter is structured as follows. First the methodology is presented, where the coupled circuit and thermal model are presented with the optimization scheme. Then, in section 6.2 the results are presented, which is followed by some conclusions regarding the study.

6.1 Methodology

In this section, a methodology is presented for optimizing the E³SPreSSO protection system for a 20 T range HTS magnet. The utilized methodology relies on a computational model consisting of a circuit model coupled with a thermal model. The model predicts the electro-thermal state of the system, in time, consisting of the magnet and the E³SPreSSO protection system. Further, the model was parametrized and an optimization problem was formulated in order to obtain the design parameters as the solution of the problem.

6.1.1 Circuit model

An E³SPreSSO unit in series connected with a section of magnet can be modelled using the circuit diagram illustrated in figure 6.1. In the modelling, it is assumed that all the pairs, consisting of a E³SPreSSO unit and a magnet section, behave identically in operation. Hence, it is sufficient to simulate a single pair. In the following formulation, the notations I , V and R stand for electric current, voltage and resistance, respectively. The subscripts \mathcal{C} , T, sc, st and p refer to capacitor, thyristor, superconductor, superconductor's stabilizer and parallel resistor, respectively.

In the circuit, a single E³SPreSSO unit consists of a superconducting switch and its trigger which consists of a capacitor and a thyristor. The switch is basically a superconducting cable, bifilarly wound into a coil shape, hence having low self-inductance. In the circuit model, the cable is divided to two components: the other

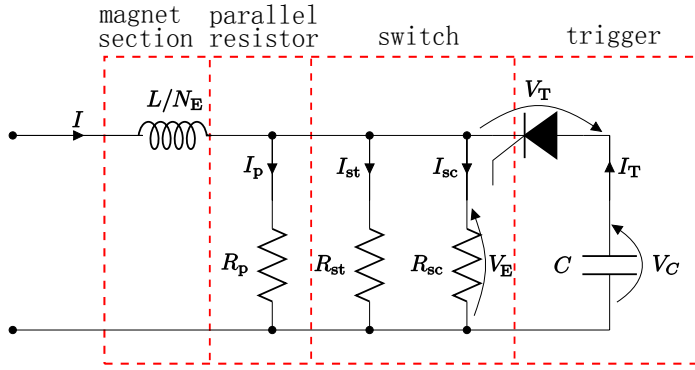


Figure 6.1 Circuit diagram of an E^3 SPreSSO unit connected in series with a magnet section.

being the superconducting part and the other, its stabilizer. The stabilizer is modelled with a resistor R_{st} and the superconducting material is modelled with a resistor R_{sc} . The parallel resistor R_p is in parallel connection with the switch, consisting of the stabilizer and the superconducting material. Therefore, once the switch is triggered, its resistance becomes so high that the operation current starts to flow in the parallel resistor where the magnet's energy consequently dissipates.

It is assumed that all the pairs, one consisting of a magnet section and a protection unit, are identical. Then, the system can be modelled as follows. The total inductive voltage over all the magnet sections is the same as the total voltage over all the protection units, i.e.

$$-L \frac{dI}{dt} = N_E V_E,$$

where L is the inductance of the whole magnet and N_E is the number of E^3 SPreSSO units in the system.

The thyristor current I_T , due to the capacitor discharge is modelled as

$$-\mathcal{C} \frac{dV_C}{dt} = I_T,$$

where \mathcal{C} is the capacitance of the capacitor, and V_C the voltage over it. Moreover, the resistances R_p and R_{st} are computed using

$$R = \rho \frac{l}{A},$$

where the resistance R is equal to the component's resistivity times the length over

the cross-sectional area. The critical current I_c of the superconductor in the switch is calculated based on a J_c -fit of the investigated superconducting material as

$$I_c(T) = \int_{A_{sc}} J_c(T) dA, \quad (6.1)$$

where J_c is integrated over the cross-sectional area of the superconducting material in the switch cable.

The rest of the unknowns in the circuit is covered with two sets of equations, based on the Kirchhoff's voltage and current laws. The two sets model the two different states of the circuit determined by the thyristor voltage V_T with respect to its threshold voltage V_{th} . Moreover, the superconductor is modelled according to the critical state model (CSM), where any voltage causes a co-directional electric current I_{sc} in the superconductor.

When the thyristor is triggered, the current I_T due to capacitor discharge flows through the thyristor in the forward direction. The voltage V_E over the superconductor causes a current I_c to flow in the superconductor according to the CSM. Consequently, the switch cable heats up and its resistivity becomes high. Consequently, the current starts to flow also in the less resistive parallel resistor. During this switch activation phase, the circuit can be approximated using the equations

$$V_T \geq V_{th} \Rightarrow \begin{cases} V_E &= V_c - V_T \\ I_T &= I_{sc} + I_{st} + I_p - I \\ I_{sc} &= I_c \\ I_{st} &= V_E / R_{st} \\ I_p &= V_E / R_p. \end{cases} \quad (6.2)$$

When the voltage over the switch increases so that $V_T < V_{th}$, any reverse direc-

tional current through the thyristor is denied by deploying the equations

$$V_T < V_{th} \Rightarrow \begin{cases} V_E &= I_p R_p \\ I_T &= 0 \\ I_{sc} &= \min(I_c, I) \\ I_{st} &= (I - I_{sc}) \frac{R_p}{R_{st} + R_p} \\ I_p &= I - I_{sc} - I_{st}, \end{cases} \quad (6.3)$$

where I_{sc} is bounded from above with I since at this point, the capacitor as a current supply is out of the system.

6.1.2 Thermal model

In order to predict the temperature of the magnet, superconducting switch and the parallel resistor, a thermal model is formulated and coupled with the circuit model. In the thermal model, the switch (s), the parallel resistor (p) and the magnet (m) are modelled adiabatically as

$$C_s \frac{dT_s}{dt} = \rho_s(T_s) \frac{I_{st}}{f_s A_s^2} (I_{st} + I_c) \quad (6.4)$$

$$C_p \frac{dT_p}{dt} = \rho_p(T_p) \left(\frac{I_p}{A_p} \right)^2 \quad (6.5)$$

$$C_m \frac{dT_m}{dt} = \rho_m(T_m, B_m(I)) \frac{I^2}{f_m A_m^2}, \quad (6.6)$$

where C , ρ , A , T and f denote effective volumetric heat capacity, effective resistivity, cross-sectional area, temperature and cable's stabilizer fraction, respectively. The adiabatic assumption for these simulations is adequate enough, since we are interested in phenomena occurring in short period of time. Moreover, the model for the switch and the magnet corresponds to the current sharing model which can be formulated as follows.

The total heat generation Q^+ in the switch cable is due to co-directional current

density and electric field in the stabilizer and in the superconducting region, i.e.

$$Q^+ = (1 - f_s)J_{sc}E_{sc} + f_sJ_{st}E_{st}, \quad (6.7)$$

where $J_{st} = I_{st}/(A_s f_s)$ is J in the stabilizer and $J_{sc} = I_{sc}/(A_s(1 - f_s))$ is J in the superconducting fraction. It is assumed that the longitudinal E in the cable is the same in the stabilizer and in the superconducting fraction, i.e. $E_{sc} = E_{st} = \rho_s J_{st}$. Now, (6.7) can be expressed as

$$Q^+ = \rho_s \frac{I_{st}}{f_s A_s^2} (I_{sc} + I_{st}). \quad (6.8)$$

The heat generation in (6.6), predicting the magnet's hot spot temperature, is deduced similarly as (6.8). However, it is assumed that all the operation current flows in the stabilizer of the magnet's cable, i.e., $I_{sc} = 0$ and thus $I_{st} = I$. In addition, in order to take into account the effect of magnetic field in the hot spot on the resistivity of the stabilizer, linear $B - I$ dependency is assumed between 0 A and I_{op} , corresponding to the magnetic field values of 0 T and B_m , respectively. The magnetic field B_m is the nominal field in the magnet's aperture, i.e. 20 T.

6.1.3 Optimization problem formulation

The circuit model and the thermal model are coupled via the electric currents and the temperatures. Using the coupled model, the system consisting of a magnet section and an E³SPreSSO unit is approximated. In order to optimize this design, the model is parametrized. The chosen parameters are listed in table 6.1.

The aim is to find an optimal solution of the design parameters such that during de-energizing the magnet, no temperatures nor voltages become too high in the system. An optimal design was defined to be the one with the minimal amount material and hence the smallest in size. Consequently, the problem turned out to be multi-objective optimization problem, where an optimal solution was such that all the design parameters were minimized. Hence, linear scalarization method was utilized for formulating the objective function. Using the method, the function to be minimized was formulated as the weighted sum of the design parameters. The

Table 6.1 Design parameters for simulations.

parameter	description	weight
l_s	length of switch cable	1/(1 m)
N_E	number of E ³ SPreSSO units	1
l_p	parallel resistor length	1/(1 m)
A_p	parallel resistor cross-section area	1/(12 mm ²)
A_s	switch cable cross-section area	1/ \hat{A}_s
$V_{\mathcal{E}0}$	initial voltage in the capacitor	1/(10 V)
\mathcal{C}	capacitor capacitance	1/(1 mF)

* Strands' cross-section areas (\hat{A}_s) are shown in table 6.3.

optimization problem was formulated as follows

$$\begin{aligned}
 & \underset{\omega}{\text{minimize}} && \omega_{l_s} + \omega_{N_E} + \omega_{l_p} + \omega_{A_p} + \omega_{A_s} + \omega_{V_{\mathcal{E}0}} + \omega_{\mathcal{C}} \\
 & \text{subject to} && V_E = V_{\max} \\
 & && T_s, T_p, T_m \leq T_{\max} \\
 & && I_c(T_{\text{op}}) \geq 1.2 \times I_{\text{op}},
 \end{aligned} \tag{6.9}$$

where the objective function corresponds to the sum of the weighted optimization parameters ω_i . They are defined by the subscripts corresponding to those in table 6.1 where the utilized weights are also listed. Hence, e.g., $\omega_{l_s} = l_s \cdot 1 \text{ m}^{-1}$.

The objective is to minimize the parameter values, i.e. the objective function, such that T_s, T_p, T_m are below certain defined maximum temperature T_{\max} . The maximum voltage to ground over the magnet section is required to be not higher than V_{\max} . However, it was noticed that setting this constraint to be an equality constraint, resulted in better solutions in terms of number of the E³SPreSSO units. This is related to requiring the maximal rate of energy-extraction, that is, when voltage to ground is V_{\max} . Moreover, the last constraint requires that the design satisfies a 20 % current margin in the switch in order to ensure that the E³SPreSSO unit will not quench accidentally in operation.

Table 6.2 Default input parameters for simulations

parameter	value	unit	description
I_{op}	12	kA	magnet operation current
T_{op}	4.2	K	system operation temperature for LTS
T_{op}	20	K	system operation temperature for HTS
E_{m}	1.86	MJ	magnet energy
B_{m}	20	T	magnetic flux density in magnet aperture
V_{max}	1000	V	maximum allowed voltage over magnet
T_{max}	300	K	maximum allowed temperature in the system

6.2 Simulation results

Using the presented methodology optimal designs were sought for different switch cables using the simulation parameters listed in table 6.2, unless otherwise stated. The tested superconducting materials for the switch cable were NbTi, MgB₂ and REBCO. As for the stabilizer compounds, 4 different materials were tested: Ag, Cu, CuNi and stainless steel. After having performed the optimization algorithm for each of the switch cable candidates, the best one was chosen as for the reference case for further analysis. Based on the reference case, results are shown on the performance of the design when simulating a de-energization of a magnet. Moreover, a parametric analysis was done on T_{max} . Where based on the switch materials of the reference case, designs were optimized for $T_{\text{max}} = 150 - 400$ K.

6.2.1 Comparing different superconductors for the switch

The E³SPreSSO design was optimized for the 9 different superconducting switch cable compounds shown in table 6.3. The obtained solutions for the design parameters in each case are shown in table 6.4, where the maximum temperature of the magnet T_{m} , switch T_{e} and the parallel resistor T_{p} , are listed as well.

According to the results, some switch cable materials required quite a large number of E³SPreSSO units with long switch cable, like in case 1. This indicates that

Table 6.3 Material fractions and cross-section area of switch cable strand. Case m denotes the fractions for the magnet cable.

Case [#]	NbTi [%]	MgB ₂ [%]	REBCO [%]	Ag [%]	Cu [%]	CuNi [%]	SS [%]	other [%]	\hat{A}_s [mm ²]
1	60	-	-	-	40	-	-	-	0.57
2	60	-	-	-	-	40	-	-	0.57
3	60	-	-	-	-	-	40	-	0.57
4	14.8*	30.6	-	-	-	54.4	-	0.2	2.3
5	14.8*	30.6	-	-	-	-	54.4	0.2	2.3
6	-	-	0.91	-	-	-	90.9	8.19	1.2
7	-	-	0.91	1.8	-	-	90.9	6.39	1.2
8	-	-	0.91	1.8	-	90.9	-	6.39	1.2
9	-	-	0.91	-	-	90.9	-	8.19	1.2
m	-	-	0.66	1.33	26.6	-	66.6	4.81	13.3**

* Nb diffusion barrier is utilized.

** Cable's cross-section area.

Table 6.4 Optimized designs for cases shown in Table 6.3.

Case [#]	l_s [m]	A_s [mm ²]	l_p [m]	A_p [mm ²]	N_E [#]	V_{Co} [V]	C [mF]	T_m [K]	T_e [K]	T_p [K]
1	19.9	2.3	7.5	30.0	25.5	31.4	1.1	64	300	143
2	8.5	2.4	8.9	72.7	4.5	30.5	1.2	285	254	278
3	4.4	2.6	7.3	59.4	6.4	31.4	1.0	178	294	290
4	8.8	44.7	9.1	42.2	4.7	85.2	15.8	299	300	262
5	6.5	37.8	8.5	52.6	4.6	34.2	14.3	291	284	293
6	8.1	8.0	7.5	56.6	5.8	158.8	8.5	207	277	293
7	9.1	8.1	16.3	85.3	12.1	99.9	4.4	104	281	98
8	14.7	8.1	7.6	45.3	6.2	75.2	13.9	189	293	284
9	12.5	10.0	7.9	54.8	5.1	91.0	18.8	267	275	295

copper is not resistive enough stabilizer material in terms of compact design. The designs in cases 2-3 look promising, but as indicated by the low required capacitor energy, LTS can be too unstable and could quench accidentally in operation, as predicted in [113]. In cases 4 and 5, A_s is a lot larger compared to other designs. From the REBCO based designs, the most compact design was obtained with CuNi stabilizer corresponding to the case 9, which was chosen to be the reference design for

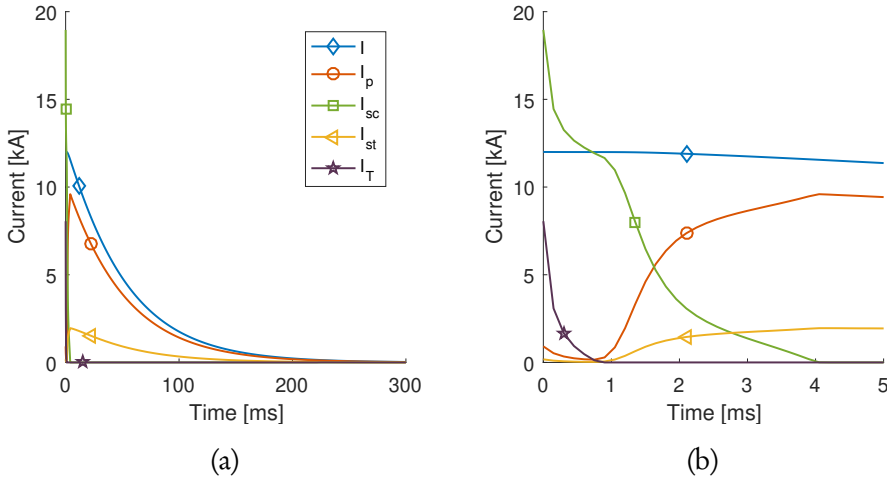


Figure 6.2 In (a) current distribution between different components in the circuit. A close-up of (a) is shown during the first 3 ms in (b).

the further analysis.

6.2.2 Electro-thermal behaviour of design based on case 9

Using the design parameter values obtained as a solution of the optimization problem based on the case 9, the electric currents in the system, during magnet de-energization are shown in figure 6.2. The temperature in the switch, dump resistor and magnet's hot spot, during discharge, are shown in figure 6.3. The voltage over an E³SPreSSO unit and the capacitor voltage are shown in figure 6.4. Moreover, in the design, the stabilizer's resistance was of the order of 0.5Ω and the resistance of the dump resistor was of the order of 0.1Ω .

As the results show, the design is performing as intended. Figure 6.2 shows, how the the over-current in the switch due to the capacitor discharge quenches the switch within 4 ms and I_{sc} goes to zero. Consequently, the operation current I starts to flow mainly in the parallel resistor as indicated by the raise in I_p . A part of the magnet's energy dissipates in the switch stabilizer, as indicated by I_{st} . In summary, using the the design based on case 9 and setting the maximum temperature in the system to 300 K and the maximum voltage-to-ground to 1 kV, the magnet can be discharged in 300 ms.

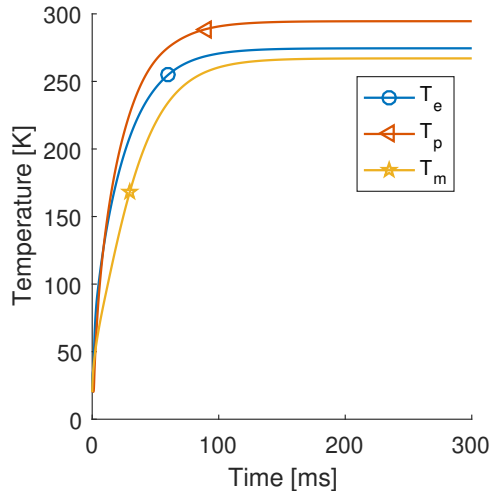


Figure 6.3 Temperature evolution in the switch, parallel resistor and the magnet.

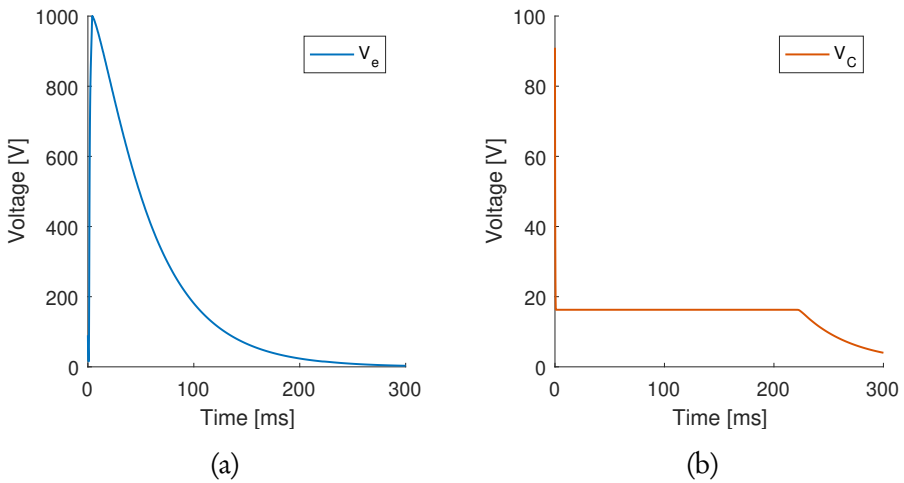


Figure 6.4 (a): Voltage over an E³SPreSSO unit during system de-energization. (b): Capacitor discharge.

6.2.3 Varying allowed maximum temperature

Next the simulation results are presented based on the study where T_{\max} was varied between 150 and 400 K and the design was optimized. The material fractions were kept as in case 9. The optimized designs for different values of T_{\max} are shown in table 6.5.

Table 6.5 Optimized designs for different allowed maximum temperatures.

T_{\max} [K]	l_s [m]	A_s [mm ²]	l_p [m]	A_p [mm ²]	N_E [#]	V_{CO} [V]	C [mF]	T_m [K]	T_c [K]	T_p [K]
150	14.9	8.4	9.9	65.2	13.0	173	13.0	97	146	144
200	11.2	10.9	7.7	48.8	11.0	200	11.5	114	199	197
250	10.2	7.6	7.0	48.3	9.0	21	29.5	135	246	246
300	12.6	10.1	11.8	79.8	5.0	89	19.4	290	268	189
350	13.6	7.7	8.0	58.7	4.0	43	10.8	357	291	340
400	10.7	8.1	10.5	73.6	4.0	46	12.5	378	390	245

According to the results, with T_{\max} of 400 K, only 4 E³SPreSSO units are needed to protect the magnet. If the value of the T_{\max} constraint was lowered to 150, the required number of units more than triples compared to the case where T_{\max} was 400 K. Other parameters did not have so clear T_{\max} -dependency.

6.3 Concluding remarks

The methodology for optimizing the E³SPreSSO protection system, designed for large magnets, was presented. The implemented methodology was utilized to optimize the E³SPreSSO protection system for a 20 T HTS magnet. In the methodology, a thermal model coupled with a circuit model, approximating the system, was parametrized and based on that an optimization problem was formulated. Minimization of the objective function subject to constraints, resulted in a system where the total amount of material needed for a protection unit was minimized so that too high resulting temperatures or voltages to ground during de-energization of the magnet were not allowed.

In the simulations, different switch cables were investigated and based on the results and one was chosen. Using the REBCO switch cable having cross-section area of 8 mm² with copper-nickel-silver stabilizer, only 5 E³SPreSSO units were needed to protect the magnet when 300 K T_{\max} and 1 kV V_{\max} were allowed. Additionally, if T_{\max} was increased to 400 K, only 4 units would be required.

These kind of methodologies, like the one presented here, can be very useful for engineers. They allow, the designer to easily tune the objective function and the constraints. Consequently, lot of computing time is saved when the designs are not

obtained via the input parameters but via optimization algorithms.

7 CONCLUSIONS

In the field of particle physics where higher particle collision energies are desired in order to reveal more about the smallest constituents of matter. This is the case at CERN where the world's largest particle accelerator Large Hadron Collider is located. Currently there is worldwide effort on ambitious future planning of the post LHC accelerator. The Future Circular Collider study proposes 100 TeV (i.e. 8 times larger than at LHC) hadron collisions with a new accelerator. The baseline option to realize that is with 16 T magnets in a 100 km tunnel. Alternatively the same energy can be reached in a 80 km tunnel with 20 T magnet. This alternative option may become more viable if an intermediate step, a lepton collider in the same tunnel, is implemented first. The low temperature superconductor technology is not sufficient for 20 T bending magnets. High temperature superconductors, in particular REBCO tapes, are the only options currently known for superconducting magnet technology beyond 20 T.

In the EUCARD2 project, the use of HTS conductors in accelerator magnets was investigated, where two REBCO Roebel cable based prototype magnets were designed, constructed and tested. As demonstrated by the measurement data, predicting their behavior is not straightforward. In order to understand better their behavior, modelling approaches need to be developed. One bottle neck in HTS modelling at the moment is the lack of proper characterization of the HTS material properties, e.g. resistivity. Due to the anisotropy the HTS material exhibit, their resistivity is difficult to characterize.

In this thesis work, modelling methodologies were developed for scrutinizing the behavior of HTS magnet and to learn about their modelling. The REBCO Roebel cable based prototype magnets Feather-M0 and Feather-M2 were especially investigated by simulating their AC losses and thermal stability using modelling approaches and simulation tools developed during my doctoral studies.

This thesis can be summarized as follows. In chapter 2, the mathematical and

physical background for understanding the work is presented, where the main attention was focused on two topics: 1) modelling AC losses, and 2) modelling thermal stability. For the methodology used for AC loss simulations, detailed formulation of the MMEV functional based on the Maxwell's equations was presented. Moreover, the mathematical background for using the Galerkin finite element method in solving heat transfer problem formulated in chapter 4 in coil shape geometries was presented.

In chapter 3 AC losses and magnetic field quality in Feather-M0 were simulated using the MMEV-principle. Moreover, the discretization of the MMEV functional, formulated in chapter 2 was detailed. This chapter was based on publication I and publication II.

Chapter 4 and chapter 5 are related to the thermal stability modelling of HTS magnets, being the second main focus in this thesis. In chapter 4, the heat transfer problem in HTS magnets was formulated in detail. In the formulation, the emphasis was on the methodology where the heat diffusion problem in HTS magnet was modelled on 1-dimensional modelling domain taking into account the heat transfer between the cable turns. In addition, a cooling model was included to take into account the heat transfer between the cooling environment and the magnet winding. The original results were first presented in publication III and publication VI.

In chapter 5 simulation results on the thermal stability modelling of Feather-M2 was presented. In the simulations, the thermal model presented in chapter 4 was utilized. In the first section, an inverse problem based approach was presented. Using the approach and the Feather-M2 measurement data, the magnet behavior was scrutinized. By solving the inverse problems, values for the model parameters of the thermal model was obtained, based on which, the magnet behavior could be analyzed. Also, the predictively capability of the formulated thermal model could be scrutinized. This was based on publication VI.

In the second section of chapter 5, a modelling methodology was developed for solving the maximum stable operation current of HTS magnet. In the methodology, an optimization problem was formulated where the operation current was maximized with the requirement of stable magnet operation. The stable operation was determined based on the balance between the total heating power and the total cooling power in the magnet winding. The methodology was applied to Feather-M0 and the simulation results were presented. This was based on publication V.

Chapter 6 presents research work based on publication IV, where an energy-extraction system (EES) design for 20 T range HTS magnets was optimized. In the developed methodology, an electric circuit model was formulated to model the system consisting of the magnet and the EES. Moreover, the circuit model was coupled with a thermal model modelling the temperatures in each of the elements of the circuit. By parametrizing the coupled model, an optimization problem was formulated with the objective of minimizing the material volume, proportional to the costs, needed for building the system. Constraints were set so that in the elements, maximum temperatures were not allowed to raise above certain value and voltage to ground was also limited.

During this thesis work, a lot of knowledge and experience on HTS modelling was gained during the 6 research projects being now the basis of this thesis. The research projects were mainly motivated by the challenges faced during the EUCARD2 project where the aim was on demonstrating the use of HTS tapes and cables as part of accelerator magnets.

The methods and modelling approaches developed in this thesis can be of great value in HTS accelerator magnet design. The community could greatly benefit from applying more the mathematical concept of inverse problems and optimization theory for solving engineering problems. However, some modelling assumptions utilized in this thesis require more investigations such as the assumption on isothermal Roebel-cable cross-section. An interesting next step would be to scrutinize the validity and the limitations of such an assumption in detail. In order to do so, perhaps already existing results in the model order reduction theory could be useful.

During the modelling work done, the major encountered obstacle in the modelling of HTS magnets was related to $E(J)$ relation of HTS material. Reliable characterization of the $E(J)$ in superconducting material of the HTS tape can be difficult when using the typical modelling approach, i.e., the power law determined by the n -value, E_c and the short-sample $V - I$ measurements based $J_c(T, \mathbf{B})$ function. When modelling high-temperature superconductors at overcritical currents, much of the uncertainty and complexity related to this approach could be avoided if the resistivity of the HTS material could be characterized independent of the whole tape and its geometry. Therefore, great efforts should be put on characterizing the resistivity of HTS material.

REFERENCES

- [1] J. Ruuskanen, A. Stenvall and V. Lahtinen. Utilizing Triangular Mesh With MMEV to Study Hysteresis Losses of Round Superconductors Obeying Critical State Model. *IEEE Transactions on Applied Superconductivity* 25.3 (2015), 8200405. DOI: 10.1109/TASC.2014.2365408.
- [2] G. Ambrosio. Nb3Sn High Field Magnets for the High Luminosity LHC Upgrade Project. *IEEE Transactions on Applied Superconductivity* 25.3 (2015), 1–7. DOI: 10.1109/TASC.2014.2367024.
- [3] *American Superconductor Corporation*. URL: http://amsc.com/solutions-products/hts_wire.html.
- [4] R. Apsey, D. Baynham, P. Clee, D. Cragg, N. Cunliffe, R. Hopes and R. Stovold. Design of a 5.5 metre diameter superconducting solenoid for the Delphi particle physics experiment at LEP. *IEEE Transactions on Magnetics* 21.2 (1985), 490–493. DOI: 10.1109/TMAG.1985.1063859.
- [5] J. Ruuskanen, A. Stenvall, V. Lahtinen and E. Pardo. Electromagnetic nonlinearities in a Roebel-cable-based accelerator magnet prototype: variational approach. *Superconductor Science and Technology* 30.2 (2016), 024008. DOI: 10.1088/1361-6668/30/2/024008.
- [6] A. Badía-Majós and C. López. Electromagnetics close beyond the critical state: thermodynamic prospect. *Superconductor Science and Technology* 25.10 (Sept. 2012), 104004. DOI: 10.1088/0953-2048/25/10/104004.
- [7] M. Ban, T. Ichiguchi and T. Onogi. Power laws in the resistive state in high- T_c superconductors. *Phys. Rev. B* 40 (7 Sept. 1989), 4419–4422. DOI: 10.1103/PhysRevB.40.4419. URL: <https://link.aps.org/doi/10.1103/PhysRevB.40.4419>.

- [8] C. Barth, G. Mondonico and C. Senatore. Electro-mechanical properties of REBCO coated conductors from various industrial manufacturers at 77 K, self-field and 4.2 K, 19 T. *Superconductor Science and Technology* 28.4 (Feb. 2015), 045011. DOI: 10.1088/0953-2048/28/4/045011.
- [9] C. P. Bean. Magnetization of hard superconductors. *Physical review letters* 8.6 (1962), 250.
- [10] L. Bottura, G. de Rijk, L. Rossi and E. Todesco. Advanced Accelerator Magnets for Upgrading the LHC. *IEEE Transactions on Applied Superconductivity* 22.3 (2012), 4002008. DOI: 10.1109/TASC.2012.2186109.
- [11] L. Bottura, G. de Rijk, L. Rossi and E. Todesco. Advanced accelerator magnets for upgrading the LHC. *IEEE Transactions on Applied Superconductivity* 22.3 (2012), 4002008.
- [12] D. Boussard and T. P. R. Linnecar. *The LHC Superconducting RF System*. Tech. rep. LHC-Project-Report-316. CERN-LHC-Project-Report-316. Geneva: CERN, Dec. 1999. URL: <http://cds.cern.ch/record/410377>.
- [13] V. Braccini, A. Xu, J. Jaroszynski, Y. Xin, D. C. Larbalestier, Y. Chen, G. Carota, J. Dackow, I. Kesgin, Y. Yao, A. Guevara, T. Shi and V. Selvamanickam. Properties of recent IBAD–MOCVD coated conductors relevant to their high field, low temperature magnet use. *Superconductor Science and Technology* 24.3 (Dec. 2010), 035001. DOI: 10.1088/0953-2048/24/3/035001.
- [14] S. Brenner and R. Scott. *The mathematical theory of finite element methods*. Vol. 15. Springer Science & Business Media, 2007, 1–66.
- [15] *Bruker*. URL: www.bruker.com.
- [16] P. Bruzzone. The index n of the voltage–current curve, in the characterization and specification of technical superconductors. *Physica C* 401.1-4 (2004), 7–14. DOI: 10.1016/j.physc.2003.09.005.
- [17] R. H. Byrd, J. C. Gilbert and J. Nocedal. A trust region method based on interior point techniques for nonlinear programming. *Mathematical programming* 89.1 (2000), 149–185.
- [18] R. H. Byrd, M. E. Hribar and J. Nocedal. An interior point algorithm for large-scale nonlinear programming. *SIAM Journal on Optimization* 9.4 (1999), 877–900.

- [19] J. Ruuskanen, A. Stenvall and V. Lahtinen. Predicting heat propagation in Roebel-cable-based accelerator magnet prototype: One-dimensional approach with coupled turns. *IEEE Trans. Appl. Supercond.* 27.4 (2017), 0600205. DOI: 10.1109/TASC.2016.2630844.
- [20] J. Chambrillon, M. Therasse, O. Brunner, P. Maesen, O. Pirotte, B. Vullierme and W. Weingarten. CERN SRF assembling and test facilities. *Proc. SRF11, Chicago* (2011).
- [21] M. Chen, L. Donzel, M. Lakner and W. Paul. High temperature superconductors for power applications. *Journal of the European ceramic society* 24.6 (2004), 1815–1822. DOI: 10.1016/S0955-2219(03)00443-6.
- [22] T. A. Collaboration. The ALICE experiment at the CERN LHC. *Journal of Instrumentation* 3.08 (Aug. 2008), S08002–S08002. DOI: 10.1088/1748-0221/3/08/s08002.
- [23] T. A. Collaboration. The ATLAS Experiment at the CERN Large Hadron Collider. *JINST* 3 (2008). Also published by CERN Geneva in 2010, S08003. 437 p. DOI: 10.1088/1748-0221/3/08/S08003.
- [24] T. C. Collaboration. The CMS experiment at the CERN LHC. *Journal of Instrumentation* 3.08 (Aug. 2008), S08004–S08004. DOI: 10.1088/1748-0221/3/08/s08004.
- [25] T. L. Collaboration. The LHCb Detector at the LHC. *Journal of Instrumentation* 3.08 (Aug. 2008), S08005–S08005. DOI: 10.1088/1748-0221/3/08/s08005.
- [26] E. Collings and M. Sumption. Stability and AC losses in HTSC/Ag multifilamentary strands. *Applied Superconductivity* 3.11 (1995), 551–557. ISSN: 0964-1807. DOI: [https://doi.org/10.1016/0964-1807\(95\)00091-7](https://doi.org/10.1016/0964-1807(95)00091-7).
- [27] L. Coull, D. Hagedorn, V. Remondino and F. Rodriguez-Mateos. LHC magnet quench protection system. *IEEE Transactions on Magnetics* 30.4 (July 1994), 1742–1745. ISSN: 0018-9464. DOI: 10.1109/20.305593.
- [28] J. Ruuskanen, A. Stenvall, J. van Nugteren and V. Lahtinen. Optimization of an E³SPreSSO Energy-Extraction System for High-Field Superconducting Magnets. *IEEE Transactions on Applied Superconductivity* 29.5 (2018), 4700805. DOI: 10.1109/TASC.2018.2794457.

- [29] J. Ruuskanen, A. Stenvall, V. Lahtinen, J. van Nugteren, G. Kirby and J. Murtomäki. How to Computationally Determine the Maximum Stable Operation Current of an HTS Magnet. *IEEE Transactions on Applied Superconductivity* 29.5 (2019), 4701204. DOI: 10.1109/TASC.2019.2898315.
- [30] L. Evans. The Large Hadron Collider. *New Journal of Physics* 9.9 (Sept. 2007), 335–335. DOI: 10.1088/1367-2630/9/9/335.
- [31] J. Ruuskanen, A. Stenvall, V. Lahtinen, J. van Nugteren, G. Kirby and J. Murtomäki. Modelling thermodynamics in a high-temperature superconducting dipole magnet: an inverse problem based approach. *Superconductor Science and Technology* 32.9 (2019), 094007. DOI: 10.1088/1361-6668/ab2bc9.
- [32] P. Ferracin, M. Devaux, M. Durante, P. Fazilleau, P. Fessia, P. Manil, A. Milanese, J. E. Munoz Garcia, L. Oberli, J. C. Perez, J. M. Rifflet, G. de Rijk, F. Rondeaux and E. Todesco. Development of the EuCARDNb₃SnDipole Magnet FRESKA2. *IEEE Transactions on Applied Superconductivity* 23.3 (June 2013), 4002005. ISSN: 1051-8223. DOI: 10.1109/TASC.2013.2243799.
- [33] J. Fleiter and A. Ballarino. Parameterization of the critical surface of REBCO conductors from Fujikura. *CERN internal note, EDMS 1426239* (2014).
- [34] *Fujikura*. URL: <http://www.fujikura.co.jp/eng/>.
- [35] *Future Circular Collider study website*. URL: <https://fcc.web.cern.ch/>.
- [36] C. Geuzaine and J.-F. Remacle. Gmsh: A 3-D finite element mesh generator with built-in pre-and post-processing facilities. *International journal for numerical methods in engineering* 79.11 (2009), 1309–1331. DOI: 10.1002/nme.2579.
- [37] A. K. Ghosh. V–I transition and n-value of multifilamentary LTS and HTS wires and cables. *Physica C: Superconductivity* 401.1 (2004). Proceedings of the International Cryogenic Materials Conference: Topical Conference on the Voltage-Current Relation in Technical Superconductors, 15–21. DOI: <https://doi.org/10.1016/j.physc.2003.09.006>.
- [38] W. Goldacker, R. Nast, G. Kotzyba, S. I. Schlachter, A. Frank, B. Ringsdorf, C. Schmidt and P. Komarek. High current DyBCO-ROEBEL Assembled Coated Conductor (RACC). *Journal of Physics: Conference Series* 43 (June 2006), 901–904. DOI: 10.1088/1742-6596/43/1/220.

- [39] W. Goldacker, A. Frank, R. Heller, S. I. Schlachter, B. Ringsdorf, K.-P. Weiss, C. Schmidt and S. Schuller. ROEBEL assembled coated conductors (RACC): preparation, properties and progress. *IEEE Transactions on Applied Superconductivity* 17.2 (2007), 3398–3401. DOI: 10.1109/TASC.2007.899417.
- [40] W. Goldacker, F. Grilli, E. Pardo, A. Kario, S. I. Schlachter and M. Vojenčiak. Roebel cables from REBCO coated conductors: a one-century-old concept for the superconductivity of the future. *Superconductor Science and Technology* 27.9 (Aug. 2014), 093001. DOI: 10.1088/0953-2048/27/9/093001.
- [41] F. Gömöry, M. Vojenčiak, E. Pardo and J. Šouc. Magnetic flux penetration and AC loss in a composite superconducting wire with ferromagnetic parts. *Superconductor Science and Technology* 22.3 (Feb. 2009), 034017. DOI: 10.1088/0953-2048/22/3/034017.
- [42] F. Grilli, F. Sirois, V. M. R. Zermeño and M. Vojenčiak. Self-Consistent Modeling of the I_c of HTS Devices: How Accurate do Models Really Need to Be?: *IEEE Transactions on Applied Superconductivity* 24.6 (Dec. 2014), 8000508. DOI: 10.1109/TASC.2014.2326925.
- [43] F. Grilli and S. P. Ashworth. Measuring transport AC losses in YBCO-coated conductor coils. *Superconductor Science and Technology* 20.8 (June 2007), 794–799. DOI: 10.1088/0953-2048/20/8/013.
- [44] F. Grilli and E. Pardo. Simulation of ac loss in Roebel coated conductor cables. *Superconductor Science and Technology* 23.11 (Oct. 2010), 115018. DOI: 10.1088/0953-2048/23/11/115018.
- [45] F. Grilli, E. Pardo, A. Stenvall, D. N. Nguyen, W. Yuan and F. Gömöry. Computation of losses in HTS under the action of varying magnetic fields and currents. *arXiv preprint arXiv:1306.6251* (2013).
- [46] E. Härö. Simulation Tool Development for Quench Modelling: Re-Thinking Heat Diffusion in High Temperature Superconductors. PhD thesis. 2016.
- [47] *HTS Modeling Workgroup*. URL: <http://www.htsmodelling.com/>.
- [48] *Introduction to IPOPT: A tutorial for downloading, installing, and using IPOPT*. URL: <https://www.coin-or.org/Ipopt/documentation/>.

- [49] Z. Jiang, K. Thakur, N. Long, R. Badcock and M. Staines. Comparison of transport AC losses in an eight-strand YBCO Roebel cable and a four-tape YBCO stack. *Physica C* 471.21-22 (2011), 999–1002. DOI: 10.1016/j.physc.2011.05.109.
- [50] *Karlsruhe Institute of Technology*. URL: <http://www.kit.edu/english/>.
- [51] Y. B. Kim, C. F. Hempstead and A. R. Strnad. Critical Persistent Currents in Hard Superconductors. *Phys. Rev. Lett.* 9 (7 Oct. 1962), 306–309. DOI: 10.1103/PhysRevLett.9.306. URL: <https://link.aps.org/doi/10.1103/PhysRevLett.9.306>.
- [52] Y. B. Kim, C. F. Hempstead and A. R. Strnad. Magnetization and Critical Supercurrents. *Phys. Rev.* 129 (2 Jan. 1963), 528–535. DOI: 10.1103/PhysRev.129.528.
- [53] G. A. Kirby, J. van Nugteren, H. Bajas, V. Benda, A. Ballarino, M. Bajko, L. Bottura, K. Broekens, M. Canale, A. Chiuchiolo, L. Gentini, N. Peray, J. C. Perez, G. de Rijk, A. Rijllart, L. Rossi, J. Murtoemaeki, J. Mazet, F. Pincot, G. Volpini, M. Durante, P. Fazilleau, C. Lorin, A. Stenvall, W. Goldacker, A. Kario and A. Usoskin. First Cold Powering Test of REBCO Roebel Wound Coil for the EuCARD2 Future Magnet Development Project. *IEEE Transactions on Applied Superconductivity* 27.4 (June 2017), 4003307. ISSN: 1051-8223. DOI: 10.1109/TASC.2017.2653204.
- [54] G. Kirby, L. Rossi, A. Badel, M. Bajko, A. Ballarino, L. Bottura, M. Dhallé, M. Durante, P. Fazilleau, J. Fleiter, W. Goldacker, E. Härö, J. Himbele, A. Kario, S. Langeslag, C. Lorin, J. Murtzomaki, J. van Nugteren, G. de Rijk, T. Salmi, C. Senatore, A. Stenvall, P. Tixador, A. Usoskin, G. Volpini, Y. Yang and N. Zangenberg. Status of the Demonstrator Magnets for the EuCARD-2 Future Magnets Project. *IEEE Transactions on Applied Superconductivity* 26.3 (Apr. 2016), 4003307. ISSN: 1051-8223. DOI: 10.1109/TASC.2016.2528544.
- [55] G. Kirby, J. van Nugteren, A. Ballarino, L. Bottura, N. Chouika, S. Clement, V. Datskov, L. Fajardo, J. Fleiter, R. Gauthier et al. Accelerator-quality HTS dipole magnet demonstrator designs for the EuCARD-2 5-T 40-mm clear aperture magnet. *IEEE Transactions on Applied Superconductivity* 25.3 (2015), 4000805. DOI: 10.1109/TASC.2014.2361933.

- [56] V. Lahtinen, M. Lyly, A. Stenvall and T. Tarhasaari. Comparison of three eddy current formulations for superconductor hysteresis loss modelling. *Superconductor Science and Technology* 25.11 (2012), 115001. DOI: 10.1088/0953-2048/25/11/115001.
- [57] V. Lahtinen. Searching for Frontiers in Contemporary Eddy Current Model Based Hysteresis Loss Modelling of Superconductors. PhD thesis. 2014.
- [58] V. Lahtinen, E. Pardo, J. Šouc, M. Solovyov and A. Stenvall. Ripple field losses in direct current biased superconductors: Simulations and comparison with measurements. *Journal of Applied Physics* 115.11 (2014), 113907. URL: 10.1063/1.4868898.
- [59] L. S. Lakshmi, M. P. Staines, R. A. Badcock, N. J. Long, M. Majoros, E. W. Collings and M. D. Sumption. Frequency dependence of magnetic ac loss in a Roebel cable made of YBCO on a Ni-W substrate. *Superconductor Science and Technology* 23.8 (July 2010), 085009. DOI: 10.1088/0953-2048/23/8/085009.
- [60] J. Lehtonen, R. Mikkonen and J. Paasi. A numerical model for stability considerations in HTS magnets. *Superconductor Science and Technology* 13.3 (2000), 251–258. DOI: 10.1088/0953-2048/13/3/301.
- [61] R. J. LeVeque. *Finite difference methods for ordinary and partial differential equations: steady-state and time-dependent problems*. Vol. 98. Siam, 2007.
- [62] J. Lu, E. Choi and H. Zhou. Physical properties of Hastelloy[®] C-276[™] at cryogenic temperatures. *Journal of applied physics* 103.6 (2008), 064908.
- [63] D. Luenberger and Y. Ye. *Linear and nonlinear programming*. Springer, 2008.
- [64] *MATLAB Optimization Toolbox, The Math Works, Natick, MA, USA*. 2018.
- [65] J. C. Maxwell. *A treatise on electricity and magnetism*. Vol. 1. Oxford: Clarendon Press, 1873.
- [66] W. Meissner and R. Ochsenfeld. Ein neuer effekt bei eintritt der supraleitfähigkeit. *Naturwissenschaften* 21.44 (1933), 787–788.
- [67] K.-H. Mess, P. Schmüser and S. Wolff. *Superconducting accelerator magnets*. World Scientific, 1996.

- [68] J. S. Murtomäki, G. Kirby, J. van Nugteren, P. Contat, O. Sacristan-de-Frutos, J. Fleiter, F. Pincot, G. de Rijk, L. Rossi, J. Ruuskanen, A. Stenvall and F. J. Wolf. 10 kA Joints for HTS Roebel Cables. *IEEE Transactions on Applied Superconductivity* 28.3 (Apr. 2018), 4801406. ISSN: 1051-8223. DOI: 10.1109/TASC.2018.2804951.
- [69] D. N. Nguyen, S. P. Ashworth, J. O. Willis, F. Sirois and F. Grilli. A new finite-element method simulation model for computing AC loss in roll assisted biaxially textured substrate YBCO tapes. *Superconductor Science and Technology* 23.2 (Dec. 2009), 025001. DOI: 10.1088/0953-2048/23/2/025001.
- [70] M. Nii, N. Amemiya and T. Nakamura. Three-dimensional model for numerical electromagnetic field analyses of coated superconductors and its application to Roebel cables. *Superconductor Science and Technology* 25.9 (July 2012), 095011. DOI: 10.1088/0953-2048/25/9/095011.
- [71] J. Nocedal, A. Wächter and R. A. Waltz. Adaptive barrier update strategies for nonlinear interior methods. *SIAM Journal on Optimization* 19.4 (2009), 1674–1693.
- [72] W. T. Norris. Calculation of hysteresis losses in hard superconductors carrying ac: isolated conductors and edges of thin sheets. *Journal of Physics D: Applied Physics* 3.4 (Apr. 1970), 489–507. DOI: 10.1088/0022-3727/3/4/308.
- [73] J. van Nugteren, G. Kirby, H. Bajas, M. Bajko, A. Ballarino, L. Bottura, A. Chiuchiolo, P.-A. Contat, M. Dhallé, M. Durante, P. Fazilleau, A. Fontalva, P. Gao, W. Goldacker, H. ten Kate, A. Kario, V. Lahtinen, C. Lorin, A. Markelov, J. Mazet, A. Molodyk, J. Murtomäki, N. Long, J. Perez, C. Petrone, F. Pincot, G. de Rijk, L. Rossi, S. Russenschuck, J. Ruuskanen, K. Schmitz, A. Stenvall, A. Usoskin, G. Willering and Y. Yang. Powering of an HTS dipole insert-magnet operated standalone in helium gas between 5 and 85 K. *Superconductor Science and Technology* 31.6 (), 065002. DOI: 10.1088/1361-6668/aab887.
- [74] J. van Nugteren, G. Kirby, J. Murtomäki, G. DeRijk, L. Rossi and A. Stenvall. Toward REBCO 20 T+ dipoles for accelerators. *IEEE Transactions on Applied Superconductivity* 28.4 (2018), 1–9.
- [75] X. Obradors and T. Puig. Coated conductors for power applications: materials challenges. *Superconductor Science and Technology* 27.4 (Mar. 2014), 044003. DOI: 10.1088/0953-2048/27/4/044003.

- [76] H. K. Onnes. The disappearance of the resistivity of mercury. *Comm. Leiden* 122 (1911).
- [77] E. Pardo. Modeling of coated conductor pancake coils with a large number of turns. *Superconductor Science and Technology* 21.6 (Apr. 2008), 065014. DOI: 10.1088/0953-2048/21/6/065014.
- [78] E. Pardo, J. Kováč and J. Šouc. Power Loss in ReBCO Racetrack Coils Under AC Applied Magnetic Field and DC Current. *IEEE Transactions on Applied Superconductivity* 23.3 (2013), 4701305. DOI: 10.1109/TASC.2012.2235518.
- [79] E. Pardo, F. Gömöry, J. Šouc and J. M. Ceballos. Current distribution and ac loss for a superconducting rectangular strip with in-phase alternating current and applied field. *Superconductor Science and Technology* 20.4 (Mar. 2007), 351–364. DOI: 10.1088/0953-2048/20/4/009.
- [80] E. Pardo, F. Gömöry, J. Šouc and J. M. Ceballos. Current distribution and ac loss for a superconducting rectangular strip with in-phase alternating current and applied field. *Superconductor Science and Technology* 20.4 (Mar. 2007), 351–364. DOI: 10.1088/0953-2048/20/4/009.
- [81] E. Pardo, J. Šouc and J. Kováč. AC loss in ReBCO pancake coils and stacks of them: modelling and measurement. *Superconductor Science and Technology* 25.3 (Jan. 2012), 035003. DOI: 10.1088/0953-2048/25/3/035003.
- [82] E. Pardo, A. Sanchez, D.-X. Chen and C. Navau. Theoretical analysis of the transport critical-state ac loss in arrays of superconducting rectangular strips. *Phys. Rev. B* 71 (13 Apr. 2005), 134517. DOI: 10.1103/PhysRevB.71.134517.
- [83] E. Pardo, J. Šouc and L. Frolek. Electromagnetic modelling of superconductors with a smooth current-voltage relation: variational principle and coils from a few turns to large magnets. *Superconductor Science and Technology* 28.4 (Feb. 2015), 044003. DOI: 10.1088/0953-2048/28/4/044003.
- [84] *Platform for programming finite element method solvers in Matlab*. URL: <https://github.com/stenvala/dp>.
- [85] L. Prigozhin. The Bean Model in Superconductivity: Variational Formulation and Numerical Solution. *Journal of Computational Physics* 129.1 (1996), 190–200. ISSN: 0021-9991. DOI: 10.1006/jcph.1996.0243.

- [86] L. Prigozhin. Analysis of critical-state problems in type-II superconductivity. *IEEE Transactions on Applied Superconductivity* 7.4 (1997), 3866–3873. DOI: 10.1109/77.659440.
- [87] L. Prigozhin and V. Sokolovsky. Computing AC losses in stacks of high-temperature superconducting tapes. *Superconductor Science and Technology* 24.7 (May 2011), 075012. DOI: 10.1088/0953-2048/24/7/075012.
- [88] J. Rhyner. Magnetic properties and AC-losses of superconductors with power law current—voltage characteristics. *Physica C: Superconductivity* 212.3 (1993), 292–300. ISSN: 0921-4534. DOI: 10.1016/0921-4534(93)90592-E.
- [89] N. Riva, S. Richard, F. Sirois, C. Lacroix, B. Dutoit and F. Grilli. Over-Critical Current Resistivity of YBCO Coated Conductors through Combination of Pulsed Current Measurements and Finite Element Analysis. *IEEE Transactions on Applied Superconductivity* 29.5 (2019), 6601705. DOI: 10.1109/tasc.2019.2902038.
- [90] L. Rossi. The LHC main dipoles and quadrupoles toward series production. *IEEE Transactions on Applied Superconductivity* 13.2 (2003), 1221–1228. DOI: 10.1109/TASC.2003.812639.
- [91] L. Rossi, A. Badel, H. Bajas, M. Bajko, A. Ballarino, C. Barth, U. Betz, L. Bottura, F. Broggi, A. Chiuchiolo, M. Dhallé, M. Durante, P. Fazilleau, J. Fleiter, P. Gao, W. Goldacker, A. Kario, G. Kirby, E. Haro, J. Himbele, C. Lorin, J. Murtomaki, J. van Nugteren, C. Petrone, G. de Rijk, J. Ruuskanen, C. Senatore, M. Statera, A. Stenvall, P. Tixador, Y. Yang, A. Usoskin and N. Zangenberg. The EuCARD2 Future Magnets Program for Particle Accelerator High-Field Dipoles: Review of Results and Next Steps. *IEEE Transactions on Applied Superconductivity* 28.3 (Apr. 2018), 4001810. ISSN: 1051-8223. DOI: 10.1109/TASC.2017.2784357.
- [92] L. Rossi, A. Badel, M. Bajko, A. Ballarino, L. Bottura, M. M. J. Dhallé, M. Durante, P. Fazilleau, J. Fleiter, W. Goldacker, E. Härö, A. Kario, G. Kirby, C. Lorin, J. van Nugteren, G. de Rijk, T. Salmi, C. Senatore, A. Stenvall, P. Tixador, A. Usoskin, G. Volpini, Y. Yang and N. Zangenberg. The EuCARD-2 Future Magnets European Collaboration for Accelerator-Quality HTS Magnets. *IEEE Transactions on Applied Superconductivity* 25.3 (June 2015), 4001007. ISSN: 1051-8223. DOI: 10.1109/TASC.2014.2364215.

- [93] T. Salmi. Optimization of Quench Protection Heater Performance in High-Field Accelerator Magnets Through Computational and Experimental Analysis. PhD thesis. Tampere University of Technology, Tampere, Finland, 2015.
- [94] T. Salmi and A. Stenvall. Modeling Quench Protection Heater Delays in an HTS Coil. *IEEE Transactions on Applied Superconductivity* 25.3 (2015), 0500205. DOI: 10.1109/tasc.2014.2363523.
- [95] U. Schoop, M. W. Rupich, C. Thieme, D. T. Verebelyi, W. Zhang, X. Li, T. Kodenkandath, N. Nguyen, E. Siegal, L. Civale, T. Holesinger, B. Maiorov, A. Goyal and M. Paranthaman. Second generation HTS wire based on RABiTS substrates and MOD YBCO. *IEEE Transactions on Applied Superconductivity* 15.2 (June 2005), 2611–2616. ISSN: 1051-8223. DOI: 10.1109/TASC.2005.847681.
- [96] B. Seeber. *Handbook of applied superconductivity*. Vol. 2. CRC press, 1998.
- [97] C. Senatore, C. Barth, M. Bonura, M. Kulich and G. Mondonico. Field and temperature scaling of the critical current density in commercial REBCO coated conductors. *Superconductor Science and Technology* 29.1 (Dec. 2015), 014002. DOI: 10.1088/0953-2048/29/1/014002.
- [98] L. F. Shampine and M. K. Gordon. Computer solution of ordinary differential equations: the initial value problem. (1975).
- [99] Y. Shiohara, M. Yoshizumi, T. Izumi and Y. Yamada. Present status and future prospect of coated conductor development and its application in Japan. *Superconductor Science and Technology* 21.3 (Feb. 2008), 034002. DOI: 10.1088/0953-2048/21/3/034002.
- [100] F. Sirois, J. Coulombe, F. Roy and B. Dutoit. Characterization of the electrical resistance of high temperature superconductor coated conductors at high currents using ultra-fast regulated current pulses. *Superconductor Science and Technology* 23.3 (Feb. 2010), 034018. DOI: 10.1088/0953-2048/23/3/034018.
- [101] F. Sirois, F. Grilli and A. Morandi. Comparison of Constitutive Laws for Modeling High-Temperature Superconductors. *IEEE Transactions on Applied Superconductivity* 29.1 (2019), 8000110. DOI: 10.1109/TASC.2018.2848219.

- [102] J. Šouc, E. Pardo, M. Vojenčiak and F. Gömöry. Theoretical and experimental study of AC loss in high temperature superconductor single pancake coils. *Superconductor Science and Technology* 22.1 (Nov. 2008), 015006. DOI: 10.1088/0953-2048/22/1/015006.
- [103] A. Stenvall, A. Korpela, R. Mikkonen and G. Grasso. Stability considerations of multifilamentary MgB₂tape. *Superconductor Science and Technology* 19.2 (Jan. 2006), 184–189. DOI: 10.1088/0953-2048/19/2/006.
- [104] A. Stenvall and T. Tarhasaari. An eddy current vector potential formulation for estimating hysteresis losses of superconductors with FEM. *Superconductor Science and Technology* 23.12 (Nov. 2010), 125013. DOI: 10.1088/0953-2048/23/12/125013.
- [105] A. Stenvall and T. Tarhasaari. Programming finite element method based hysteresis loss computation software using non-linear superconductor resistivity and $T - \varphi$ formulation. *Superconductor Science and Technology* 23.7 (June 2010), 075010. DOI: 10.1088/0953-2048/23/7/075010.
- [106] *SuNam Co., Ltd.* URL: www.i-sunam.com.
- [107] *SuperOx.* URL: <http://superox.ru/en/products/42-2G-HTS-tape>.
- [108] *SuperPower, Inc.* URL: <http://superpower-inc.com>.
- [109] A. Tarantola. *Inverse problem theory and methods for model parameter estimation*. Vol. 89. siam, 2005.
- [110] *The European Organization for Nuclear Research.* URL: <http://home.web.cern.ch/>.
- [111] *The Large Hadron Collider.* URL: <https://home.cern/science/accelerators/large-hadron-collider>.
- [112] J. van Nugteren, G. A. Kirby, G. de Rijk, L. Rossi, H. H. J. ten Kate and M. M. J. Dhallé. Study of a 5 T Research Dipole Insert-Magnet Using an Anisotropic ReBCO Roebel Cable. *IEEE Transactions on Applied Superconductivity* 25.3 (June 2015), 4000705. ISSN: 1051-8223. DOI: 10.1109/TASC.2014.2361797.

- [113] J. van Nugteren, J. Murtomäki, J. Ruuskanen, G. Kirby, P. Hagen, G. de Rijk, H. T. Kate, L. Bottura and L. Rossi. A Fast Quench Protection System for High-Temperature Superconducting Magnets. *IEEE Transactions on Applied Superconductivity* 29.1 (Jan. 2019), 4700108. ISSN: 1051-8223. DOI: 10.1109/TASC.2018.2848229.
- [114] J. van Nugteren, B. van Nugteren, P. Gao, L. Bottura, M. Dhallé, W. Goldacker, A. Kario, H. ten Kate, G. Kirby, E. Krooshoop, G. de Rijk, L. Rossi, C. Senatore, S. Wessel, K. Yagotintsev and Y. Yang. Measurement and Numerical Evaluation of AC Losses in a ReBCO Roebel Cable at 4.5 K. *IEEE Transactions on Applied Superconductivity* 26.3 (Apr. 2016), 8201407. ISSN: 1051-8223. DOI: 10.1109/TASC.2016.2525919.
- [115] J. Van Nugteren. High temperature superconductor accelerator magnets. PhD thesis. Twente U., Enschede, Enschede, 2016.
- [116] A. Wächter. An interior point algorithm for large-scale nonlinear optimization with applications in process engineering. PhD thesis. Carnegie Mellon University, Pittsburgh, PA, USA, 2002.
- [117] A. Wächter and L. T. Biegler. On the implementation of an interior-point filter line-search algorithm for large-scale nonlinear programming. *Mathematical Programming* 106.1 (Mar. 2006), 25–57. ISSN: 1436-4646. DOI: 10.1007/s10107-004-0559-y.
- [118] R. Waltz, J. Morales, J. Nocedal and D. Orban. An interior algorithm for nonlinear optimization that combines line search and trust region steps. *Mathematical Programming* 107.3 (July 2006), 391–408. DOI: 10.1007/s10107-004-0560-5.
- [119] J. Weidmann. *Linear operators in Hilbert spaces*. Vol. 68. Graduate Texts in Mathematics. Translated from the German by Joseph Szücs. Springer-Verlag, New York-Berlin, 1980, xiii+402. ISBN: 0-387-90427-1.
- [120] H. Weijers, U. Trociewitz, W. Markiewicz, J. Jiang, D. Myers, E. Hellstrom, A. Xu, J. Jaroszynski, P. Noyes, Y. Viouchkov et al. High field magnets with HTS conductors. *IEEE Transactions on Applied Superconductivity* 20.3 (2010), 576–582. DOI: 10.1109/TASC.2010.2043080.

- [121] G. P. Willering, D. C. van der Laan, H. W. Weijers, P. D. Noyes, G. E. Miller and Y. Viouchkov. Effect of variations in terminal contact resistances on the current distribution in high-temperature superconducting cables. *Superconductor Science and Technology* 28.3 (Jan. 2015), 035001. DOI: 10 . 1088 /0953 - 2048/28/3/035001.
- [122] M. N. Wilson. *Superconducting magnets*. 1983.
- [123] S. C. Wimbush and N. M. Strickland. A Public Database of High-Temperature Superconductor Critical Current Data. *IEEE Transactions on Applied Superconductivity* 27.4 (June 2017), 8000105. ISSN: 1051-8223. DOI: 10 . 1109/TASC . 2016 . 2628700.
- [124] K. Yosida. *Functional analysis*. Vol. Fifth edition. Springer, 1980.

PUBLICATIONS

PUBLICATION

I

Utilizing Triangular Mesh With MMEV to Study Hysteresis Losses of Round Superconductors Obeying Critical State Model

J. Ruuskanen, A. Stenvall and V. Lahtinen

IEEE Transactions on Applied Superconductivity 25.3 (2015), 8200405

DOI: 10.1109/TASC.2014.2365408

Publication reprinted with the permission of the copyright holders

Utilizing Triangular Mesh with Minimum Magnetic Energy Variation to Study Hysteresis Losses of Superconductors Obeying Critical State Model

Janne Ruuskanen, Antti Stenvall, and Valtteri Lahtinen

Abstract—Nature’s minimum energy principle formulated in minimum magnetic energy variation (MMEV) and coupled with the Bean’s critical state model (CSM) has resulted in feasible tools to model hysteresis losses in superconductors. These tools have been applied for single wires as well as for multi-turn coils in two-dimensional modelling domains. However, so far the discretization of the modelling domain has always relied on regular rectangular meshes. Therefore, the mesh representation of round filaments suffers from large discretization error if the mesh is not refined considerably more than triangular meshing would need. In this paper, we study the utilisation of triangular mesh in such a hysteresis loss modelling tool. We present the required extension to the already available knowledge that is needed to implement such a modelling tool. With our home-brewed tool, we study the convergence of computed loss for triangular and rectangular meshes of different types and of different densities. According to the results, triangular meshes are considerably more efficient than rectangular meshes for simulating transport current losses in round filaments.

Index Terms—critical state model, hysteresis losses, minimum magnetic energy variation, numerical modelling

I. INTRODUCTION

SUPERCONDUCTORS are lossless only when no time varying magnetic fields are directed to them and when the transport current does not vary. In any other case, so called AC-losses arise [1]. These may be due to, e.g., functional characteristic of the device, like harmonic excitation or ramping of the magnet to a desired current, or due to unwanted effects like leaking ripple flux from the stator winding of a motor having a superconducting field winding. The AC-losses cause undesired heat dissipation inside the superconductor. Then, the local operation temperature increases which can jeopardize the stable operation of the device. Therefore, the analysis of AC-losses is essential in the design phase of a superconducting system.

The AC-losses can be divided into three parts: hysteresis, eddy current and coupling [2]. The hysteresis losses arise in the superconducting domains due to locally time varying magnetic flux which produces electric field parallel to the current density. The eddy current losses arise in normal conducting components of the superconducting wires and cables. The resistivity of the superconductors is orders of magnitude

lower than that of the matrix metal. Consequently, the superconducting filaments in a multifilamentary wire may behave like galvanically isolated individual monofilament conductors. However, if this is not the case, the coupling losses arise. Depending on the application, all the forms of AC-losses can be important [1]. In this paper we focus on the hysteresis losses, which have negligible frequency-dependence [3], [4].

Hysteresis losses are computationally studied primarily with two different approaches [5]–[7]. In the first one, superconductor is treated like a normal conductor but with highly non-linear resistivity. The isotropic power-law characterizes the relation between parallel electric field E and current density J as

$$\|E\| = E_c \left(\frac{\|J\|}{J_c} \right)^n, \quad (1)$$

where $\|\cdot\|$ denotes the Euclidean norm, E_c is the critical electric field criterion, J_c is the critical current density (i.e. current density at which $E = E_c$) and n characterizes the steepness of the resistive transition [8]. When this model is used, the AC-loss analysis can be performed with a transient magnetoquasistatic computational tool. Different formulations for such tools exist. For example, H [9], [10], $T - \Omega$ [11], $A - V - j$ [12] and $H - \varphi - \Psi$ [13] can be utilized. Such a model leads to frequency-dependent hysteresis losses, but can still adequately predict losses over an AC cycle around 50 Hz [14]. However, so far this approach has not been utilized to study ramp losses in magnets.

The second approach assumes that superconductors obey the critical state model (CSM) [5]. Then, any B causes a never vanishing perpendicular J having magnitude of critical current density J_c . The sign of J may change as well as the norm, but only if J_c changes due to the variation of field or temperature. In Bean’s original CSM J_c was assumed to be constant, but the idea that the magnitude of J is J_c is in the core of CSM. CSM is independent of time variable. Consequently, ramp losses can be studied as well as situations with cyclic excitations.

For the hysteresis losses of superconductors obeying CSM, analytical solutions exist when the shape of the superconducting domain is simple, like strip or elliptical one [16]–[19]. Also, situations where isolated domains interact have been solved [20].

On the numerical side, successful tools have been developed using the concept of minimum magnetic energy variation (MMEV) which solve for AC-losses in superconductors obeying Bean’s critical state model. The physical principle of MMEV is related to variation of energy as the system

This work was supported by Stability Analysis of Superconducting Hybrid magnets (Academy of Finland, #250652).

Manuscript received August 11, 2014.

The authors are with Tampere University of Technology, Electromagnetics, P.O. Box 692, FIN-33101 Tampere, Finland (e-mail: antti.stenvall@tut.fi; www: http://www.tut.fi/smg).

tends towards minimum energy, and correspondingly, changes incorporate minimum variation of energy. [21]. Also, other numerical schemes for solving CSM are possible [15]. The advantage of the MMEV approach is discretization of computational domain into elements allowing representation of various shapes. However, to date only square elements have been used with the approach. Consequently, large number of elements are needed to discretize round domains, although this approach suits well, for example, for modelling coated conductors [22].

In this paper we present a computational tool based on MMEV and CSM where we utilize triangular elements to discretize the modelling domain. In the results, we compare the performance of triangular elements and rectangular elements to an analytical solution.

II. COMPUTATIONAL MODEL

The computational tool based on the MMEV utilized in this work follows similar principles as the one in [23]–[25]. To extend it for triangular elements, one only needs to know how to compute the vector potential caused by a homogeneous current in a triangular element. Next, we introduce the algorithm for solving current distribution on a conductor, then, we show how it was utilized to compute the hysteresis losses. Finally, we present the investigated meshes and consider the implications of using a triangular mesh.

A. Algorithm for MMEV based computational tool

We implemented the MMEV solver within the open source platform GMSH [27], which is a three-dimensional finite element mesh generator with built-in pre- and post-processing facilities, with the help of its Riemannian manifold interface for representing the field quantities [28]. For simplicity, we consider here only the transport current and field independent critical current density J_c . The algorithm that solves for a current density distribution J from a known distribution \hat{J} (in this paper, $\hat{\cdot}$ refers to previous data), when the applied net current I_a changes by $\Delta I_a = I_a - \hat{I}_a$, is described in Alg. 1.

The algorithm consists of two functions named SOLVEJDIST and WHERETOADD. For a given $mesh$ SOLVEJDIST solves a new current distribution by adding small current density steps $\Delta J \ll J_c$ into elements chosen by the function WHERETOADD until the applied net current change ΔI_a is fulfilled. The value of added current is $\Delta J \times area_{elem}$. The current density step ΔJ can be chosen by dividing the J_c by an integer m . In our calculations we used value 20 for m . This smoothens up the current front and reduces discretization error.

The function WHERETOADD chooses the element j which minimizes the functional

$$MEV_j[\Delta I] = C_{jj} \left(\frac{1}{2} (\Delta I)^2 + I_j \Delta I \right) + \sum_{\substack{k=1 \\ k \neq j}}^N C_{jk} \hat{I}_k \Delta I, \quad (2)$$

where N is the number of elements, ΔI is the current change in element j , and $I_j = \hat{I}_j + \Delta I$ is the new current in element j . ΔI is defined from the area of the smallest element in the

mesh such that $\Delta I = \Delta J \times \min\{\text{element areas}\}$. This is how we can neutralize the effect of variation of element area. The coefficients C'_{jj} and C'_{jk} are geometrical parameters, which can be interpreted as the self-inductance of element j and the mutual inductance between element k and the barycenter of element j , respectively. The coefficients are calculated before running the algorithm. The details are given in [23] and [29].

In function WHERETOADD, by taking the first non-saturated element i , we calculate the magnetic energy variation (2) due to the hypothetical addition of ΔJ into the element. In the loop beginning from line 13 to find the element j , which gives the minimum of (2), we go through all the elements. Then, we add ΔJ to this element j in SOLVEJDIST. New current density distribution is ready when the loop beginning at line three has finished.

Algorithm 1 Algorithm for solving current density distribution in a superconductor obeying CSM with MMEV.

```

1: procedure SOLVEJDIST( $mesh, \hat{J}, \Delta J, \Delta I_a$ )
2:    $added \leftarrow 0$ 
3:   while  $added < \Delta I_a$  do
4:      $i \leftarrow$  WHERETOADD( $mesh, \hat{J}, \Delta J$ )
5:     In  $\hat{J}$  add  $\Delta J$  to element  $i$ 
6:      $added += \Delta J \times area_{elem_i}$ 
7:   end while
8:   return  $\hat{J}$  ▷ This is now new  $J$  distribution
9: end procedure

10: procedure WHERETOADD( $mesh, \hat{J}, \Delta J$ )
11:    $i \leftarrow$  first element index where  $\hat{J}_i < J_c$ 
12:    $\Delta I \leftarrow \Delta J \times \min\{\text{element areas}\}$ 
13:    $MEV \leftarrow$  magnetic energy variation in element  $i$ , if
     adding  $\Delta I$  to element  $i$ 
14:   for  $j=1 \rightarrow \#\text{elements in } mesh$  do
15:     if  $J_{prev}^j < J_c$  then
16:        $MEV_{test} \leftarrow$  magnetic energy variation in ele-
         ment  $j$ , if adding  $\Delta I$  to element  $j$ 
17:       if  $MEV_{test} < MEV$  then
18:          $i \leftarrow j$ 
19:          $MEV \leftarrow MEV_{test}$ 
20:       end if
21:     end if
22:   end for
23:   return  $i$ 
24: end procedure

```

B. Calculation of AC-loss

When considering a current ramp from zero to its amplitude, the current distribution for the peak state of transport current can be obtained iteratively from a known (time-)step to another using the presented algorithm. The magnetic vector potential at \mathbf{r} due to current density $J(\mathbf{r}')$ can be calculated using

$$A(\mathbf{r}) = -\frac{\mu_0}{2\pi} \int_S J(\mathbf{r}') \ln \left(\sqrt{(\mathbf{r}' - \mathbf{r}) \cdot (\mathbf{r}' - \mathbf{r})} \right) dS'. \quad (3)$$

Analytical solution of (3) is derived for rectangular elements in [29] and the extension for triangular ones is presented in the next subsection.

In the case of monotonous current penetration the AC-loss Q of the whole AC-cycle can be computed from the current density profile at the peak state of transport current using

$$Q = 4J_c \int_S [A_m^c - A_m(\mathbf{r})] dS, \quad (4)$$

where J_c is the critical current density, A_m^c is the constant magnetic vector potential of the flux free core at the peak state of transport current, and A_m is the corresponding magnetic vector potential. Derivation of (4) can be found in [23]. Integration is done in such a way that $A_m(\mathbf{r})$ is computed at element barycenter and assumed constant for the element.

C. Extending the algorithm for triangular elements

For triangular elements, the analytic formulas for rectangular elements for calculating vector potential no longer hold. One needs to begin the derivation from (3). In our modelling tool, integration over triangular element carrying constant current density is done utilizing the formulas presented in [26].

Furthermore, when calculating the coefficients of (2) the integration is similar because the coefficients C_{jk} are defined as vector potentials per unit current (and can be interpreted via inductances) generated by element j [29].¹ Otherwise, the Alg. 1 itself is exactly the same for meshes of triangular and rectangular elements.

D. Description of the modelling domain and meshes

We studied a superconducting round monofilament with the radius r of 1 mm, i.e., our modelling domain was a disc in two dimensions with the current flowing perpendicularly to the disc. The critical current density of the domain was 318 A/mm². Then, the critical current I_c was 1000 A.

For an elliptical wire carrying transport current i normalized to the critical current, the analytical solution for the hysteresis losses during one cycle, namely the Norris (ellipse) loss with which we compare our results, is [16]

$$L_c = \frac{I_c^2 \mu_0}{\pi} \left((1-i) \ln(1-i) + \frac{(2-i)i}{2} \right), \quad (5)$$

where μ_0 is the vacuum permeability.

To study the benefits of using triangular meshes in simulating round superconductors, we constructed four different types of meshes. The triangular mesh type **Tri** was parametrized by number of concentric rings (n) and the rectangular mesh types **Squ In**, **Squ Out**, and **Squ IO** were parametrized by the number of layers of elements n on top of each other.

- 1) **Triangular (Tri)**: We added concentric rings into the disc and distributed nodes evenly to the rings. Then, we utilized Delaunay triangulation to mesh the domain [30].

¹Note, the averaging of vector potential over an element area like in [29] is not possible due to the element size variation.

The meshes were parametrized by the number of rings. The distances between the rings as well as position of the first node for positioning the points evenly were optimized with local optimization algorithm Sequential Quadratic Programming [31] to attain minimum standard deviation in the element size.

- 2) **Squares inside (Squ In)**: We added squares to form the disc so that they became located completely inside the disc. The uppermost row had always two elements and the element side length l was determined as

$$l = \frac{r}{\sqrt{1 + \frac{1}{4}n^2}}. \quad (6)$$

The corner nodes of successive layers were not necessarily in the same location. This is the case for all the square meshes.

- 3) **Squares outside (Squ Out)**: We added squares so that the disc just fits inside the mesh. The element side length was

$$l = \frac{2r}{n}. \quad (7)$$

- 4) **Squares inside or outside (Squ IO)**: We added squares that were allowed to be slightly outside the disc too, but they did not need to cover the whole disc. We added elements to rows until they filled more space outside the disc than inside. The element side length was determined to be the average of the two other square meshing methods.

The mesh types are shown in Fig. 1.

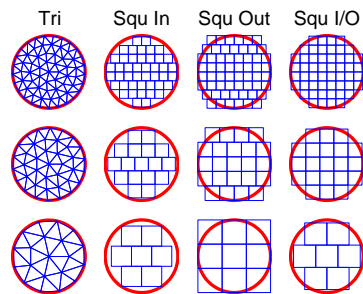


Fig. 1. Investigated mesh types. Rows from the topmost: **Tri** (parametrization numbers n : 2, 3, and 4 from bottom to top); **Squ I**; **Squ O**; and **Squ IO**. All the square meshes have parametrization numbers n 3, 5, and 8 from bottom to top.

Mesh areas normalized to the area of the disc as functions of elements in the mesh are shown in Fig. 2. The figure shows that with 100 elements the areas of **Tri** and **Squ IO** meshes differ from that of a disc by less than 2% where as the other meshes differ by more than 10 %.

III. RESULTS AND DISCUSSION

Using the mesh type **Tri** and the square mesh types we computed the hysteresis losses as a function of number of the elements in the cases where the amplitudes of transport current were $0.7I_c$ and $0.5I_c$. The current ramp was applied from zero

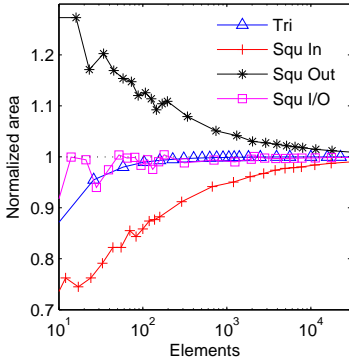


Fig. 2. Normalized area of all the elements in the mesh. Normalization is done with respect to the area of a circle having radius of 1 mm.

to its amplitude at frequency of 50 Hz using 25 time-steps for the ramp.

A. Comparison of triangular and rectangular meshes

The results normalized to the Norris loss are presented in Fig. 3. The figure shows that the mesh type **Tri** converges to the Norris loss the fastest and after 508 elements the relative error stays under 2.5 % and at 1806 elements the relative error has decreased down to 0.5 % (see Fig. 3 a)). The second best mesh type **Squ I/O** decreases down to the relative error of 2.5 % at around 1250 elements (Fig. 3 a)). Within the investigated range of elements, mesh types **Squ In** and **Squ Out** had errors larger than 4.0%.

The results for $0.7I_c$ show similar behaviour with even faster and smoother convergence. The peaks in the graphs can be explained by the large size of the elements resulting in non-smooth current penetration fronts. In addition, the accuracy of the calculated hysteresis loss depends on the smoothness of the current front at the border of the current free core. Especially in the case of mesh type **Tri**, in which the discretization is made by dividing the disc into rings, the current front at maximum applied transport current penetrates so that it fulfills one whole ring. When this occurs, the current front is smooth and the result is close to the analytical solution. Of course, with different penetration pattern, like in case of an applied field, the convergence results could vary. Discretization error might occur with a different amplitude of I_a if the current has failed to penetrate into all elements of the ring at the current front (Fig 4).

In square mesh types the peaks and slower convergence compared to the Fig. 3 b) can be explained also by the form of current front. If the mesh is not round, as in the case of sparse meshes, and the amplitude of I_a is small, the current front follows the form of the mesh as it penetrates. When using greater amplitude of I_a , such as $0.7I_c$, the current front rounds itself as it penetrates further and more accurate result is obtained. Current penetration during an AC cycle is shown in Fig. 4.

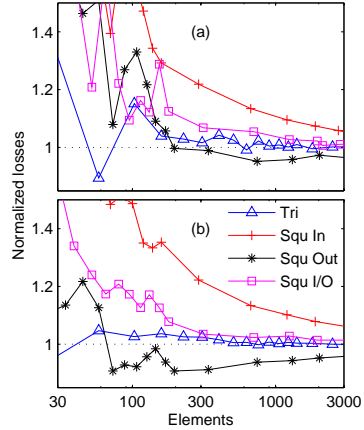


Fig. 3. Norris-normalized losses as a function of number of elements in the meshes. I_a was $0.5I_c$ (a) and $0.7I_c$ (b).

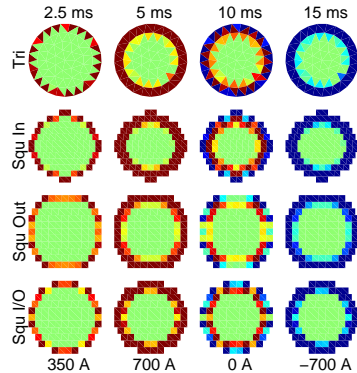


Fig. 4. Current penetration for investigated meshes of AC cycle at frequency of 50 Hz with amplitude of $0.7I_c$.

IV. CONCLUSIONS

Numerical schemes combining MMEV and CSM have so far been lacking the extension to triangular elements. In this paper, we have developed such an extension. We show that triangular meshes converge more rapidly (i.e. with less elements) towards analytical solutions than square meshes at least for a round conductor carrying a transport current. As a consequence of using sparse meshes, the computation time is significantly shorter. According to the results, the fastest convergence to the Norris loss is obtained using triangular elements in the modelling domain of a round conductor.

V. ACKNOWLEDGMENT

The authors thank Dr. Enric Pardo, Slovak Academy of Sciences, Bratislava, Slovakia for helpful hints in implementing the computational tool used in this publication.

REFERENCES

- [1] F. Grilli, E. Pardo, A. Stenvall, D.N. Nguyen, W. Yuan, and F. Gömör, "Computation of losses in HTS under the action of varying magnetic fields and currents," *IEEE Trans. Appl. Supercond.* vol. 24, 8200433, 2014.
- [2] M.N. Wilson, "NbTi superconductors with low ac loss: A review," *Cryogenics* vol. 48, pp. 381-395, 2008.
- [3] S. Stavrev, and B. Dutoit, "Frequency dependence of AC loss in Bi(2223)Ag-sheathed tapes," *Physica C* vol. 310, pp. 86-89, 1998.
- [4] M. Majoros, B.A. Glowacki, A.M. Campbell, G.A. Levin, P.N. Barnes, and M. Polak, "AC losses in striated YBCO coated conductors," *IEEE Trans. Appl. Supercond.* vol. 15, pp. 2819-2822, 2005.
- [5] C.P. Bean, "Magnetization of hard superconductors," *Phys. Rev. Lett.*, vol. 8, pp. 250-253, 1962.
- [6] J. Paasi, J. Lehtonen, M. Lahtinen, and L. Kettunen, "Computation of AC-losses in high-temperature superconductors" *Physica C*, vol. 310, pp. 62-66, 1998.
- [7] V. Lahtinen, and A. Stenvall, "Scientific research in the field of mesh method based modeling of AC losses in superconductors: a review", *J. Supercond. Nov. Magn.*, vol. 27, pp. 641-650, 2014.
- [8] P. Bruzzone, "The index n of the voltage-current curve, in the characterization and specification of technical superconductors", *Physica C*, vol. 401, pp. 7-14, 2004.
- [9] Z. Hong, A. M. Campbell, and T. A. Coombs, "Numerical solution of critical state in superconductivity by finite element software," *Supercond. Sci. Technol.*, vol. 19, pp. 1246-1252, 2006.
- [10] R. Brambilla, F. Grilli, and L. Martini, "Development of an edge-element model for AC loss computation of high-temperature superconductors," *Supercond. Sci. Technol.*, vol. 20, pp. 16-24, 2007.
- [11] N. Amemiya, S. Murasawa, N. Banno, and K. Miyamoto, "Numerical modelings of superconducting wires for AC loss calculations," *Physica C*, vol. 310, pp. 16-29, 1998.
- [12] A. Stenvall, and T. Tarhasaari, "An eddy current vector potential formulation for estimating hysteresis losses of superconductors with FEM," *Supercond. Sci. Technol.*, vol. 23, 125013, 2010.
- [13] V. Lahtinen, A. Stenvall, F. Sirois, and M. Pelliikka, "A modelling tool for simulating hysteresis losses in superconductors utilizing an H -oriented finite element method formulation with cohomology basis functions," *Submitted for publication*
- [14] V. Lahtinen, E. Pardo, J. Šouc, M. Solovyov, and A. Stenvall, "Ripple field losses in direct current biased superconductors: Simulations and comparison with measurements," *J. Appl. Phys.* vol. 115, 113907, 2014.
- [15] A. M. Campbell, "A new method of determining the critical state in superconductors" *Supercond. Sci. Technol.*, vol. 20, pp. 292-295, 2007.
- [16] W.T. Norris, "Calculation of hysteresis losses in hard superconductors carrying ac: isolated conductors and edges of thin sheets," *J Phys. D Appl. Phys.*, vol. 3, pp. 489-507, 1970.
- [17] E.H. Brandt, and M. Indenbom, "Type-II-superconductor strip with current in a perpendicular magnetic field," *Phys. Rev. B*, vol. 48, 12893, 1993.
- [18] E. H. Brandt, "Thin superconductors in a perpendicular magnetic ac field: general formulation and strip geometry," *Phys. Rev. B*, vol. 49, pp. 9024-9040, 1994.
- [19] Y. Mawatari, "Superconducting tubular wires in transverse magnetic fields," *Phys. Rev. B*, vol. 83, 134512, 2011.
- [20] G.P. Mikitik, Y. Mawatari, A.T.S. Wan, F. Sirois, "Analytical Methods and Formulas for Modeling High Temperature Superconductors," *IEEE Trans. Appl. Supercond.*, vol. 23, 8001920, 2013.
- [21] A. Sanchez, and C. Navau, "Magnetic properties of finite superconducting cylinders. I. Uniform applied field," *Phys. Rev. B*, vol. 64, 214506, 2001.
- [22] E. Pardo, "Modeling of AC Loss in Coils Made of Thin Tapes Under DC Bias Current," *IEEE Trans. Appl. Supercond.*, vol. 24, 4700105, 2014.
- [23] E. Pardo, F. Gömör, J. Šouc, and J. M. Ceballos, "Current distribution and ac loss for a superconducting rectangular strip with in-phase alternating current and applied field," *Supercond. Sci. Technol.*, vol. 20, pp. 351-364, 2007.
- [24] E. Pardo, "Modeling of coated conductor pancake coils with a large number of turns," *Supercond. Sci. Technol.*, vol. 21, 065014, 2008.
- [25] J.Šouc, E. Pardo, M. Vojenčiak, and F. Gömör, "Theoretical and experimental study of ac loss in high temperature superconductor single pancake coils," *Supercond. Sci. and Technol.*, vol. 22, 015006, 2009.
- [26] F. Sirois, and F. Roy, "Computation of 2-D current distribution in superconductors of arbitrary shapes using a new semi-analytical method," *IEEE Trans. Appl. Supercond.*, vol. 17, pp. 3836-3845, 2007.
- [27] C. Geuzaine, and J.-F. Remacle, "Gmsh: a three-dimensional finite element mesh generator with built-in pre- and post-processing facilities," *Int. J. Numer. Meth. Eng.*, vol. 79, pp. 1309-1331, 2009.
- [28] M. Pelliikka, T. Tarhasaari, S. Suuriniemi, and L. Kettunen, "A Programming Interface to the Riemannian Manifold in a Finite Element Environment," *J. Comput. Appl. Math.*, vol. 246, pp. 225-233, 2013.
- [29] E. Pardo, Alvaro Sanchez, Du-Xing Chen, and Carles Navau, "Theoretical analysis of the transport critical-state ac loss in arrays of superconducting strips," *Phys. Rev. B*, vol. 71, 134517, 2005.
- [30] M. de Berg, O. Cheong, M. van Kreveld, and M. Overmars, "Computational Geometry, Algorithms and Applications," 3rd ed. Germany, Heidelberg: Springer-Verlag, 2008.
- [31] J. Nocedal, and S. J. Wright, "Numerical Optimization," 2nd ed. NY: Springer-Verlag, 2006.

PUBLICATION

II

**Electromagnetic nonlinearities in a Roebel-cable-based accelerator magnet
prototype: variational approach**

J. Ruuskanen, A. Stenvall, V. Lahtinen and E. Pardo

Superconductor Science and Technology 30.2 (2016), 024008

DOI: 10.1088/1361-6668/30/2/024008

Publication reprinted with the permission of the copyright holders

PAPER

Electromagnetic nonlinearities in a Roebel-cable-based accelerator magnet prototype: variational approach

To cite this article: J Ruuskanen *et al* 2017 *Supercond. Sci. Technol.* **30** 024008

View the [article online](#) for updates and enhancements.

Related content

- [Electromagnetic modelling of superconductors with a smooth current–voltage relation: variational principle and coils from a few turns to large magnets](#)
Enric Pardo, Ján Šouc and Lubomir Frolek
- [Modeling of screening currents in coated conductor magnets containing up to 40000 turns](#)
E Pardo
- [Ac loss modelling and measurement of superconducting transformers with coated-conductor Roebel-cable in low-voltage winding](#)
Enric Pardo, Mike Staines, Zhenan Jiang *et al.*

Recent citations

- [The 5th international workshop on numerical modelling of high temperature superconductors](#)
Antonio Morandi *et al*



IOP | ebooks™

Bringing you innovative digital publishing with leading voices to create your essential collection of books in STEM research.

Start exploring the collection - download the first chapter of every title for free.

Electromagnetic nonlinearities in a Roebel-cable-based accelerator magnet prototype: variational approach

J Ruuskanen¹, A Stenvall¹, V Lahtinen¹ and E Pardo²

¹Electromagnetics, Tampere University of Technology, PO Box 692, 33101 Tampere, Finland

²Institute of Electrical Engineering, Slovak Academy of Sciences, Dubravska 9, 84104 Bratislava, Slovakia

E-mail: janne.ruuskanen@tut.fi

Received 13 July 2016, revised 21 October 2016

Accepted for publication 24 October 2016

Published 23 December 2016



CrossMark

Abstract

Superconducting magnets are the most expensive series of components produced in the Large Hadron Collider (LHC) at the European Organization for Nuclear Research (CERN). When developing such magnets beyond state-of-the-art technology, one possible option is to use high-temperature superconductors (HTS) that are capable of tolerating much higher magnetic fields than low-temperature superconductors (LTS), carrying simultaneously high current densities. Significant cost reductions due to decreased prototype construction needs can be achieved by careful modelling of the magnets. Simulations are used, e.g. for designing magnets fulfilling the field quality requirements of the beampipe, and adequate protection by studying the losses occurring during charging and discharging. We model the hysteresis losses and the magnetic field nonlinearity in the beampipe as a function of the magnet's current. These simulations rely on the minimum magnetic energy variation principle, with optimization algorithms provided by the open-source optimization library interior point optimizer. We utilize this methodology to investigate a research and development accelerator magnet prototype made of REBCO Roebel cable. The applicability of this approach, when the magnetic field dependence of the superconductor's critical current density is considered, is discussed. We also scrutinize the influence of the necessary modelling decisions one needs to make with this approach. The results show that different decisions can lead to notably different results, and experiments are required to study the electromagnetic behaviour of such magnets further.

Keywords: accelerator magnets, AC loss, magnetization, high-temperature superconductors, interior point optimizer, nonlinear optimization, minimum magnetic energy variation

(Some figures may appear in colour only in the online journal)

1. Introduction

Thanks to superconductors [1], high magnetic fields can be generated with low, or zero, dissipative losses. One very important application area in which superconductors are used is in producing the magnetic fields required in accelerator complexes, such as the Large Hadron Collider (LHC) in the European Organization for Nuclear Research [2] (CERN).

Even though superconductors are lossless in DC operation well below the critical current (I_c), losses arise when the current or magnetic field vary in time, inducing an electric field [3]. Modelling these losses, and the nonlinearity in the magnetic field arising from current penetration into a current carrying superconductor, is of utmost importance in designing magnets for particle accelerators, including the research and development programmes of possible LHC successors [4].

The LHC is based on conventional NbTi [1, 5] superconductor technology. Modelling this is well understood, but as superconductivity is limited by the magnetic field [1, 5],

³ <http://www.notjargon.org>

new solutions are required for accelerators with more demanding magnetic field requirements. In principle, there are two options: use Nb₃Sn superconductors, which limit the magnetic field to around 16 T, or high-temperature superconductors (HTSs), which allow fields of over 20 T at 4.2 K.

EuCARD-2, the Enhanced European Coordination for Accelerator Research and Development, is a consortium and European-Commission-funded project partially targeting HTS-based accelerator research and development⁴ [6]. The aim is to build HTS magnets carrying transport currents of several kA, which must therefore be wound from HTS cables. The conductor of choice for the cables is coated with REBCO [7, 8] (REBCO is a rare earth–barium–copper oxide-based superconducting compound; the rare earth material is typically yttrium or gadolinium). In EuCARD-2, the focus is on dipole magnets. These are the components that keep the particles in a circular orbit in synchrotron-type accelerators like the LHC. REBCO-based cables cannot, however, be manufactured in the same way as NbTi or Nb₃Sn. The primary reason for this is material technology: REBCO conductors are rectangular tapes with an aspect ratio of up to 100, whereas LTS conductors are round wires. Furthermore, the aspect ratio of the superconducting layer in the tape is of the order of 10 000. Therefore, a relevant scientific question is whether these new magnets exhibit too high losses or a too distorted magnetic field in the beampipe to eventually prevent their usage as accelerator magnets. We are not ready to answer these questions yet, but we are able to develop the methodology to study them and use the developed simulation tool to consider a prototype magnet which has not been designed with field quality in mind, however, but merely for learning about its construction.

In this paper we consider the prototype magnet, Feather-M0 [9] (FM0), collaboratively designed by EuCARD-2 and currently under construction in CERN. Because the main focus of European HTS accelerator magnet research and development is on these kinds of magnet, and their basic ingredients—Roebel cables [10] assembled from REBCO-tapes—we only focus on these in this paper and leave the so-called BSCCO-based alternatives out [11].

In terms of AC losses, REBCO-based Roebel cables are an attractive option. Comparing an untransposed stack of tapes with a Roebel cable with the same cross-sectional area, the latter reduces the AC loss as follows. For high applied perpendicular magnetic fields, the Roebel cable transposition reduces the AC loss significantly. Transposition also ensures good current sharing between the tapes or strands during ramps. If the magnetic field is mostly parallel, the Roebel cable is able to reduce the AC loss significantly. Roebel cables can then virtually eliminate parallel field AC loss and, in addition, reduce perpendicular field loss. Thus, the ideal Roebel cables regarding AC loss are those made of many

narrow strands, with a small total cable width and high thickness.

Losses in superconductors can be separated into four different types: hysteresis losses, coupling losses, eddy current losses and resistive losses. The first of these is the point of interest in this paper. This is the dominant loss mechanism in REBCO conductors [12–14].

Hysteresis losses in superconductors can be predicted with different models considering superconducting behaviour. The most common ones are the critical state model [15] (CSM) and the eddy current model [16] (ECM). In the CSM, the $E(J)$ relation, where E is the electric field intensity and J is the current density, is sharp: any E will cause a J with a magnitude J_c in the direction of E . In the ECM, the $E(J)$ dependency is assumed to be smooth and it follows a power law. This has its weaknesses in some cases. If the applied magnetic fields or applied currents have low frequencies and the magnetic field does not fully penetrate the conductor, the electric field is hence small, the modelling tools utilizing the ECM tend to homogenize the current density distribution, and thus they possibly over-estimate the low-frequency loss [17]. CSM-based solvers are frequency-independent, which corresponds to most of our observations on hysteresis losses, especially for currents significantly below I_c [18, 19]. This is especially the case in magnet applications where a large fraction of the cables is exposed to low magnetic fields when compared to the cable determining the magnet's critical current. In [20], it was suggested that the frequency-dependent properties of hysteresis losses in HTS conductors may be better reflected by a generalized critical state model, which associates no loss with $J \ll J_c$, but exhibits a smooth, power-law type of E - J dependence near J_c . In simulations, we focus on two different models, namely Bean and Kim, representing the relation between J_c and B . In the Bean model [15] the $J_c(B)$ relation is not B -dependent, while in the Kim model [21, 22] J_c depends on the magnitude, and in the case of anisotropic REBCO-conductors, on the direction of B .

In this paper, the focus is on modelling the hysteresis losses related to charging and discharging the magnet. Here, we discuss ramping the current and the $B(J)$ nonlinearity in the aperture, where the beampipe of an actual accelerator resides. Our simulations consider the so-called Roebel-cable-based magnet prototype FM0 [23]. The hysteresis losses that occur in an accelerator magnet during a current ramp are computed, and additionally, the computation results of the magnetization and the magnetic field at the magnet's aperture during the AC cycle are presented. The current penetration into the superconductor determines the two characteristics we are interested in. These are computed based on the minimum magnetic energy variation (MMEV) principle for the CSM, which states that the current penetrates the superconductor so that the energy of the system related to the change in current between two adjacent time instants ignoring interaction with the pre-existing current is minimized, while the required constraints, such as the cables' net currents, are satisfied. It has also been shown that the minimum magnetic energy variation MMEV principle is equivalent to the minimum entropy production (MEMEP) [24, 25], the latter being

⁴ EuCARD-2 is an Integrating Activity Project for coordinated Research and Development on Particle Accelerators, co-funded by the European Commission under the FP7 Capacities Programme, home page: <http://eucard2.web.cern.ch/>

applicable to any $E(J)$ relation. In the simulations, the $E(J)$ relation for MMEV principle is the CSM.

The difference between classical electromagnetic (EM) modelling and superconductor modelling is in the $E(J)$ relation. The generalization of the $E(J)$ relation for both cases is the power law

$$E(J) = E_c \left(\frac{J}{J_c} \right)^n. \quad (1)$$

When $n = 1$ the material has linear resistivity, as e.g. copper has at a given temperature. Increasing the exponent n , we get closer to the discrete critical state model. The need for other solving methods arises because of the discontinuity of CSM, as it cannot be used directly with ECM considering the magnetoquasistatic Maxwell's theory. However, such simulations can be done with the MMEV principle.

The mathematical minimization problem consists of an objective function subject to linear or nonlinear equality or inequality constraints with variable boundaries. In MMEV, the objective function to be minimized is a quadratic functional of the N variables, which, defining the current density distribution in the discretized modelling domain, represents the variation of magnetic energy, subject to linear equality and nonlinear inequality constraints. These constraints correspond to the net current condition and the $J_c(B)$ relation of each variable. For this kind of large-scale nonlinear optimization problem, the interior point optimizer [26] (IPOPT) is a reasonable choice of solver. The simplicity in posing the problem using IPOPT's interface, as well as the effective algorithms behind the interface, make it an attractive option in various areas of nonlinear physics.

Roebel cables can be modelled using 2D cross-sectional methods. The reason for this is that the longitudinal segments of the strands are usually much longer than their crossing diagonal parts, and hence the component of J perpendicular to the average current flow is negligible [27, 28]. Later, 3D calculations and experiments confirmed this assumption, with a discrepancy only at low applied perpendicular magnetic fields [29]. This is largely due to the crossing strands which break the translation symmetry. At low applied magnetic fields, other effects may also become important, such as lateral nonhomogeneities [30] and eddy current loss [31].

Several authors have made their own modelling tools based on the MMEV principle to simulate hysteresis losses. The variational principle was first developed by Prigozhin [32, 33]. The first steps in developing MMEV-based modelling tools were made in the single rectangular modelling domain [34, 35] and later on, the use of these tools has been extended to the solving of AC losses in coils with multi-tape cables such as Roebel cables [36–40]. The AC loss in Roebel cables and coils made of them has been modelled in [28, 31, 41], although only for sinusoidal excitations, which are not applicable to accelerator magnet energization and de-energization. In [40], Zhang *et al* made MMEV-principle-based simulations with a constant $J_c(B)$ dependency, i.e. the Bean model, utilizing IPOPT. However, so far, MMEV-principle-based AC loss computations have not been made

utilizing IPOPT and the Kim model yet. Using the Kim model as an extension requires an important supplement, as each variable requires its own nonlinear inequality constraint. From a practical point of view this extension is very important as J_c depends notably on B . Furthermore, this approach has not been utilized to study $B(I)$ nonlinearity in the aperture of a Roebel-cable-based magnet.

Roebel cables with a power law $E(J)$ relation instead of the CSM have also been modelled using other methods. The finite element method with the H formulation has been applied to the 2D [28] and 3D [29] computations of Roebel cables and coils made of them (2D approximation) [31, 41]. Integral equations employing the T formulation of the eddy current problem have provided valuable results for quasi-3D shapes (surfaces with 3D bending) [42, 43], which present essentially the same results as fully 3D models. Promising calculations for Roebel cables have been made with an integral equation method utilizing a fast multipole extension implemented on graphical process units (GPUs) [44]. MEMEP has also been applied to Roebel solenoid coils with many turns in the 2D approximation [31].

Let us summarize the novel contributions of this paper. According to our knowledge, utilization of the MMEV-principle-based simulation tool in the hysteresis loss modelling of Roebel-cable-based accelerator magnets has not been documented prior to this work. Since such magnets are operated at low frequencies, the advantage of the MMEV approach with CSM stands out: tools utilizing the power-law-based ECM tend to over-estimate the low-frequency loss, as the power law associates E even with a very low J . Moreover, we utilize the powerful open-source optimization library IPOPT for performing the required minimization procedures to solve the losses in Roebel-cable-based multi-turn coils employing the Kim model. An advantage in using a combination of the IPOPT interface and the MMEV principle is the ability to solve large nonlinear problems in a reasonable time frame.

The article is structured as follows: in section 2 we summarize the numerical method, section 3 presents the simulation results, and in section 4 the conclusions are drawn.

2. Numerical method

This paper is restricted to the two-dimensional (2D) modelling domain, where the current and electric field are perpendicular to the modelling plane.

2.1. The variational formulation of the CSM

In this section, we outline the variational principle for solving the current density for a smooth $E(J)$ relation, and later we extend it to the CSM depicted in figure 1. The current density is found by minimizing this functional. Although the functional was already presented in [33], here we outline an alternative deduction based on [25].

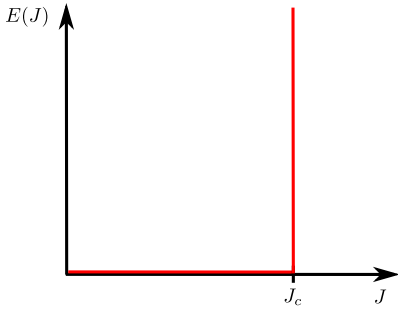


Figure 1. The $E(J)$ relation of the critical state model (CSM) is a highly nonlinear multi-valued function.

The basic partial differential equation (PDE) for the $A - \phi - J$ formulation in magnetoquasistatics is [45]

$$\text{curl}(\mu^{-1} \text{curl}(A)) = g \left(-\frac{\partial A}{\partial t} - \text{grad}(\varphi) \right), \quad (2)$$

where A and ϕ are the vector and scalar potentials, respectively, and g is defined by $J = g(E)$, being a nonlinear constitutive relation. The PDE above is the Euler equation of the functional below [25], and hence the PDE is followed for the A (or J) at the functional minimum. The functional is

$$\mathcal{F} = \int_{\Omega} L \, d\Omega, \quad (3)$$

where the functional density L , in the time discretized situation, is

$$L = \frac{1}{2} \frac{\Delta A_J}{\Delta t} \cdot \Delta J + \frac{\Delta A_a}{\Delta t} \cdot \Delta J + U(J_0 + \Delta J) + \text{grad}(\varphi) \cdot (J_0 + \Delta J) \quad (4)$$

with $U(J) = \int_0^J E(J') \cdot dJ'$. In (4), J_0 and J are the current densities at times $t = t_0$ and $t = t_0 + \Delta t$, respectively; ΔJ is $\Delta J = J - J_0$; $\frac{\Delta A_J}{\Delta t}$ is the average time derivative between $t = t_0$ and $t = t_0 + \Delta t$ of the vector potential generated by the current density in the sample, and $\frac{\Delta A_a}{\Delta t}$ is the same quantity but relative to the applied vector potential, created by currents outside Ω .

Although this reasoning assumes that the $E(J)$ relation is differentiable, we can also apply it to the CSM. The reason for this is that we can approximate the CSM by a continuous $E(J)$ relation such as $E(J) = E_c (J/J_c)^n$ with a constant E_c and n , the limit of $n \rightarrow \infty$ corresponding to the CSM. Since the deduction is valid for any n , however large, it will also be valid for the CSM. For the CSM, $U(J) = 0$ for $|J| \leq J_c$ and $U(J) \rightarrow \infty$ for $|J| > J_c$. The problem can then be solved by setting the $U(J)$ to zero and posing an additional constraint for the minimization procedures, i.e. $|J| \leq J_c$.

As shown in [25], the term with $\text{grad}(\varphi)$ for the translation of symmetric problems becomes $\int_{\Omega} \text{grad}(\phi) \cdot J \, d\Omega = \varphi I$, and hence any current distribution that transports a current I results in the same value of the functional density. Now, this term can be dropped from the functional density, as long as the current constraint is imposed separately, and so the

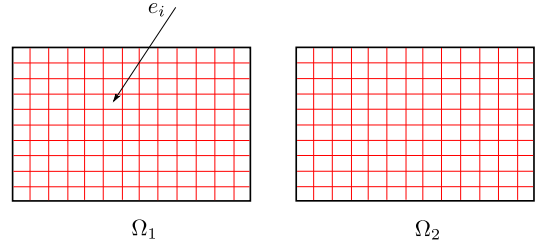


Figure 2. Each sub-domain Ω_s is meshed into the elements, such as e_i in the sketch above.

functional density

$$L' = \frac{1}{2} \Delta A_J \cdot \Delta J + \Delta A_a \cdot \Delta J \quad (5)$$

also minimizes the functional \mathcal{F} , where we multiplied the whole functional density by Δt . The functional \mathcal{F} , with L' , represents the magnetic energy of the current variation due to a change of applied net current and a change of applied magnetic field in domain Ω , ignoring the interaction with the pre-existing current density J_0 .

2.2. Discretization of the functional and constraints

The implementation of the discrete simulation tool was programmed using the Riemannian manifold interface [46] of Gmsh [47]⁵ in C++. With IPOPT [26]⁶, the tool solves the minimization problem: find such $J(I(t))$ that (3) is minimized, where the integrand is (5), and the constraints on $J_c(B)$ and the net current are satisfied.

The modelling domain is discretized using a mesh with rectangular elements. Each variable ΔJ_i in the vector ΔJ represents the change in the current density of the i th element. Thus, each element has a homogeneous current density. The functional \mathcal{F} and the constraints in discretized form are

$$F(\Delta J) = \frac{1}{2} \Delta J^T M \Delta J + C^T \Delta J \quad (6a)$$

$$\text{subjected to} \quad (6a)$$

$$(\mathcal{A}^i \Delta J)_s = \Delta I_s \quad (6b)$$

$$-(J_0 + \Delta J)_j + J_c(B)_j \geq 0 \quad (6c)$$

$$(J_0 + \Delta J)_j + J_c(B)_j \geq 0, \quad (6d)$$

where $F: \mathbb{R}^N \rightarrow \mathbb{R}$. In constraint (6b), by using Einstein's summation notation over the indices i , the \mathcal{A}^i is the area of the i th element. Element i belongs to the subdomain $\Omega_s \subset \Omega$, such that $\Omega_1 \cup \dots \cup \Omega_s \cup \dots \cup \Omega_m = \Omega$. m refers to the number of superconducting subdomains (see figure 2). Every Ω_s has its own net current constraint ΔI_s ; however, Ω_s can be unconnected. In addition, the number of equality constraints in this minimization problem is m . The constraints (6c) and (6d) constrain the total current density $(J_0 + \Delta J)$ in the

⁵ Gmsh is an open-source finite element mesh generator: <http://geuz.org/gmsh/>.

⁶ The interior point optimizer is an interior point filter line search algorithm for large-scale nonlinear programming: <https://projects.coin-or.org/Ipopt/>.

element j from below to $-J_c(B)$ and from above to $J_c(B)$ respectively. In other words, the number of inequality constraints, (6c) and (6d), in this minimization problem is $2 \times N$ in total, where N is the number of elements, i.e. the number of variables. The magnetic flux density B , in element i can be computed from J in all the elements with, for example, the Biot–Savart law [48].

In (5), the change of magnetic vector potential ΔA_j , due to the change of current density ΔJ , is calculated using

$$\Delta A_j(\mathbf{r}) = -\frac{\mu_0}{2\pi} \int_{\Omega} \Delta J(\mathbf{r}') \ln(\|\mathbf{r} - \mathbf{r}'\|) d\Omega', \quad (7)$$

which is valid in our approach utilizing translation symmetry. Then, the integral in (3) over the domain Ω is

$$W = \int_{\Omega} \Delta A_j(\mathbf{r}) \Delta J(\mathbf{r}) d\Omega. \quad (8)$$

In the discrete problem, the current density ΔJ is constant element-wise, and the coefficient matrix $M \in \mathbb{R}^{N \times N}$ in (6a) is

$$M_{ij} = -\frac{\mu_0}{2\pi} \int_{e_i} \int_{e_j} \ln(\|\mathbf{r} - \mathbf{r}'\|) d\mathbf{r}' d\mathbf{r}. \quad (9)$$

The matrix M represents the mutual inductances between the elements in the mesh of the modelling domain Ω .

The vector C in (6a) can be obtained from the integral of the second term in (5). Calculating the contribution of the external applied vector potential ΔA_a to each element, the vector C becomes

$$C_i = \int_{e_i} \Delta A_a(\mathbf{r}) d\mathbf{r}. \quad (10)$$

The computation of the coefficient matrices M and C for a mesh with rectangular elements is detailed in appendix A.

Now, the finite dimensionalization of the problem is complete and it can be posed for IPOPT to be minimized.

2.3. Computation of current distribution

The computation of the current distribution in the modelling domain Ω is done by interacting with IPOPT's interface. At each time step of a current ramp we compute the change in the current distribution, ΔJ in Ω , by solving the minimization problem (6). The applied transport current is ramped from zero to a certain amplitude I , and back down to zero to close one AC cycle. The ramping of a cycle repeats the desired number of cycles until the steady state loss over a cycle is reached. The amplitude of the transport current is divided into current steps ΔI such that during a time step Δt , the applied transport current changes by a current step ΔI . The current distributions at each time step are saved for post-processing purposes.

2.4. $J_c(B)$ dependency

For cuprate superconductors, such as REBCO, the critical current density depends not only on the magnitude but also strongly on the direction of the magnetic field. If the magnetic field is parallel to the c crystallographic direction (usually

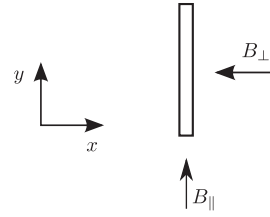


Figure 3. The parallel and perpendicular magnetic flux density components with respect to the wide face of a superconducting tape, when the wide face of the surface is parallel to the y -axis.

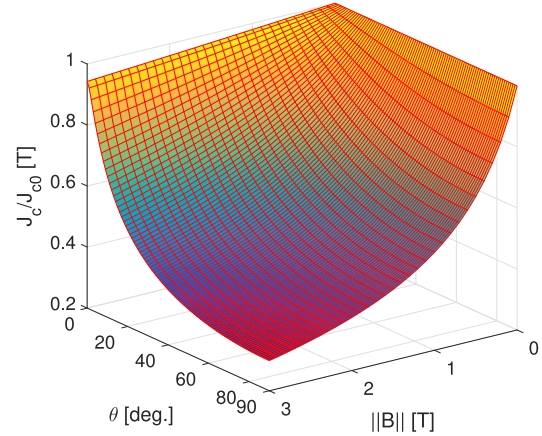


Figure 4. The J_{c0} normalized J_c is shown as a function of the magnitude of B ($\|B\|$) and its direction (θ) with respect to the wide face of the tape, where 90 degrees corresponds to the fully perpendicular direction. The values, used in the plot and in the further simulations, for the parameters of the relation (11) are: $J_{c0} = 2.787 \cdot 10^{11}$ A m $^{-2}$, $k = 0.019$, $B_0 = 0.65$ and $\beta = 0.7$.

perpendicular to the wide face of the tape) the effect on the J_c of the tape is particularly significant.

In the simulations, we use the elliptical anisotropic magnetic field dependence for the element-wise constant J_c :

$$J_c(B_{\parallel}, B_{\perp}) = \frac{J_{c0}}{\left(1 + \frac{\sqrt{k^2 B_{\parallel}^2 + B_{\perp}^2}}{B_0}\right)^{\beta}}, \quad (11)$$

where J_{c0} , k , B_0 and β are constants characterizing the magnetic field dependence of the superconducting tape, and the magnetic flux density is locally divided into two components, such that $B = [B_{\parallel} \ B_{\perp}]^T$ [49]. With these parameters, the relation can be fit to the approximate measurements of a superconducting sample. This relation has been used by Šouc *et al* in [39]. Following the notations of Šouc *et al*, B_{\parallel} and B_{\perp} are the magnetic flux density components parallel and perpendicular with respect to the wide face of the tape, respectively, at the element's centre of mass (see figure 3). In this paper we use $k = 0.019$, $B_0 = 0.65$, $\beta = 0.7$ and $J_{c0} = 2.787e11$ for the Kim model. The parameters are chosen such that the Kim model fits the measured data of the actual

cable that the modelled magnet is made of [44]. The dependency on the chosen parameters is presented in figure 4. Moreover, in the simulations we assume that for the thickness of the superconducting tape, the superconducting properties do not vary.

For later use, we define the parallel and perpendicular magnetic flux density in an element of the modelling domain. First, we define the integration matrices $B_x, B_y \in \mathbb{R}^{N \times N}$ to calculate the magnetic field components in one element. These matrices are calculated before any optimization routines, because they depend only on the geometry and the mesh of the modelling domain. Moreover, N is the number of elements in the modelling domain $\Omega \subset \mathbb{R}^2$, which consists of the superconducting tapes only.

The calculation of the integration matrices B_x and B_y , is done by utilizing the two-dimensional Biot-Savart law for infinitely long bodies

$$B(\mathbf{r}) = \frac{\mu_0}{2\pi} \begin{bmatrix} 0 & -1 \\ 1 & 0 \end{bmatrix} \int_{\Omega} \frac{J(\mathbf{r}')(\mathbf{r} - \mathbf{r}')}{\|\mathbf{r} - \mathbf{r}'\|^2} d\mathbf{r}', \quad (12)$$

where $B(\mathbf{r})$ is a vector having the components of B at \mathbf{r} . In element-wise form we get the matrices B_x and B_y , corresponding to the unit current density in each element as

$$\begin{bmatrix} B_x^{ij} \\ B_y^{ij} \end{bmatrix} = \frac{\mu_0}{2\pi} \begin{bmatrix} 0 & -1 \\ 1 & 0 \end{bmatrix} \int_{e_j} \frac{\mathbf{r}_i - \mathbf{r}_j}{\|\mathbf{r}_i - \mathbf{r}_j\|^2} d\mathbf{r}_j, \quad (13)$$

where the integration is over the element e_j . The symbol \mathbf{r}_i denotes the centre of mass at $e_i \subset \Omega$, and the operator $\|\cdot\|$ is the Euclidean norm in \mathbb{R}^2 . Thus, B_x^i refers to the x -component of B in the element i generated by the current in element j .

Assuming that the tapes lie in the xy -plane, such that the wide face of the tape is parallel with respect to the y -axis (see figure 3), then the parallel magnetic field in element i is

$$B_{\parallel}^i = B_y^{ij} J_j, \quad (14)$$

where J_j is the constant current density in element j , i.e. B_{\parallel}^i is a sum over indices $j = 1 \dots N$. Similarly, following Einstein's summation notation, the perpendicular magnetic field component in element i , with respect to the wide face of the tape, is

$$B_{\perp}^i = B_x^{ij} J_j. \quad (15)$$

The matrices B_x and B_y can be computed before the minimization procedures, thus the computation of the local magnetic flux density components during the iterations in the minimization is fast. The analytic formulas for B_x and B_y are presented in appendix A.

2.5. AC loss computation

The desired quantity to be computed is the current distribution at each discretized instant of time in intervals Δt . From the current distribution, the AC losses and magnetization in the magnet's bore are solved in the post-processing. The computation of the current distribution is done by interacting with the IPOPT. The details about posing the minimization problem for the IPOPT are presented in appendix B.

When the current distribution is computed for each time step, the loss at time t in the superconductor is computed with

$$P(t) = \int_{\Omega} J(\mathbf{r}; t) E(\mathbf{r}; t) d\mathbf{r}, \quad (16)$$

where $E = -\partial_t A - \text{grad}(\varphi)$, and $\text{grad}(\varphi) = -\partial_t A_c$; A_c being the magnetic vector potential in the sub-critical region of Ω . In the absence of a sub-critical region, like for saturation with magnetization currents, A_c can be taken at the border between $J = +J_c$ and $J = -J_c$. Note that E is considered to be caused by the time derivative of A , not directly from J and the $E(J)$ relation. Moreover, $\partial_t A_c$ is constant in Ω [34].

Numerically differentiating (16) at time $t = t_i + \Delta t/2$, it becomes

$$P\left(t_i + \frac{\Delta t}{2}\right) = \int_{\Omega} \frac{J(\mathbf{r}; t_i + \Delta t) + J(\mathbf{r}; t_i)}{2} \times \left(\frac{A_c(\mathbf{r}; t_i + \Delta t) - A_c(\mathbf{r}; t_i)}{\Delta t} - \frac{A(\mathbf{r}; t_i + \Delta t) - A(\mathbf{r}; t_i)}{\Delta t} \right) d\mathbf{r} \quad (17)$$

where t_i is the time at time step i . The hysteresis loss Q over one cycle per unit length from t_1 to t_2 is obtained by the integration

$$Q = \int_{t_1}^{t_2} P(t) dt. \quad (18)$$

The integral of $P(t)$ can be computed utilizing a numerical integration method. We have used the trapezoid rule.

2.6. Magnetization

Magnetization, the magnetic distortion in the magnet's bore, describes the nonlinear behaviour of the produced magnetic field. We define the magnetization current $J_M(I(t))$ as the difference between the current density distribution $J(I(t))$, obtained as the solution of the minimization problem (6), and the homogeneous current density distribution $J_H(I(t))$ in which the applied net current is evenly spread into Ω . Here, $I(t)$ is the applied current at time t . Consequently, the magnetization current density in element i , is $J_{Mi}(I(t)) = J_i(I(t)) - J_{Hi}(I(t))$. Now, using (12), the magnetic flux density produced by the magnetization currents is computed at the magnet's bore over one AC cycle as a function of the transport current per cable [25].

3. Results and discussion

This section is divided into four subsections: convergence analysis, current distributions, hysteresis losses in the FM0, and magnetization of the FM0. The aim is to analyze the behaviour of the Roebel-cable-based magnet under AC conditions, i.e. ramping the applied current between zero and the amplitude. The utilized simulation tool is benchmarked against an analytical solution to validate the predictions. Moreover, by solving the current distribution with the presented simulation tool at each time step during six cycles of

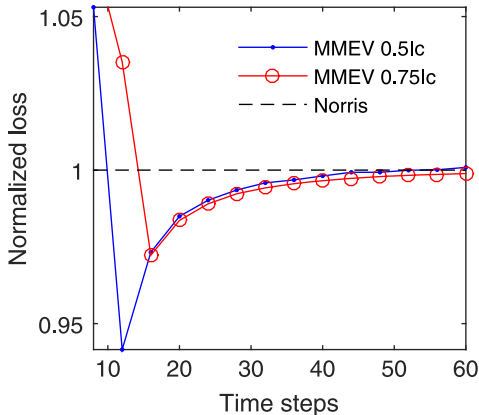


Figure 5. The Norris normalized hysteresis losses computed with the MMEV principle, utilizing the CSM with the Bean model. The time step (per cycle) convergence comparison between two different amplitudes of transport current.

applied transport current, computation of the hysteresis losses and magnetization loops was done as a post-process procedure.

3.1. Convergence analysis

Convergence analysis was done to validate the predictions of the developed simulation tool. This validation is a benchmark with an analytical solution of a superconductor obeying CSM with the Bean model, not with an actual conductor. The analysis was done for a single thin superconducting tape in the case of the applied transport current and constant $J_c(B)$ dependency, i.e. with the Bean model. The analysis was performed as a function of elements in the mesh and as a function of time steps in one AC cycle. In the tape, the elements were in one layer. We benchmark the computation results against the analytical solution of hysteresis losses for a one-dimensional superconducting strip obeying the CSM and Bean model [50]. The dimensions of the tape were $4 \text{ mm} \times 1 \mu\text{m}$ and the critical current density J_c was $2.5 \cdot 10^{11} \text{ A m}^{-2}$ resulting in a critical current I_c of 1000 A, which is of the order of magnitude of the measurements at 4.2 K and a 1 T perpendicular applied flux density [51].

In simulations, sinusoidal transport current was applied to the superconducting tape. The number of time steps per cycle was chosen according to the time step convergence computations, presented in figure 5, such that the losses converged to within 1.2% from the analytic solution, i.e. 24. One should note that here we have a finite thickness of $1 \mu\text{m}$ for the strip since the tool is built for analyzing 2D domains.

The convergence for amplitudes $0.5I_c$ and $0.75I_c$ as a function of the number of time steps in one cycle for a tape of 400 elements is presented in figure 5. The loss convergence for the applied current with an amplitude I_a of $0.5I_c$, with 24 time steps per cycle, as a function of the number of elements

in the tape is presented in figure 6, and for reference compared with the results given by the ECM-based tool detailed in [52]. The power law exponent in the ECM-based computations was 30. The same convergence for an applied current amplitude of $0.75I_c$ is shown in figure 7.

From these analyses one can conclude the valid implementation of the developed tool.

3.2. Current distributions

The modelling domain is presented in figure 8, representing half of the cross-section on the straight side of the investigated magnet, FM0 [9]. The cross-section of the magnet is symmetrical with respect to the y -axis⁷. A 3D depiction of the magnet is illustrated in figure 9. The magnet consists of five turns of Roebel cable, each cable consisting of 15 superconducting tapes. The dimensions of the superconducting layer in each tape are $1 \mu\text{m} \times 5.5 \text{ mm}$. The layers in the tape with zero or negligible conductance, resulting in negligible current density, are not modelled as they do not contribute to (5). The dimensions of one cable are $12 \text{ mm} \times 1 \text{ mm}$.

In a superconducting magnet, the turns are electrically insulated and in series. The tapes in a single turn, i.e. in a Roebel cable, are galvanically connected and their locations are transposed along the cable [53]. However, because an assembled Roebel cable consists of multiple tapes with a layered structure of materials other than the superconductor, it is not straightforward to say for a given cable how the current is shared between the tapes in the cable. Therefore, there are two ways to determine the net currents in 2D. The first way is to force the same current through each tape (CC/tape). This means that there is no current diffusion between the tapes and the transposition balances the effects of magnetic field on the cable at different locations. The second way is to force a current through an entire cable (CC/cable). Therefore, it is distributed by the solver in an optimal way between the tapes. The actual situation is something between these two, depending essentially on the homogeneity of the tapes and contact resistances between them. An approach for solving these intermediate situations in 2D for two and three round superconducting domains was presented in [54].

The nominal transport current of the FM0 magnet is 6000 A at 4.2 K [9] and the critical current I_c of the coil is 11.5 kA. The I_c of the coil was determined by increasing the transport current up to the point where one of the cables was fully saturated (see figure 10(a)). This was computed by setting the current constraints equal to each cable and using the $J_c(B)$ relation (11), i.e. the Kim model. By knowing the critical current of the magnet we determined the critical current density J_c for the Bean model to be: $1.3939 \cdot 10^{11} \text{ A m}^{-2}$.

In the AC loss simulations, the coil was charged and discharged, as shown in figure 11. The current distributions at times (a)–(f) (see figure 11), computed utilizing the MMEV

⁷ This manifests itself in the calculation of the coefficient matrices: the currents flowing in the other direction on the other side of the cross-section need to be taken into account as well.

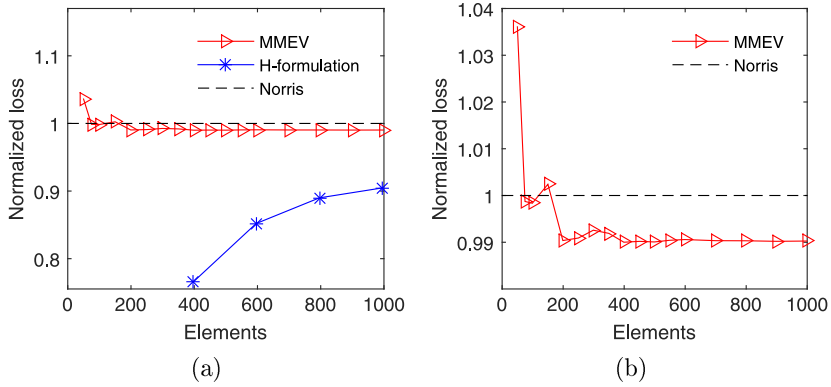


Figure 6. The Norris normalized hysteresis losses computed with the MMEV principle, utilizing the CSM with the Bean model, and an *H* formulation, utilizing the power law with an exponent of 30. The MMEV computations use 24 time steps per sine cycle. The horizontal axis describes the number of elements in the superconducting region. For comparison, in (a), four points are computed utilizing the *H* formulation; (b) is a close-up of the losses computed using MMEV; $I_a = 0.5I_c$.

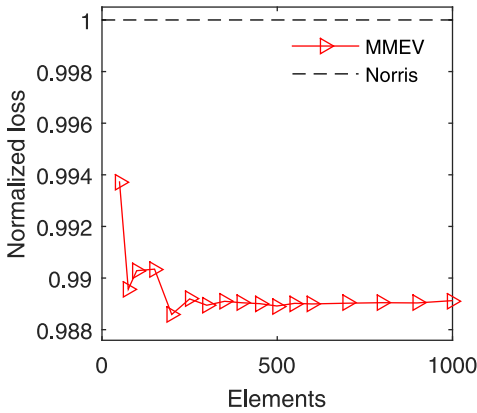


Figure 7. The Norris normalized hysteresis losses computed with the MMEV principle, utilizing the CSM with the Bean model; $I_a = 0.75I_c$. The number of time steps per cycle is 24.

principle with the Bean model are shown in figure 12. The upper row presents the distributions, where the current condition is given for each tape. The lower row presents the results, where the current condition is for each cable. The difference between the distributions simulated with different current conditions is significant. Therefore, for reliable modelling of the aperture field, it is important to know via experiments how a cable behaves in a magnet. Now, consider distribution (c), which is the current distribution at the amplitude of the applied transport current. In the case of CC/cable, negative current has to penetrate fully into some of the tapes in order to satisfy the current condition set for each cable. From the physical point of view, the negative and the positive current density regions are produced by the magnetic field parallel to the cable’s long face. The innermost cable (the one on the left-hand side) is in a high parallel

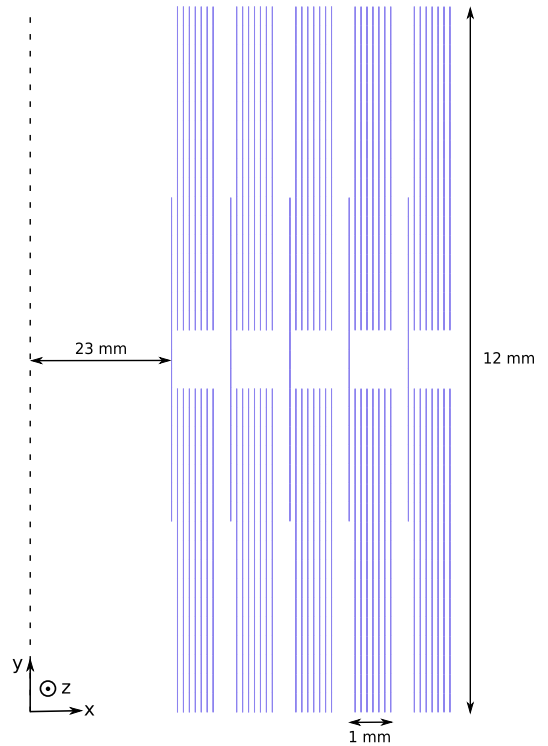


Figure 8. Half of the magnet’s cross-section, where the lines represent the superconducting tapes. The dashed line represents the symmetry axis, and the orientation of the modelling domain is fixed; the figure is not to scale.

magnetic field (see figure 10(c)), thus screening currents appear in order to cancel the changing magnetic field produced by currents in the other cables. In addition, the use of the CSM can be seen from the distributions very

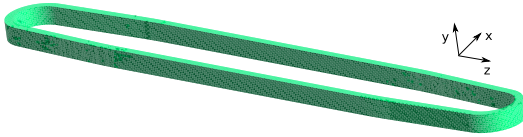


Figure 9. The modelled FM0 magnet is a racetrack coil with flat sides. Therefore, the model utilized here gives an approximation of the losses and magnetization for the flat sides neglecting the end effects.

clearly: the current density drops to zero at the front of the penetrated regions.

The current distributions computed with the Kim model, at the same instants of time as with the Bean model, are presented in figure 13. As can be seen from figure 10(c), the magnetic field is high and perpendicular with respect to the orientation of the tapes at the top and bottom of the modelling domain. This reduces the current density locally, which can be seen well from figure 13(c).

3.3. Hysteresis losses in FM0

The hysteresis losses in the magnet were also computed utilizing both the Bean and Kim models. A transport current ramp of amplitude 6 kA with a frequency of 0.2 Hz was applied to the magnet (see figure 11). However, the frequency does not play a role in the loss integrated over a cycle. Simulations were performed with both current conditions: the CC/tape and CC/cable.

The results computed for both current conditions utilizing the Bean model are presented in figure 14. It can be seen that the simulated losses in the case of CC/tape are smaller. The occasional non-smoothness in the curves is caused by the discretization of the cross-section, although its impact on the loss per cycle is negligible (see figures 6 and 7). The results performed with the Kim model are presented in figure 15. These simulations show very similar loss generation to the simulations utilizing the Bean model. A comparison between the different cases is shown in figure 16.

In addition, hysteresis losses over the sixth cycle in different simulation cases are presented in table 1. The smallest loss generation was obtained with the Kim model and setting the current with the CC/tape constraints. The largest amount of loss generation was simulated when we considered the Bean model and set the net current constraints for each cable. The Kim model causes lower loss because some turns present higher J_c than the average in the I_c limiting turn, which determines J_c for the Bean model. For both the Bean and Kim models, the losses considering CC/cable are higher than those with CC/tape because the CC/cable case presents the magnetization currents which are due to the parallel magnetic field.

Next, we make a few remarks and comparisons on a similar study that has been done by Xia *et al* [55]. They computed the hysteresis losses for REBCO pancake coil using the H formulation. Unlike our study, their simulations predict a dependence on the transport current ramp rate for the

hysteresis loss over the cycle. This is due to the utilization of the power-law-based ECM, which leads to noticeable frequency dependence, especially at relatively low frequencies. The advantage of using the MMEV principle with the CSM is that it predicts low-frequency losses in a way that better reflects our observations on hysteresis losses, i.e. independent of time over the cycle [18, 19].

3.4. Magnetization of the FM0

In this section, the nonlinearity of the generated magnetic field in the magnet's bore is investigated as a function of the applied transport current. Magnetization loops are computed as a post-process procedure from the current distributions of all four simulation cases: Kim CC/cable, Kim CC/tape, Bean CC/cable and Bean CC/tape. The loops in all four cases are presented in figures 17(a) and (b) as a function of the net current in one cable over the sixth AC cycle.

In figure 17(a), all the loops are presented. Considering that both loops present magnetic distortion in the cases of CC/tape, namely 'Kim, CC/tape' and 'Bean, CC/tape', the magnetic distortion is significant. The maximum values in these loops are 3.23 mT and 2.89 mT in the Kim and Bean cases respectively (see table 2). In both loops, the initial curve, corresponding to the positive ramp of the transport current, increases up to its peak. During the descending current ramp, the magnetic distortion in the bore decreases back to its minimum, with smaller amounts of distortion than during the positive current ramp, and closes the loop.

In figure 17(b), the loops present the simulation cases in which the current conditions were given per cable. These loops show less distortion in the bore's magnetic field during the cycle than in the CC/tape computations. The magnetic distortion with CC/cable is lower because the magnetization currents due to the parallel flux density contribute to the opposite sign of those caused by the perpendicular flux density, partially cancelling each other out. The effects of parallel and perpendicular magnetic flux in a cable are illustrated in figure 18. The maximum magnetic distortion in the Kim and Bean cases at 6000 A were 1.71 mT and 1.92 mT, respectively (see table 2).

The differences in AC losses and magnetic distortion between the different coupling scenarios are large, and experiments are required to learn about the actual behaviour of the cable. The level of magnetization is important because dipoles in accelerators are operated at different currents, at low particle energies, and at full collision energy. The more distortion from the linear behaviour there is, the more corrector magnets are required. From the loss point of view, it is beneficial if the tapes have equal currents, but in accelerators less magnetization is preferred [56].

4. Conclusions

A very important application area of superconductivity is in producing the magnetic fields required in accelerator

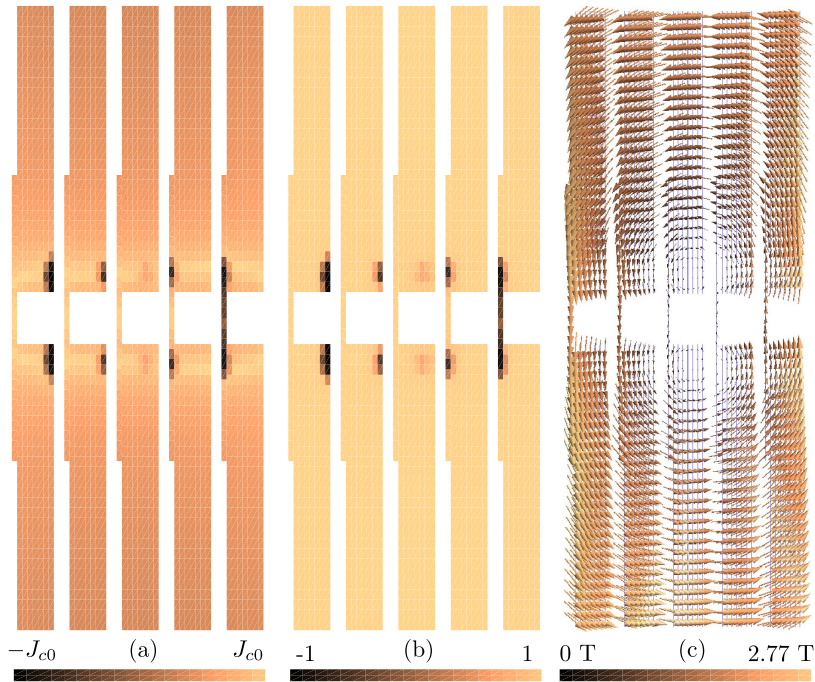


Figure 10. The coil I_c determination with the Kim model. Figures (a)–(c) present the state of the system just before saturation. (a) Current distribution, (b) element-wise J/J_c distribution, (c) magnetic field B .

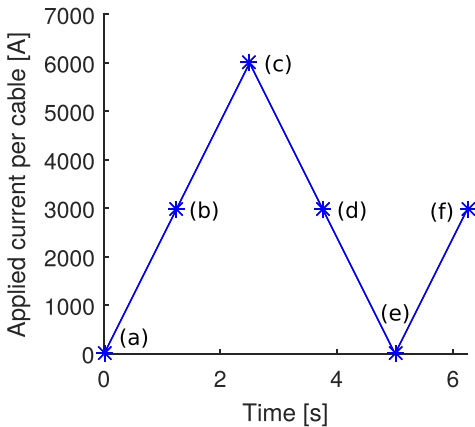


Figure 11. The coil is submitted to subsequent ramp charges and discharges.

complexes such as the LHC in CERN. One promising successor for existing accelerator magnets is based on Roebel cables, which consist of HTS conductors. In designing these magnets, modelling the generated losses and the nonlinearity of the generated magnetic field in the magnet’s aperture is of utmost importance. In addition, by predicting the generated losses and the $B(I)$ nonlinearity in the magnet’s aperture, one

can conclude whether a design can be protected reasonably, and if it has adequate field quality or not.

In this paper, an MMEV-principle-based simulation tool was presented and benchmarked against the analytical Norris formula for a single tape with the Bean model. Then, a Roebel-cable-based accelerator magnet research and development prototype was simulated with our MMEV-principle-based simulation tool made in-house, utilizing IPOPT for the minimization procedures with the Kim and Bean models. Losses under triangular transport current ramps of 6 kA amplitude and 0.2 Hz were simulated for six cycles. The current distributions in the magnet were computed at each discretized instant of time. From the current distributions, the hysteresis losses in the magnet and magnetic field distortion in the magnet’s bore were computed as a post-process procedure.

The shapes of the loss curves differed from each other in the case of the different current conditions and models. The modelled losses computed with the Bean model were greater than the losses computed with the Kim model. The distortion in the magnetic field in the magnet’s bore was greater when the transport current conditions were given for each tape, compared to the case where the conditions were given per cable. The differences between the different modelling cases are large in magnetic distortion, and experiments are required to study the actual behaviour of the magnets and the appropriateness of our approach for the whole coil.

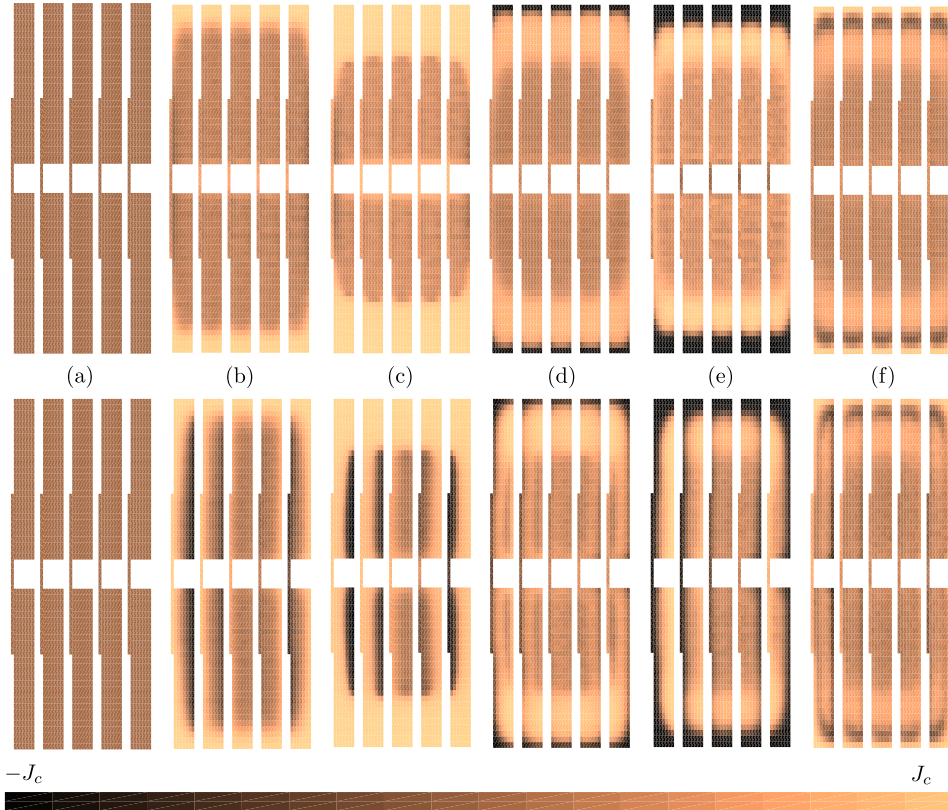


Figure 12. The current distributions of points marked in figure 11 of the first cycle computed using the Bean model. The first row of figures presents the current distributions in the case where the current conditions were set per tape, while the second row of figures presents the current distributions where the current conditions were set per cable.

Acknowledgments

This research was supported in part by the Academy of Finland projects #250652 and #287027 and in part by EuCARD-2, which is co-funded by the partners and the European Commission under the Capacities Seventh Framework Programme, under Grant 312453.

Appendix A. Computation of coefficient matrices

Computation of the inductance matrix M , of (6), can be done utilizing the analytical formulae integrated from (9), as follows:

$$\begin{aligned}
 M_{ij} &= -\frac{\mu_0}{2\pi} \int_{e_i} \int_{e_j} \ln(\|\mathbf{r} - \mathbf{r}'\|) d\mathbf{r}' d\mathbf{r} \\
 &= -\frac{\mu_0}{4\pi} \int_{e_i} \int_{e_j} \ln[(x - x')^2 + (y - y')^2] dS' dS.
 \end{aligned}$$

Performing the integrations, we obtain

$$\begin{aligned}
 M_{ij} &= -\frac{\mu_0}{2\pi} [g(x_j - x_i + t_j, y_j - y_i + d_j; t_i, d_i) \\
 &\quad - g(x_j - x_i + t_j, y_j - y_i - d_j; t_i, d_i) \\
 &\quad - g(x_j - x_i - t_j, y_j - y_i + d_j; t_i, d_i) \\
 &\quad + g(x_j - x_i - t_j, y_j - y_i - d_j; t_i, d_i)], \quad (\text{A.1})
 \end{aligned}$$

where

$$\begin{aligned}
 g(u, v; t', d') &= F(u - t', v - d') \\
 &\quad - F(u - t', v + d'), -F(u + t', v - d') \\
 &\quad + F(u + t', v + d') \quad (\text{A.2})
 \end{aligned}$$

and

$$\begin{aligned}
 F(u', v') &= -\frac{25}{48} u'^2 v'^2 \\
 &\quad - \frac{1}{48} (v'^4 + u'^4 - 6u'^2 v'^2) \ln(u'^2 + v'^2) \\
 &\quad + \frac{u'^3 v'}{6} \arctan\left(\frac{v'}{u'}\right) + \frac{u' v'^3}{6} \arctan\left(\frac{u'}{v'}\right). \quad (\text{A.3})
 \end{aligned}$$

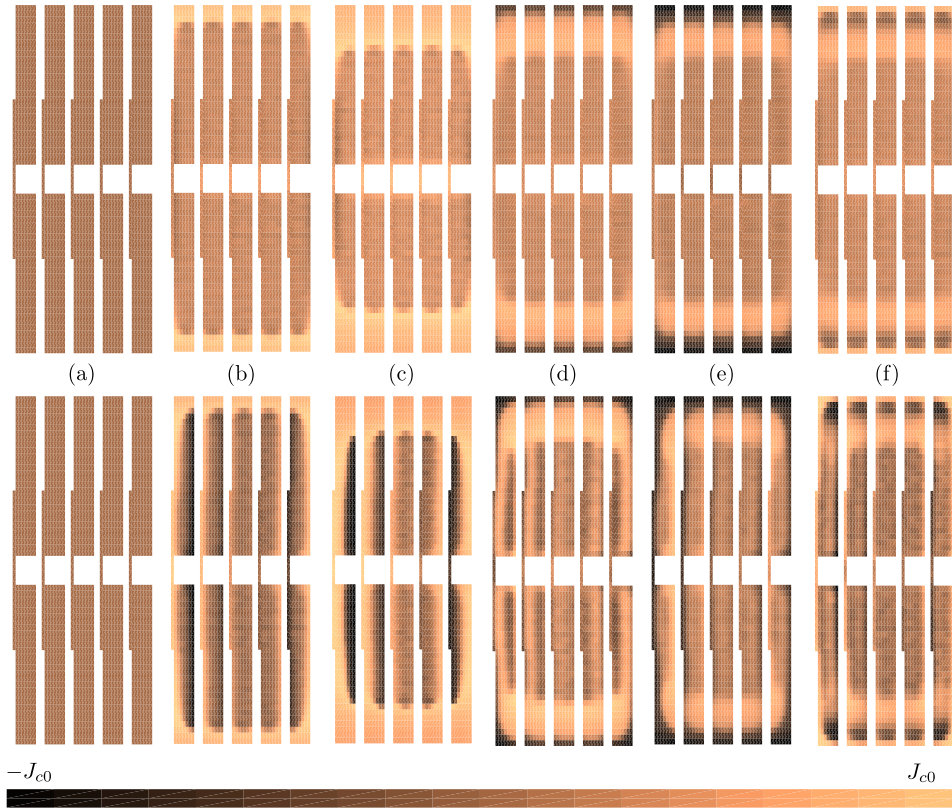


Figure 13. The current distributions of points marked in figure 11 of the first cycle computed using the Kim model. The first row of figures presents the current distributions in the case where the current conditions were set per tape, while the second row of figures presents the current distributions where the current conditions were set per cable.

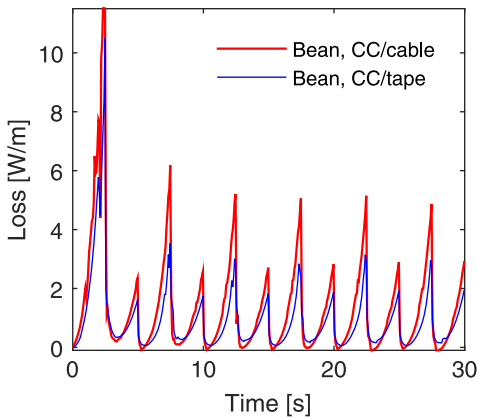


Figure 14. The loss curves of the magnet during six ramps. The thicker line presents the case where the current condition is per cable, and the thin line presents the loss in the case of current condition per tape. Both curves were computed utilizing the Bean model.

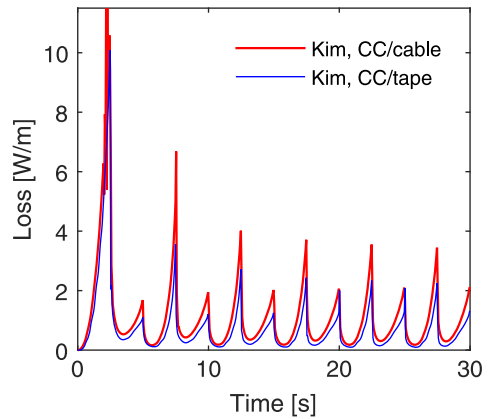


Figure 15. The loss curve of the magnet during six ramps. The thicker line presents the case in which the current condition is given for each cable, and the thin line presents the loss in the case of current condition per tape. Both curves were computed utilizing the Kim model, i.e. the nonconstant $J_c(B)$ relation.

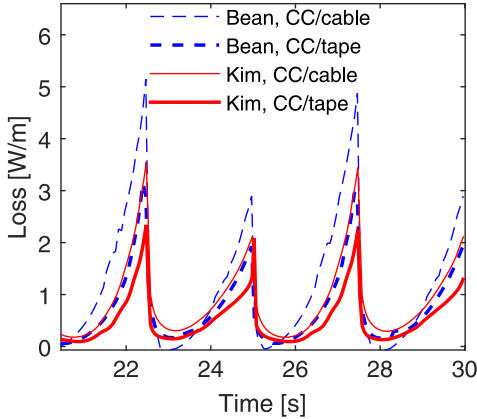


Figure 16. A close up of the two last cycles of all the computed loss curves.

Table 1. Hysteresis losses in the modelling domain over the sixth cycle of the transport current ramp in different simulation cases.

Model	CC	Loss/cycle [J m ⁻¹]
Bean	cable	5.38
Bean	tape	3.52
Kim	cable	4.33
Kim	tape	2.47

In (A.1), (x_i, y_i) and (x_j, y_j) are the central coordinates of elements i and j , respectively. Their dimensions are $2t_i \times 2d_i$ and $2t_j \times 2d_j$, where $2t$ is the width and $2d$ the thickness of the element. The above formula for M_{ij} is related to the coefficients C_{ij} presented in [57] by $M_{ij} = \mathcal{A}_i \mathcal{A}_j C_{ij}$, since in [57], the functional to be minimized is presented in terms of ΔJ instead of ΔJ , as is done here.

The analytic formulae for calculating the matrices B_x and B_y in (13) are obtained by direct integration. Thus,

$$\begin{aligned}
 B_x^{ij} &= -\frac{\mu_0}{2\pi} \int_{x_{j0}}^{x_{j1}} \int_{y_{j0}}^{y_{j1}} \frac{y_{ic} - y_j}{\|\mathbf{r}_i - \mathbf{r}_j\|^2} dy_j dx_j \\
 &= -\frac{\mu_0}{2\pi} [\alpha(x_{ic} - x_{j0}, y_{ic} - y_{j0}) \\
 &\quad - \alpha(x_{ic} - x_{j0}, y_{ic} - y_{j1}) \\
 &\quad - \alpha(x_{ic} - x_{j1}, y_{ic} - y_{j0}) \\
 &\quad + \alpha(x_{ic} - x_{j1}, y_{ic} - y_{j1})]
 \end{aligned} \quad (\text{A.4})$$

and

$$\begin{aligned}
 B_y^{ij} &= \frac{\mu_0}{2\pi} \int_{x_{j0}}^{x_{j1}} \int_{y_{j0}}^{y_{j1}} \frac{x_{ic} - x_j}{\|\mathbf{r}_i - \mathbf{r}_j\|^2} dx_j dy_j \\
 &= \frac{\mu_0}{2\pi} [\alpha(y_{ic} - y_{j0}, x_{ic} - x_{j0}) \\
 &\quad - \alpha(y_{ic} - y_{j0}, x_{ic} - x_{j1}) \\
 &\quad - \alpha(y_{ic} - y_{j1}, x_{ic} - x_{j0}) \\
 &\quad + \alpha(y_{ic} - y_{j1}, x_{ic} - x_{j1})],
 \end{aligned} \quad (\text{A.5})$$

where

$$\alpha(a_0, a_1) = \frac{1}{2} a_0 \ln(a_1^2 + a_0^2) + \arctan\left(\frac{a_0}{a_1}\right) a_1, \quad (\text{A.6})$$

and where $x_{j0} = x_{jc} - t_j$, $x_{j1} = x_{jc} + t_j$, $y_{j0} = y_{jc} - d_j$, and $y_{j1} = y_{jc} + d_j$; (x_{jc}, y_{jc}) are the central coordinates of element j . Similarly, (x_{ic}, y_{ic}) are the central coordinates of element i .

A_{ij} , in (17) can be obtained by integration as follows.

$$\begin{aligned}
 A_{ij} &= -\frac{\mu_0}{4\pi} \int_{y_{j0}}^{y_{j1}} \int_{x_{j0}}^{x_{j1}} \ln[(x_{ic} - x_j)^2 + (y_{ic} - y_j)^2] dy_j dx_j \\
 &= -\frac{\mu_0}{4\pi} [f(x_{ic} - x_{j1}, y_{ic} - y_{j1}) \\
 &\quad - f(x_{ic} - x_{j1}, y_{ic} - y_{j0}) \\
 &\quad - f(x_{ic} - x_{j0}, y_{ic} - y_{j1}) \\
 &\quad + f(x_{ic} - x_{j0}, y_{ic} - y_{j0})],
 \end{aligned} \quad (\text{A.7})$$

where

$$\begin{aligned}
 f(u, v) &= -3uv + uv \ln(u^2 + v^2) + u^2 \arctan\left(\frac{v}{u}\right) \\
 &\quad + v^2 \arctan\left(\frac{u}{v}\right)
 \end{aligned}$$

and where $x_{j0} = x_{jc} - t_j$, $x_{j1} = x_{jc} + t_j$, $y_{j0} = y_{jc} - d_j$, and $y_{j1} = y_{jc} + d_j$; (x_{ic}, y_{ic}) are the central coordinates of element i .

Appendix B. IPOPT's interface

IPOPT is an open-source software package for large-scale nonlinear optimization. A tutorial for downloading, installing, and using IPOPT can be found from [58]. IPOPT is made for solving general nonlinear programming problems of the form

$$\min_{x \in \mathbb{R}^N} f(x) \quad (\text{B.1a})$$

$$\text{s.t. } g^L \leq g(x) \leq g^U \quad (\text{B.1b})$$

$$x^L \leq x \leq x^U, \quad (\text{B.1c})$$

where x are the optimization variables with lower and upper bounds x^L and x^U respectively, $f: \mathbb{R}^N \rightarrow \mathbb{R}$ is the objective function and $g: \mathbb{R}^N \rightarrow \mathbb{R}^M$ are the general nonlinear constraints. [58] In the case of an equality constraint, the lower and upper bound are set to be the same. The constraints $g(x)$, with the lower and upper bounds g^L and g^U , should be twice continuously differentiable. The mathematical background of IPOPT is described in several publications, such as [26, 59–61]. In short, IPOPT is based on an interior point line search filter method.

Let us consider how to pose the minimization problem (6) for IPOPT's interface. The information required for IPOPT is listed in [58] on page 26. Starting from the problem dimensions, the number of variables is N , and the number of constraints is the number of equality constraints (6b) plus the number of inequality constraints (6c) and (6d), making it in total $m + 2 \times N$ constraints.

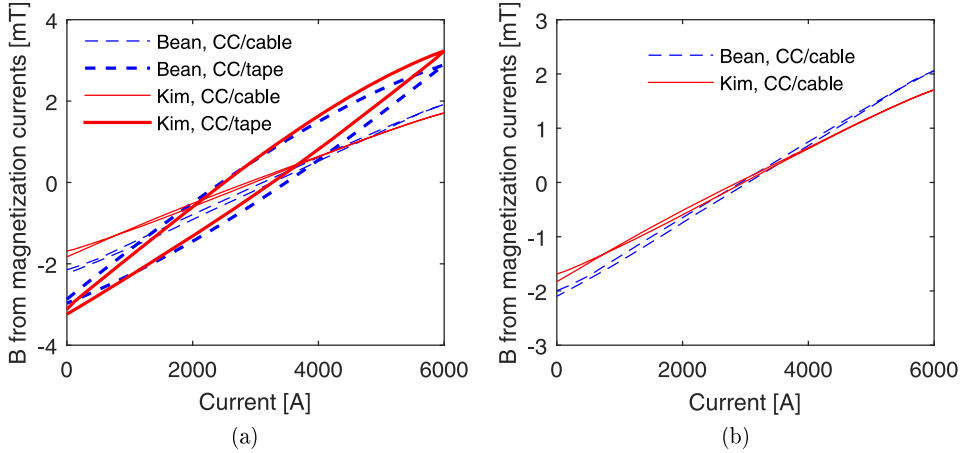


Figure 17. In (a) all the magnetization loops are presented; (b) is a close-up of the loops, where the current condition is per cable.

Table 2. The largest magnetization was obtained in the CC/tape cases and the smallest in the CC/cable cases. The ‘Max distortion’ data presents the maximum difference from the linear $B(I)$ field at a certain current.

Model	CC/	Max distortion [mT]
Bean	cable	1.92 (6 kA)
Bean	tape	2.89 (6 kA)
Kim	cable	1.71 (6 kA)
Kim	tape	3.23 (6 kA)

The problem bounds are given for both the variables and for the constraints. As in (6c) and (6d), the lower bounds g_i^L are zero. The upper bounds g_i^U are $2 \times J_{c0}$, where J_{c0} is the zero-magnetic field current density in the superconductor. After the problem bounds are set, the initial starting point needs to be given. We found 0.01 to be a good guess. One can also use the ΔJ solution from the previous time step.

The problem structure defines the sparsity of the derivative matrices of the constraints for IPOPT. The number of nonzeros in the Jacobian of the constraints depends on the $J_c(B)$ relation. In our simulations, the relation is either constant or described by (11). For both cases, the part of the constraints (6b) in the Jacobian is the same. As discussed in the paper, all the elements are grouped into subdomains Ω_s having their own current constraint ΔI_s . The s th net current constraint is then $g_s(\Delta J) = (\mathcal{A}^i \Delta J)_s$, where index i is a sum over the elements that belong to Ω_s . The Jacobian matrix of the constraints (6b) is

$$\frac{\partial g_s}{\partial \Delta J_j} = \mathcal{A}^i \delta^{ij} \quad (\text{B.2})$$

being nonzero in N entries, where δ^{ij} is the Kronecker delta function. The indices $j \in \{1, 2, \dots, N\}$ and $s \in \{1, 2, \dots, m\}$, where m is the number of constraints (6b). The other blocks of the Jacobian matrix ∇g are contributed by the constraints (6c) and (6d). In the case of a constant $J_c(B)$ relation, the entries in

the Jacobian matrix of the constraint $g_j = -(J_0 + \Delta J)_j + J_c(B)_j$ in (6c) are

$$\frac{\partial g_{kl}}{\partial \Delta J_l} = -\delta^{jl}, \quad (\text{B.3})$$

where $k \in \{m+1, m+2, \dots, m+N\}$. Similarly for the constraint $g_j = (J_0 + \Delta J)_j + J_c(B)_j$ in (6d), the entries in the Jacobian matrix are

$$\frac{\partial g_{kl}}{\partial \Delta J_l} = \delta^{jl}, \quad (\text{B.4})$$

where $k \in \{m+N+1, m+N+2, \dots, m+2N\}$ and the number of nonzeros is N . In addition, the number of nonzeros in the Jacobian of the constraints is $3N$.

However, in the case of a nonconstant $J_c(B)$ relation, i.e. (11), the derivative blocks of (6c) and (6d) in the Jacobian matrix are both dense. To make the execution of the optimization procedures feasible, approximative derivative matrices have to be used. We found the diagonal approximation for the derivative blocks very efficient and thus used it in the computations. Thus, the number of nonzeros in the Jacobian of the constraints is the same in this case as well, i.e. $3N$. To demonstrate the feasibility of the diagonal Hessian approach, the current distribution in the tape is computed with both the Hessians and compared in figure B1. The figure shows that the Hessian of the constraints does not have any effect on the solution as long as the minimum is found, but it does, for instance, affect the speed of convergence. In this case, for a single tape and for one time step, the computation time with the full Hessian was found to be 326 times the computation time with the diagonal Hessian.

The sparsity structure of the Jacobian of the constraints is given with the indices of the nonzero entries, i.e. **iRow** and **iCol**, which are the ones where the delta function is nonzero in (B.2), (B.3) and (B.4).

The sparsity structure of the Hessian of the Lagrangian function $\sigma_f \nabla^2 f(x) + \lambda \nabla^2 g_i(x)$, where the sum is over the number of constraints. Since the Hessian is symmetric, its

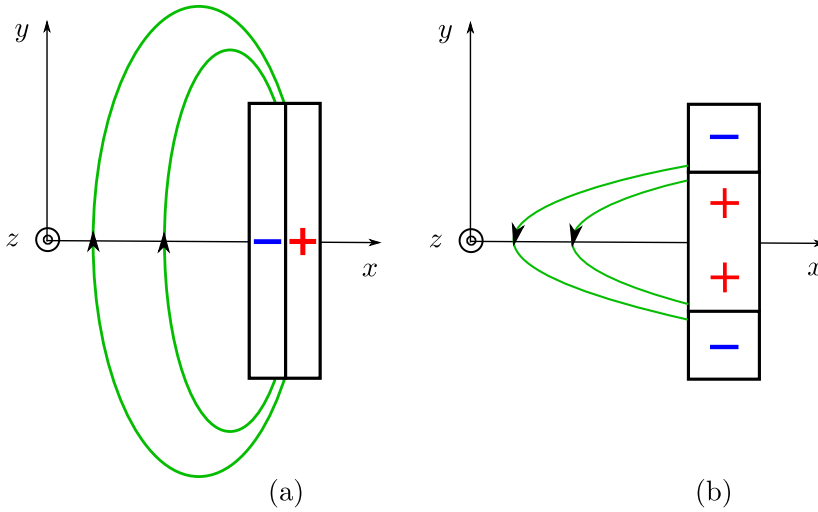


Figure 18. The magnetization field and currents due to the parallel (figure (a)) and perpendicular (figure (b)) magnetic field in a cable partially cancel each other out.

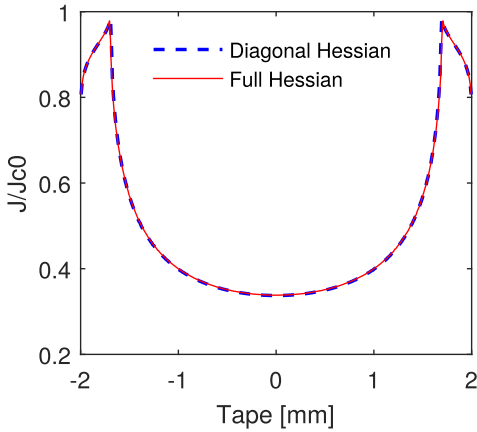


Figure B1. The current distribution along a single HTS tape is computed using the diagonal Hessian and the full one.

structure is only the lower left triangle, since it is a symmetric $N \times N$ square matrix.

Evaluation of the problem functions is done using a given point (x, λ, σ_f) , coming from IPOPT, where x are the values of the problem variables, λ are the constraint multipliers, and σ_f is the objective function factor. The objective function (6a) is simply evaluated in two nested for-loops. Emphasizing the fact that when coding the objective function for IPOPT's interface, the problem variables $x[i]$ correspond to ΔJ_i . The gradient of the objective function is evaluated in a similar way as the objective function: in two nested for-loops. The gradient of the objective function F is

$$\nabla F = M\Delta J + C^T. \quad (\text{B.5})$$

The constraint function values are evaluated as described above. However, in the case of a nonconstant $J_c(B)$ dependency, the critical current densities $J_c(B)_j$, have to be computed before evaluating the constraints. This is done utilizing (11), (14) and (15).

The Jacobian of the constraints in the case of a constant $J_c(B)$ is already derived—the blocks in the Jacobian are (B.2), (B.3) and (B.4). When the nonconstant $J_c(B)$ relation is deployed, the derivative blocks—(6c) and (6d)—in the Jacobian become dense. The derivatives of (6c) are

$$\begin{aligned} \frac{\partial J_c(B)_i}{\partial \Delta J_j} &= -\delta^{ij} - \frac{\beta J_{c0}}{B_0} \\ &\times \frac{k^2 B_{\parallel}^i B_y^{ij} + B_{\perp}^i B_x^{ij}}{\sqrt{(kB_{\parallel}^i)^2 + (B_{\perp}^i)^2} \cdot \left(1 + \frac{1}{B_0} \sqrt{(kB_{\parallel}^i)^2 + (B_{\perp}^i)^2}\right)^{\beta+1}}, \end{aligned} \quad (\text{B.6})$$

and the derivative block of (6d) is

$$\begin{aligned} \frac{\partial J_c(B)_i}{\partial \Delta J_j} &= \delta^{ij} - \frac{\beta J_{c0}}{B_0} \\ &\times \frac{k^2 B_{\parallel}^i B_y^{ij} + B_{\perp}^i B_x^{ij}}{\sqrt{(kB_{\parallel}^i)^2 + (B_{\perp}^i)^2} \cdot \left(1 + \frac{1}{B_0} \sqrt{(kB_{\parallel}^i)^2 + (B_{\perp}^i)^2}\right)^{\beta+1}}. \end{aligned} \quad (\text{B.7})$$

As mentioned earlier, only the diagonals of these derivative blocks (B.6) and (B.7) are utilized. This turned out to be a very effective modelling decision. The convergence per time step was reasonably fast even with the domains consisting of several cables.

The Hessian of the Lagrangian function $\sigma_f \nabla^2 f(x) + \lambda^T \nabla^2 g_i(x)$, for the Bean model is $\sigma_f \nabla^2 f(x)$, because none of the constraints in (6) has a nonzero second derivative. So, it becomes $\sigma_f M$, as discussed earlier. For the Kim model, the Hessian of the constraints is nonzero. For both constraints, (6c) and (6d), the Hessian of the

constraints is

$$\begin{aligned} \lambda^i \frac{\partial^2 J_c(B)_i}{\partial \Delta J_k \partial \Delta J_j} &= \lambda^i \frac{\partial}{\partial \Delta J_k} \left[-\frac{\beta J_{c0}}{B_0} (h_1 (h_2 h_3)) \right] \\ &= -\lambda^i \frac{\beta J_{c0}}{B_0} [h_1' (h_2 h_3) + h_1 (h_2' h_3 + h_2 h_3')], \end{aligned} \tag{B.8}$$

where e.g. $h_i' = \frac{\partial h_i}{\partial \Delta J_k}$, and

$$\begin{aligned} h_1 &= k^2 B_{\parallel}^i B_y^{ij} + B_{\perp}^i B_x^{ij} \\ h_2 &= ((k B_{\parallel}^i)^2 + (B_{\perp}^i)^2)^{-\frac{1}{2}} \\ h_3 &= \left(1 + \frac{1}{B_0} h_2^{-1} \right)^{-(\beta+1)} \\ h_1' &= k^2 B_y^{ik} B_y^{ij} + B_x^{ik} B_x^{ij} \\ h_2' &= - (h_2)^3 (k^2 B_{\parallel}^i B_y^{ik} + B_{\perp}^i B_x^{ik}) \\ h_3' &= - \frac{\beta + 1}{B_0} \left(1 + \frac{1}{B_0} h_2^{-1} \right)^{-(\beta+2)} h_2 (k^2 B_{\parallel}^i B_y^{ik} + B_{\perp}^i B_x^{ik}). \end{aligned}$$

Again, we only take the diagonal terms.

In the Kim model, before evaluating the Hessian of the Lagrangian function, the magnetic flux density components have to be computed, evaluating the constraint function values and the Jacobian of the constraints as before.

In addition, the evaluation of the Hessian of the Lagrangian function is done in nested for-loops according to $\sigma_f \nabla^2 f(x) + \lambda \nabla^2 g_i(x)$, where λ_i corresponds to the i th constraint in (6), and $i \in \{1, 2, \dots, m + 2N\}$.

B.1. Ramping the applied current or magnetic field

Starting from the zero current density distribution, i.e. $J_0 = 0$ everywhere in Ω , we compute the current distribution due to the change in applied current in the domain. This is done by minimizing (6a) subject to the constraints. When this first minimization has converged to an optimal solution or to an acceptable level, the IPOPT returns the solution ΔJ via the interface. This solution is added to J_0 , stored, and used as an initial current distribution J_0 for computing the change in current density distribution of the next time step. In addition, J_0 is the net current distribution accumulated from all the previous ΔJ . Solving the next ΔJ after the previous one is done utilizing IPOPT's reoptimize TNLP function.

References

- [1] Seeber B 1998 Fundamental theory, basic hardware and low-temperature science and technology *Handbook of Applied Superconductivity* vol 1 (Bristol and Philadelphia, PA: Institute of Physics Publishing)
- [2] The European Organization for Nuclear Research <http://home.web.cern.ch/>
- [3] Grilli F, Pardo E, Stenvall A, Nguyen D, Yuan W and Gomory F 2014 *IEEE Trans. Appl. Supercond.* **24** 78
- [4] Benedikt M and Zimmermann F 2015 *Future circular colliders XXVII Int. Symp. on Lepton Photon Interactions at High Energies (Ljubljana, Slovenia)* <http://cds.cern.ch/record/2110739> CERN-ACC-2015-165
- [5] Wilson M N 1987 *Superconducting Magnets* (New York: Oxford University Press) p 423
- [6] Rossi L *et al* 2015 *IEEE Trans. Appl. Supercond.* **25** 4001007
- [7] Chen M, Donzel L, Lakner M and Paul W 2004 *J. Eur. Ceram. Soc.* **24** 1815
- [8] Weijers H W *et al* 2010 *IEEE Trans. Appl. Supercond.* **20** 576
- [9] Kirby G *et al* 2015 *IEEE Trans. Appl. Supercond.* **25** 4000805
- [10] Goldacker W *et al* 2007 *IEEE Trans. Appl. Supercond.* **17** 3398
- [11] Lorin C *et al* 2015 *IEEE Trans. Appl. Supercond.* **25** 4000305
- [12] Grilli F and Ashworth S 2007 *Supercond. Sci. Technol.* **20** 794
- [13] Lakshmi L S *et al* 2010 *Supercond. Sci. Technol.* **23** 085009
- [14] Jiang Z, Thakur K P, Long N J, Badcock R A and Staines M 2011 *Physica C* **471** 999
- [15] Bean C P 1962 *Phys. Rev. Lett.* **8** 250
- [16] Bruzzone P 2004 *Physica C* **401** 7
- [17] Lahtinen V, Pardo E, Souc J, Solovyov M and Stenvall A 2014 *J. Appl. Phys.* **115** 113907
- [18] Ciszek M *et al* 1996 *Supercond. Sci. Technol.* **9** 379
- [19] Herrmann J, Muller K-H, Savvides N, Gnanarajan S, Thorley A and Katsaros A 2000 *Physica C* **341–348** 2493
- [20] Yamafuji K, Wakuda T and Kiss T 1997 *Cryogenics* **37** 421
- [21] Kim Y B, Hempstead C F and Strnad A R 1963 *Phys. Rev.* **129** 528
- [22] Kim Y B, Hempstead C F and Strnad A R 1962 *Phys. Rev. Lett.* **9** 306
- [23] Kirby G *et al* 2016 *IEEE Trans. Appl. Supercond.* **26** 4003307
- [24] Badia-Majos A and Lopez C 2012 *Supercond. Sci. Technol.* **25** 104004
- [25] Pardo E, Souc J and Prolek L 2015 *Supercond. Sci. Technol.* **28** 044003
- [26] Wächter A and Biegler L 2005 *Math. Program.* **106** 25
- [27] Terzieva S *et al* 2011 *Supercond. Sci. Technol.* **24** 045001
- [28] Grilli F and Pardo E 2010 *Supercond. Sci. Technol.* **23** 115018
- [29] Zermeno V, Grilli F and Sirois F 2013 *Supercond. Sci. Technol.* **26** 052001
- [30] Solovyov M *et al* 2013 *Supercond. Sci. Technol.* **26** 115013
- [31] Pardo E, Staines M, Jiang Z and Glasson N 2015 *Supercond. Sci. Technol.* **28** 114008
- [32] Prigozhin L 1996 *J. Comput. Phys.* **129** 190
- [33] Prigozhin L 1997 *IEEE Trans. Appl. Supercond.* **7** 3866
- [34] Pardo E, Gömöry F, Souc J and Ceballos J M 2007 *Supercond. Sci. Technol.* **20** 351
- [35] Gömöry F *et al* 2006 *Supercond. Sci. Technol.* **19** S60–66
- [36] Pardo E 2008 *Supercond. Sci. Technol.* **21** 065014
- [37] Pardo E, Souc J and Kováč J 2012 *Supercond. Sci. Technol.* **25** 035003
- [38] Prigozhin L and Sokolovsky V 2011 *Supercond. Sci. Technol.* **24** 075012
- [39] Souc J, Pardo E, Vojenčiak M and Gömöry F 2008 *Supercond. Sci. Technol.* **22** 015006
- [40] Zhang Y, Song Y, Wang L and Liu X 2015 *Supercond. Sci. Technol.* **28** 085002
- [41] Grilli F *et al* 2014 *IEEE Trans. Appl. Supercond.* **24** 4801005
- [42] Nii M, Amemiya N and Nakamura T 2012 *Supercond. Sci. Technol.* **25** 095011
- [43] Amemiya N, Tsukamoto T, Nii M, Komeda T, Nakamura T and Jiang Z 2014 *Supercond. Sci. Technol.* **27** 035007
- [44] van Nugteren J *et al* 2016 *IEEE Trans. Appl. Supercond.* **26** 8201407
- [45] Lahtinen V, Lyly M, Stenvall A and Tarhasaari T 2012 *Supercond. Sci. Technol.* **25** 115001
- [46] Pellikka M, Tarhasaari T, Suuriniemi S and Kettunen L 2013 *J. Comput. Appl. Math.* **246** 225
- [47] Geuzaine C and Remacle J-F 2009 *Int. J. Numer. Methods Eng.* **79** 1309

- [48] Cheng D K 1993 *Fundamentals of Engineering Electromagnetics* (Reading, MA: Addison-Wesley) p 488
- [49] Gömöry F 2006 *Appl. Phys. Lett.* **89** 072506
- [50] Norris W T 1970 *J. Phys. D: Appl. Phys.* **3** 489
- [51] Hilton D K, Gavrilin A V and Trociewitz U P 2015 *Supercond. Sci. Technol.* **28** 074002
- [52] Lahtinen V 2014 Searching for frontiers in contemporary eddy current model based hysteresis loss modelling of superconductors *Doctoral Thesis* (Tampere University of Technology, Tampere, Finland) <http://urn.fi/URN:ISBN:978-952-15-3352-5>
- [53] Goldacker W *et al* 2006 *J. Phys.: Conf. Ser.* **43** 901
- [54] Lahtinen V and Stenvall A 2014 *IEEE Trans. Appl. Supercond.* **24** 8200205
- [55] Xia J, Bai H, Lu J, Gavrilin A, Zhou Y and Weijers H 2015 *Supercond. Sci. Technol.* **28** 125004
- [56] Mess K-H, Schmüser P and Wolff S 1996 *Superconducting Accelerator Magnets* (Singapore: World Scientific)
- [57] Pardo E, Sanchez A, Chen D X and Navau C 2005 *Phys. Rev. B* **71** 134517
- [58] Introduction to IPOPT: a tutorial for downloading, installing, and using IPOPT 2013 Revision 2422 http://web.mit.edu/ipopt_v3.11.6/doc/documentation.pdf
- [59] Nocedal J, Wächter A and Waltz R 2009 *SIAM J. Optim.* **19** 1674
- [60] Wächter A and Biegler L 2005 *SIAM J. Optim.* **16** 1
- [61] Wächter A and Biegler L 2005 *SIAM J. Optim.* **16** 32

PUBLICATION

III

**Predicting heat propagation in Roebel-cable-based accelerator magnet
prototype: One-dimensional approach with coupled turns**

J. Ruuskanen, A. Stenvall and V. Lahtinen

IEEE Trans. Appl. Supercond. 27.4 (2017), 0600205

DOI: 10.1109/TASC.2016.2630844

Publication reprinted with the permission of the copyright holders

Predicting Heat Propagation in Roebel-Cable Based Accelerator Magnet Prototype: One-Dimensional Approach with Coupled Turns

Janne Ruuskanen, Antti Stenvall and Valtteri Lahtinen

Abstract—When designing superconductor based magnets, it is of the utmost importance to be prepared for the loss of thermal stability under operation. In this paper, heat propagation during a quench in Roebel-cable based accelerator magnet prototype is predicted using one-dimensional approach. The heat diffusion equation is solved using the finite element method and thermal coupling between the turns is taken into account using thermal network model. However, when reducing the dimensions of the problem, modelling decisions are often unavoidable. Here, we present the challenges of this approach and discuss the appropriateness of these decisions via simulations.

Index Terms—Accelerator magnets, Finite element methods, HTS cables, Quench

I. INTRODUCTION

LOCAL vanishment of the superconducting state in an accelerator magnet leads to serious heat generation and device breakdown is highly likely if one is not prepared for quench. To be prepared for a quench one needs to simulate various quench events before the magnet operation to be able to predict if a quench can be safely carried through. In addition, simulations are needed in designing adequate protection systems for such magnets.

The field of quench modelling has become a long way up to the present state-of-the-art. The first method for simulating this event was presented by Wilson in 1968 [1]. Wilson’s approach on quench simulation problem is based on normal zone propagation in magnet’s volume and later on development of this approach has been continued by others [2]. Another way to model quench is to solve the heat diffusion equation. It can be solved numerically, for example, using finite element method (FEM) [3] or using thermal network model based on the finite difference method.

The magnet under study in this work is a REBCO Roebel-cable based R&D accelerator magnet prototype, namely the Feather-M0 magnet (FM0) [4]. As a part of the EuCARD-2 project [5], few this kind of magnets are under construction and study in CERN [6] for quench detection and protection measurement purposes [7]. Nominal current for a five turn version of FM0 is 6 kA and the coil produces 1.5 T to its bore. One topic in the EuCARD-2 project is in designing and

developing high temperature superconducting (HTS) magnets for particle accelerators including possible Large Hadron Collider successors [8].

Modelling heat diffusion in a superconducting multi-turn magnet can be time consuming especially if three dimensional mesh is utilized. To be able to simulate consequences of a quench in highly detailed coils in a reasonable time frame, simplifications are needed. The approach in this paper is to model the heat propagation in a magnet by reducing the dimension of the modelling domain from three to one. Thus, we solve the heat diffusion equation in 1-D using FEM. The heat flux between cables is taken into account in computations by means of the thermal network model. In addition, in this paper the computation results of the normal zone length, resistive voltage, coil current and hot spot temperature as a function of time are presented. Based on these, conclusions on different modelling decisions are made, concerning this approach.

In section II, the problem formulation is detailed, and in section III, results are presented with appropriate discussion. Finally, in section IV, conclusions take place.

II. THE PROBLEM FORMULATION

The Feather-M0 magnet, under investigation here, has five turns of Roebel-cable [9] consisting of 15 REBCO tapes. In the modelled magnet design, the width and the thickness of the cable, including insulation and impregnation material, is 12.2 mm and 1 mm, respectively. Simulations are carried out utilizing an in-house simulation tool that runs in Matlab [10]. Tool is tailored for quench analysis of HTS based accelerator magnets, and is built on an open-source platform *dp* [11].

A. Problem Setup

The primary quantity to be solved, when modelling quench, is the temperature as a function of time in the modelling domain. Thus, FEM is used to solve the heat diffusion equation

$$C(T) \frac{\partial T}{\partial t} = \nabla \cdot \lambda(T) \nabla T + Q(T, \mathbf{B}), \quad (1)$$

where C is the effective volumetric heat capacity, λ is the effective thermal conductivity along the cable, and Q is the heat generation due to current in the resistive path. The magnetic flux density \mathbf{B} is decomposed into two components: parallel and perpendicular with respect to the cable’s wide face. Effective material parameters, for heat capacity and thermal conductivity, are computed like in [12]. Insulation material

Tampere University of Technology, Electromagnetics, P.O. Box 692, FIN-33101 Tampere, Finland; e-mail: janne.ruuskanen@tut.fi; www: www.notjargon.org

Manuscript received . This research was supported in part by The Academy of Finland project #287027 and in part by EuCARD-2, which is cofunded by the partners and the European Commission under Capacities Seventh Framework Programme, under Grant Agreement 312453.

between the cable turns is kapton. The heat generation, Q is computed using the current sharing model [1]. For the critical current $I_c(T, B, \theta)$, which is a function of temperature, norm of magnetic field and direction of the magnetic field, respectively, a fit based on measurements [13] is used that was also utilized in [7]. For the present magnet, this fit results approximately in coil critical current of 11.5 kA. Fractions in computing the effective material parameters are listed in Table I [14].

TABLE I
MATERIAL FRACTIONS OF THE ROEBEL-CABLE

Material	fraction [%]
Silver	2.3
Hastelloy	30.8
REBCO	0.6
Copper	24.6
Kapton	9.1
Epoxy	32.6

The 1-D modelling domain represents the center line of the coil's cable. Temperature is considered to be homogeneous in the cross-section of the cable. Therefore, it is possible to reduce the modelling dimension down to one. However, since the cross-section of cable is in the same temperature, this raises a question on how one should take the magnetic field into account. Obviously \mathbf{B} varies in the cross-section area. Here, we will investigate the two extreme cases: \mathbf{B} from the center of the cable and \mathbf{B} from the edge of the cable, i.e., where the J_c is the highest and the lowest, respectively. Moreover, the magnetic field in the 3-D geometry is computed for unit of coil current and then scaled point-wise with the current in the coil. In other words, we consider linear $\mathbf{B}(I)$ -relation, which is an adequate modelling decision for this the magnet [15]. In addition, the modelling domain is discretized into finite elements and linear basis functions are utilized.

B. Heat flux between the cable turns: Thermal network model

Heat flux between the cables is taken into account, in the simulations, using the thermal network model. The interaction between the cable turns is represented by a matrix D^1 . This matrix adds the information about the additional heat flux to different turns, i.e., how the elements are thermally connected to ones in the neighboring turns. Since the magnet under study has cable turns only in one layer, the heat flux between the turns is in one plane.

Taking a look at an element in the 1-D modelling domain ($\Omega \subset \mathbb{R}$) corresponding to the element e_i (see Fig. 2) in the

3-D domain ($\Omega^3 \subset \mathbb{R}^3$) shown in Fig. 1, the heat flux q_i , to it from cable layers next to it is

$$\begin{aligned} q_i &= q_{mn} + q_{jk} \\ &= -k_i \frac{T_i - T_{mn}}{\Delta r} - k_i \frac{T_i - T_{jk}}{\Delta r}, \end{aligned} \quad (2)$$

where k is the thermal conductivity, and Δr the thickness, of the insulation material between the cable turns. Furthermore, q_i is integrated along the width of the element e_i using the basis functions for the varying temperatures along the integration path in the involving elements. As a result of this integration, one gets coefficients for every element node and they together form the matrix D .

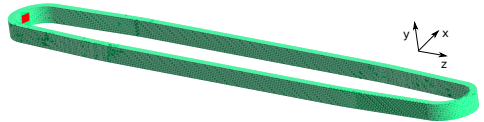


Fig. 1. Three dimensional depiction of the magnet under study. Hot spot is marked at the end of the coil into the innermost cable.

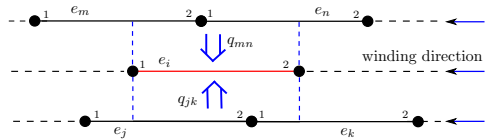


Fig. 2. Top view: Depiction of the thermal network between the turns.

C. Protection Scheme

In the quench event, due to current flow in the matrix metal of tapes in cable, heat generation occurs and the coil's resistive voltage rises. When the resistive voltage reaches a certain detection voltage, the protection system is activated.

In the protection analysis of this paper, discharge of the coil, in case of a quench, is done by dumping the coil energy in a dump resistor R_d . For the small prototype magnet under study, the charged energy is low enough so that it can be protected using only a dump resistor. However, large magnets cannot be protected like this [16]. Quench is detected when magnet's resistive voltage v_c has reached a certain threshold value. From that time instant, dumping is started after switch delay, which also includes the validation time. Switch delay is the time it takes for the system to validate the overshoot of the threshold voltage and for the power electronics to switch off the current source and connect the dumping resistor with the magnet. Typical switch delays are on the order of 20 ms [17]. The protection system is depicted in Fig. 3.

The coil current, during the discharging phase, can be computed using the Kirchhoff's voltage law, which states that $v_L + v_c + v_d = 0$, where the quantities are coil's inductive voltage, resistive voltage and dump resistor's voltage, respectively. Re-writing it in terms of coil current (I), it becomes

$$L \frac{dI}{dt} + R_{coil} I + R_d I = 0. \quad (3)$$

¹When solving (1) with FEM, one arrives via weak formulation [3, p. 310] at a matrix equation of the form $M\dot{x} = Kx + f$ where K is the stiffness matrix, M is the mass matrix of the problem and vector f represents the term of the boundary conditions and the heat source. x is the vector of unknown coefficients to be solved for. M represents the heat storage per unit volume and K represents the heat diffusion in the domain to which the matrix D is added.

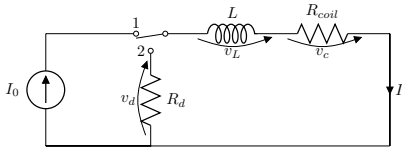


Fig. 3. Circuit diagram of the protection scheme: In case of a quench, coil current is dumped in to a protection resistor.

Time discretizing this formula into time intervals Δt , one is left to solve iteratively for each time step k

$$I^{k+1} = I^k \left(\frac{L}{\Delta t} - R_{coil}^k - R_d \right) \frac{\Delta t}{L}. \quad (4)$$

III. RESULTS AND DISCUSSION

In this section, computation results based on the problem setup of the one dimensional heat propagation approach are presented. In the forthcoming analysis operation current of 6 kA, detection voltage of 50 mV and switch delay of 20 ms is used, unless otherwise stated. Moreover, the inductance of the magnet is 8.16 μ H and for the resistance of the dump resistor, value of 0.15 Ω was used [18].

A. Quenching the magnet using low hot spot I_c

Based on research done in [19] the most natural way to quench a magnet is to set low I_c into a small area of the magnet. When operating the magnet, heat generation will occur in that area. To investigate this, we use the nominal case setup.

In Fig. 4, we present the effect of the hot spot I_c on the resulting maximum temperature during the quench and magnet discharge. Results indicate that the hot spot I_c reduction has a minor effect, or no effect at all, to occurring maximum temperature. Time to reach the detection threshold voltage though, is faster the lower the hot spot I_c is.

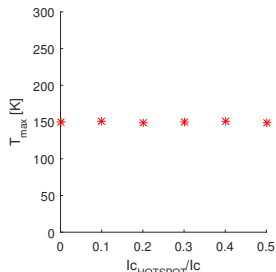


Fig. 4. The resulting maximum temperature in the magnet does not depend on the hot spot I_c reduction utilized for quenching the magnet.

B. Varying detection voltage

In this study, we investigate, how the quench detection voltage affects the detection time, and on the other hand,

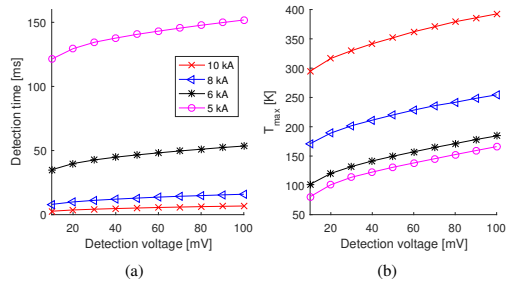


Fig. 5. Detection time (Fig. a) and maximum temperature (Fig. b) as a function of detection voltage.

what are the resulting hot spot temperatures in the magnet. Simulation results are presented in Fig. 5.

At higher operation currents it is harder to protect the magnet due to switch delay of power electronics.

C. Varying switch delay

The switch delay has an immense impact on whether a magnet can be protected or not. Study on this is shown in Fig. 6. At all the investigated operation currents, the maximum temperature rises steeply as a function of switch delay.

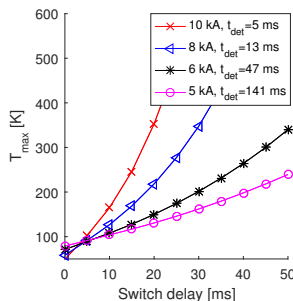


Fig. 6. Maximum temperature as a function of switch delay after quench detection time (t_{det}). Detection voltage was 50 mV.

D. An analysis of the nominal quench

Here we present quench simulation results on the nominal case of Feather-M0. Parameters used in these computations are listed in Table II. The hot spot length was 10 mm. When detection voltage is observed, the protection is enabled after switch delay. It takes only 0.5 ms for the current to decay down to 0 A, due to small inductance of the magnet (see Fig. 7(a)). The resulting resistive voltage (see Fig. 7(b)) in the whole magnet reaches up to its maximum (\sim 250 mV) and then goes fast to zero, after the current dump starts. Therefore FMO magnets are built more for studying quench detection than protection systems.

Maximum temperature, during the quench and protection in two different cases, is presented in Fig. 8. In this approach

TABLE II
SIMULATION PARAMETERS

Parameter	Value
Inductance	8.16 μH
Protection resistance	0.15 Ω
Threshold voltage	50 mV
Switch delay	20 ms
Operation current	6 kA
Operation temperature	4.2 K
$I_{c\text{HOTSPOT}}/I_c$	0.4

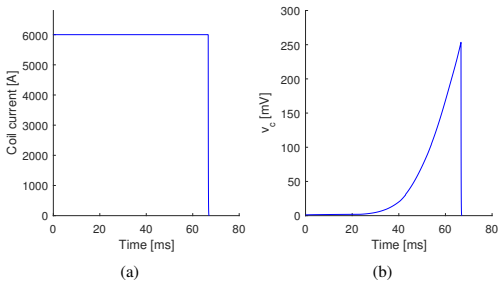


Fig. 7. (a): Coil current as a function of time. Current decreases to zero in 0.5 ms. (b): Coil's resistive voltage as a function of time.

the modelling decision on from which part of the cable one should take the magnetic field plays a big role. In reality, only a small area of the magnet's cable is in perpendicular magnetic field [15], so to the best of our knowledge choice is the center of the cable. How the magnet's $I_c(\mathbf{B})$ -relation should be considered in this 1-D approach, is still a challenge to be investigated.

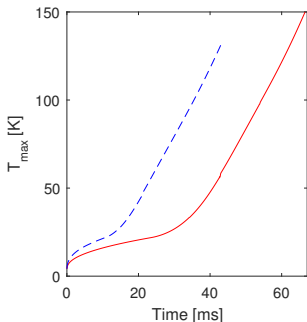


Fig. 8. Hot spot temperature as a function of time. Two cases compared: Magnetic field \mathbf{B} taken from the center of the cable (solid line) and \mathbf{B} taken from the middle of the center and top of the cable (dashed line). Quench detected at 47 ms.

In Fig. 9, the temperature distribution is presented when the hot spot temperature is at its maximum value. The close-up of the length of the first turn of the magnet shows that heat diffusion is minor to the second turn during the quench.

In Fig. 10, the normal zone propagation is shown. The

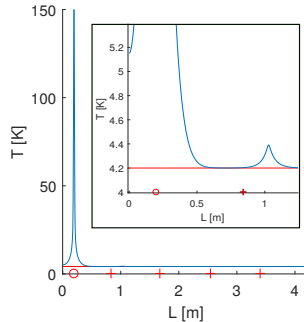


Fig. 9. Temperature distribution along the coil length, when hot spot temperature is at its maximum. Hot spot location is marked with circle and the change between cable turns is marked with crosses.

normal zone is determined from the current sharing temperature, which is the temperature when the coil current I , locally flows in the matrix metal, i.e., the temperature when $I_c < I$. The normal zone grows slowly which is in agreement with the results presented in [20]. Moreover, in HTS cables the quench propagation does not play significant role during the quench, but only the time margin provided by the stabilizing material. This poses challenges to large magnets because quench propagation cannot be used for protecting the magnet almost at all. Once again: Successful detection and fast switching is crucial in order to avoid device breakdown.

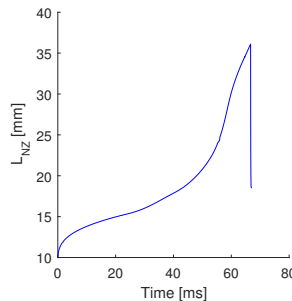


Fig. 10. Length of the normal zone in the magnet as a function of time. Normal zone is determined from the current sharing temperature.

IV. CONCLUSIONS

In this work, a simulation tool with a one-dimensional approach for predicting heat propagation in an HTS Roebel-cable based accelerator magnet was developed. It is shown via results that it is possible to model heat propagation in 1-D with coupled turns. Based on the results, successful detection and short switch delay of the power electronics are of ample importance in magnet protection. To explore strengths and limitations of this approach, validation against full 3-D models is needed and also benchmarking should be done against measurement data.

REFERENCES

- [1] M. N. Wilson, *Superconducting magnets* (p. 78). Oxford, U.K.: Clarendon, 1983.
- [2] L. Rossi and M. Sorbi, *QLASA: a computer code for quench simulation in adiabatic multicoil superconducting windings*. Istituto Nazionale Di Fisica Nucleare, INFN-TC-04-13, 2004.
- [3] G. Strang and G. Fix, *An analysis of the finite element method*. Wellesley MA, Wellesley-Cambridge Press. 2nd ed., 2008.
- [4] G. Kirby *et al.*, "Accelerator-Quality HTS Dipole Magnet Demonstrator Designs for the EuCARD-2 5-T 40-mm Clear Aperture Magnet" *IEEE Trans. Appl. Supercond.* vol. 25, no. 3, 2015, Art. ID. 4000805.
- [5] L. Rossi *et al.*, "The EuCARD-2 Future Magnets European Collaboration for Accelerator-Quality HTS Magnets" *IEEE Trans. Appl. Supercond.* vol. 25, no. 3, 2015, Art. ID. 4001007.
- [6] The European Organization for Nuclear Research, home page: <http://home.web.cern.ch/>
- [7] J. van Nugteren, G. A. Kirby, G. de Rijk, L. Rossi, H. H. J. ten Kate, and M. M. J. Dhalle, "Study of a 5 T Research Dipole Insert-Magnet Using an Anisotropic ReBCO Roebel Cable" *IEEE Trans. Appl. Supercond.* vol. 25, no. 3, 2015, pp. 1-5.
- [8] M. Benedikt and F. Zimmermann, 2015 *Future Circular Colliders* CERN-ACC-2015-165 (Presented at 27th International Symposium on Lepton Photon Interactions at High Energies Ljubljana, Slovenia) Available online at: <http://cds.cern.ch/record/2110739>
- [9] W. Goldacker *et al.*, "Status of high transport current ROEBEL assembled coated conductor cables" *Supercond. Sci. Technol.* vol. 22, no. 3, 2009, Art. ID. 034003.
- [10] MATLAB, The MathWorks, Inc., Natick, Massachusetts, United States
- [11] Platform for programming finite element method solvers in Matlab. <https://github.com/stenvala/dp>
- [12] A. Stenvall, A. Korpela, R. Mikkonen, and G. Grasso, "Stability considerations of multifilamentary MgB₂ tape" *Supercond. Sci. Technol.* vol. 19, no. 2, 2006, pp. 184-189.
- [13] A. Xu *et al.*, "Angular dependence of J_c for YBCO coated conductors at low temperature and very high magnetic fields" *Supercond. Sci. Technol.* vol. 23, no. 1, 2009, Art. ID. 014003.
- [14] V. Lombardo, E. Barzi, D. Turrioni, A. V. Zlobin, N. J. Long, and R. A. Badcock, "Fabrication, Qualification and Test of High J_c Roebel YBa₂Cu₃O_{7-δ} Coated Conductor Cable for HEP Magnets" *IEEE Trans. Appl. Supercond.* vol. 21, no. 3, 2011, pp. 2331-2334.
- [15] J. Ruuskanen *et al.*, "Electromagnetic Nonlinearities in a Roebel-Cable Based Accelerator Magnet Prototype: Variational Approach" *Supercond. Sci. Technol.* To be published.
- [16] T. Salmi, and A. Stenvall, "Modeling Quench Protection Heater Delays in an HTS Coil" *IEEE Trans. Appl. Supercond.* vol. 25, no. 3, 2015, Art. ID. 0500205.
- [17] T. Salmi *et al.*, "Suitability of different quench protection methods for the 16 T Nb₃Sn accelerator dipoles designed for the Future Circular Collider" To be presented in this conference.
- [18] E. Härö, A. Stenvall, J. van Nugteren, and G. Kirby, "Hot Spot Temperature in an HTS Coil: Simulations With MITTs and Finite Element Method" *IEEE Trans. Appl. Supercond.* vol. 25, no. 2, 2015, Art. ID. 4901107.
- [19] E. Härö, *Simulation Tool Development for Quench Modelling*. Doctoral thesis, Tampere University of Technology, Tampere, Finland.
- [20] E. Härö *et al.*, "Quench Considerations and Protection Scheme of a High Field HTS Dipole Insert Coil" *IEEE Trans. Appl. Supercond.* vol. 23, no. 3, 2013, Art. ID. 4600104.

PUBLICATION

IV

Optimization of an E³SPreSSO Energy-Extraction System for High-Field Superconducting Magnets

J. Ruuskanen, A. Stenvall, J. van Nugteren and V. Lahtinen

IEEE Transactions on Applied Superconductivity 29.5 (2018), 4700805

DOI: 10.1109/TASC.2018.2794457

Publication reprinted with the permission of the copyright holders

Optimization of E³SPreSSO Energy-Extraction System for High-Field Superconducting Magnets

J. Ruuskanen, A. Stenvall, J. van Nugteren and V. Lahtinen

Abstract—High temperature superconducting magnets (HTS) suffer from slow quench propagation and have in large fraction high thermal margin. Due to the high thermal margin, quench protection systems (QPS) based on initiating large normal zones, with e.g. quench protection heaters or CLIQ, are not effective with HTS and energy extraction is needed. In large magnets, energy extraction with a single dump is not effective and new solutions are looked for. Recently a concept E³SPreSSO, for HTS magnet protection have been presented in the scope of European project EuCARD-2. E³SPreSSO utilizes a series connected bifilar HTS or LTS coil. In this work we present a methodology to design QPS based on E³SPreSSO for HTS magnets. Then we utilize this methodology to design and analyze the suitability of such QPS for a 20 T HTS accelerator dipole.

Index Terms—Accelerator magnets, HTS cables, Modeling, Quench protection

I. INTRODUCTION

High-field high-temperature superconducting (HTS) magnets typically have high average energy density. Therefore, special care in designing a magnet protection system must be taken to prevent too high hot spot temperature during a magnet quench.

In case of a quench of a typical large HTS magnet, the normal zone is very localized due to low thermal conductivity and high current sharing temperatures T_{cs} . The natural increase of normal zone resistance cannot therefore have significant effect on the current decay. One option to increase the resistance is to cause a wide spread quench. To spread the quench artificially, large energy densities must be dissipated, or diffused, into the magnet. However, due to the large thermal margin, the efficiency of the technologies used with LTS magnets, quench protection heaters or CLIQ, is not adequate [1]. This poses a whole new research problem in the field of HTS accelerator magnet quench protection R&D.

One possible energy extraction concept was developed at CERN [2] in the scope of European project EuCARD-2 [3], namely E³SPreSSO (External Energy Extraction Symbiotic Protection System for Series Operation) [4]. The idea is to divide magnet into multiple sections each in series connection with an E³SPreSSO protection unit. The unit consists of a superconducting cable, working as a switch, and of a parallel connected dump resistor - both wound bifilarly into a coil

shape. In normal operation the unit is practically invisible: bifilarly wound superconducting switch has almost zero resistance and negligible inductance; dump resistor in parallel carries no current when the switch is superconducting.

The efficiency of single dump resistor that can be connected to the current terminal after the quench is detected and current source bypassed is limited by the requirement of certain terminal voltage (typically 1-2 kV). Therefore, series connection for the dump resistors is required and this can be effectively achieved with superconducting switches. This allows fast current decay and limits the voltage-to-ground to an acceptable level when simultaneously triggered. Such an approach can also be possible to protect strings of magnets in Future Circular Collider [5] instead of utilizing links to shorten the strings [6]. The triggering of the switch, i.e. transferring the superconductor in the switch to a normal state, can be done, for example, with a parallel connected capacitor that is discharged to the E³SPreSSO via thyristor.

In this paper, one possible approach is presented for designing E³SPreSSO-based protection system for high-current HTS magnets. To consider a state-of-the-art design where new protection solutions are required, we study a REBCO based 20 T accelerator dipole magnet design presented in [7]. It is designed to operate at 12 kA current. It has inductance of 26 mH per meter and consists of 236 insulated cable turns. The E³SPreSSO concept is analyzed using a simulation approach developed here. The advantage of the approach, compared to the analysis done in [4], is its capability to model the thyristor, capacitor and current sharing between superconductor and matrix in the switch.

Our analysis relies on considering different components: magnet's hot spot, superconductor switch and parallel resistor in E³SPreSSO, adiabatic in the thermal model. Circuit model governs the current flow in the system and therefore the heat generation - the crucial input to the thermal model. It is assumed that the normal zone resistance of the magnet is negligible. Furthermore, we present how E³SPreSSO design, based on such a modelling approach, can be optimized with a tunable target function and specified (non-linear and linear) constraints. Our computational tool is implemented in Matlab [8].

The paper is structured as follows. In section II the simulation approach is presented in detail with the optimization procedure. Section III presents the results. We consider the suitability of different superconductors for the switch of E³SPreSSO for protecting 20 T HTS magnet by comparing resulted optimized designs. Then one of the most promising switch cables is chosen to investigate how maximum allowed

Tampere University of Technology, Electromagnetics, P.O. Box 692, FIN-33101 Tampere, Finland; e-mail: janne.ruuskanen@tut.fi; www: www.notjargon.org

Manuscript received 28th of August 2017. This research was supported in part by The Academy of Finland project #287027 and in part by EuCARD-2, which is cofunded by the partners and the European Commission under Capacities Seventh Framework Programme, under Grant Agreement 312453.

temperature in the magnet governs the required number of E³SPreSSO units. Finally conclusions are drawn.

II. SIMULATION APPROACH

In the simulation approach the aim is to find an optimal feasible design for a protection system consisting of E³SPreSSO units. Electro-thermal behaviour of the magnet and components of its protection system can be predicted using circuit models and thermal models. In this section, a circuit model for the whole system is presented. Then the circuit model is coupled with an adiabatic thermal model to predict the heat generation in different components of the circuit. Finally the optimization problem is formulated based on the system of equations presenting the state of the system.

In the simulation of the E³SPreSSO unit we solve for the electrical currents in the circuit model and the adiabatic temperatures of the components as a function of time simultaneously. As a post-processing result we get the maximum voltage-to-ground during a quench. In the optimization procedure we optimize switch cable length (l_s), switch cable cross-section area (A_s), i.e. number of strands in the cable, number of E³SPreSSO units (N_E), parallel resistor length (l_p), parallel resistor cross-section area (A_p), capacitor's initial voltage (V_{C0}) and capacitor's capacitance (C). Therefore, obtained design parameters are such that the maximum temperatures and voltage-to-ground are below a given limit as well as certain operation limit for the superconducting switch of the E³SPreSSO. This multi-objective optimization is a challenging problem and we use a tunable target function with a cost coefficient for each design parameter to find a feasible solution. Next we present first the circuit model, then the thermal model and finally our optimization approach. This modelling approach is fully independent of the magnet where this kind of a protection is to be applied.

A. Circuit model

The magnet to be protected is divided to N_E sections each connected in series with E³SPreSSO protection unit. The circuit diagram of a magnet section and its protection unit is depicted in Fig. 1. The unit consists of a superconducting switch and a parallel dump resistor (p). In the model, switch cable is divided into stabilizer (st) and superconducting (sc) part. A capacitor, having capacitance C and voltage V_C over it, is used for quenching the superconductor with an over-current pulse. In series connection with capacitor a thyristor (T), with threshold voltage (V_{th}) of 1 V, is utilized to enforce current not to flow back to the capacitor. Therefore, the capacitor is unconnected in normal operation and connected to the circuit by triggering the thyristor when quench is detected. Moreover, the sum of the operation current (I) and the current flowing through the thyristor (I_T) from the capacitor equals to the sum of current I_p flowing through the parallel resistor (R_p), stabilizer current (I_{st}) resisted by superconductor's stabilizer's resistance (R_{st}) and current, I_{sc} , flowing through the superconducting part of the switch having resistance of R_{sc} .

For simplicity, we assume that each subdivided part, a magnet section, has equal effective inductance L/N_E , where L

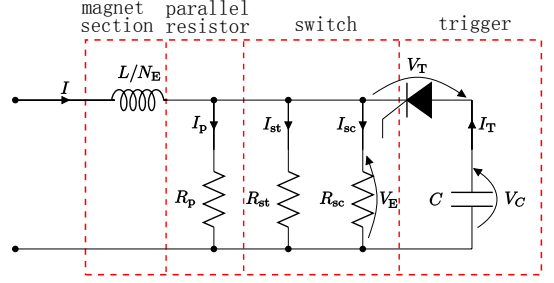


Fig. 1. Circuit diagram of an E³SPreSSO unit connected in series with a magnet section.

is magnet's total inductance. Therefore, it is enough to model one E³SPreSSO unit in a system under study.

To formulate the circuit model, the inductive voltage over the magnet and the capacitor voltage are described, respectively, as

$$-L \frac{dI}{dt} = N_E V_E \quad -C \frac{dV_C}{dt} = I_T.$$

Note that signs are chosen such that positive current decreases capacitor voltage. Furthermore, the superconductor is modelled according to the current sharing model [9].

To cover the rest of the unknowns, two sets of equations are utilized. They are based on Kirchoff's voltage and current laws. To deny any thyristor current when $V_T < V_{th}$, two sets of equations are needed. In the first one, the capacitor's current (I_T) is flowing into the forward direction and thus the behaviour of the circuit can be approximated using the equations

$$V_T \geq V_{th} \implies \begin{cases} V_E = V_C - V_T \\ I_T = I_{sc} + I_{st} + I_p - I \\ I_{sc} = I_c \\ I_{st} = V_E / R_{st} \\ I_p = V_E / R_p. \end{cases} \quad (1)$$

When $V_T < V_{th}$, used equations are

$$V_T < V_{th} \implies \begin{cases} V_E = I_p R_{st} \\ I_T = 0 \\ I_{sc} = \min(I_c, I) \\ I_{st} = (I - I_{sc}) \frac{R_p}{R_{st} + R_p} \\ I_p = I - I_{sc} - I_{st}. \end{cases} \quad (2)$$

B. Thermal model

The temperatures in the magnet's (m) hot spot assumed to locate at the highest field, the switch (s) and the parallel resistor (p) are modelled adiabatically as

$$C_s \frac{dT_s}{dt} = \rho_s(T_s) \frac{I_{st}}{f_s A_s^2} (I_{st} + I_c) \quad (3)$$

$$C_p \frac{dT_p}{dt} = \rho_p(T_p) \left(\frac{I_p}{A_p} \right)^2 \quad (4)$$

$$C_m \frac{dT_m}{dt} = \rho_m(T_m, B_m(I)) \frac{I^2}{f_m A_m^2}, \quad (5)$$

where C , ρ , A , T and f denote effective volumetric heat capacity, effective resistivity, cross-sectional area, temperature and cable's stabilizer fraction, respectively. Moreover, in the magnet, linear $B_m - I$ dependency is assumed between 0 A and I_{op} , which accounts for the magnetoresistance of the copper stabilizer. All the material properties utilized in this study were taken from CryoComp [10].

C. Optimization problem

In the optimization procedure the objective function is a weighted sum of the design parameters listed in Table I. The objective function is minimized subject to constraints. For the minimization interior-point optimization algorithm was utilized [11]. The optimization problem can be summarized as

$$\begin{aligned} \underset{\omega}{\text{minimize}} \quad & \omega_{l_s} + \omega_{N_E} + \omega_{l_p} + \omega_{A_p} + \omega_{A_s} + \omega_{V_{CO}} + \omega_C \\ \text{subject to} \quad & V_E = V_{\max} \\ & T_s, T_p, T_m \leq T_{\max} \\ & I_c(T_{op}) \geq 1.2 \times I_{op}, \end{aligned} \quad (6)$$

where ω_i 's are weighted optimization parameters. Subscripts correspond to those in Table I. In the table, the weights, chosen such that optimization parameters are approximately of the same order of magnitude, are also shown. Moreover, the first constraint requires resulting maximum voltage over an E³SPreSSO unit to the maximum allowed value: By requiring this, the fastest current decay is obtained. The second limits the resulting temperature below the maximum allowed value in switch, parallel resistor and magnet's hot spot, respectively. Last constraint is for requiring current margin for the switch in normal operation, here chosen to 20 %. Moreover, optimization is performed for real numbers.

TABLE I
DESIGN PARAMETERS FOR SIMULATIONS.

parameter	description	weight
l_s	length of switch cable	1/(1 m)
N_E	number of E ³ SPreSSO units	1
l_p	parallel resistor length	1/(1 m)
A_p	parallel resistor cross-section area	1/(12 mm ²)
A_s	switch cable cross-section area	1/ \hat{A}_s *
V_{CO}	initial voltage in the capacitor	1/(10 V)
C	capacitor capacitance	1/(1 mF)

* Strands' cross-section areas (\hat{A}_s) are shown in Table III.

III. RESULTS

In this section, the E³SPreSSO protection system is optimized for various chosen superconducting switch materials. The most promising one is chosen and thermo-electrical behaviour of the system is presented. Finally, for the chosen superconductor switch, the number of required protection units is studied as a function of maximum allowed temperature in the system. The default input parameters for the simulations are shown in Table II and the cable of the magnet is described in Table III. Moreover, material utilized for the parallel resistor is stainless steel (SS).

TABLE II
DEFAULT INPUT PARAMETERS FOR SIMULATIONS

parameter	value	unit	description
I_{op}	12	kA	magnet operation current
T_{op}	4.2	K	system operation temperature for LTS
T_{op}	20	K	system operation temperature for HTS
E_m	1.86	MJ	magnet energy
B_m	20	T	magnetic field in magnet aperture
V_{\max}	1000	V	maximum allowed voltage over magnet
T_{\max}	300	K	maximum allowed temperature

A. Comparing different superconductors for the switch

The requirements for the switch cable are such that it has to have high resistivity once quenched. On the other hand, it has to be stable enough so that the temperature will not rise too high. Here a comparison of 9 possible switch strands is presented. Three different superconducting materials were utilized: NbTi, MgB₂ and REBCO, for which the used critical current fits are described in [12]–[14]. For the stabilizer, three different stabilizers were considered. Strand candidates are listed in Table III.

TABLE III
MATERIAL FRACTIONS AND CROSS-SECTION AREA OF SWITCH CABLE STRAND. CASE M DENOTES THE FRACTIONS FOR THE MAGNET CABLE.

Case	NbTi	MgB ₂	REBCO	Ag	Cu	CuNi	SS	other	\hat{A}_s
[#]	[%]	[%]	[%]	[%]	[%]	[%]	[%]	[%]	[mm ²]
1	60	-	-	-	40	-	-	-	0.57
2	60	-	-	-	40	-	-	-	0.57
3	60	-	-	-	-	40	-	-	0.57
4	14.8*	30.6	-	-	-	54.4	-	0.2	2.3
5	14.8*	30.6	-	-	-	-	54.4	0.2	2.3
6	-	-	0.91	-	-	-	90.9	8.19	1.2
7	-	-	0.91	1.8	-	-	90.9	6.39	1.2
8	-	-	0.91	1.8	-	90.9	-	6.39	1.2
9	-	-	0.91	-	-	90.9	-	8.19	1.2
m	-	-	0.66	1.33	26.6	-	66.6	4.81	13.3**

* Nb diffusion barrier is utilized [15].

** Cable's cross-section area.

The optimized designs for the different cases are summarized in Table IV. Design based on case 1 shows, that copper is not resistive enough material for switch stabilizer: Long switch cable is needed and the number units is high. Cases 2-3 look promising but LTS might be too unstable as predicted in [4]. Cases 4-5 do not compete with REBCO based designs in terms of A_s or resulting maximum T_m . From cases 6-9, the last one was chosen due to relatively compact resulting design and least number of required units.

B. Electro-thermal behaviour of design based on case 9

The case 9 (See Table III) was chosen. Here its electro-thermal behaviour during magnet de-energization is presented. Currents in the circuit are shown in Fig. 2 and temperature evolution in the switch, parallel resistor and magnet are shown in Fig. 3. Voltage over the magnet and capacitor's voltage are presented in Fig. 4. The resulting stabilizer's resistance was of the order of 0.5 Ω and dump resistance was of the order of 0.1 Ω .

TABLE IV
OPTIMIZED DESIGNS FOR CASES SHOWN IN TABLE III.

Case [#]	l_s [m]	A_s [mm ²]	l_p [m]	A_p [mm ²]	N_E [#]	V_{C0} [V]	C [mF]	T_m [K]	T_e [K]	T_p [K]
1	19.9	2.3	7.5	30.0	25.5	31.4	1.1	64	300	143
2	8.5	2.4	8.9	72.7	4.5	30.5	1.2	285	254	278
3	4.4	2.6	7.3	59.4	6.4	31.4	1.0	178	294	290
4	8.8	44.7	9.1	42.2	4.7	85.2	15.8	299	300	262
5	6.5	37.8	8.5	52.6	4.6	34.2	14.3	291	284	293
6	8.1	8.0	7.5	56.6	5.8	158.8	8.5	207	277	293
7	9.1	8.1	16.3	85.3	12.1	99.9	4.4	104	281	98
8	14.7	8.1	7.6	45.3	6.2	75.2	13.9	189	293	284
9	12.5	10.0	7.9	54.8	5.1	91.0	18.8	267	275	295

As can be seen from Fig. 2, the E³SPreSSO unit is fully quenched in 4 ms. Immediately after the thyristor is triggered a large voltage is over the switch causing the superconductor to carry high current. The current rising time is negligible because of the bifilar configuration which has zero inductance. With 1 kV terminal voltage limit for the given magnet the current decay time below 300 ms can be achieved.

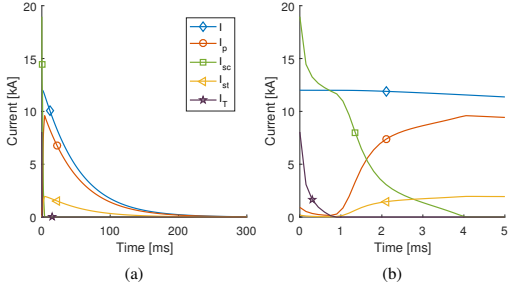


Fig. 2. In Fig. (a) current distribution between different components in the circuit. In Fig. (b) a close-up of (a) is shown during the first 3 ms.

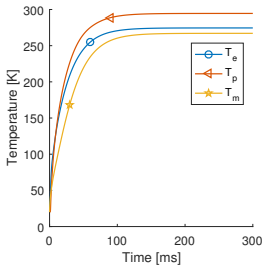


Fig. 3. Temperature evolution in the switch, parallel resistor and the magnet.

C. Varying allowed maximum temperature

Here we investigate required number of E³SPreSSOs to protect a magnet having energy of 1.86 MJ (See Table II). Maximum allowed temperature is varied from 150 to 400. The material fractions in E³SPreSSO are according to the

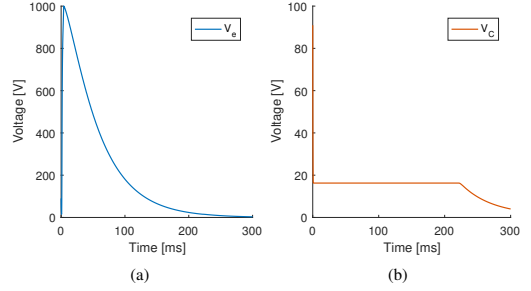


Fig. 4. (a): Voltage over an E³SPreSSO unit during system de-energization. (b): Capacitor's discharge.

reference case 9 (See Table III). Results are shown in Table V. If maximum temperature of 400 K is allowed, then magnet can be protected with 4 E³SPreSSO units. The number of units however more than triples when T_{max} criterion is lowered to 150 K.

TABLE V
OPTIMIZED DESIGNS FOR DIFFERENT ALLOWED MAXIMUM TEMPERATURES.

T_{max} [K]	l_s [m]	A_s [mm ²]	l_p [m]	A_p [mm ²]	N_E [#]	V_{C0} [V]	C [mF]	T_m [K]	T_e [K]	T_p [K]
150	14.9	8.4	9.9	65.2	13.0	173	13.0	97	146	144
200	11.2	10.9	7.7	48.8	11.0	200	11.5	114	199	197
250	10.2	7.6	7.0	48.3	9.0	21	29.5	135	246	246
300	12.6	10.1	11.8	79.8	5.0	89	19.4	290	268	189
350	13.6	7.7	8.0	58.7	4.0	43	10.8	357	291	340
400	10.7	8.1	10.5	73.6	4.0	46	12.5	378	390	245

IV. CONCLUSIONS

A quench protection method E³SPreSSO, designed for large HTS magnets was analyzed and investigated using a simulation and optimization approach developed here. In the approach, the circuit consisting of the magnet and its protection system was parametrized and formulated to be solved as an optimization problem. Minimization for objective function subject to constraints ensures that too high resulting temperatures or voltages to ground during de-energization of the magnet are not allowed. In the simulations, designs obtained, for protecting a 20 T HTS magnet, using different possible switch cables for the E³SPreSSO were studied and compared. Moreover, one switch cable was chosen and the number of required protection units were computed as a function of maximum allowed temperature in the system. Results show that using a switch cable having cross-section area of 8 mm² with copper-nickel-silver stabilizer results in QPS of 5 E³SPreSSO units when 300 K maximum temperature is allowed. Moreover, optimization algorithm based simulation tool is practical for designer. It allows one to freely tune the design into the desired direction of performance via easily changeable constraints. Therefore, a lot of effort can be saved when designs are not obtained via input parameters.

REFERENCES

- [1] T. Salmi, and A. Stenvall, "Modeling Quench Protection Heater Delays in an HTS Coil" *IEEE Trans. Appl. Supercond.* vol. 25, no. 3, 2015, Art. ID. 0500205.
- [2] The European Organization for Nuclear Research, home page: <http://home.web.cern.ch/>
- [3] L. Rossi *et al.*, "The EuCARD-2 Future Magnets European Collaboration for Accelerator-Quality HTS Magnets" *IEEE Trans. Appl. Supercond.* vol. 25, no. 3, 2015, Art. ID. 4001007.
- [4] J. van Nugteren *et al.*, "E³SPreSSO: A Quench Protection System for High Field Superconducting Magnets," *IEEE Transactions on Applied Superconductivity*, 2017, under preparation.
- [5] Future Circular Collider web site: <http://fcc.web.cern.ch>.
- [6] M. Prioli *et al.*, "Strategies to reduce the voltage to ground in the FCC main dipole circuits," Poster presented in FCC Week 2017, Berlin.
- [7] J. van Nugteren, F. Wolf, J. Murtoimäki *et al.*, "Conductor Cost Optimized Idealized Dipole Cross-Sections for Accelerator Applications," *IEEE Transactions on Applied Superconductivity*, 2017, under preparation.
- [8] MATLAB, The MathWorks, Inc., Natick, Massachusetts, United States.
- [9] M. N. Wilson, *Superconducting magnets* (p. 78). Oxford, U.K.: Clarendon, 1983.
- [10] P. Eckels, "CryoComp Rapid Cryogenic Design: 88 Materials in Properties Database". Thermal Analysis Software.
- [11] R. Byrd, J. Gilbert, and J. Nocedal, "A trust region method based on interior point techniques for nonlinear programming" *Math. Program.* vol. 89, no. 1, 2000, pp. 149-185.
- [12] L. Bottura, "A practical fit for the critical surface of NbTi" *IEEE Transactions on Applied Superconductivity* vol. 10, no. 1, 2000, pp. 1054-1057.
- [13] V. Lahtinen, M. Lyly, A. Stenvall, and T. Tarhasaari, "Comparison of three eddy current formulations for superconductor hysteresis loss modelling" *Supercond. Sci. Technol.* vol. 25, no. 11, 2012, Art. ID. 115001.
- [14] J. Fleiter and A. Ballarino, "Parameterization of critical surface of REBCO conductors from Fujikura." CERN internal note, 2014, EDMS 1426239.
- [15] M. D. Sumption, M. Bhatia, X. Wu, M. Rindfleisch, M. Tomsic, and E. W. Collings, "Multifilamentary, in situ route, Cu-stabilized MgB₂ strands" *Supercond. Sci. Technol.* vol. 18, no. 5, 2005, pp. 730-734.

PUBLICATION

V

How to Computationally Determine the Maximum Stable Operation Current of an HTS Magnet

J. Ruuskanen, A. Stenvall, V. Lahtinen, J. van Nugteren, G. Kirby and
J. Murtomäki

IEEE Transactions on Applied Superconductivity 29.5 (2019), 4701204

DOI: 10.1109/TASC.2019.2898315

Publication reprinted with the permission of the copyright holders

How to Computationally Determine the Maximum Stable Operation Current of an HTS Magnet

Janne Ruuskanen, Antti Stenvall, Valteri Lahtinen, Jeroen van Nugteren, Glyn Kirby, and Jaakko Murtomäki

Abstract—The short-sample critical current is only an indicative property for the maximum current a magnet can be continuously operated with. This was especially visible in the experiments of one of the world’s first Roebel-cable based HTS dipole magnet prototype built and tested at CERN in 2017 where the thermal runaway developed very slowly in many cases. Consequently, the maximum stable operation current could be overstepped and stable operation could be recovered by lowering the current below the maximum of the stable range again. It is non-trivial to quantitatively predict this behaviour from the critical current measurements which are observed under specific cooling conditions and based on an arbitrarily selected electric field criterion for the critical current. To make more rigorous predictions on the maximum stable operation current, one needs to consider in detail the interplay of cooling over the magnet surface and heat generation in the winding. This paper presents a methodology to determine the maximum stable operation current for a given magnet, as well as studies its mathematical background. Insight to this problem comes from the Roebel-cable based dipole magnet studied at CERN during 2017.

Index Terms—HTS magnets, Modeling, Finite element methods, Optimization

I. INTRODUCTION

REBCO based high temperature superconductors (HTS) have prospects for producing magnetic fields beyond 20 T at low temperatures. Therefore, they enable a field range that cannot be reached with low temperature superconductors. Possible applications are high frequency NMR devices and high-field accelerator magnets. Currently, the use of REBCO based magnets in future accelerators is under consideration at CERN. [1]

Recently, a project EUCARD-2 [2] was finished with the aim of demonstrating the performance of HTS based accelerator magnet prototype. In the project, a Roebel-cable [3] based HTS dipole-magnet, Feather-M2 depicted in Fig. 1, was designed and built. The magnet was tested for the first time in 2017. The test results were presented in [4]. During the measurements, unexpected behavior was observed: the magnet could be operated at higher currents than the short sample

critical current measurement predicted. This behavior is believed to be linked with the measured low n -value, which can be typical for Roebel-cables. However, the research problem on predicting the maximum stable operation current is clearly related to the thermal balance between the heat generation in the winding and the cooling of the magnet. This is different to magnets made from low temperature superconductors (LTS) where maximum currents can be predicted from near-adiabatic short-sample currents. The possibility of operating an HTS magnet at currents above its short sample critical current seems to be related to the cooling and gradual $V - I$ dependency.

Consequently, the critical current concept, based on arbitrarily selected voltage criterion, does not work for HTS coils having gradual $V - I$ dependency, as reported in [5] and already by Ishiyama *et al.* in [6] where they proposed a definition for the coil’s maximum current to be based on the balance between the heat generation and cooling in the coil. Their approach was for a cryocooler-cooled system, hence the cooling power could be obtained directly from the cooler’s cooling curve. However, in modelling thermodynamics in fluid cooled HTS coils, it is necessary to take the local cooling into account. Several different cooling models are utilized for example in [7], where the thermal stability of HTS composite tapes was numerically modelled.

In this paper, a method for computationally determining the maximum stable operation current is presented. We scrutinize the helium gas cooled Feather-M2 to demonstrate the feasibility of the proposed methodology. In the method, an optimization problem is formulated and solved to compute the maximum stable operation current. The method is based on the thermal model detailed in [8]. Using this methodology, we investigate the influence of cooling efficiency and cable properties on the maximum stable operation current. The paper is outlined as follows. Next, the methodology, utilized for determining the maximum stable operation current of an HTS magnet, is discussed. Then, the simulation results are presented with appropriate discussion, and finally, conclusions are drawn.

II. METHODOLOGY

This section reviews first the thermal model detailed in [8]. Then, we present a concept for the stability of HTS magnets which does not seem to depend on short-term disturbances of low magnitude, on contrary to LTS magnets [9], [10]. Finally, we present a mathematically rigorous way to find the maximum stable operation current of an HTS magnet.

Manuscript received October 30, 2018. This work was supported by the EuCARD2 project, which is cofunded by the partners and the European Commission under Capacities 7th Framework Programme, Grant Agreement 312453 and the Academy of Finland project #287027. (Corresponding author: Janne Ruuskanen)

J. Ruuskanen, A. Stenvall, V. Lahtinen and J. Murtomäki are with Tampere University, Unit of Electrical Engineering, Research Group on Modelling and Superconductivity, FIN-33101 Tampere, Finland; e-mail: janne.ruuskanen@tuni.fi.

J. van Nugteren, G. Kirby and J. Murtomäki are with CERN, Geneva CH-1211, Switzerland.

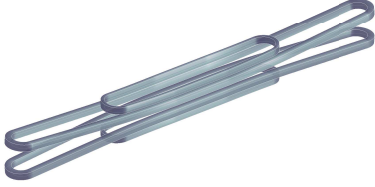


Fig. 1. Depiction of the dipole magnet Feather-M2. Both of the poles, Feather-M2.1 and Feather-M2.2 consist of two racetrack shaped coils, a longer and a shorter one.

A. Computational model

In this work, a simulation tool for performing thermal simulations for superconducting magnets was utilized. The discretization method is based on an assumption on homogeneous temperature in the cable's cross-section. Therefore, the temperature in the magnet can be modelled on 1-dimensional domain. The equation to be solved is

$$C_V \frac{d}{dt} T = \frac{d}{dx} \left(\lambda \frac{d}{dx} T \right) + Q^+ + Q^- + Q^{\parallel}, \quad (1)$$

where T and λ represent the temperature along the cable and the thermal conductivity in the cable's longitudinal direction, respectively. The terms C_V , Q^+ , Q^- and Q^{\parallel} represent the volumetric heat capacity, the volumetric heat generation, the volumetric cooling and the heat transfer between the cable turns, respectively. In this paper, we only revise the terms Q^+ and Q^- , which are essential for understanding the methodology presented and utilized in this work. Details on discretizing and solving (1) are presented in [8], [11].

The heat generates in the cable's superconducting (sc) and in the normal conducting (nc) fractions, f_{sc} and f_{nc} , respectively. Hence, the heat generation in the cable can be expressed as

$$Q^+ = f_{sc} E_{sc} J_{sc} + f_{nc} E_{nc} J_{nc}, \quad (2)$$

where the current density in the superconducting fraction and in the normal conducting fraction of the cross-section are $J_{sc} = I_{sc}/A_{sc}$ and $J_{nc} = I_{nc}/A_{nc}$, respectively. Here I_{\pm} refers to current and A_{\pm} to area. The electric field in the superconducting material E_{sc} is expressed using the power law as

$$E_{sc} = E_c \left(\frac{I_{sc}}{I_c} \right)^n, \quad (3)$$

where E_c and n are the electric field criterion and the n -value, respectively.

In the cable's longitudinal direction, the local critical current I_c is computed by integrating the critical current density function J_c over the superconducting fraction of the cable's cross-section A_{sc} as

$$I_c = \int_{A_{sc}} \alpha J_c(T, \hat{\mathbf{B}} I) dA,$$

where $\hat{\mathbf{B}}$ is the magnetic flux density per magnet's unit current. This means that that assumption on linear $\mathbf{B}(I_{op})$, where I_{op}

is the magnet's operation current, dependency is deployed. Moreover, a J_c scaling law is scaled with α to represent the J_c characteristic of our application. We utilize the scaling law presented in [12].

The electric field in the normal conducting material composite is modelled using

$$E_{nc} = \rho_{nc} J_{nc},$$

where ρ_{nc} is the resistivity of the normal conducting fraction [13]. Furthermore, our assumption is that $E_{sc} = E_{nc}$ everywhere and hence I_{sc} and $I_{nc}(= I_{op} - I_{sc})$, where I_{op} is the operation current, can be solved.

As emphasized already, it is necessary to take the cooling into account in the modelling. In the utilized computational model, the cooling in the winding is modelled using

$$Q^- = h \frac{T_{op} - T}{c}, \quad (4)$$

where $(T_{op} - T)$ is the temperature difference between the coolant and the winding, respectively. The parameter h represents heat transfer coefficient. The coefficient c is defined as $c = A/p$, where A is the the cross-section area of the homogenized cable and p is the wetted perimeter of the cable's cross-section.

B. Stability concept

In this work, we define the stability of HTS magnet by investigating the interplay between heat generation and cooling in the winding. This concept was proposed in [6] and utilized already at least in [8].

The heating power P and the cooling power C in the magnet volume are used to determine, whether the magnet is thermally stable or not. The heating power represents the power at which heat is generated in the winding volume Ω , and is computed as

$$P(t) = \int_{\Omega} Q^+ d\Omega = A \int_0^L Q^+ dx, \quad (5)$$

where L is the cable length, i.e. $[0, L]$ form the modelling domain at which (1) is solved. We used adiabatic boundary conditions at 0 and L in this work. The counterpart of heating power, the cooling power, is computed as

$$C(t) = \int_{\Omega} Q^- d\Omega = \int_0^L ph(T_{op} - T) dx. \quad (6)$$

The cooling power represents the cooling power in the magnet volume due to the heat flux between the surface of the winding and the coolant.

Based on the quantities P and C , we define a magnet to be thermally stable according to the following definition.

Definition 1. A magnet, operated in constant conditions (T_{op}, I_{op}) , is thermally stable if and only if $\exists t_0 > 0$ such that

$$(P + C)(t) \leq 0, \quad \forall t \geq t_0. \quad (7)$$

Corollary 1. At constant operation conditions,

$\exists t_0 > 0$ s.t. $(P + C)(t_0) \leq 0 \Rightarrow (P + C)(t) \leq 0, \forall t \geq t_0$.

In summary, in constant operation conditions, we can determine, whether the magnet is stable or not by computing if there is a time when the balance between the heating and the cooling exists. This is computationally possible to achieve unlike testing the balance when time goes to infinity.

C. Determining the maximum stable operation current

The maximum stable operation current I_{mas} of an HTS magnet can be determined by solving an optimization problem. The formulation of the problem is intuitive: maximize the operation current such that, the magnet is stable. Hence, the problem can be expressed as

$$\begin{aligned} \max \quad & I \\ \text{s.t.} \quad & (P + C)(t_0) \leq 0 \end{aligned} \quad (8)$$

where the non-linear inequality constraint define the solution of the optimization problem to be feasible, only if the current I , results in stable magnet operation as defined in Definition 1. As the stability criterion, the result of Corollary 1 is utilized.

III. RESULTS AND DISCUSSION

In this section, we utilize the presented methodology for determining the maximum stable operation current of the HTS magnet, Feather-M2. We let this simulation result be the reference case for the following three parametric studies, where the model parameters n , α and h were varied and I_{mas} computed in order to investigate the influence of those parameters on the stability of the magnet. Moreover, in all of the simulations that are next presented we utilize the parameters listed in Table I unless otherwise stated. The model

TABLE I
SIMULATION PARAMETERS.

parameter	value	unit	description
α	0.17		scaling factor of J_c scaling law
n	2.8		n -value
E_c	109	$\mu\text{V/m}$	electric field criterion
h	85	$\text{W/m}^2\text{K}$	heat transfer coefficient
t_0	200	s	stability criterion time
T_{op}	21	K	coolant temperature

parameters $\mathbf{x} = [\alpha \ n \ E_c \ h]$ were obtained as a solution of an inverse problem $E = M(\mathbf{x}, I_{\text{op}})$, where the thermal model M describes the relationship between the model parameters and the measured average electric field E in the magnet due to operation current I_{op} . This process is detailed in [8]. These particular values for the model parameters were achieved for the data shown in Fig. 2, where the model predictions $M(\mathbf{x}, I_{\text{op}})$ are compared with the measured data E .

A. Reference case

The I_{mas} of the reference case was solved using the parameters listed in Table I. The obtained solution for I_{mas} was 5162 A. Fig. 3 shows the maximum temperature T_{max} and the power balance $P + C$ in the magnet as a function of

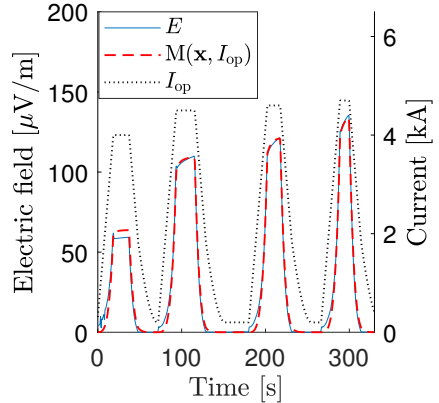


Fig. 2. Measured and simulated average electric field in the magnet and corresponding magnet operation current I_{op} as a function of time. Figure adopted from [8].

time for the three different operation currents $0.99I_{\text{mas}}$, I_{mas} and $1.01I_{\text{mas}}$ from left to right, respectively.

The results show that the maximum stable operation current is within 1% from the simulated I_{mas} . At 1% lower operation current, the maximum temperature in the magnet stabilized to 3.1 K lower value (30.34 K) than at simulated I_{mas} . However, when the operation current was increased to 1% above the I_{mas} , thermal runaway occurred before 100 s simulation time was reached.

As seen, the thermal runaway develops very slowly (in tens of seconds rather than in milliseconds like with LTS windings) when I_{op} is slightly above the stable operation current range. Therefore, in terms of magnet protection, there is plenty of time to react before reaching temperatures that might damage the magnet. Similarly, one could operate for a short period of time above the maximum stable operation current and return to safe range without a quench and magnet de-energization. This kind of operation is typically not possible with LTS magnets.

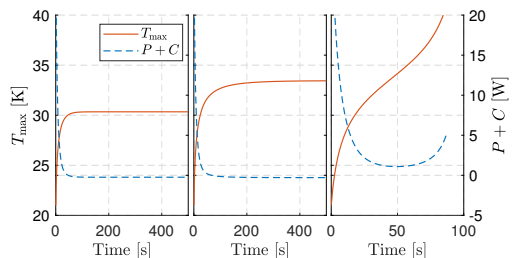


Fig. 3. The maximum temperature and the power balance as a function of time in the magnet at three different operation currents. The figures from left to right correspond to I_{op} of $0.99I_{\text{mas}}$, I_{mas} and $1.01I_{\text{mas}}$, respectively.

B. The effect of n -value, α and h on I_{mas}

The maximum stable operation current was computed as a function of n -value, α and the heat transfer coefficient. By performing these parametric analyses, we simulated, how the cable properties, related to n and α , and the cooling efficiency, related to the heat transfer coefficient, affect to the maximum stable operation current of the magnet.

Fig. 4 shows that I_{mas} decreased in this case as a function of n -value. This can be explained as follows. For lower n -values the heat generation is more gradual and therefore it is possible to balance P with C up to operation currents above 6 kA with $n = 2$. At high n -values, I_{mas} decreased gradually down to 3550 A. This is due to more aggressive heat generation with higher n -values which the cooling cannot balance at as high operation currents as in case of lower n . As a conclusion, lower n -value results in higher I_{mas} but more heat is generated at lower currents than in case of high n . Consequently, more cooling power is required in order to balance the heat generation if the cable has low n -value.

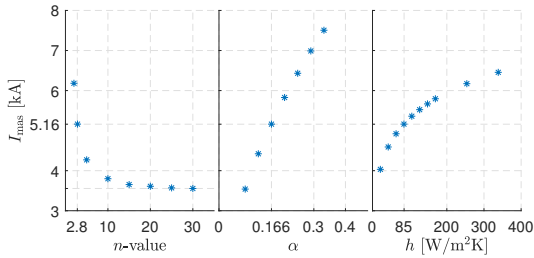


Fig. 4. From left to right, respectively, the maximum stable operation current as a function of n -value, α and the heat transfer coefficient.

The influence of α and h on I_{mas} is more obvious. For cable, having higher critical current density, I_{mas} was higher. Similarly for higher heat transfer coefficient, I_{mas} was higher but the dependency was not as linear as in case of α . These results indicate that I_{mas} would saturate at some point if h was increased to a value high enough. As a conclusion, with more powerful cooling system, low n -value or with cable having higher J_c , the magnet could be operated at higher operation currents.

In summary, as expected, magnet's I_{mas} was higher for higher h and α . The n -value dependency was not trivial: for lower n -values, I_{mas} was higher and for higher n -values, above 20, stable magnet operation was not possible anymore above operation currents of 3.6 kA due to more aggressive heat generation, the cooling could not compensate anymore.

IV. CONCLUSIONS

Due to the slanted $V - I$ behavior of HTS based magnets, determining the maximum current based on voltage criterion is arbitrary. A concept for determining the maximum current based on investigating the interplay between heat generation and cooling in the winding is adapted in this paper. Using the concept, the maximum stable operation current was determined by formulating and solving an optimization problem.

Three parametric studies were performed on the heat transfer coefficient h , the scale α of J_c scaling law and cable's n -value.

According to the results, with higher values of α and h , higher I_{mas} was predicted. Conversely, higher I_{mas} was predicted for lower n -values while for higher n , I_{mas} decreased to a value around 3550 A. This behavior is due to the more aggressive heat generation at higher n than at lower n . Consequently, for lower n and hence more gradual heat generation, the magnet can be operated at overcritical currents, above E_c . We also found out, like the experiments demonstrated too, that there are tens of seconds time to react before thermal runaway, even if operation current is above I_{mas} .

Further, there is still lot to explore on this topic even with the current model, for example, how do the investigated parameters influence on the allowed time to operate with a current above I_{mas} . In addition, the optimization problem could be solved, and I_{mas} predicted, in case if a thermal disturbance occurred in the magnet during the simulation. Then the maximum stable operation current would be such that the magnet would remain stable even if the disturbance occurred.

REFERENCES

- [1] J. van Nugteren, G. Kirby, J. Murtoimäki, G. DeRijk, L. Rossi, and A. Stenvall, "Toward REBCO 20 T+ Dipoles for Accelerators" *IEEE Trans. Appl. Supercond.* vol. 28, no. 4, 2018, pp. 1-9.
- [2] L. Rossi *et al.*, "The EuCARD2 Future Magnets Program for Particle Accelerator High-Field Dipoles: Review of Results and Next Steps" *IEEE Trans. Appl. Supercond.* vol. 28, no. 3, 2018, pp. 1-10.
- [3] W. Goldacker *et al.*, "ROEBEL Assembled Coated Conductors (RACC): Preparation, Properties and Progress" *IEEE Trans. Appl. Supercond.* vol. 17, no. 2, 2007, pp. 3398-3401.
- [4] J. van. Nugteren *et al.*, "Powering of an HTS dipole insert-magnet operated standalone in helium gas between 5 and 85 K" *Supercond. Sci. Technol.* vol. 31, no. 6, 2018, Art. ID. 065002.
- [5] V. S. Vysotsky, A. L. Rakhmanov Yu. A. Ilyin, "Novel approaches to describe stability and quench of HTS devices," in *Superconductivity Research Developments*. Commack, NY, USA: Nova, 2008, ch. 9.
- [6] A. Ishiyama, and H. Asai, "A stability criterion for cryocooler-cooled HTS coils" *IEEE Trans. Appl. Supercond.* vol. 11, no. 1, 2001, pp. 1832-1835.
- [7] J. Lehtonen, R. Mikkonen, and J. Paasi, "Stability considerations of a high-temperature superconductor tape at different operating temperatures" *Physica C* vol. 310, no. 1-4, 1998, pp. 340-344.
- [8] J. Ruuskanen *et al.*, "Model-based interpretations on thermodynamics in a high-temperature superconducting dipole magnet" *Supercond. Sci. Technol.* Submitted to the focus issue on Numerical Modelling of High Temperature Superconductors 2019.
- [9] MN. Wilson, and R. Wolf, "Calculation of minimum quench energies in Rutherford cables" *IEEE Trans. Appl. Supercond.* vol. 7, no. 2, 1997, pp. 950-953.
- [10] E. Härö, A. Stenvall, J. van Nugteren, and G. Kirby, "Modelling of Minimum Energy Required to Quench an HTS Magnet with a Strip Heater" *IEEE Trans. Appl. Supercond.* vol. 25, no. 6, 2015, Art. ID. 4701505.
- [11] J. Ruuskanen, A. Stenvall, and V. Lahtinen, "Predicting Heat Propagation in Roebel-Cable-Based Accelerator Magnet Prototype: One-Dimensional Approach With Coupled Turns" *IEEE Trans. Appl. Supercond.* vol. 27, no. 4, 2017, pp. 1-5.
- [12] J. Fleiter and A. Ballarino, "Parameterization of the critical surface of REBCO conductors from Fujikura", CERN Internal Note, EDMS Nr: 1426239, 2014.
- [13] A. Stenvall, A. Korpela, R. Mikkonen, and G. Grasso, "Stability considerations of multifilamentary MgB₂ tape" *Supercond. Sci. Technol.* vol. 19, no. 2, 2006, pp. 184-189.

- [14] J. Murtomäki, J. van Nugteren, G. Kirby, G. de Rijk, L. Rossi, and A. Stenvall, "ICED—Inductively Coupled Energy Dissipater for Future High-Field Accelerator Magnets" *IEEE Trans. Appl. Supercond.* vol. 28, no. 8, 2018, pp. 1-15.

PUBLICATION

VI

Modelling thermodynamics in a high-temperature superconducting dipole magnet: an inverse problem based approach

J. Ruuskanen, A. Stenvall, V. Lahtinen, J. van Nugteren, G. Kirby and
J. Murtomäki

Superconductor Science and Technology 32.9 (2019), 094007

DOI: 10.1088/1361-6668/ab2bc9

Publication reprinted with the permission of the copyright holders

PAPER

Modelling thermodynamics in a high-temperature superconducting dipole magnet: an inverse problem based approach

To cite this article: J Ruuskanen *et al* 2019 *Supercond. Sci. Technol.* **32** 094007

View the [article online](#) for updates and enhancements.






IOP | ebooks™

Bringing you innovative digital publishing with leading voices to create your essential collection of books in STEM research.

Start exploring the collection - download the first chapter of every title for free.

Modelling thermodynamics in a high-temperature superconducting dipole magnet: an inverse problem based approach

J Ruuskanen¹ , A Stenvall¹, V Lahtinen¹ , J van Nugteren² ,
G Kirby² and J Murtomäki¹

¹Tampere University, Korkeakoulunkatu 6, FI-33101 Tampere, Finland

²CERN, CH-1211 Geneva 23, Geneva, Switzerland

E-mail: janne.ruuskanen@tuni.fi

Received 18 January 2019, revised 29 May 2019

Accepted for publication 21 June 2019

Published 2 August 2019



CrossMark

Abstract

The use of practical high temperature superconductors (HTS), REBCO tapes especially, in magnet applications has become possible thanks to the increasing interest of manufacturers. One difficulty has been the nonlinear material properties that are challenging to measure and model. To advance in such, demo systems are needed and they must be thoroughly analyzed. Recently, one of the first HTS dipole magnets was built to study the usability of REBCO Roebel cables in particle accelerator magnets. The prototype magnet Feather-M2 was designed, constructed and tested within EUCARD2 collaboration project at CERN in 2017. In the measurements, the magnet behaved in an unexpected way: the magnet was able to be operated at operation currents above the maximum current that was predicted based on short-sample measurements. Additionally, unexpectedly gradual dependency between magnet's resistive voltage and operation current was observed. In this work, a thermodynamical model is formulated in order to study the behavior of Feather-M2. The model was parametrized and the parameters were solved via inverse problem by finding the best match to experimental results. Thereby insight was gained on the prospects of the utilized thermodynamical model and also on the behavior and operation conditions of the magnet via the inverse problem solutions. To summarize, this paper presents a new methodology for analyzing magnets in operation and applies it to a state-of-the-art magnet.

Keywords: HTS magnets, thermal stability, modelling, optimization

(Some figures may appear in colour only in the online journal)

1. Introduction

High electric current carrying capability of practical high-temperature superconductors (HTS) has been a tempting property to harness into use in applications [1–3]. The main problem in the design process of HTS based devices arises from the highly nonlinear material properties that are challenging to measure and model. Recently, however, the suitability of using high HTS in particle accelerator dipole-magnets was experimentally investigated: a REBCO Roebel cable [4] based prototype magnet, Feather-M2, was designed, constructed and tested within EUCARD2 [5] collaboration

project at CERN [6] in 2017. The specifications in regards of the magnet, measurement set-up and the results were presented in [7].

The measurements revealed magnet behavior not yet in detail analyzed within the HTS community—the magnet could be operated above its critical current (I_c) without quench, where I_c was defined using electric field criterion of $10 \mu\text{V m}^{-1}$. In other words, it was not possible to predict the quench current based on the short sample measurements. This is different behavior from what is expected for low-temperature superconductor (LTS) based magnets since the quench current of an LTS magnet is limited above by the

short-sample I_c . However, the observed unpredicted behavior needed to be investigated and explained.

To study the observed behavior, the heat equation can be solved in the modelling domain representing the magnet under investigation. Research on the thermal modelling of HTS magnets has been done by many authors, e.g. [8–13]. Typically the focus has been on investigating the fast during- and after-quench effects such that the use of adiabatic boundary conditions (cooling is neglected) could have been justified. Typically this kind of modelling is related to the quench simulations in which the focus is mainly on magnet protectability in the occurrence of thermal runaway. However, in order to simulate situation in which the magnet is operated with relatively high currents for long periods of time, the cooling should be taken into account in the modelling as done and discussed in [14–16] to name some.

Modelling thermodynamics in a superconducting magnet is a multiphysical problem. When formulating the problem using different models, the values of some model parameters may be unknown, such as, the value for the heat transfer coefficient in the model describing the cooling at the boundary of the winding. Values for such model parameters can be hard to find from literature for a particular case. However, if there exists measured data on the phenomenon one is trying to model, it can be used to solve unknown model parameters. Such problems, in which based on results known beforehand one calculates the causes, are called inverse problems.

An inverse problem can be solved in various different ways depending on their nature. One way of obtaining a solution for such a problem is to re-formulate it as an optimization problem and solve it using optimization algorithms. For example in [17], the Kim model used to describe the critical electric current density in REBCO superconducting material was parametrized and the parameters were obtained as a solution of an optimization problem based on measured data. In the field of astronomy and astrophysics, recently, the parameters of the equation of state of the cold dense matter inside neutron stars based on x-ray measurements [18] were determined by solving an Bayesian parameter optimization problem. In [19], magnet cross-section was parametrized and optimized based on minimum cost criterion.

This paper focuses on modelling thermodynamics in an HTS magnet and studying its thermal stability in operation. In this work, a thermodynamical model is formulated in order to model the thermal behavior of an HTS magnet. The aim is to improve our understanding on the magnet behavior and on the other hand, gain insight on the capability of the implemented modelling tool in predicting the thermodynamics in the magnet. In order to do so, the model is parametrized and the parameters are obtained based on measured data on the HTS magnet Feather-M2 by means of formulating and solving an inverse problem.

The paper is outlined as follows. Section 2 continues the introductory part of the paper by reviewing the essential information on the measurements of Feather-M2 for this work. In sections 3 and 4, the methodology utilized in this work is presented. Section 3 concentrates on the multiphysical model of the magnet and section 4 on solving via



Figure 1. Depiction of the dipole magnet Feather-M2. © 2019 IEEE. Reprinted, with permission, from [20].

Table 1. Magnet specifications, as used in the modelling.

Dimension	Value	Unit
Number of turns (wing deck)	4	
Number of turns (central deck)	8	
Total cable length	37	m
Total tape length	555	m
Magnet length	720	mm
Peak field (6.5 kA, 5.7 K)	3.3	T

inverse problem the unknown parameters. In section 5, the simulation results are shown with appropriate discussion. Finally conclusions are drawn in section 6.

2. Measured data on HTS magnet Feather-M2

Feather-M2, a Roebel cable based accelerator magnet prototype, studied in this work, is one of the first magnets of its type built and tested. In this section, the physical system, consisting of the magnet and the cooling environment, are presented to sufficient detail. In addition, the measurement data, adequate for this work, is shown. The original work regarding to the measurement results was presented in [7].

2.1. Feather-M2

A representation of Feather-M2 is shown in figure 1 and the magnet specifications are listed in table 1. The magnet has two poles, named as Feather-M2.1 and Feather-M2.2. Both of them consists of two race track shape coils—a larger central deck and a smaller wing deck. The central deck has 8 turns of Roebel cable and the wing deck has 4 turns. The total length of Roebel cable required for the 0.7 m long magnet was 37 m, i.e. 18.5 m per pole. It was reported that the maximum achieved magnetic field in the magnet aperture was 3.3 T, at 5.7 K, at the current of 6.5 kA [7].

The Roebel cable was made by SuperOx [21]. The REBCO tapes utilized in making the cable were manufactured by Sunam [22]. The cable specifications are listed in table 2 and the specifications related to the tape, as used in the modelling, are listed in table 3. The cable consists of 15 tapes that are cabled into Roebel form (see [7]). This results in cable cross-sectional dimensions of 1.2 mm × 12.0 mm. In addition, the cable was insulated with 0.1 mm thick G10 fiber glass, functioning as electric insulation. Hence, the cable's total thickness

Table 2. Roebel-cable specifications, as used in the modelling.

Dimension	Value	Unit
Number of tapes	15	
Cable width	12.0	mm
Cable thickness	1.2	mm
Cable insulation thickness (G10)	0.1	mm

Table 3. Tape specifications, as used in the modelling.

Dimension	Value	Unit
Tape width	5.5	mm
Tape thickness	150	μm
Ag	1	μm
Cu	40	μm
REBCO	1.4	μm
Hastelloy	100	μm
Buffer	7.6	μm

d_i is 1.4 mm and the total width d_w is 12.2 mm. Between two cable turns, the total insulation thickness d_i is 0.2 mm. Each of the tapes in the cable has cross-sectional dimensions of $150 \mu\text{m} \times 5.5 \text{ mm}$, and consists of several different material layers as listed in table 3. Total tape length is 555 m.

2.2. Measurements

The magnet, under investigation in this work, was tested at CERN in SM18 facility [23]. Cooling was realized in a cryostat using forced helium gas flow with adjustable flow rate and temperature. The measurement data shown in figure 2 represents the resistive average electric field over the Feather-M2.1 pole, as a function of operation current I_{op} and time. The average electric field is calculated as the resistive voltage over the pole divided by the cable length. For simplicity, in this paper, we assume the two poles are identical in behavior. Therefore, it is sufficient in the thermal computations to investigate only one of the two magnet poles. Moreover, magnet’s operation temperature T_{op} was measured using temperature sensors mounted inside the magnet structure.

The measurement data in figure 2 shows magnet behavior in various temperatures with different operation currents varying in time. In this work, using this data we will investigate how well the thermodynamical model, next formulated, is capable of predicting the thermodynamical behavior of the magnet.

3. A thermodynamical model for HTS magnet

In this section, a model for predicting thermodynamics in HTS magnets is formulated. In this work the formulation of the model is based on the heat diffusion equation

$$C_v \frac{d}{dt} T = \frac{d}{dx} \left(\lambda \frac{d}{dx} T \right) + Q^+ + Q^- + Q^{\parallel}, \quad (1)$$

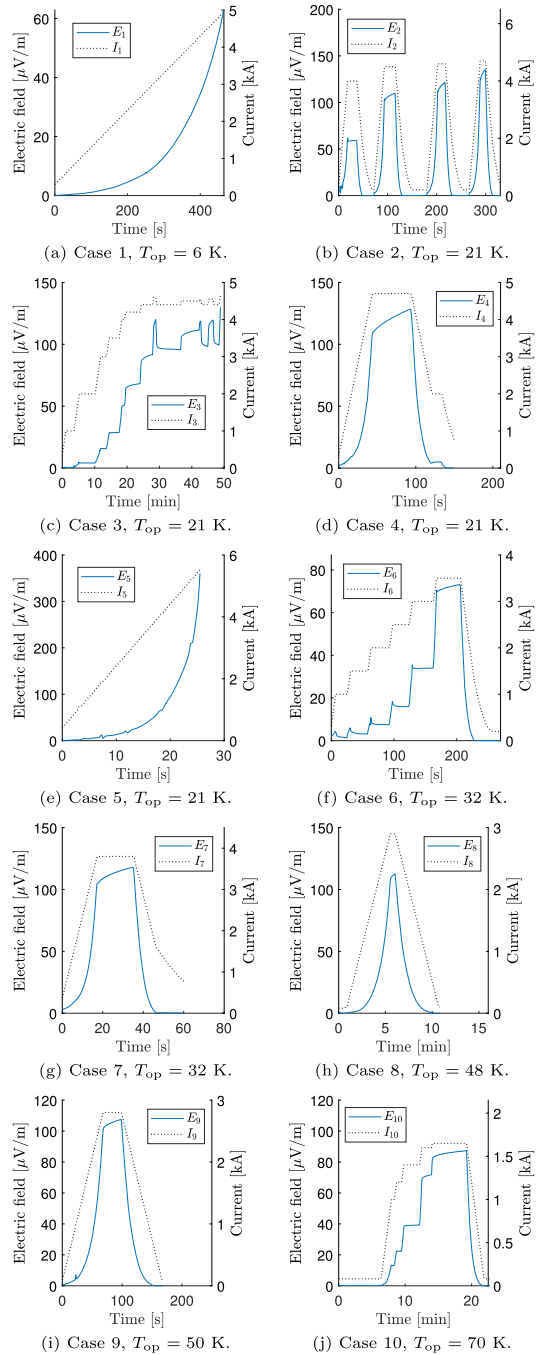


Figure 2. Figures (a)–(j) represent, in each case $i = 1 \dots 10$, the measured average electric field E_i as a function of the operation current I_i and time in Feather-M2.

where T , λ are the temperature and the thermal conductivity, respectively. The terms C_V , Q^+ , Q^- and Q^{\parallel} represent the volumetric heat capacity, the heat generation, the cooling and the heat transfer between the cable turns, respectively.

We omit the magnetoquasistatic phenomena and assume constant electric current density in the cable's normal- and superconducting cross-sectional fraction. Furthermore, homogeneous temperature in the cable cross-section is assumed. Therefore, the temperature in the cable, and hence in the magnet, can be modelled in one-dimensional modelling domain.

This section goes through the constructive framework for performing thermal simulations in a superconducting magnet by formulating the terms of (1). In addition, a discretization method is presented for numerical solution of the heat equation in coil shaped domains.

3.1. Domain and discretization

When solving for continuous field quantities in three-dimensional (3D) geometries, such as electromagnetic fields in coils, the fine details in the geometry require a fine mesh resulting in a large number of degrees of freedoms. However, in some cases, fine meshing can be avoided by choices on the dimension of the modelling domain and its discretization, as done in this work.

In this simulation approach, the modelling decision on homogeneous temperature in the cable cross-section is deployed [10]. Therefore, the heat transfer along the cable can be modelled utilizing one-dimensional (1D) modelling domain, which in this work was discretized using the Galerkin finite element method with linear basis functions.

The 3D to 1D reduction in dimension can be illustrated by first having a look at figure 3, where a part of a coil, a piece of two adjacent insulated cable turns, is depicted. After homogenizing the cable cross-section, a coil can be illustrated as a spiral shown in figure 4, where the cable progression and adjacency is visualized. To emphasize, even though we have formulated our model for 1D modelling domain, we still utilize the cable-to-cable heat conduction as will be shown.

3.2. Material properties

Due to modelling decision on dimension reduction to 1D, the properties, C_V , λ and ρ_{nc} must be homogenized over the cable cross-section [24].

The formulae for computing the material properties of homogenized materials are the following three.

$$C_V = \sum_{i=1}^m f_i \cdot C_V^i \quad (2)$$

$$\lambda = \sum_{i=1}^m f_i \cdot \lambda^i \quad (3)$$

$$\rho_{nc} = \left(\sum_{i=1}^n \frac{g_i}{\rho_{nc}^i} \right)^{-1}. \quad (4)$$

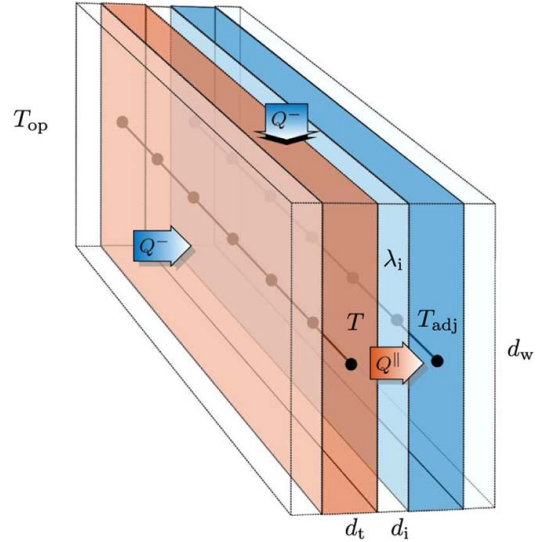


Figure 3. An illustration of a piece of two adjacent insulated cable turns. Figure illustrates the different heat flux terms, i.e. the one from turn to another (Q^{\parallel}), and also the cooling flux (Q^-) on the exposed surfaces of the winding. Cable insulation is visible only in between the cable turns.

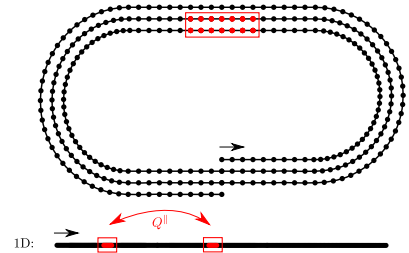


Figure 4. A visualization of the progression and adjacency of the homogenized cable. The coil piece shown in figure 3 is marked as the boxed regions.

In equations (2) and (3), m refers to the number of different materials in the cable, including the superconducting material, such that $\sum_{i=1}^m f_i = 1$, where f_i is the fraction of material i . Equation (4) describes the resistivity of the homogenized normal conducting materials of the cable, where superconducting material is not involved, i.e. $\sum_{i=1}^n g_i = 1$ where $n = m - 1$ is the number of normal conducting materials, including the insulators which naturally have very high resistivity, in the cable and g_i is the fraction of material i in the cross-sectional area of normal conducting materials.

3.3. Critical current

Critical current is a quantity used to describe the $E_{sc}(I_{sc})$ relation, i.e. the power law (6), in the superconducting material of the cable together with the electric field criterion and

the n -value. On its own, it is a somewhat arbitrary quantity for superconductors with low n -value due to gradual dependency. It is, however, necessary data on the superconductor's behavior that is utilized in the power law model.

The measurement data on superconductor's I_c properties is typically obtained and performed for single superconducting wires, short samples. A single I_c measurement point is determined in certain cooling conditions and temperature by increasing sample's current until the voltage reaches arbitrarily selected value—the critical voltage (V_c). For modelling purposes, the obtained values for critical voltage criterion V_c and critical current are often scaled to critical field quantities critical current density J_c and critical electric field E_c . Using this data, interpolating function J_c is fitted to match the measured data. In addition to temperature, magnetic field is one variable in the measurements and thus in the J_c function. In the case of REBCO tapes, wide compared to their thickness, the direction of the magnetic field has a significant influence on J_c .

In this work, we take a measurement based J_c scaling law and commence formulating a computational model for I_c in the superconducting material used in the magnet.

As the modelling domain in the approach utilized in this work is one-dimensional, we are interested in the local cross-sectional critical current along the length of the cable in the magnet. It is computed by integrating J_c over the superconducting parts of the cable cross-section as

$$I_c(T, I_{op}, \alpha) = \int_{A_{sc}} \alpha J_c(T, \hat{\mathbf{B}}_{I_{op}}) dA, \quad (5)$$

where $\hat{\mathbf{B}}$ is pre-computed local magnetic flux density per unit current in the three-dimensional magnet geometry. Note that the function parameters are denoted here for clarification. Furthermore, linear $\mathbf{B}(I_{op})$ dependency is assumed, where I_{op} is the operation current of the magnet. The scaling coefficient α is utilized to scale a J_c scaling law to describe the J_c characteristics of the utilized superconductor in the application to be modelled. Furthermore, this I_c is needed for computing the local cross-sectional electric field and eventually for computing the local heat generation in the modelling domain.

3.4. Heat generation

In superconducting wire, losses can be generated in both, the superconducting fraction (f_{sc}) and in the normal conducting fraction (f_{nc}) of the conductor. Due to significantly different E (J) behavior in f_{sc} and f_{nc} , the heat generation in the two fractions is modelled separately by solving the electric current division based on the $E - J$ characteristics in the two fractions.

In the superconducting material the electric field is modelled using the power law

$$E_{sc} = E_c \left(\frac{I_{sc}}{I_c} \right)^n, \quad (6)$$

where E_c is the electric field criterion and n the n -value that characterizes the steepness of the relation. The electric current

I_{sc} is the current flowing in the f_{sc} with constant density of J_{sc} . Hence, the heat generation in f_{sc} is computed as $E_{sc} J_{sc} = E_{sc} I_{sc} / A_{sc}$, where A_{sc} is the area of superconducting material in the cross-section of the cable (A). In the normal conducting fraction, E_{nc} due to the electric current density $J_{nc} = I_{nc} / A_{nc}$ is modelled according to the Ohm's law as $E_{nc} = \rho_{nc} J_{nc}$, where ρ_{nc} is the effective resistivity of the homogenized materials of f_{nc} having cross-sectional area of $A_{nc} = f_{nc} A$.

The total current, i.e. the operation current (I_{op}), is assumed to divide between the two fractions into I_{sc} and I_{nc} such that $E_{sc} = E_{nc}$ and $I_{op} = I_{sc} + I_{nc}$ hold. Consequently the current in the normal conducting part of the cross-section, can be derived as follows.

$$\begin{aligned} E_{nc} &= E_{sc} \\ \Leftrightarrow \rho_{nc} \frac{I_{nc}}{A_{nc}} &= E_c \left(\frac{I_{sc}}{I_c} \right)^n \\ \Leftrightarrow I_{nc} &= E_c \left(\frac{I_{sc}}{I_c} \right)^n \frac{A_{nc}}{\rho_{nc}} \\ \Leftrightarrow I_{nc} &= E_c \left(\frac{I_{op} - I_{nc}}{I_c} \right)^n \frac{A_{nc}}{\rho_{nc}}. \end{aligned} \quad (7)$$

Hence, the electric current in the normal conducting fraction can be solved from the nonlinear equation

$$I_{nc} - E_c \left(\frac{I_{op} - I_{nc}}{I_c} \right)^n \frac{A_{nc}}{\rho_{nc}} = 0 \quad (8)$$

and consequently I_{sc} can be calculated as $I_{sc} = I_{op} - I_{nc}$.

As now the current division in the superconducting and normal conducting fractions is known, the volumetric heat generation Q^+ in the homogenized cable is derived as

$$\begin{aligned} Q^+ &= f_{sc} E_{sc} J_{sc} + f_{nc} E_{nc} J_{nc} \\ &= f_{sc} E_c \left(\frac{I_{sc}}{I_c} \right)^n \frac{I_{sc}}{A_{sc}} + f_{nc} \rho_{nc} \left(\frac{I_{nc}}{A_{nc}} \right)^2. \end{aligned} \quad (9)$$

Note that $f_{sc} + f_{nc} = 1$ has to hold.

3.5. Cooling

Cooling is necessary to take into account when modelling thermodynamics in HTS magnets, as demonstrated for example in [20].

In this work, local cooling on the cable is taken into account in the computations using

$$Q^- = h \frac{T_{op} - T}{c}, \quad (10)$$

where the heat flux between the coolant and the surface of the winding is determined by cooling coefficient h and the temperature difference between the cooling environment (T_{op}) and the cable (T). Moreover, the scaling factor c is calculated as

$$c = \frac{A}{p}, \quad (11)$$

where A is the cross-sectional area of the cable and p is the local wetted perimeter³. The purpose of c is to scale the cooling on the surface of an element to cooling in the volume of the element.

There are many uncertainties related to this cooling model. The largest error comes with the facts that Q^- , in reality, is doubtedly a linear function of T , and h varies also as a function of location on the magnet surface in the cryostat. Moreover, due to various structures covering the winding it is hard to determine, how the wetted perimeter should be chosen for each cable turn. However, in this work, we chose this simple model for cooling in order to investigate its prospects.

3.6. Heat transfer between cable turns

The heat transfer between the cable turns in one-dimensional modelling domain is modelled as local heat flux similarly as the cooling model. Figures 3 and 4 illustrate how two adjacent turns are coupled in the one-dimensional domain.

The local flux to a cable turn from an adjacent one is expressed as

$$Q^{\parallel} = \lambda_i \frac{T_{\text{adj}} - T}{d_i c}, \quad (12)$$

where T and T_{adj} represent temperatures in two adjacent points in two neighboring cable turns separated by insulation material, having the thickness of d_i . The material property of the insulation material λ_i , describes the temperature dependent thermal conductivity of the insulation material. The thermal conductivity is evaluated at the average temperature of T and T_{adj} . In this case, in the computation of c , the wetted perimeter is the width of the cable.

4. The inverse problem formulation

Often some parameters related to mathematical theories or models are unknown or difficult to determine for a particular case of interest. This is the case in this work too. For example, the cooling coefficient h in the utilized cooling model (10) is difficult to estimate. The same applies to three other parameters: α , n -value and E_c . It is not straight-forward to give values for the parameters such that the model is able to predict as well as possible the behavior of the device in various different situations. In this work we formulate and solve an inverse problem in order to obtain the unknown parameters of our thermodynamical model.

The parameters to be solved, as elements of \mathbf{x} , are $\mathbf{x} = [\alpha, n, E_c, h]$. Recall, α is the J_c scaling coefficient in (5) and h the cooling coefficient of the cooling model (10). Parameters n and E_c characterize the $E_{sc}(J_{sc})$ relation in (6). The model M , i.e. the thermodynamical model, relates the parameters \mathbf{x} with the observed data on average resistive electric field, computed as measured resistive voltage divided by cable length. We want the model M to predict the

³ For example, if at a given point in the modelling domain, all the faces of cable were exposed to the cooling, then the wetted perimeter would be calculated as $p = 2d_w + 2d_t$.

measured E of the magnet as well as possible in given operation conditions ($T_{\text{op}}, I_{\text{op}}$). Hence, the inverse problem can be expressed as: Find α, n, E_c and h such that

$$E_i = M(\mathbf{x}, I_i), \quad (13)$$

where I_i represent the operation current as a function of time and E_i is the corresponding measurement data on average electric field. The problem is nonlinear, therefore, (13) has to be reformulated to an optimization problem in order to obtain the best candidate for \mathbf{x} so that $M(\mathbf{x}, I_{\text{op}})$ is as close as E as possible.

An optimization problem consists of an objective function to be minimized subject to constraints that define the set of feasible solutions. In this work, the objective is to minimize the difference between the measured and simulated average electric field in the time interval $[0, t_m]$, where t_m corresponds to duration of the measurement which started at $t = 0$ s. For the norm, measuring the difference $E - M(\mathbf{x}, I_{\text{op}})$, we chose the time integral of the absolute value of difference. Hence, the minimization problem can be formulated as

$$\begin{aligned} \min_{\mathbf{x}} \int_0^{t_m} |E_i - M(\mathbf{x}_i, I_i)(t)| dt \\ \text{s.t. } \mathbf{b}_l \leq \mathbf{x} \leq \mathbf{b}_u, \end{aligned} \quad (14)$$

where the vectors \mathbf{b}_l and \mathbf{b}_u are the parameter-wise lower- and upper bounds, respectively. These bounds are used to guide the optimization algorithm. The subscript $i = 1 \dots 10$ is the number of the case.

5. Interpreting measured data on Feather-M2

In this section, an implementation of the thermal model, formulated in section 3, is utilized for investigating the thermal behavior of Feather-M2 in various operation conditions. The measurement data on the magnet shown in figure 2 is utilized for obtaining values for the unknown parameters of the thermal model as a solution of an inverse problem (14).

The simulation tool was programmed on top of the *dp* framework [25] using Matlab [26]. *Field* was utilized for creating the magnet geometry and for pre-computing the magnetic field in three-dimensional magnet geometry [27]. For solving the heat diffusion equation, the numerical method presented in [28] was utilized. In solving the inverse problems, the optimization algorithm presented in [29] was utilized.

Next, we formulate the thermal problem and solve the inverse problems in all the measured cases in order to obtain solutions for the model parameters. From all of the solutions, we choose the inverse problem solution \mathbf{x} that resulted in smallest difference between E and $M(\mathbf{x}, I_{\text{op}})$ as a function of time. Using those parameter values, we benchmark the model against all the measured cases in order to study the predictive capability of the thermal model.

Table 4. References for the material properties.

Material	Property	Reference
Cu	C_V, λ, ρ	[31]
G10	C_V, λ	[31]
Hastelloy	C_V, λ, ρ	[32]
Ag	C_V	[33]
Ag	λ, ρ	[34]

5.1. Problem formulation

The problem is formulated, or instantiated, by fixing the material properties and other known parameters. Starting from the magnet geometry, depicted in figure 1 and specified in table 1, the heat equation (1) is discretized for one-dimensional modelling domain as explained in section 3. The material properties for computing C_V and λ in (1), and the resistivity ρ_{nc} in (9), are obtained from the references listed in table 4, where the electrical resistivity of Silver was calculated from λ using the Wiedemann–Franz law. The REBCO material, in the sense of C_V and λ , is considered as G10. The material fractions are calculated using the cable and tape specifications listed in tables 2 and 3, respectively. The critical current I_c in (5) is computed using a J_c scaling law fitted to match with measurement data on REBCO tape manufactured by Fujikura [30]. The scaling law is described in [8, p 246–248]. Moreover, in regards of (10), an assumption on constant temperature outside magnet’s winding is deployed.

The wetted perimeter p in the cooling model (10) is determined as follows. Figure 5 shows the Feather-M2 cross-section of the upper magnet pole during operation⁴. According to the study [35], during magnet operation, the winding detaches from the pole. Using this result, we choose the wetted perimeter such that the cooling is neglected from the inner wide face of the innermost cable turns, i.e. we assume a vacuum in those spaces. Therefore, the wetted perimeter in the inner turns is $p = 2d_t$. In the outermost turns of the wing and central decks $p = d_w + 2d_t$. In the rest of the turns in between $p = 2d_t$, i.e. cooling flux affects through the narrow faces of cable.

Furthermore, in solving the inverse problem (14), the lower bounds \mathbf{b}_l and the upper bounds \mathbf{b}_u for the optimization parameters are shown in table 5. Next, the solutions of the inverse problems presented.

5.2. Inverse problem solutions

The inverse problem is solved for each of the measured cases shown in figure 2. The solutions of the model parameters, \mathbf{x}_i , are shown in table 6. Figure 6 shows, in each of the cases, the measured average electric field and the prediction of the model, parametrized with the corresponding solution.

The difference between the model predictions and the experimental data is calculated as the relative and maximum

⁴ In this particular study, a different cable was utilized. Therefore the magnet has more cable turns than in the design investigated in this work.

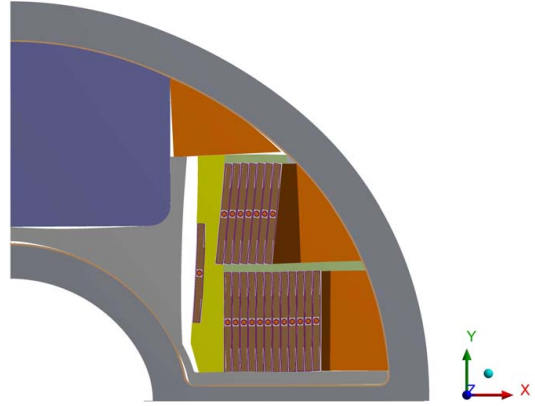


Figure 5. An exaggerated view on the deformation of the magnet’s cross-section during its operation. A quarter of magnet’s cross-section is shown.

Table 5. Lower- and upper bounds for the model parameters.

Parameter	\mathbf{b}_l	\mathbf{b}_u	Unit
α	0.1	0.3	
n	1	30	
E_c	1	150	$\mu\text{V m}^{-1}$

Table 6. The solutions of the inverse problems.

	α	n	E_c	h	T_{op}
\mathbf{x}_1	0.17	2.3	102	69	6
\mathbf{x}_2	0.17	2.8	109	85	21
\mathbf{x}_3	0.16	3.1	91	55	21
\mathbf{x}_4	0.18	3.0	108	45	21
\mathbf{x}_5	0.15	2.9	84	75	21
\mathbf{x}_6	0.17	2.9	90	77	32
\mathbf{x}_7	0.17	3.3	87	86	32
\mathbf{x}_8	0.19	2.8	74	60	48
\mathbf{x}_9	0.20	2.5	72	42	50
\mathbf{x}_{10}	0.19	3.1	10	44	70
unit			$\mu\text{V m}^{-1}$	$\text{W m}^{-2} \text{K}^{-1}$	K

difference. The relative difference Δ_r is calculated as

$$\Delta_r = 1 - \frac{\int_0^{t_m} (M(\mathbf{x}, I_{op}))(t) dt}{\int_0^{t_m} E(t) dt} \tag{15}$$

and the maximum difference Δ_m as

$$\Delta_m = \max\{|(E - M(\mathbf{x}, I_{op}))(t)|\}, t \in [0, t_m]. \tag{16}$$

According to the relative differences shown in table 7, the best solution was found in the case 6, where the relative difference was 0.4% and the maximum difference was $4 \mu\text{V m}^{-1}$. The solved parameter values in each of the 10

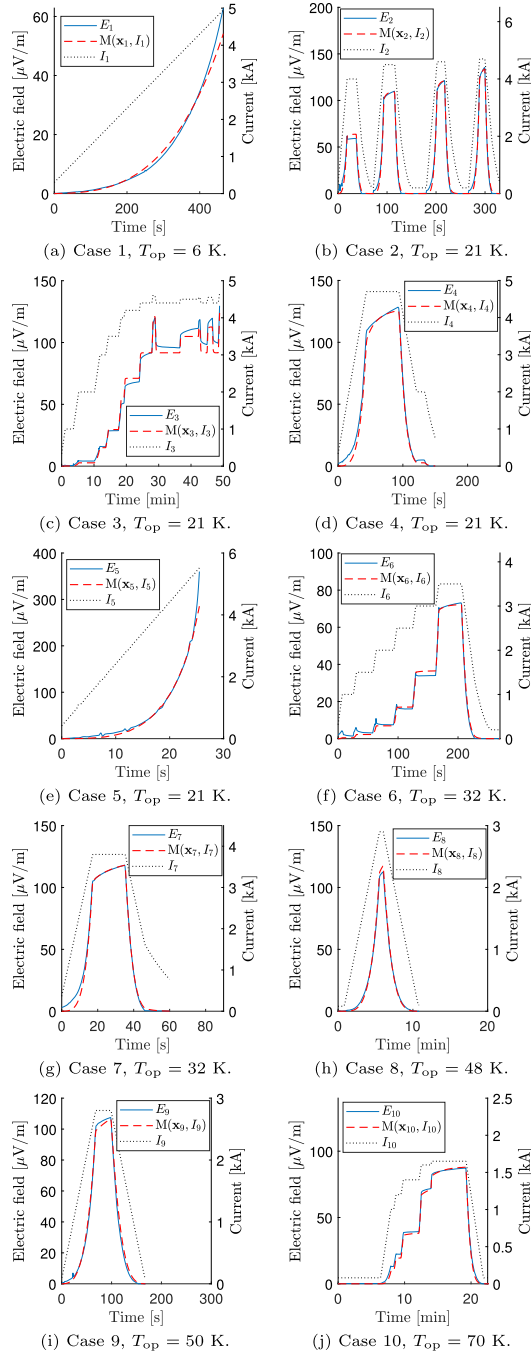


Figure 6. Figures (a)–(j) represent, in each case $i = 1..10$, the measured and simulated average electric field E_i as a function of the operation current I_i and time in Feather-M2.

Table 7. Relative and maximum differences of the inverse problem solutions.

Case	Δ_r (%)	Δ_m ($\mu\text{V m}^{-1}$)	T_{op} (K)
1	1.5	9	6
2	0.9	10	21
3	2.8	9	21
4	5	11	21
5	5.6	75	21
6	0.4	4	32
7	2.6	9	32
8	-0.7	5	48
9	-1.9	6	50
10	2.4	4	70

cases are shown in table 6. The parameters that vary the most from case to case are E_c and h while the variance in α and n is smaller.

The results suggest relatively low n -values, i.e. between 2.3 and 3.1. Similar low n -values have also been reported in the original test results of Feather-M2 [7]. The reason for the low n can be related to the J_c (or I_c) variation between the different tapes in the cable [36].

Based on the results, no systematic relation were found between a case and its solution. The reason for this can be that all the cases represent very different operation conditions. Moreover, as the cooling of the magnet was realized with forced flow helium gas, the cooling efficiency can vary significantly in the cryostat. In addition, we had no data on, whether the flow rate of the helium gas was kept the same in all of the measured cases. As for the future analysis of this kind, simpler measurements could be more useful, where the operation current could be ramped up close to a maximum current at which the magnet could be operated for long time at constant operation current. With such measurement, the parameters related to the heat generation could be found and the constant operation current phase would give information on the balance between heat generation and cooling, making it possible to find a solution for the cooling coefficient.

5.3. Predictiveness of the thermal model

Next we study, how well the thermal model is able to predict the magnet behavior in various different operation conditions. This is done by fixing the model with parameter values corresponding to the best solution. Hence, we chose the parameter values of the solution \mathbf{x}_6 and utilized the model M to test if it was able to predict the thermal behavior of Feather-M2 in all of the investigated cases. The solution was obtained using the data measured at 32 K operation temperature. The results are shown in figure 7 and table 8.

According to the results, it can be noticed that the model is not able to describe the magnet behavior in the whole range of operation temperatures (5–70 K). Relatively good predictions are obtained in the cases where the operation

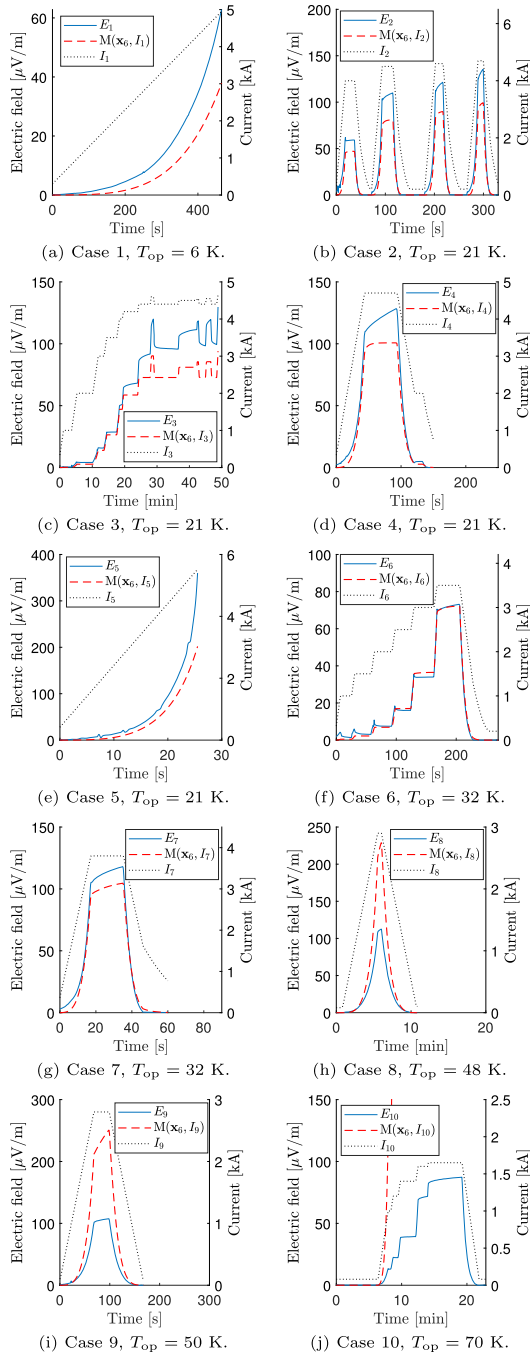


Figure 7. Figures (a)–(j) represent, in each case $i = 1 \dots 10$, the measured and simulated average electric field E_i as a function of the operation current I_i and time in Feather-M2. Simulations were performed using parameter values of the solution \mathbf{x}_6 .

Table 8. Relative and maximum differences of $M(\mathbf{x}_6)$ in all of the simulation cases. In case 10, the differences could not be computed due to the early thermal runaway.

Case	Δ_r (%)	Δ_m ($\mu\text{V m}^{-1}$)	T_{op} (K)
1	44.0	25	6
2	26.8	36	21
3	22.5	36	21
4	18.7	28	21
5	31.6	158	21
6	0.4	4	32
7	10.5	13	32
8	-81.9	116	48
9	-113.4	144	50
10	—	—	70

temperature is 21–32 K. Clearly, the linear cooling model (10) does not work well if the operation temperature is significantly different compared to the case at which the value was obtained as a solution of an inverse problem. This is especially visible in figure 7(j) where the model $M(\mathbf{x}_6)$ predicts the magnet to quench in the case 10 where T_{op} was 70 K. Moreover, if T_{op} was higher than in the case 6, the model predicted higher values for electric field than measured. If T_{op} was lower, than in case 6, the model predicted too low electric field. This indicates too that the cooling model should be more detailed if better correspondence is searched for.

In case 7, the difference was the smallest with differences of $\Delta_r = 10.5$ and $\Delta_m = 13$. In both cases, T_{op} is the same and the model is able to describe magnet's behavior relatively well.

5.4. Prospects and outlook

Next, as an outlook, discussion on the prospects of the developed simulation tool is carried out using an example of one possible use of the simulation tool as follows. Given that, the computational model is parametrized such that it is able to predict $E(I_{op})$ behavior of an HTS magnet in some operation conditions. Then, using the simulation tool, investigations could be done on the behavior of the magnet if it was made of cable having higher J_c or steeper $E_{sc}(J_c)$ relation in the sense of n -value. To demonstrate the use of the tool in the described situation, a parametric study for n -value and α was done in case 5 using the inverse problem solution \mathbf{x}_5 as the reference values for the parameters.

The average electric field, the maximum temperature in the magnet (T_{max}), and its time derivative were computed for n -values from 3 to 30 while keeping the other parameter values at \mathbf{x}_5 . The simulation results of this parametric study are shown in figure 8. As could have been expected, the electric field, shown in figure 8(a), develops faster with higher values of n . The maximum temperature in the magnet develops relatively fast too as shown in figure 8(b). This is visible also in figures 8(c) and (d), where T_{max} and the time derivative of T_{max} as a function of electric field E are shown,

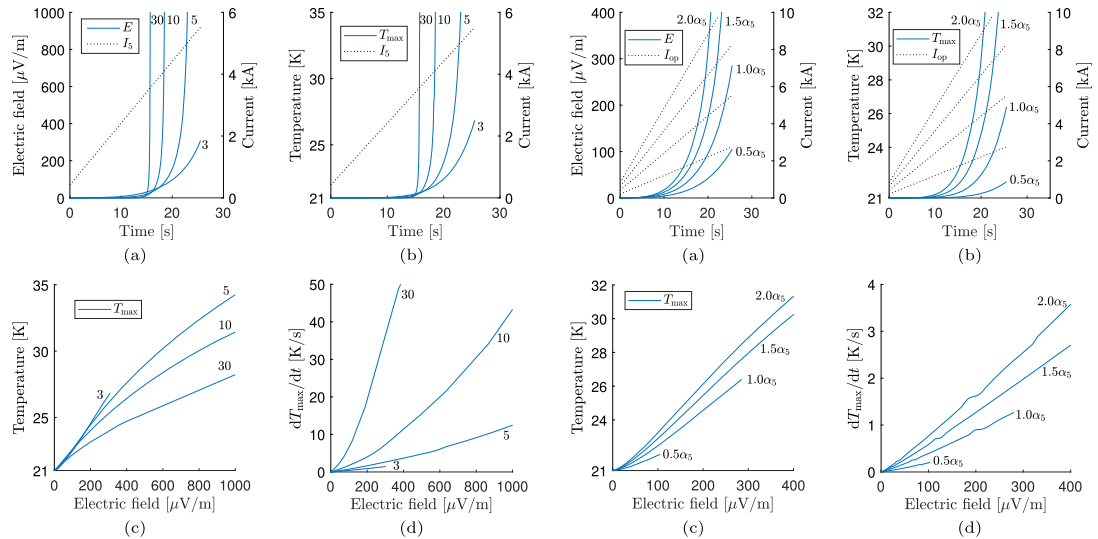


Figure 8. In (a) and (b), the average electric field E and the maximum temperature T_{max} in the magnet as a function of operation current and time for n -values 3, 5, 10 and 30 is shown, respectively. In (c) and (d), T_{max} and its time derivative as a function of E is shown, respectively. The other parameters of the model were kept at x_5 . The graphs are labeled with the corresponding n -values.

Figure 9. In (a)–(d), the same quantities are shown as in figure 8 for different scale values of the J_c scaling law. The other model parameter values were kept at x_5 . The utilized scale values were $0.5\alpha_5, 1.0\alpha_5, 1.5\alpha_5$ and $2.0\alpha_5$, where $\alpha_5 = 0.15$ as in x_5 . The graphs are labeled with the corresponding scales. The operation current I_{op} is obtained by scaling I_5 with 0.5, 1.0, 1.5 and 2.0.

respectively. For example with n -value of 10, at E of $200 \mu\text{V m}^{-1}$ corresponding to T_{max} of 26.5 K, the time derivative of T_{max} is already 11 K s^{-1} . Based on these results, further investigations on the protectability of the magnet could be done for example.

The scale α of J_c law was varied and the other parameters were kept constant in order to investigate a situation where the magnet was made of different cables each having different critical current density. The utilized J_c scaling law was scaled with $0.5\alpha_5, 1.0\alpha_5, 1.5\alpha_5$ and $2.0\alpha_5$, where $\alpha_5 = 0.15$ as in x_5 . Respectively, the magnitude of the operation current was scaled with factors 0.5, 1.0, 1.5 and 2.0. The same simulations were performed in this case as done in studying the effects of different n -values. The simulation results are shown in figure 9. The results show that it could be beneficial to have low n -value cable with high electric current carrying capability. Thus, the T_{max} development would be gradual and there would be more time for protecting the magnet in case of unexpected rising in voltage, as shown in figures 9(c) and (d) where at $E = 400 \mu\text{V m}^{-1}$, corresponding to $T_{max} = 31 \text{ K}$, the time derivative of T_{max} is only 3.5 K s^{-1} .

6. Conclusions

In order to study the thermal behavior of an HTS dipole magnet Feather-M2, a thermal model was formulated and parametrized. The parameters were obtained as a solution of inverse problems in 10 cases. These represent various

observed magnet behaviors in test cryostat (different operation temperature, operation current and average electric field timeseries). The simulation results show that individual inverse problems could find such model parameters that the corresponding behavior could be very well replicated. The model corresponded to the measured average electric field over the magnet with the average relative and the average maximum absolute difference of 2.4% and $15 \mu\text{V m}^{-1}$, respectively, for the ten cases.

When the parameters obtained from one particular inverse problem (32 K and staircase like current ramp for about 4 min) were applied to simulate other experimented electric field timeseries, the correspondence between observations and model deteriorated. The smallest error was achieved at the same operation temperature for another current timeseries: the relative error in the average electric field was 10.5%. At lower temperatures the simulated electric field underestimated the measured electric field whereas at higher temperature it overestimated it. In one case (at 70 K), the model predicted an early thermal runaway that was not observed. Possible reasons, that the model prediction capability deteriorated for other cases than for which the model parameters were solved for, can be related to the simplified cooling model—or for example to the fact that the helium gas flow rate was not possible to measure during the experiments.

The presented methodology, in which model parameters are solved from an inverse problem, can be utilized in investigating the predictive capability of computational models and their sub-models such as the cooling model in this

work. Moreover, the presented simulation tool can be utilized to predict the behavior of a magnet under study in different operation conditions to ensure safe operation.

ORCID iDs

J Ruuskanen  <https://orcid.org/0000-0001-9551-0086>

V Lahtinen  <https://orcid.org/0000-0002-3054-7571>

J van Nugteren  <https://orcid.org/0000-0001-8072-7725>

References

- [1] Winkler T and EcoSwing Consortium 2019 *IOP Conf. Ser.: Mater. Sci. Eng.* **502** 012004
- [2] van Nugteren J, Kirby G, Murtomaki J, DeRijk G, Rossi L and Stenvall A 2018 *IEEE Trans. Appl. Supercond.* **28** 4008509
- [3] Yanagi N et al 2014 *IEEE Trans. Appl. Supercond.* **24** 4202805
- [4] Goldacker W et al 2007 *IEEE Trans. Appl. Supercond.* **17** 3398
- [5] Rossi L et al 2018 *IEEE Trans. Appl. Supercond.* **28** 4001810
- [6] The European Organization for Nuclear Research, Geneva, Switzerland
- [7] van Nugteren J et al 2018 *Supercond. Sci. Technol.* **31** 065002
- [8] van Nugteren J 2016 High temperature superconducting accelerator magnets *Doctoral Thesis* University of Twente, Twente, Netherlands
- [9] Härö E et al 2013 *IEEE Trans. Appl. Supercond.* **23** 4600104
- [10] Ruuskanen J, Stenvall A and Lahtinen V 2017 *IEEE Trans. Appl. Supercond.* **27** 0600205
- [11] Breschi M, Cavallucci L, Ribani P L, Gavrilin A V and Weijers H W 2016 *Supercond. Sci. Technol.* **29** 055002
- [12] Denis M W, Jaroszynski J, Abraimov D, Joyner R and Khan A 2015 *Supercond. Sci. Technol.* **29** 025001
- [13] Hahn S, Park D, Bascunan J and Iwasa Y 2011 *IEEE Trans. Appl. Supercond.* **21** 1592
- [14] Lehtonen J, Mikkonen R and Paasi J 1998 *Physica C* **310** 340
- [15] Ishiyama A and Asai H 2001 *IEEE Trans. Appl. Supercond.* **11** 1832
- [16] Vysotsky V S, Rakhmanov A L and Ilyin Y A 2008 Novel approaches to describe stability and quench of HTS devices *Superconductivity Research Developments* (Commack, NY, USA: Nova) ch 9
- [17] Rostila L et al 2007 *Supercond. Sci. Technol.* **20** 1097
- [18] Nättilä J 2017 X-ray bursts as a tool to constrain the equation of state of the ultra-dense matter inside neutron stars *Doctoral Thesis* University of Turku
- [19] van Nugteren J et al 2018 *IEEE Trans. Appl. Supercond.* **28** 4901505
- [20] Ruuskanen J, Stenvall A, Lahtinen V, van Nugteren J, Kirby G and Murtomaki J 2019 *IEEE Trans. Appl. Supercond.* **29** 4701204
- [21] SuperOx, 2G HTS wire
- [22] SuNAM Co., Ltd., Superconducting Wire
- [23] Chambrillon J et al 2011 *CERN SRF assembling and test facilities Proc. SRF11* vol 5 (Chicago) pp 530–2
- [24] Stenvall A, Korpela A, Mikkonen R and Grasso G 2006 *Supercond. Sci. Technol.* **19** 184
- [25] Stenvall A Platform for programming finite element method solvers in Matlab
- [26] MATLAB, The MathWorks, Inc., Natick, Massachusetts, United States.
- [27] van Nugteren J 2011 Internship report: CERN, software development for the science and design behind superconducting magnet systems *Tech. Rep.* University of Twente: Energy Materials and Systems and CERN: ATLAS magnet team
- [28] Hosea M E and Shampine L F 1996 *Appl. Numer. Math.* **20** 21
- [29] Byrd R, Gilbert J and Nocedal J 2000 *Math. Program.* **89** 149
- [30] Fujikura Europe Ltd., 2G YBCO High Temperature Superconductors
- [31] Manfreda G ‘Review of ROXIE’s Material Properties Database for Quench Simulation’, CERN Internal Note 2011-24, EDMS 1178007.
- [32] Lu J, Choi E S and Zhou H D 2008 *J. Appl. Phys.* **103** 064908
- [33] Smith D R and Fickett F R 1995 *J. Res. Natl Inst. Stand. Technol.* **100** 119
- [34] Naito T et al 2010 *Supercond. Sci. Technol.* **23** 105013
- [35] Murtomaki J, van Nugteren J, Kirby G, Rossi L, Ruuskanen J and Stenvall A 2017 *IEEE Trans. Appl. Supercond.* **27** 4100405
- [36] Edelman H S and Larbalestier D C 1993 *J. Appl. Phys.* **74** 3312–5

